

20 January 2012 | \$10

Science

 AAAS

EDITORIAL

- 263 Trivializing Science Education
Bruce Alberts

NEWS OF THE WEEK

- 268 A roundup of the week's top stories

NEWS & ANALYSIS

- 272 A Tantalizing View of What Set Off Japan's Killer Quake
>> Science Express Report by A. Kato et al.
- 273 Engineered Superbugs Boost Hopes of Turning Seaweed Into Fuel
>> Research Article p. 308
- 274 Report Notes China's Influence in Emerging Asian Science Zone
- 276 Society for Integrative and Comparative Biology Meeting
Heads-Up on a Whale's Gulp
Robotic Fish Point to Schooling Gene
Clingfish Stick Like Geckos

NEWS FOCUS

- 278 Patrick Feaster: Archaeologist of Sound
- 281 Explaining Exercise
- 282 Experimental Cancer Therapies Move to the Front Line
>> Science Podcast

LETTERS

- 284 Good News for European Vultures
A. Margalida et al.
Global Endemism Needs Spatial Integration
F.-M. Lei
Response
B. Sandel et al.
Readers' Poll Results:
The Well-Behaved Scientist
- 286 TECHNICAL COMMENT ABSTRACTS
- 286 CORRECTIONS AND CLARIFICATIONS

BOOKS ET AL.

- 287 Remedy and Reaction
P. Starr, reviewed by J. Oberlander
- 288 DDT and the American Century
D. Kinkela, reviewed by F. R. Davis

POLICY FORUM

- 289 What Next for Agriculture After Durban?
J. R. Beddington et al.

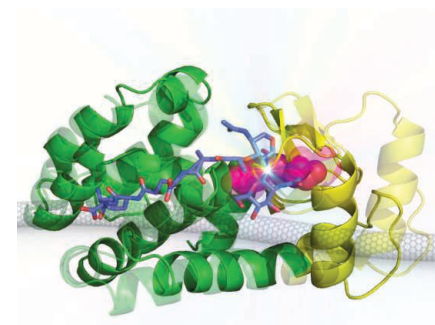
PERSPECTIVES

- 292 Bird-Brained Illusionists
B. L. Anderson
>> Report p. 335
- 293 Taking a Back Door to Target Myc
G. Evan
>> Report p. 348
- 294 Moving Beyond Trust in Quantum Computing
V. Vedral
>> Research Article p. 303
- 296 The Final Flight of a Sun-Diving Comet
C. M. Lisse
>> Report p. 324
- 297 Transforming Earthquake Detection?
R. M. Allen
- 299 Sowing the Seeds of Centromeres
L. E. T. Jansen
- 300 Enzymes in Coherent Motion
H. P. Lu
>> Report p. 319
- 302 Retrospective: Lynn Margulis (1938–2011)
M. Schaechter

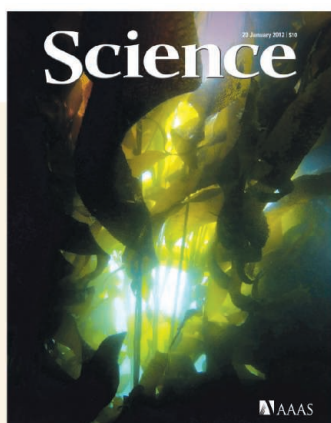
CONTENTS continued >>



page 278



pages 300 & 319



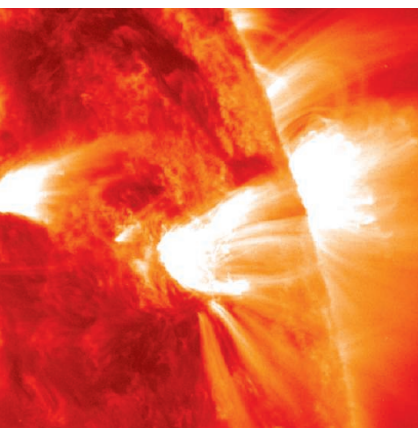
COVER

Brown seaweed (*Macrocystis pyrifera*), commonly known as giant kelp, off the coast of Chiloe Island, Chile (image width ~1 meter). Traditionally, seaweed has been ignored as a source of renewable fuel and chemical compounds for bioconversion, because its primary sugar component is not easily fermented. Wargacki *et al.* engineered a microbe to extract sugars from brown seaweed and convert them into low-carbon, renewable fuels and chemicals. See page 308.

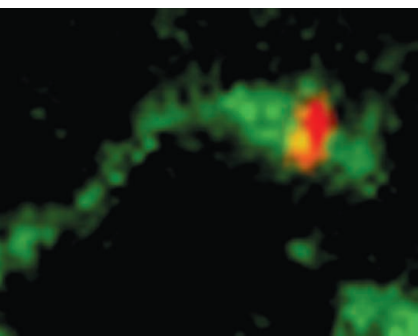
Photo: Julián Fernández

DEPARTMENTS

- 261 This Week in *Science*
- 264 Editors' Choice
- 266 *Science* Staff
- 357 New Products
- 358 *Science* Careers



pages 296 & 324



page 332



pages 292 & 335

RESEARCH ARTICLES

- 303** **Demonstration of Blind Quantum Computing**
S. Barz et al.
 A protocol is implemented that can ensure secure client-server interactions on a quantum computer architecture.
 >> *Perspective p. 294*
- 308** **An Engineered Microbial Platform for Direct Biofuel Production from Brown Macroalgae**
A. J. Wargacki et al.
 Metabolic engineering showcases a preliminary route to generating ethanol from seaweed.
 >> *News story p. 273*

REPORTS

- 314** **Synthetic Partial Waves in Ultracold Atomic Collisions**
R. A. Williams et al.
 A pair of lasers is used produce complex interactions between bosons in an ultracold gas.
- 317** **Visualizing Gas Molecules Interacting with Supported Nanoparticulate Catalysts at Reaction Conditions**
H. Yoshida et al.
 Electron microscopy reveals how adsorbed carbon monoxide molecules restructure the surface of gold nanoparticles.
- 319** **Single-Molecule Lysozyme Dynamics Monitored by an Electronic Circuit**
Y. Choi et al.
 Changes in protein conformation can be detected via changes in electrostatic potential with a carbon nanotube transistor.
 >> *Perspective p. 300*
- 324** **Destruction of Sun-Grazing Comet C/2011 N3 (SOHO) Within the Low Solar Corona**
C. J. Schrijver et al.
 The NASA Solar Dynamics Observatory detected and tracked a comet as it penetrated the solar atmosphere.
 >> *Perspective p. 296; Science Podcast*
- 328** **Polymerase Exchange During Okazaki Fragment Synthesis Observed in Living Cells**
G. Lia et al.
 Single-molecule microscopy suggests that a new core polymerase is used to synthesize each Okazaki fragment.

- 332** **Manganese Blocks Intracellular Trafficking of Shiga Toxin and Protects Against Shiga Toxicosis**
S. Mukhopadhyay and A. D. Linstedt
 Manganese may represent a low-cost therapeutic agent for the treatment of a type of *Escherichia coli* food poisoning.
 >> *Science Podcast*
- 335** **Illusions Promote Mating Success in Great Bowerbirds**
L. A. Kelley and J. A. Endler
 Males that are more successful at tricking female senses mate more often.
 >> *Perspective p. 292*
- 338** **Activation-Induced B Cell Fates Are Selected by Intracellular Stochastic Competition**
K. R. Duffy et al.
 Cell-fate decisions in activated B lymphocytes are determined by stochastic competition.
- 342** **Asymmetric B Cell Division in the Germinal Center Reaction**
B. E. Barnett et al.
 Germinal center B cells undergo asymmetric cell division.
- 344** **Tuning of Natural Killer Cell Reactivity by NKp46 and Helios Calibrates T Cell Responses**
E. Narni-Mancinelli et al.
 The activating receptor NKp46 is important for keeping the responses of natural killer cells in check.
- 348** **A SUMOylation-Dependent Transcriptional Subprogram Is Required for Myc-Driven Tumorigenesis**
J. D. Kessler et al.
 An RNA interference screen identifies a "druggable" enzyme whose inhibition halts tumor cell growth.
 >> *Perspective p. 293*
- 353** **Locally Synchronized Synaptic Inputs**
N. Takahashi et al.
 The computational power of individual neurons is determined by a surprisingly precise wiring of neuronal networks.

SCIENCEONLINE

SCIENCEEXPRESS

www.sciencexpres.org

Propagation of Slow Slip Leading Up to the 2011 M_w 9.0 Tohoku-Oki Earthquake

A. Kato et al.

Two sequences of slow slip preceded and migrated toward the main rupture.

10.1126/science.1215141

>> *News story p. 272*

Determination of Noncovalent Docking by IR Spectroscopy of Cold Gas-Phase Complexes

E. Garand et al.

Conformationally freezing a weakly bound complex in the gas phase sheds light on its likely binding motifs in solution.

10.1126/science.1214948

Biased Signaling Pathways in β_2 -Adrenergic Receptor Characterized by ^{19}F -NMR

J. J. Liu et al.

Selective effects of different ligands provide insights into the structural plasticity of receptor signaling.

10.1126/science.1215802

Rescued Tolerant CD8 T Cells Are Preprogrammed to Reestablish the Tolerant State

A. Schietinger et al.

Maintenance of T cell tolerance is likely regulated by epigenetic mechanisms.

10.1126/science.1214277

Restricted Data on Influenza H5N1 Virus Transmission

R. Fouchier et al.

10.1126/science.1218376

H5N1 Debates: Hung Up on the Wrong Questions

D. R. Perez

10.1126/science.1219066

Life Sciences at a Crossroads: Respiratory Transmissible H5N1

M. Osterholm and D. A. Henderson

10.1126/science.1218612

The Limits of Government Regulation of Science

J. Kraemer and L. Gostin

10.1126/science.1219215

TECHNICALCOMMENTS

Comment on "Probing the Ultimate Limit of Fiber-Optic Strain Sensing"

G. A. Cranch and S. Foster

Full text at www.sciencemag.org/cgi/content/full/335/6066/286-a

Response to Comment on "Probing the Ultimate Limit of Fiber-Optic Strain Sensing"

G. Gagliardi et al.

Full text at www.sciencemag.org/cgi/content/full/335/6066/286-b

SCIENCENOW

www.sciencenow.org

Highlights From Our Daily News Coverage

Scientists Create World's Tiniest Ear

'Nano-ear' detects sound a million times fainter than our ears can hear.

http://scim.ag/Tiniest_Ear

New Animal Virus Takes Northern Europe by Surprise

Agent causes stillbirths and is 'a serious threat to animal health,' scientists say.

http://scim.ag/Animal_Virus

Global Warming May Trigger Winter Cooling Arctic melting can lead to cooler temperatures and increased snowfall.

http://scim.ag/Winter_Cooling

SCIENCE SIGNALING

www.sciencesignaling.org

The Signal Transduction Knowledge Environment
17 January issue: <http://scim.ag/ss011712>

RESEARCH ARTICLE: Interleukin-11 Links Oxidative Stress and Compensatory Proliferation

T. Nishina et al.

Dying liver cells produce a cytokine that triggers healthy neighboring cells to proliferate.

RESEARCH ARTICLE: Plexins Are GTPase-Activating Proteins for Rap and Are Activated by Induced Dimerization

Y. Wang et al.

Semaphorin-mediated growth cone collapse may result from the Rap GTPase-activating protein activity of dimerized plexin receptors.

PERSPECTIVE: A Sweet Spot in the FGFR Signal Transduction Pathway

A. S. Ghabrial

Signaling through the fibroblast growth factor receptors Heartless and Breathless requires O-GlcNAcylation of an adaptor protein.

PERSPECTIVE: LRRK2 and Human Disease—A Complicated Question or a Question of Complexes?

P. A. Lewis and C. Manzoni

The kinase LRRK2 is genetically linked to diverse pathologies, including Parkinson's and Crohn's diseases.

GLOSSARY

Find out what HCN, CRISP, and SACO mean in the world of cell signaling.

SCIENCE TRANSLATIONAL MEDICINE

www.sciencetranslationalmedicine.org

Integrating Medicine and Science

18 January issue: <http://scim.ag/stm011812>

RESEARCH ARTICLE: Skin Effector Memory T Cells Do Not Recirculate and Provide Immune Protection in Alemtuzumab-Treated CTCL Patients

R. A. Clark et al.

FOCUS: Immunology Taught By Humans

M. M. Davis

A therapeutic antibody depletes malignant T cells but spares skin resident effector memory T cells, treating L-CTCL without increased risk of infection.

RESEARCH ARTICLE: *Notch4* Normalization Reduces Blood Vessel Size in Arteriovenous Malformations

P. A. Murphy et al.

FOCUS: Arteriovenous Malformations in Five Dimensions

J. Kitajewski

Correction of Notch expression restores enlarged blood vessels to microvessels through EphB4-mediated reprogramming of arterial endothelial cells.

RESEARCH ARTICLE: Cigarette Smoke Induction of Osteopontin (SPP1) Mediates $\text{T}_\text{H}17$ Inflammation in Human and Experimental Emphysema

M. Shan et al.

The destruction of lung tissue in emphysema is orchestrated by antigen-presenting cells that have been activated by smoke.

SCIENCE CAREERS

www.sciencereers.org/career_magazine

Free Career Resources for Scientists

Tooling Up: Forecasting the Fit

D. Jensen

Is your work style a match for your prospective boss?

http://scim.ag/TU_ForecastingFit

Genetic Engineering on Steroids

V. Venkatraman

Synthetic biologist Ron Weiss has moved from programming computers to programming cells.

<http://scim.ag/RonWeissProfile>

SCIENCE PODCAST

www.sciencemag.org/multimedia/podcast

Free Weekly Show

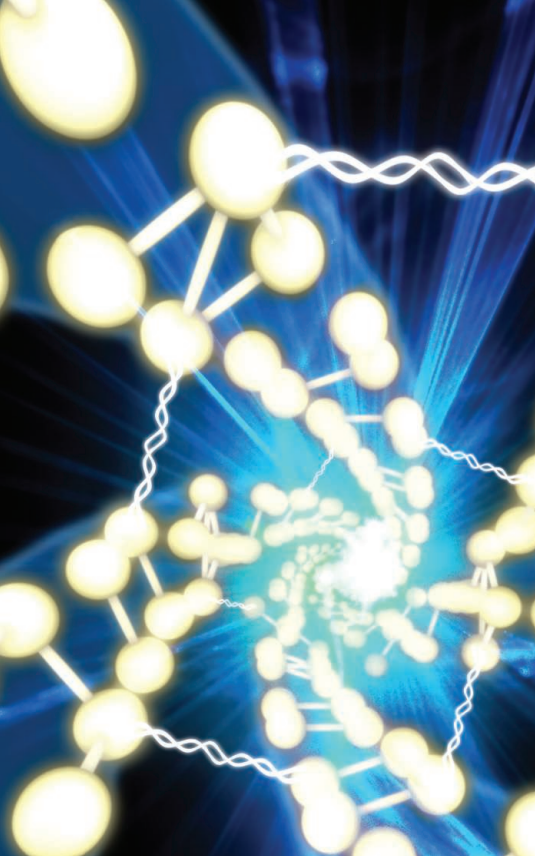
On the 20 January *Science* Podcast: a Sun-grazing comet, protecting against the shiga toxin, the risks of experimental cancer therapies, and more.

SCIENCE (ISSN 0036-8075) is published weekly on Friday, except the last week in December, by the American Association for the Advancement of Science, 1200 New York Avenue, NW, Washington, DC 20005. Periodicals Mail postage (publication No. 484460) paid at Washington, DC, and additional mailing offices. Copyright © 2012 by the American Association for the Advancement of Science. The title SCIENCE is a registered trademark of the AAAS. Domestic individual membership and subscription (51 issues): \$149 (\$74 allocated to subscription). Domestic institutional subscription (51 issues): \$990; Foreign postage extra: Mexico, Caribbean (surface mail) \$55; other countries (air assist delivery) \$85. First class, airmail, student, and emeritus rates on request. Canadian rates with GST available upon request, GST #1254 88122. Publications Mail Agreement Number 1069624. Printed in the U.S.A.

Change of address: Allow 4 weeks, giving old and new addresses and 8-digit account number. **Postmaster:** Send change of address to AAAS, P.O. Box 96178, Washington, DC 20090-6178. **Single-copy sales:** \$10.00 current issue, \$15.00 back issue prepaid includes surface postage; bulk rates on request. **Authorization to photocopy** material for internal or personal use under circumstances not falling within the fair use provisions of the Copyright Act is granted by AAAS to libraries and other users registered with the Copyright Clearance Center (CCC) Transactional Reporting Service, provided that \$30.00 per article is paid directly to CCC, 222 Rosewood Drive, Danvers, MA 01923. The identification code for *Science* is 0036-8075. *Science* is indexed in the *Reader's Guide to Periodical Literature* and in several specialized indexes.



ADVANCING SCIENCE. SERVING SOCIETY



Quantum Blindness

While quantum computers offer speed advantages over their classical counterparts, the technological challenges facing their eventual realization suggest that they will need to be located in specialized facilities. Thus, interaction would then need to be on a quantum client:quantum server basis. **Barz et al.** (p. 303; see the Perspective by **Vedral**) implemented a proof-of-principle protocol that illustrates complete security in such a setup—for both the client and the server. In this blind quantum computing protocol, the client maintains the security of their data and the specifics of the calculation they want to perform, and the server cannot access the data or calculation of the client.

Sourced from Seaweed

Using seaweed as a raw material for bio-fuels has received relatively little attention, in part because their primary sugar constituent, alginate, is not readily fermented by industrially tractable microbes. **Wargacki et al.** (p. 308; see the cover) now demonstrate that metabolically engineered bacteria can degrade seaweed and subsequently ferment the sugars into ethanol at laboratory scale.

Tracking Reaction Surfaces

Gold becomes a remarkably active catalyst for CO oxidation when it is dispersed as nanoparticles

on the surface of reducible metal oxides such as ceria, so much so that the reaction proceeds at room temperature. **Yoshida et al.** (p. 317) used an aberration-corrected, environmental transmission electron microscope to follow the changes in both ceria-supported gold nanoparticles and the adsorbed species for this reaction.

Observing Protein Dynamics

Following the dynamics of protein conformational changes over the relatively long periods of time typical of enzyme kinetics can be challenging. **Choi et al.** (p. 319; see the Perspective by **Lu**) were able to observe changes in lysozyme conformation, which changes its electrostatic potential, by using a carbon-nanotube field-effect transistor. Slower hydrolysis steps were compared with faster, but unproductive, hinge motion, and changes in lysozyme activity that occur with pH were shown to arise from differences in the relative amount of time spent in processive versus nonprocessive states.

Star Grazing

Some comets come perilously close to the Sun. **Schrijver et al.** (p. 324; see the Perspective by **Lisse**) describe observations made by the Solar Dynamics Observatory of one such Sun-grazing comet, which penetrated into, fragmented, and completely sublimated within the solar atmosphere. More than 2000 Sun-grazing comets have been observed in the past 15 years but none could be followed into the Sun's atmosphere. By showing that comets can be observed at such small distances from the Sun, this study opens up new ways to study comets and also the solar atmosphere.

Dynamic Replication

In all organisms, DNA replication involves a multiprotein complex called the replisome. Active *Escherichia coli* replisomes contain three copies of DNA polymerase III (Pol III). **Lia et al.** (p. 328, published online 22 December) used single-molecule spectroscopy to probe the dynamics of single proteins during *E. coli* replication in vivo. The results confirmed the presence of three Pol III molecules in the active replisome, with regular exchange of one of these Pol III's with one from the pool. Coordination with single-stranded DNA content suggests the Pol III that performs lagging-strand synthesis is exchanged so that a new Pol III is used for the synthesis of each Okazaki fragment.

Shunning Shiga

Infection with bacteria harboring Shiga toxin is responsible for more than 1 million deaths annually worldwide. Antidotes for the toxin are not available, and treatment with antibiotics is contraindicated because it increases the risk of toxin release (from dead bacteria) and leads to severe forms of the disease. Manganese is an essential nutrient and its toxicology in humans is well studied; it inhibits the normal trafficking of Shiga toxin in tissue culture cells. **Mukhopadhyay and Linstedt** (p. 332) found that levels of Mn^{2+} that caused no deleterious effects to normal cellular processes nevertheless altered intracellular trafficking of Shiga toxin so that it was degraded in lysosomes. This conferred very high levels of protection of cultured cells against toxin-induced death and made mice completely resistant to Shiga toxin-induced paralysis and death.

Extending the Range

Ultracold atomic gases are attractive for quantum simulations of condensed-matter systems because of their tunability; however, while the strength of interactions can be tuned, their range is effectively zero.

Williams et al. (p. 314, published online 8 December) used a pair of Raman lasers to modify the interaction between two colliding Bose-Einstein condensates to include beyond-*s*-wave (*d*- and *g*-wave) contributions. This technique should enable the simulation of more complicated solid-state systems, including those supporting exotic superfluidity.

Trick of the Eye of the Beholder

Male bowerbirds build elaborate bowers, or display areas, that consist of an avenue where the female stands and an arena where the male displays. Males decorate their arenas meticulously with stones, flowers, and found objects. Previous work has shown that these bowers induce forced perspective illusions in the observing females. Now **Kelley and Endler** (p. 335; see the Perspective by **Anderson**) show

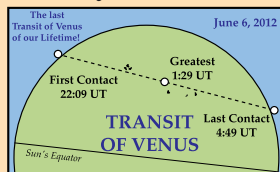


Continued on page 262

AAAS Travels

Lake Baikal June 4-12, 2012

Discover the delights of Siberia and Lake Baikal and see the 2012 **Transit of Venus** which has fascinated astronomers for 380 years! This will be the last one for a century and a **true once-in-a-lifetime opportunity!** \$5,995 + air



Hawaii

June 4-12, 2012

Explore the greatest place to view our solar system and navigational understanding of the stars. A unique look at one of the rarest astronomical events of our lifetime! \$3,495 + air

For a detailed brochure, please call (800) 252-4910

All prices are per person twin share + air

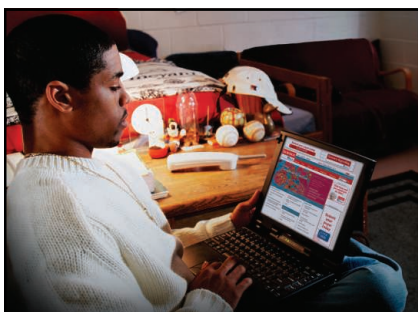


BETCHART EXPEDITIONS inc.

17050 Montebello Road

Cupertino, California 95014

Email: AAASInfo@betchartexpeditions.com
www.betchartexpeditions.com



AAAS is here – preparing minority students for careers in science.

Part of AAAS's mission is to diversify and strengthen the scientific work force. To help achieve this goal, AAAS partners with NSF to present the Historically Black Colleges and Universities Undergraduate Program, a conference where students from HBCUs get experience presenting their research, networking with peers, meeting with representatives from graduate schools, and learning about career opportunities. If you're not yet a AAAS member, join us. Together we can make a difference.

To learn more, visit
aaas.org/plusyou/hbcuup



This Week in *Science*

Continued from page 261

that mating success is based on components of the illusion, rather than the physical nature of the bower. Thus, females choose their mates based on a visual illusion painstakingly constructed and maintained by the displaying male.

Stochastic or Asymmetric Fate Determination?

During an adaptive immune response, B lymphocytes rapidly divide and differentiate into effector cell populations, including antibody-secreting plasmablasts and memory B cells. Many also change the class of antibody they secrete, through a process called isotype switching. During this process, some cells die. Whether cells acquire these different fates in a stochastic or programmed manner, however, is unclear. **Duffy et al.** (p. 338, published online 5 January) used single-cell tracking to determine the times to division, differentiation into a plasmablast, isotype switching, and death of stimulated B lymphocytes. Statistical analysis and mathematical modeling revealed that these cell-fate decisions appear to be the result of random clocks: Which clock went off first (division, differentiation, or death), determined the fate of the cell. **Barnett et al.** (p. 342, published online 15 December) sought to determine whether asymmetrical cell division, which is thought to contribute to effector cell-fate decisions in T cells, may be at work in B lymphocytes. Indeed, factors important for the initiation and maintenance of germinal center B lymphocyte identity, along with an ancestral polarity protein, were asymmetrically distributed and maintained their asymmetry during cell division.

Natural Killer Controls

Cytolytic natural killer (NK) cells participate in both antimicrobial and antitumor immunity. Their responsiveness is tuned through signals received through a variety of inhibitory and activating receptors expressed on their cell surface. **Narni-Mancinelli et al.** (p. 344) now show that signaling through the activating receptor NKp46 paradoxically keeps NK cell responses in check. NK cells from mice with disrupted NKp46 expression were hyperresponsive to stimulation and better protected against viral infection. NK cell responses, which are part of the early response to infection, may thus need to be carefully tuned to ensure optimal initiation of adaptive immunity and formation of protective long-lived memory cells.

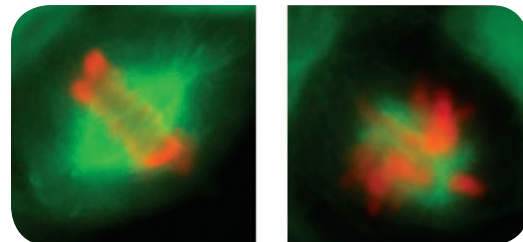
Taking the Myc

Despite nearly 30 years of research into the mechanisms by which Myc oncogene dysregulation contributes to tumorigenesis, there are still no effective therapies that inhibit Myc activity.

Kessler et al. (p. 348, published online 8 December; see the Perspective by

Evan) searched for gene products that support Myc-driven tumorigenesis. One pharmacologically tractable target that emerged from the screen was the SUMO-activating enzyme complex SAE1/2, which catalyzes a posttranslational modification (SUMOylation) that alters protein behavior and function.

SUMOylation was found to control the Myc transcriptional response, and its inhibition caused mitotic defects and apoptosis in Myc-dependent breast cancer cells.



Coordinating Synapses

Cortical microcircuits produce cell assemblies that emit spatiotemporally orchestrated spiking activity. These activity patterns are decoded by the dendrites of downstream neurons. Whether synaptic inputs are clustered or dispersed over target dendrites at a given time is critical for determining dendritic computational power. However, such subcellular dynamics are poorly understood. In rodent organotypic slice cultures, **Takahashi et al.** (p. 353) found that dendritic spine activities were frequently synchronized within a group of spines in the immediate vicinity of one another. This local synchronization seems to reflect convergent synaptic inputs from intrinsically synchronized pre-synaptic neuron populations.



Bruce Alberts is Editor-in-Chief of *Science*.

Trivializing Science Education

I WAS PROMPTED TO WRITE THIS EDITORIAL AFTER PLAYING AN ELECTRONIC VERSION OF THE old board game Trivial Pursuit with my grandchildren over the holiday break. For decades, my favorite category of questions to answer had been “Science and Nature.” But in this 2009 edition, I could answer almost none of those questions—because “science” had apparently been redefined as knowing what disease killed character X in movie Y. Trivial Pursuit is of course merely a game; but it reminded me of the much more serious battle over the California State Science Education Standards that I and many others lost in 1998. As a result, for my grandchildren, “science” includes being able to regurgitate the names of parts of the cell in 7th grade, after memorizing terms such as Golgi apparatus and endoplasmic reticulum. Those of us who are passionate about science have thus far failed to get real science taught in most of our schools. Is it time to regroup with a different strategy?

Few people are aware of what has been learned from research about the teaching of complex scientific concepts to young people, and there is a strong tendency to assume that the best science curricula are the most “rigorous.” Although rigor might appear to be a worthy goal, the unfortunate result of this persistent view is that difficult concepts are taught too early in the science curriculum, and they are taught with an overly strict attention to rules, procedure, and rote memorization. Below is an excerpt from my testimony to the California Standards Commission in 1998, when unsuccessfully opposing such ideas as teaching the periodic table of the elements in 5th grade:

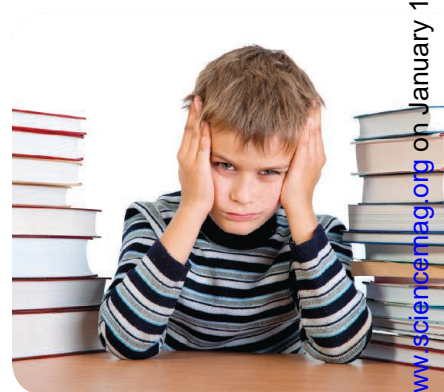
“When we teach children about aspects of science that the vast majority of them cannot yet grasp, then we have wasted valuable educational resources and produced nothing of lasting value. Perhaps less obvious, but to me at least as important, is the fact that we take all the enjoyment out of science when we do so. Consider my field, for example. I have spent 30 years of my life working out the mechanisms that allow the DNA in our chromosomes to replicate. The entire DNA story is a beautiful one that should produce aesthetic enjoyment in the student when first learned. I was fortunate enough to have finished my precollege biology education before Watson and Crick unraveled this mystery with their discovery of the DNA double helix in 1953. I can therefore still remember the joy that I felt when I first learned about DNA. Unfortunately, most students today are taught about DNA at such an early age that they are forced to merely memorize the fact that ‘DNA is the material from which genes are made,’ a chore that brings no enjoyment or understanding whatsoever. Much later, when they do have the background to understand both the structure of the DNA molecule and its explanatory power, I fear that the joy of discovery has been eliminated by their earlier memorization of boring DNA facts. We have spoiled a beautiful story for them, by teaching it at the wrong time.”

The preference for “rigor” in science education can also interfere with the teaching of science at the college level. For example, in an introductory biology class, students are often required to learn the names of the 10 enzymes that oxidize sugars in a process called glycolysis. But an obsession with such details can obscure any real understanding of the central issue, leaving students with the impression that science is impossibly dull, causing many to shift to a different major.

Tragically, we have managed to simultaneously trivialize and complicate science education. As a result, for far too many, science seems a game of recalling boring, incomprehensible facts—so much so that it may make little difference whether the factoids about science come from the periodic table or from a movie script. For my thoughts on how we can do better, stay tuned for next week’s Editorial.

— Bruce Alberts

10.1126/science.1218912





ECOLOGY

Not Extinct After All?

Extinction is forever, but determining when a species has truly become extinct is tricky, particularly for species that live in remote regions. In such regions, species are often categorized as extinct when no individuals have been seen for decades. This “absence of evidence” is imperfect, however, and occasionally individuals resurface. Up until now, such rediscoveries have been serendipitous and rare, but Garrick *et al.* now show that modern genetics has the potential to help facilitate such rediscoveries. Sampling of 20% of the giant tortoise population on Isabela Island in the Galápagos revealed a clear genetic signature of recent hybridization between the native species and pure members of a species from Floreana Island, thought to be extinct since the mid-1800s. Using rapidly evolving nuclear and mitochondrial markers, in conjunction with population simulations, they determined that 0.5% of the sampled individuals on Isabela had a 99% chance of having a pure Floreana parent. Furthermore, nearly a third of the Floreana descendants were less than 15 years old, which suggests that the hybridization events were the result of a healthy, reproductively active population of pure Floreana tortoises on Isabela. — SNV

Curr. Biol. **22**, R10 (2012).

MATERIALS SCIENCE

Carnivorous Cloth

The surface of most objects exposed to the environment eventually becomes colonized by living microorganisms, which may have a variety of, but not necessarily malign, effects. For example, edible molds form coatings on cheese which impart delicious odors and flavors and protect the



interior from invasion by spoilage organisms. Taking inspiration from camembert, Gerber *et al.* have developed a living fabric composed of a base layer of impermeable polymer and a nanoporous surface film sandwiching agar inoculated with the mold *Penicillium roqueforti*. The pore size of the surface film was adjusted to prevent release of mold spores but allow ingress of gases and nutrients. If food (glucose) was “spilt” onto the experimental fabric, the mold grew as it consumed the stain, changing the opacity of the material. The fabric was fairly resistant to being rinsed by ethanol or washed by soap, but desiccation did inhibit growth. The drawback: It took

11 days for the mold to consume the glucose, but perhaps that’s okay if you are waiting for your favorite tie to clean itself. More significantly, such fabrics have obvious bioremediation or biomedical applications, especially if, for instance, antibiotic-producing molds can be incorporated. — CA

Proc. Natl. Acad. Sci. U.S.A. **109**, 90 (2012).

CELL BIOLOGY

Gained in the Translation

Natural selection favors cells or organisms that are able to adapt quickly and effectively to changes in their environment. Baumgartner *et al.* report new insights into such regulation in a relatively simple system in which yeast cells growing in medium containing galactose respond to the presence of glucose by decreasing the half-life of mRNA encoding the GAL1 protein, which functions in conversion of galactose to glucose 6-phosphate. By following responses of individual cells in a microfluidic device that was used to change the medium around the cells, they showed that the decreased abundance of GAL1 mRNA was critical for signaling to cells to increase their growth rate in response to abundant glucose. Total amounts of mRNA in the cell did not change. Instead, GAL1 mRNA and the cyclin CLN3, whose translation promotes cell division, competed for access to a localized pool of ribosomes or other components of the translation machinery. Reciprocally, enhanced translation of CLN3 was detrimental to production of GAL1 when cells were grown in

galactose. Thus, removal of excess transcripts is an important component that allows yeast cells to optimize growth rates in a glucose-rich environment. — LBR

Proc. Natl. Acad. Sci. U.S.A. **108**, 21087 (2011).

CLIMATE SCIENCE

How Wet Will It Get?

Theory and models agree that global mean precipitation should increase as global warming continues, but they differ on the extent of that increase, and even different models vary by a factor of 3 in their predictions of how much more rain will fall. Why do models differ so dramatically? Pendergrass and Hartmann examine how black carbon forcing influences the amount of global mean precipitation calculated by models used in the A1b scenario (assuming rapid economic growth and a balance of fossil fuel and non-fossil fuel energy sources) of the IPCC’S AR4, and find that black carbon has a significant effect on clear-sky atmospheric shortwave absorption, which drives precipitation changes, whereas the radiative forcing supplied by CO₂ does not substantially affect the model spread. Therefore, they conclude, black carbon forcing differences between models can explain a substantial portion, but not all, of the inter-model spread in global mean precipitation in the A1b scenario of AR4. These results may help reconcile disagreements between models, leaving the differences between models and theory still to be bridged. — HJS

Geophys. Res. Lett. **39**, L01703 (2012).

EDUCATION

Physical Meets Virtual

Studies designed to evaluate the relative educational merit of two modes of laboratory instruction—physical manipulatives (PMs) consisting of real-world physical apparatus, or virtual manipulatives (VMs) consisting of computer-based simulations—have produced inconsistent results. These studies have examined PM and VM used individually in a sequential order, revealing little insight into whether a blended PM/VM combination would enhance students' learning. Using a laboratory unit on light and color, Olympiou and Zacharia identified the affordances of PM and VM that support students' conceptual understanding and developed a framework that blended them accordingly. To test the framework's effectiveness, the authors randomly assigned freshmen in an introductory physics course to PM, VM, and PM/VM groups sharing the same instructors and laboratory space, and administered conceptual tests before, during, and after the study. Analysis showed no difference in pretest scores, yet revealed that the blended PM/VM framework enhanced students' understanding of light and color concepts more than PM or VM alone. Test scores from the PM and VM groups were similar, implying that for this study, the use of either was equally effective. More research on how to optimize PM and VM blends is needed before generalized conclusions can be reached. — MM

Sci. Educ. **96**, 21 (2012).

BIOTECHNOLOGY

Watching DNA Charge Ahead

A prospective alternative approach to direct DNA sequencing is to monitor changes in ion current as a DNA strand translocates through a nanopore. However, the speed of the translocation process—about 1 base per microsecond—exceeds the response speed of the electronics needed to amplify the small changes in current when measured with microelectrodes in solution. A field-effect transistor (FET) close to the pore should have sufficient speed and sensitivity to resolve these signals, but charge signals might be screened by the high ionic strength of the solvent. Xie *et al.* fabricated a silicon nanowire FET with a very short channel length (200 nm) on a silicon nitride membrane. They then etched a nanopore (7 to 10 nm in diameter) through the membrane and along the edge of the nanowire, and measured ion currents and FET signals for translocation of 2.6-kbp double-stranded DNA in 1 M KCl. The signal from the nanowire FET tracked that of the ion current measurement if a hundredfold dilution (10 mM KCl) was used in

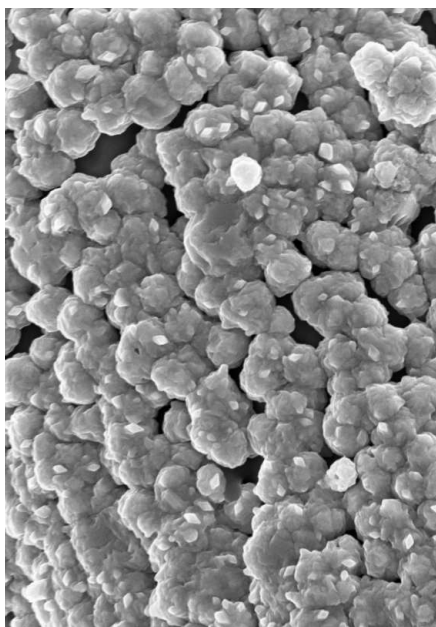
the receiving solution. Measurement of base-pair changes for single-stranded DNA will require further improvements in signal-to-noise ratio and spatial resolution. — PDS

Nat. Nanotechnol. 10.1038/nnano.2011.217 (2011).

MATERIALS SCIENCE

A Layer-by-Layer Amplifier

A number of biological specimens, such as butterfly wings or diatom frustules, have been used as templates for making optical, catalytic, or electrical materials. This requires a process that conformally coats the template while retaining its detailed features. Diatom frustules are of particular interest because each species gener-



ates a unique shell morphology. Fang *et al.* have developed a wet chemical process to convert the silica shell wall into free-standing copper or nickel structures. The key steps are functionalization of the hydroxyl-bearing surfaces with an aminosilane, followed by layer-by-layer deposition of polyacrylate and polyamine, which amplifies the concentration of surface amines. The structures are then treated with palladium chloride, which acts as a catalyst for the electrodeless deposition of copper or nickel. The fidelity of the original diatom structures was greatly enhanced through the use of this layer-by-layer amplification technique, with deposition of much finer metal particles and almost no loss of the original template features. The authors were able to extend the process to multilayered copper/gold structures or multicomponent nickel/phosphorus alloys. — MSL

J. Mater. Chem. **22**, 1305 (2012).

58,905

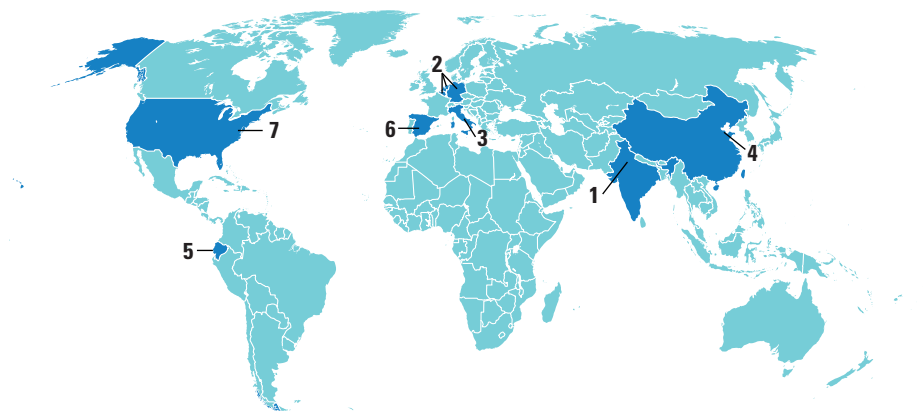
polysyllabic
words
reexamining
Ardipithecus
ramidus.

One more data point on why you should spend more time at membercentral.aaas.org. There you can enjoy members-only downloads, videos, webinars, blogs, discounts, and other content geared for people who aren't afraid of footnotes.

AAAS
MEMBERCENTRAL

membercentral.aaas.org

AROUND THE WORLD



India 1

Country Marks Year Without Polio

The country celebrates a hard-won victory in its fight against polio: As of 13 January, India appears to have gone 1 year without a single case of the disease.

Since the Global Polio Eradication Initiative (GPEI) began in 1988, polio cases worldwide have dropped by more than 99%. The disease has remained in a few strongholds, including India, Afghanistan, Pakistan, and Nigeria, where wild poliovirus transmission has never been interrupted. And for years, India reported more cases than any other country. But cases there dropped from 741 in 2009 to zero in 2011, thanks to the redoubled efforts of India, the GPEI partners, and a recent infusion of support from the Bill and Melinda Gates Foundation.

India's achievement is a major boost to the beleaguered GPEI, which has spent more than \$8 billion over the past 23 years trying to rid the world of the disease. Still, success is not assured. More than 600 cases of polio were recorded worldwide last year, with an alarming rise in neighboring Pakistan, which poses a huge threat to India's fragile success. <http://scim.ag/IndiaPolio>

Germany, the Netherlands, and Belgium 2

New Virus Spreads to Dozens Of Farms in Three Countries

The Schmallenberg virus, a newly discovered pathogen infecting cattle, sheep, and goats, has now been found at 86 farms across Germany, the Netherlands, and Belgium, animal health officials have reported—and the number is rapidly climbing. The virus, named after the German town from which the first positive tissue samples came last November (*Science*, 2 December 2011, p. 1186), causes

drastically reduced milk production as well as fetal malformations and stillbirths.

Infections likely began during the summer and autumn of last year, but fetuses exposed to the virus in the womb are only now being born, meaning that cases seen so far could just be the first wave. "This is a serious threat to animal health in Europe,"



says Wim van der Poel of the Dutch Central Veterinary Institute in Lelystad.

A team at the Friedrich Loeffler Institute, a German federal animal health lab, has isolated the virus and has sequenced its genome. Experts say that it's unlikely that Schmallenberg can cause human disease, but urge monitoring of those who come into contact with infected animals.

<http://scim.ag/Schmallenberg>

Milan, Italy 3

Health Mogul Nabs Bid For Research Center

A long-running Italian drama takes another twist: The imperiled hospital and research center run by the San Raffaele del Monte Tabor Foundation may have found a buyer. But it's not the Vatican Bank as many expected. On 10 January, health industry entrepreneur Giuseppe Rotelli won the bidding for the Milan center, which specializes

in gene therapy and molecular medicine.

Last year, San Raffaele had announced that it was facing a €1.5 billion debt, a short-fall that media reports suggested led to the July suicide of center vice president Mario Cal. In October 2011, a bankruptcy court ruling paved the way for the Vatican Bank to assume leadership. But in a surprising turn, Rotelli outbid the Vatican City-based private institute, promising to take on more than €500 million of debt and to invest a further €405 million.

Although the agreement isn't final, some San Raffaele scientists have expressed doubts about Rotelli's support of basic research. In a statement, the entrepreneur addressed those worries, saying that his first priority "is the protection and further development of the professional skills of all those involved." <http://scim.ag/GRotelli>

Beijing 4

Ministry Moves Against Unauthorized Stem Cell Treatments

China's Ministry of Health has announced that it will crack down on unproven stem cell treatments. Representatives from the ministry and the State Food and Drug Administration will inspect approved stem cell clinics and hospitals while rooting out unauthorized ones—desperate mainlanders and medical tourists have fueled to a boom in such clinics. A hold will also be put on new approvals of stem cell clinics until 1 July, ministry spokesman Deng Haihua said at a press con-

NOTED

>The German chemical company BASF will **move the headquarters of its plant science division** from Limburgerhof, Germany, to Raleigh, North Carolina, officials announced 16 January. BASF will also shut down two more research facilities in Europe. European consumers and farmers are leery of genetically modified crops, officials said, so the company will no longer develop crops for that market.



ference in Beijing on 10 January.

The government introduced a regulation in 2009 requiring health ministry approval of stem cell clinics. But it has been widely flouted, says Douglas Sipp, an expert on stem cell ethics and policy at the RIKEN Center for Developmental Biology in Japan. While Sipp is skeptical that the latest announcement will be thoroughly enforced, Deng Hongkui of Peking University's Laboratory of Stem Cell and Generative Biology in Beijing says the plan is a "good sign." "In the long run, this action will push stem cell trials in China to follow international standards," he says.

Quito 5

Rainforest Conservation Effort Passes Hurdle

After receiving pledges totaling more than its goal of \$100 million by a year-end deadline, the Ecuadorian government has announced that it will move forward with its Yasuni-ITT Initiative. This innovative plan aims to leave untapped more than 900 million barrels of crude oil beneath a pristine Amazonian nature reserve in exchange for annual international donations (*Science*, 26 November 2010, p. 1170). Last summer, many in the conservation community



Protected. One of Yasuni Forest's birds.

feared that Germany would back away from a nearly \$50 million pledge to the effort. But now \$116 million in contributions have been collected from that nation, other foreign governments, foundations, and individual donors, according to Iyonne Baki, the head of the initiative. "We've created amazing momentum," says Baki. That momentum will be needed as the Ecuadorian government has set a new goal of securing \$291 million in contributions in both 2012 and 2013 to keep the initiative going. <http://scim.ag/YasuniITT>

Madrid 6

Government Takes Aim At Science Funding

Warning of unemployment and a "brain drain," Spanish scientists are anxiously waiting to hear exactly which programs will be affected by another round of belt-

tightening. A package of austerity measures announced late last month by Spain's new, conservative-leaning government seeks to cut about €600 million from the nation's science budget. That amounts to nearly a 7% decrease from 2011 spending levels.

Many scientists have raised concerns that Spain's national research centers, which have absorbed a significant part of past funding cuts, will be hit again. The National Research Council (CSIC), for example, has already seen delays and cancellations in some programs.

Adding to researcher's apprehensions, the Spanish government also abolished the Ministry of Science and Innovation. The country's new top scientist, biochemist Carmen



Vela, has taken on a leadership role under the new Ministry of Economy and Competitiveness. Vela, who has gained the ire of some Spanish conservatives for her support of socialist political candidates, moved to reassure the scientific community. "The panorama is difficult," she told the Spanish press. But "we are going to do the impossible." <http://scim.ag/VelaSpain>

Washington, D.C. 7

Reshuffle Would Shift NOAA To Interior

The National Oceanic and Atmospheric Administration (NOAA) would move to the Interior Department under a White House plan announced last week that would eliminate the Department of Commerce. President Barack Obama said the proposed changes, which include a new agency focused on trade and business development, would save \$3 billion over 10 years and make government more efficient. >>



Meet the World's Smallest Vertebrate

Drop a dime in the middle of an eastern New Guinea rainforest, and you might squash a newly discovered frog species. *Paedophryne amauensis* has taken the top spot as the world's smallest vertebrate. Adults attain an average size of 7.7 millimeters in length, less than half the diameter of a U.S. dime. That beats out the former record holder, an Indonesian fish from the carp family whose females grow to about 7.9 millimeters. The new frog species lives in rainforest leaf litter, likely dining on springtails, mites, and ticks, the researchers report online in *PLoS ONE*. Miniaturization is nothing new for frogs. The 29 smallest species all come in under 13 millimeters. The researchers propose that the repeated evolution of extreme small size in frogs, coupled with their exclusivity to moist habitats, has allowed them to exploit the nooks and crannies in the vegetation of the rainforest floor. <http://scim.ag/DimeFrog>



Kepler Spies Smallest Alien Worlds Yet

NASA's Kepler space telescope has found the three smallest extrasolar planets known to science, researchers reported 11 January at the 219th meeting of the American Astronomical Society in Austin, Texas. The planets, the tiniest of which has a radius barely larger than Mars, orbit a star called KOI-961. This red dwarf isn't too big itself—only 70% larger than Jupiter. The entire planetary system stretches less than 5 million kilometers across, which makes the trio plus star more akin to Jupiter and its moons than to our solar system.

Using data from two other telescopes, John Johnson of the California Institute of Technology in Pasadena and colleagues confirmed that periodic dips in KOI-961's brightness were due to passing planets. While the star is a relatively cool dwarf, the three rocky planets are likely too hot to sustain life because of their closeness to the star, Johnson says.

According to a very rough statistical analysis from his team, the new discovery suggests that up to one-third of all red dwarf stars in the Milky Way galaxy could be accompanied by similar small, rocky planets. <http://scim.ag/TinyPlanets>

>> AROUND THE WORLD

Commerce now includes NOAA, the National Institute of Standards and Technology, the U.S. Patent and Trademark Office, and the Census Bureau. The latter three agencies would be part of a new department with a technology and innovation office and a statistical branch that would also include the Bureau of Labor Statistics.

The president is taking the first step by making the Small Business Administration a Cabinet-level agency. But demolition of the Commerce Department, creation of a new agency, and any additional reshuffling will require approval from Congress. Such bipartisanship is rare these days on Capitol Hill.

NEWSMAKERS

SFI Gets New Chief

Ireland's largest public source of funding for science this week appointed Professor **Mark Ferguson** to its top leadership position. Science Foundation Ireland (SFI) named the Northern Ireland native, of the University of Manchester in the United Kingdom, to succeed interim Director General Graham Love on 16 January.



Ferguson

THEY SAID IT

"This is simply not censorship; it is scientific responsibility. We must all remember that science research is a privilege, not a right. If our work can potentially harm the world, we must consider that alongside any benefit."

—Michael Osterholm, influenza expert and National Science Advisory Board for Biosecurity member

"Without all the details of these experiments, follow-up studies will be difficult to perform and [those studies] may also be subjected to some form of redaction. This short-circuits the entire scientific process."

—Virologist Andrew Pekosz of Johns Hopkins University

Both comments from "Should Science Be Censored?" the 12 January *ScienceLive* chat on how to safely publish recent avian influenza studies. <http://scim.ag/flu-chat>

Expectations for Ferguson are high, as many in the Irish science community will be looking to him to protect government funding for science. He's also stepping into a spot vacated by Frank Gannon, who was hugely influential and had the ear of government ministers. Gannon resigned from SFI at the end of 2010 following a major slash to SFI's research budget from €171 million in 2009 to €150 million in 2010.

Ferguson, for his part, has been adamant that the huge advances made in Irish science since SFI was launched in 2000 could be put at risk by more cuts to its research budget.

"We cannot afford slippage to occur," he says. "If due consideration is given by key decision makers to our scientific achievements thus far, I am confident that every effort will be made to accommodate Ireland's continued development as an emergent force in science."

Red Wine Researcher Accused of Fraud

A 3-year fraud investigation at the University of Connecticut Health Center in Farmington has come to a close. The school alleged on 11 January that **Dipak Das**, who heads the cardiovascular research center, “is guilty of 145 counts of fabrication and falsification of Data.” The university dispatched a 60,000-page report to the federal Office of Research Integrity, which is now conducting its own inquiry. The University of Connecticut also says it has “declined to accept \$890,000” awarded to Das in federal funding.

Das worked in the hot field of resveratrol, a molecule found in red wine. Dozens of papers co-authored by Das assert that resveratrol protects the heart.



The university says it has begun dismissal proceedings against the scientist. Meanwhile Das, who is of Indian descent, has charged that racism is behind the allegations. The goal, he wrote in a 2010 document released by the university, was to “remove the Indians in a well planned CONSPIRACY.” He also wrote that he has “not performed bench work for at least 20 years” and thus did not construct the images the university has accused him of manipulating.

FINDINGS

Common Origin for Dog and Human Skin Disorders

Some skin diseases in humans and those iconic pooches, golden retrievers, appear to share a common genetic origin. In golden retrievers, as well as the more twee Jack Russell and Norfolk terriers, the disorders, types of ichthyosis, have cropped up more and more, likely due to inbreeding. The canine conditions resemble a cluster of maladies in people that often cause the skin to form scaly patches. While these diseases are rare in humans—one form, called Harlequin ichthyosis, occurs so seldom that scientists can’t even estimate its prevalence—they can be fatal.

Researchers report online 15 January in *Nature Genetics* that the human diseases and the more common golden retriever variants stem from similar mutations. The scientists first sequenced the genomes of

Random Sample

Funky Fresh Science

“Tevatron, OG atom smasher/say hello to CERN’s party crasher/the new ‘Lord of the Rings’ LHC, hear me/this be competitive collaboration baby.” That’s the opening verse of rapper funky49’s song “Particle Business” off his latest album *Dirty Apes Discover Science*. funky49, whose real name is Steve Rush, is a self-described “IT worker/nerd/science enthusiast.” He raps about what he loves: particle accelerators, Benjamin Franklin, and, uh, swapping genes.

Rush, who works for a company that manages radiology labs, says that growing up he was inspired equally by Philadelphia’s Franklin Institute and the Beastie Boys. As funky49, he fused his passions together and began rapping about science over beats and samples he produced himself on his computer.

In 2008, he recorded the album *Rapbassador* to promote the Tampa Museum of Science and Industry. Its success has kept him busy performing on the nerd circuit, including gigs at an arcade and pinball convention in Atlanta and an upcoming performance at the USA Science & Engineering Festival this April in Washington, D.C.

But just because Rush writes songs rather than journal articles doesn’t make his rhymes immune to criticism. “I’ve been peer-reviewed by scientists,” he says. “With ‘Gene Swap,’ some scientists e-mailed me to tell me that genes don’t really get swapped, they get exchanged.” That they were paying enough attention catch that, though, was “kind of an honor.”

Hear Rush’s rhymes at www.funky49.com.



ichthyosis-affected and healthy golden retrievers. In the dogs, ichthyosis seemed to stem from mutations in a gene called *PNPLA1*. Six people with ichthyosis also carried mutations on both copies of that gene. *PNPLA1* produces a protein that helps to break down fats, an important process in forming cellular membranes. Indeed, the research team spotted abnormal cell membranes in skin biopsies taken from several afflicted dogs and one person. http://scim.ag/dog_scratch

BY THE NUMBERS

\$10 million Winnings offered in the Qualcomm Tricorder X Prize to the researcher that can design a hand-held device capable of diagnosing certain diseases (think *Star Trek* tricorders).

13% Percentage of about 2700 academic and medical researchers that had witnessed scientific misconduct in the past, according to an informal survey by the *British Medical Journal* released at a research integrity meeting in London 11 January. <http://scim.ag/BMJsurvey>



Triggered. Slow slip on an offshore fault preceded the megaquake and its tsunami last March.

SEISMOLOGY

A Tantalizing View of What Set Off Japan's Killer Quake

Japanese scientists combing through the vast jumble of seismic signals recorded in the days before the great magnitude-9.0 earthquake that ravaged their homeland have just sorted out more than 1000 newly recognized earthquakes. The find reveals how the lethal offshore fault slipped slowly just before it ripped loose. That slow slip now appears to have loaded the fault to the breaking point, triggering the devastating quake last March.

The work—the fruit of decades of intensive monitoring around Japan—gives seismologists a much-anticipated peek into a fundamental mystery: “How does a big earthquake happen?” asks seismologist Lucile Jones of the U.S. Geological Survey (USGS) in Pasadena, California. Although it is a long-sought precursor to a big quake, the slow slip “is not a tool for prediction,” she quickly adds, at least not by itself. It does, however, suggest that this time, in this place, Earth held one clue that a big quake was imminent. Researchers’ next step—learning whether such a clue is rare or commonplace—will require close looks at many more earthquakes.

To get a clear view of what preceded the Tohoku-Oki quake, researchers had to pick out much smaller quakes from the seismic record that standard methods had missed. The standard earthquake catalog contained 333 identifiable quakes in the same area in the month before the magnitude-9 quake.

But with so much going on seismically, many other quakes must have remained buried in the seismic records. So seismologist Aitaro Kato (<http://scim.ag/A-Kato>) and

his colleagues at the Earthquake Research Institute (ERI) at the University of Tokyo in effect filtered out much of the record’s noise. They used the fingerprint-like seismograph wiggles of each of the known 333 quakes to go fishing for computerized matches in the churning sea of signals that is the seismic record. They pulled out 1416 matches, more than quadrupling the number of quakes whose timing and location might speak to what the fault had been up to.

It turned out that before a north-south, 500-kilometer length of fault ripped loose in the magnitude-9 quake, the fault just north of the great quake’s starting point slowly slipped, not once but twice. Sections of faults that will eventually rupture in large quakes are generally stuck tight, with not even small patches breaking in small earthquakes. But some fault segments are just slick enough for their opposing sides to slowly slide past each other. When the slip comes episodically, it is called slow slip, a slow earthquake, or a silent quake.

Slow slip generates no seismic waves; researchers can directly monitor truly silent quakes only by exquisitely precise measurements made on or in the crust by instruments such as tiltmeters. Such measurements are not routinely made on the sea floor. But if the slipping fault has a few small sticky spots, they will snag and then break free in small quakes. Among the 1749 quakes the ERI group ended up with, about 25 turned out to be quakes that repeat on the same fault patch as long as slip continues.

By following the location, timing, and size

of the repeating earthquakes that they had found, the ERI group could track any slow slip before the magnitude-9 quake. A first episode of slow slip began in mid-February about 40 kilometers north of the megaquake’s starting point, or epicenter. It progressed south until it reached the megaquake’s eventual epicenter by the end of February and stopped. Nothing happened, not until 9 March, when a magnitude-7.3 foreshock struck at the starting point of the first pulse of slow slip. That set off a second, faster pulse of southward slow slip. This time, when the slip about reached the eventual megaquake’s starting point, the magnitude-9 quake let loose.

From that sequence of events, the ERI group concludes that the second pulse of slow slip “may have” triggered the megaquake. That makes good sense, other seismologists say. Earthquakes let go when enough stress accumulates to break the fault. The Tohoku-Oki segment of fault had been slowly accumulating stress for about a millennium when the second slow-slip pulse delivered a load of stress equivalent to about one-quarter of that released in the magnitude-7.3 foreshock. That, apparently, was the last straw.

So that’s how at least one great earthquake seems to have happened. “It suggests there’s a lot more going on there than we suspected,” says seismologist William Ellsworth of USGS in Menlo Park, California. But Kato of ERI is the first to caution that they have not found the key to earthquake prediction. For one thing, prediction would require knowing how close to failure the locked fault segment had become. That has proved devilishly difficult to determine.

And then there is the as-yet-unknown frequency of slow-slip precursors. “You can’t expect a slow precursor—like the Japanese have been expecting—for all events,” says seismologist Hiroo Kanamori of the California Institute of Technology in Pasadena. “Prediction on the basis of slow slip must be extremely difficult.”

Not that slow slip couldn’t cause a bit of a stir. If a similar sequence were detected off the U.S. Pacific Northwest, where a similar megaquake struck in 1700, “it would certainly be setting alarm bells off,” Ellsworth says. As it happens, says seismologist Jeffrey McGuire of Woods Hole Oceanographic Institution in Massachusetts, he and colleagues will soon be installing a tiltmeter in the sea floor off the Pacific Northwest that would detect any slow slip there in real time. So with luck, they will at least know when something unusual gets going.

—RICHARD A. KERR

BIOFUELS

Engineered Superbugs Boost Hopes Of Turning Seaweed Into Fuel

In the search for renewable fuels, there's no perfect solution. Biofuels can be readily made from corn starch and sugar cane, but they take land and resources away from food crops. Feedstocks such as switchgrass and wood sidestep that problem—but they are hamstrung by a molecule called lignin, which makes it harder to extract the sugars that ferment into ethanol.

Enter seaweed: It has no lignin and requires no land, fresh water, or fertilizer. Several countries have pilot programs for generating biofuels from seaweed. But there's a hitch: About a third of the sugars in seaweed take the form of alginate, a complex polymer that industrial microbes can't convert into ethanol.

On page 308, researchers led by Yasuo Yoshikuni of Bio Architecture Lab (BAL), a 4-year-old biotech company in Berkeley, California, describe a strain of *Escherichia coli* that they have genetically engineered to break down and ferment alginate and all the other major sugars in seaweed into ethanol. "This is very impressive work," says James Liao, a metabolic engineer at the University of California (UC), Los Angeles. But experts wonder whether enough seaweed can be harvested to make it a significant contributor to petroleum independence or even a lower-carbon economy. "Is this a game-changer? Probably not," says molecular biologist Stephen Mayfield of UC San Diego. "But it's a step in the right direction."

Yoshikuni's team started by giving *E. coli* a gene that enabled it to break down alginate, a polymer of uronic acids, into short fragments called oligomers. The gene—for an enzyme called alginate lyase (Aly)—came from the marine bacterium *Pseudoalteromonas sp.* To beef up the modified bug's alginate-busting ability, the researchers tacked on a so-called autotransporter molecule that forced the cells to secrete all the Aly they made.

Next, the researchers had to modify *E. coli* so that it could take up the alginate oligomers floating nearby. The plan was to install a cellular transport system for the oligomers, but first they had to find one. "It wasn't an easy process," Yoshikuni says. Their clue was pectin, another kind of polymer abundant in fruit peels and other plant materials. Because the genes behind the pectin transport system are known, the team could search for similar

genes in a genomics database. Bingo; they found that the bacterium *Vibrio splendidus* 12B01 carries a stretch of DNA similar to that for pectin transport and bearing genes for alginate-degrading enzymes.

But the researchers weren't sure which genes in this stretch they needed because many of their exact functions were a mystery. Turning to natural selection for help, they created thousands of random snippets of *V. splendidus* 12B01's genome and tucked them individually into *E. coli* cells. Then they dropped



Fuel line? Refiners will need a cheap supply of seaweed to make it a feasible biofuel.

cells into a thin alginate-oligomer broth to see which ones could use it as food. One 13-gene snippet allowed the *E. coli* to thrive.

The team then deleted individual genes to figure out their functions. Additionally, the team sought and introduced other *V. splendidus* genes that might function in alginate metabolism. The resulting *E. coli* strain was able to take up all the available alginate oligomers and further break them down into even simpler components. Thanks to the added DNA, the *E. coli* could also convert them into molecules, such as pyruvate, used to make chemical building blocks. Finally, the researchers added a pathway—borrowed from *Zymomonas mobilis*, a bacterium originally isolated from fermented cane juice—that turns the pyruvate into ethanol.

When the fully engineered *E. coli* was fed a slurry of the common brown seaweed called kombu (*Saccharina japonica*), the cells fermented the brew up to a concentration of 5% ethanol—comparable to the benchmark for

yeast-based fermentation of woody biomass. It's also more than twice as good as existing fermentation methods for seaweed and can produce more than 80% of the theoretical maximum yield of ethanol from sugars in seaweed. "This is a big step," says Richard Sayre of Los Alamos National Laboratory in New Mexico. As with other microbial systems, BAL's *E. coli* could be modified to create other fuels and valuable chemicals.

A big question, especially for the United States, is where to get enough seaweed. "It's cultivation at the scale that we need—that is a major hurdle," says Guri Roesijadi of Pacific Northwest National Laboratory (PNNL) in Sequim, Washington. In a 2010 report on seaweed for the Department of Energy, he and other PNNL researchers calculated that

replacing 1% of the U.S. gasoline supply with ethanol would require growing seaweed over nearly 11,000 square kilometers. Several other countries grow seaweed for food, animal feed, fertilizer, or polymers, but there is almost no such farming in U.S. waters.

Seaweed supply directly affects two other key factors: cost and sustainability. If refiners have to haul seaweed long distances, that will raise the cost of seaweed-based ethanol and give it a larger carbon footprint, which in turn can reduce tax breaks and other subsidies from the federal government. "This technology will be competitive only in locations where very large amounts of seaweed are readily available, such as coastal areas," predicts Michael Henson, a chemical engineer at the University of Massachusetts, Amherst. BAL's CEO, Daniel Trunfio, says the company has contracted a life-cycle analysis to show exactly how competitive and "green" its process is; results should be available later this year.

—ERIK STOKSTAD

SCIENCE INDICATORS 2012

Report Notes China's Influence In Emerging Asian Science Zone

Pumping money into research has made China a scientific force to be reckoned with. A new report from the U.S. National Science Foundation (NSF) documents the impact of that investment on how scientists interact.

"We're seeing the beginning of an Asian science zone," says NSF's Rolf Lehming, who oversees the biennial *Science and Engineering Indicators* report. The 2012 edition, a 575-page compendium of global trends in science

and engineering released this week, provides a glimpse of that new landscape, including a sharp rise in intra-Asian collaborations and the growing share of top-cited papers by Chinese authors. The report also traces the impact of China's sustained investment in engineering, on everything from university graduates to high-tech trade surpluses.

Indicators also shows how Asia's influence is being felt in the United States. The

large number of Asian students who remain after being trained at U.S. universities, for example, has led to a steady rise in the percentage of the U.S. scientific workforce that is foreign-born. And a growing share of R&D jobs at U.S. companies are now located overseas.

In addition to these international trends, the report adds texture to perennial U.S. science policy debates such as the level of federal and state support for research and how to ensure that the country is producing enough scientists and engineers. The full report is available at nsf.gov/statistics/indicators/.

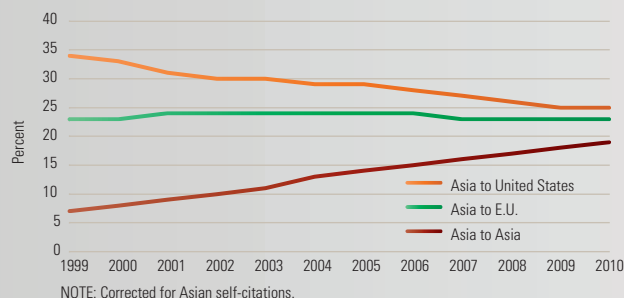
—JEFFREY MERVIS

INTERNATIONAL DATA



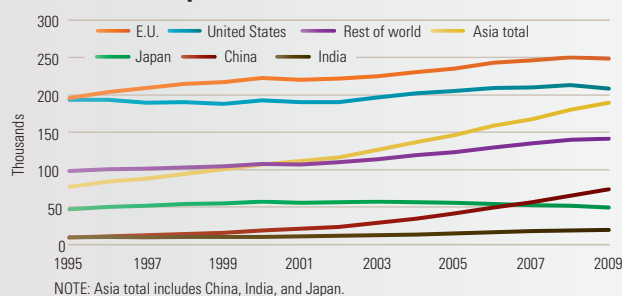
PUBLICATIONS

Whom Asians Cite



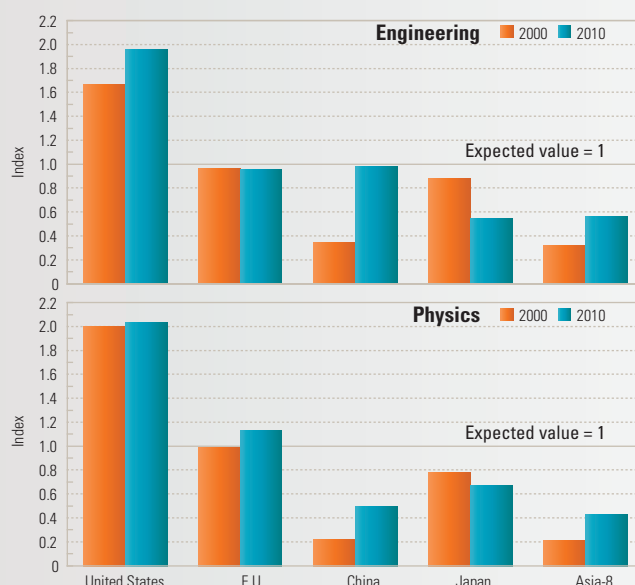
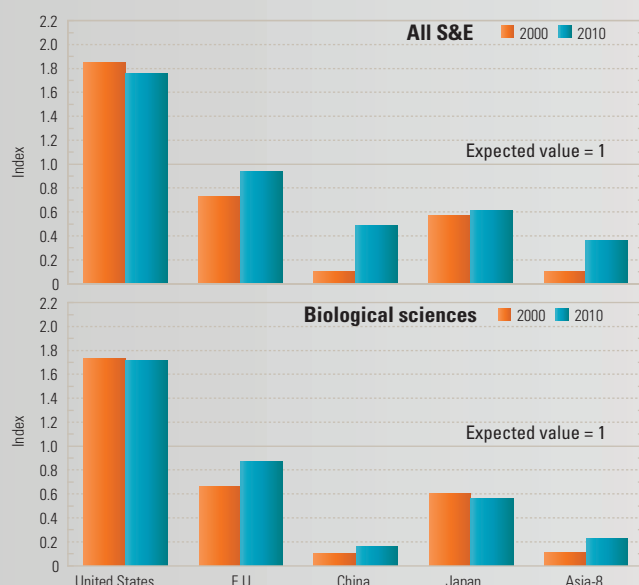
Closer to home. Asian scientists are almost as likely to cite their regional colleagues as U.S. or European scientists, a remarkable shift from a decade ago. (Many articles cannot be assigned to a geographic location.)

Where the Papers Come From



All join in. The 27-country European Union has widened its lead in generating the most science and engineering articles. But Asia, fueled by China's rising contribution, has nearly caught up to the runner-up, the United States.

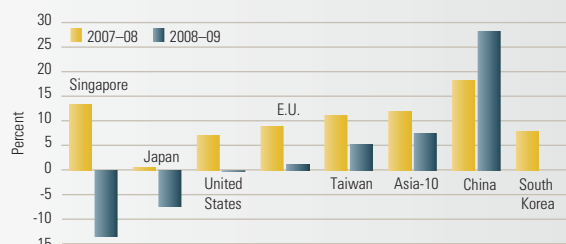
Whose Articles Attract the Most Buzz



A surge in quality. U.S. scientists still rule the roost, but the quality of Chinese science has risen sharply, especially in engineering. The graphs show the number of most highly cited articles—the top 1% overall and by field—from each country or region, normalized by that country's share of global output. Countries with an index larger than one are punching above their weight. China's output in engineering has reached the world's standard after a threefold rise in the past decade.

SPENDING

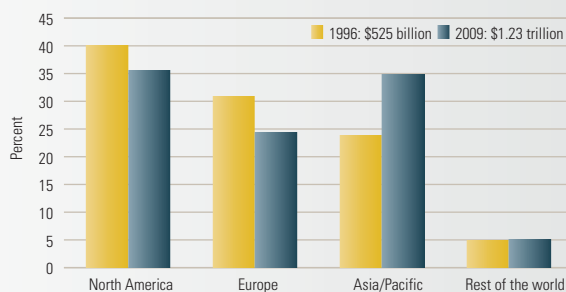
Recession Takes a Toll



NOTE: Asia-10 = China, India, Indonesia, Japan, Malaysia, Philippines, Singapore, South Korea, Taiwan, and Thailand.

More ups than downs. The 2008 financial crisis had a debilitating effect on research spending in most of the world and turned 2007-08 gains into losses the next year in Singapore and Japan. China bucked that trend, however, with continued double-digit growth.

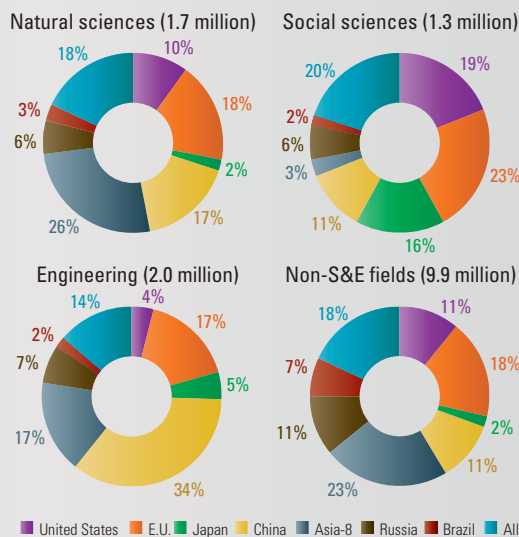
A Global Balance



Two leaders. Asia finally pulled even with North America in research spending in 2009 thanks to sustained growth in science budgets across the region. The European Union has slipped into third place.

WORKFORCE

What They Study

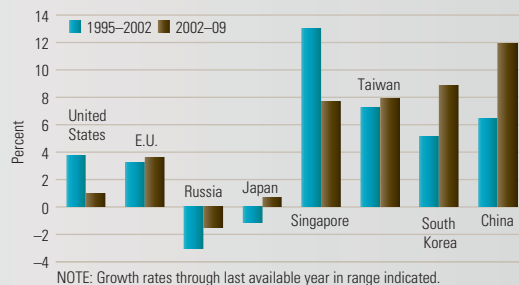


United States E.U. Japan China Asia-8 Russia Brazil All others

NOTE: Asia-8 = India, Indonesia, Malaysia, Philippines, Singapore, South Korea, Taiwan, Thailand

To a degree. What college students choose to study varies widely around the world. Chinese universities account for one-third of all the first degrees awarded globally in engineering, for example, compared with only 4% for U.S. institutions. A group of eight Asian countries, including India, leads the way in the natural sciences, while the United States and the European Union dominate in the social sciences.

Changes in the R&D Workforce



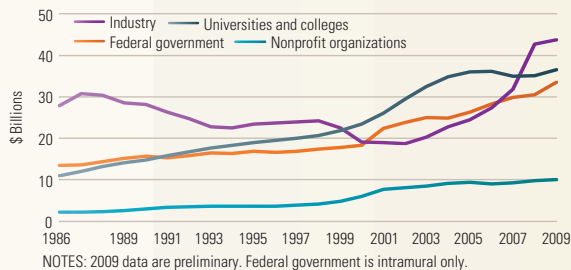
NOTE: Growth rates through last available year in range indicated.

Filling the pool. The annual growth rate of a nation's scientific workforce is influenced by many factors. Despite those fluctuations, much of Asia experienced significant growth in both the 1990s and the 2000s. U.S. growth has slowed in recent years, whereas Russia continues to suffer losses.

U.S. DATA

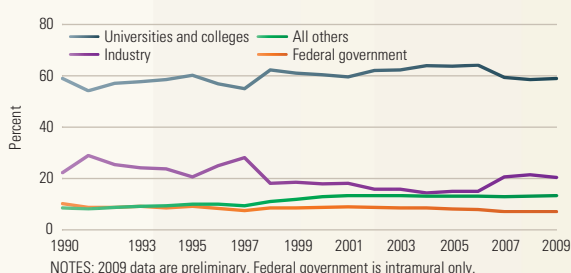
Company town. Fueled by rising defense spending after the 2001 terrorist attacks, industry has regained its place as the largest recipient of federal research funds. Universities benefited from NIH's budget doubling and the 2009 stimulus funding.

Where Science Is Done



NOTES: 2009 data are preliminary. Federal government is intramural only.

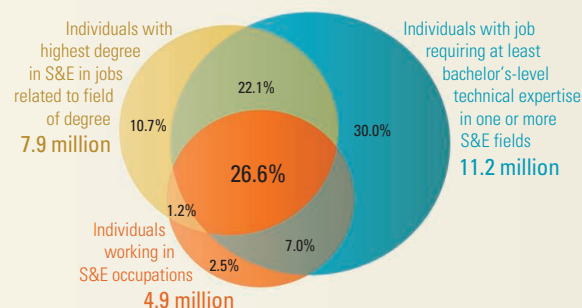
Where Basic Research Gets Done



NOTES: 2009 data are preliminary. Federal government is intramural only.

Steady as she goes. Notwithstanding the outcries from academic lobbyists, the share of basic research dollars spent by Washington at U.S. universities has held steady for 2 decades. Industry holds a clear lead for second place after a recent bump-up.

Using Your U.S. Degree



A special niche. The debate about supply and demand turns out to be far more complicated than simply churning out more science and engineering degrees and creating more S&E jobs. NSF data suggest that the connection between who gets trained and who fills those jobs is surprisingly tenuous. These circles present the results of a survey of those with at least a bachelor's degree in an S&E field. It finds that barely one-quarter (26.6%) hold an S&E job that is related to their degree and that requires at least a bachelor's degree to perform. Remarkably, more than four in 10 (43.2%) satisfy only one of those criteria.



Heads-Up on a Whale's Gulp

Talk about a mouthful. In one giant gulp, a blue whale—the biggest creature on Earth—takes in 125% of its 150-metric-ton body weight in water and krill. And less than a minute later, it's ready for another bite.

Studying such extraordinary behavior sometimes requires extraordinary measures. At the meeting, paleontologist Nicholas Pyenson of the Smithsonian National Museum of Natural History in Washington, D.C., recounted traveling to a shore-based whaling station in Iceland where he and colleagues cut into carcasses and discovered a new sensory organ in jaws of gulping whales. And a comparative physiologist, Jeremy Goldbogen of the Cascadia Research Collective in Olympia, Washington, described motoring right up to blue whales at sea to attach innovative sensors with radio transmitters on their backs. With colleagues, including a physicist and a computer scientist, he has come up with a detailed accounting of whale feeding bouts, showing how the animals unexpectedly twist as they take in water. The work has also revealed that the energy gained and expended by gulping may help explain why certain whales are as big as they are, and, perhaps, why they are no bigger.

Earlier studies with simpler monitoring tags had revealed how blue whales and other so-called rorqual whales are lunge-feeders. The creatures ram into patches of prey, such as krill, opening their mouths wide and wrapping their jaws around krill-laden water, a move that nearly stops them short because of the ingested weight. The whales then close their mouths and push water through baleen, keratin plates that retain just the food, then

speed up for another feeding bout.

This past summer, Goldbogen monitored several blue and fin whales with new tags, ones that use three-axis accelerometers and magnetometers to detect changes in the whales' orientation in space, much as smart phones do to adjust their displays to a horizontal or vertical position. For the 6 to 24 hours they are attached to the whale, the tags also record depth and sound. (From the loudness of the water rushing past a diving whale, researchers can calculate its speed.) With Colin Ware, a computer scientist at the University of New Hampshire in Durham who specializes in visualizing very large amounts of information, Goldbogen used the tag data to approximate the paths of the whales underwater, presenting each as an animated whale traveling along a ribbon demarking its course. As they gulp, the whales, with surprising agility, often twirl around like a corkscrew, Goldbogen reported at the meeting. They will also lunge into pockets of krill from all different angles, not just horizontally as previously thought.

Goldbogen "could not have explained [what happened] without that additional technology for visualization," says Michael Dickinson, a neuroscientist at the University of Washington, Seattle.

Goldbogen also teamed up with Jean Potvin, a physicist at St. Louis University in Missouri who studies parachutes—in lunge-feeders, the whale's mouth expands as it gulps water, similar to an opening parachute filling with air. Together with comparative physiologist Robert Shadwick of the University of British Columbia (UBC), Vancouver,

Big gulp. Bryde's whales (left) and other rorqual whales feed by filling their mouths with a body's weight of water and prey.

in Canada, they modeled the physical forces involved in lunge-feeding and from that estimated the energetic costs involved in taking in so much water. They compared those costs with the energy gained from consuming various volumes of krill in blue, fin, and humpback whales. The feeding whale requires up to 15 times the energy required to remain still and five times more than swimming, Potvin reported at the meeting. "At some point there's going to be a limit" on how big a lunge-feeding whale can be and still feed effectively, Goldbogen noted. Potvin's calculations suggest 33 meters—blue whale size—is about at that limit.

Another new insight into lunge-feeding whales came from the whale tissue Pyenson collected in Iceland. He, Shadwick, Goldbogen, and colleagues found a fluid-filled cavity in the chin tissue that connects the two sides of the jaws. After imaging it with MRI and CT scans, Pyenson hypothesized that this whoopee cushion-sized organ helps guide the rotation of the jaws needed during gulping. The cavity has a lot of blood vessels, as well as nerves that came from what was a tooth socket earlier in whale evolution, Pyenson also reported. Inside are fingerlike structures that look like the mechanoreceptors in our skin that sense movement. "To identify such a new sensory structure in a vertebrate is quite remarkable," says Douglas Altshuler, an integrative biologist at UBC.

Understanding lunge feeding "is a challenging thing to do when dealing with creatures that are a mile deep," adds David Coughlin, an integrative biologist at Widener University in Chester, Pennsylvania. Goldbogen, Pyenson, and their colleagues "are very creative in trying really novel approaches." —ELIZABETH PENNISI

Robotic Fish Point To Schooling Gene

Thirty-five years ago, researchers noticed something peculiar about certain three-spined sticklebacks living at the bottom of Paxton Lake in British Columbia, Canada. A tiny fish, this species dwells in both salt and fresh water and typically swims in schools. But the bottom-dwelling Paxton Lake

three-spined sticklebacks tended to go it alone. Now scientists studying this idiosyncratic behavior with the aid of robotic fish may have pinpointed a gene important for schooling. Unexpectedly, it is the same gene, called *Eda*, that's responsible for marine sticklebacks having bony plates (*Science*, 25 March 2005, pp. 1890 and 1928).

If *Eda* proves key to schooling, it will expand the small roster of behavior genes identified in vertebrates. "Trying to make the connection between behavior and genes is a difficult thing to do in any biological system," says John Robertson, a comparative physiologist at Westminster College in New Wilmington, Pennsylvania.

Why would the bottom-dwelling, or benthic, Paxton Lake fish behave differently? The lake bottom is covered with vegetation, providing lots of hiding places. So, unlike fish in the open seas, they don't need to seek safety in numbers, Anna Greenwood, an evolutionary neurobiologist at the Fred Hutchinson Cancer Research Center in Seattle, Washington, explained at the meeting.

After verifying the lack of schooling instinct in the benthic sticklebacks, she and Abigail Wark, now a Harvard University postdoc, looked in more detail at the sensory and genetic underpinnings of the differences between the lake and marine versions of the species. Wark found differences in the lateral line, bunches of hair cells along the sides of fish that sense the position of other fish in the school. In the solitary Lake Paxton sticklebacks, a single row of these bunches make up the lateral line, but in the marine fish, there are two rows, Greenwood reported.

Tracking down genes for schooling requires a very precise way of measuring the behavior. Live schools of fish were too variable, Greenwood and Wark concluded, so they built a robotic replacement: eight plastic stickleback mimics suspended like a mobile into a circular water tank. This fishy array was hooked up to a motor so that it could "swim" around the tank. Greenwood and Wark placed individual fish into the tank with the circulating school and monitored how the fish reacted for up to 5 minutes. Each marine stickleback quickly fell in with the robotic fish, sometimes swimming with the school for the entire test period. The fish originating in the bottom of Lake Paxton either didn't follow the school at all or did so for just a few seconds at a time, Greenwood reported. "The assay was perfectly matched to the problem," says Michael



Clingfish Stick Like Geckos

On the Pacific Northwest coast, the northern clingfish braves the breaking waves and lives up to its name by prying limpets off the rocks for dinner, thanks to modified fins that form a suction cup on its belly. The unusual body feature outdoes synthetic suction cups, as it can stick even on rough surfaces, Dylan Wainwright of Duke University in Durham, North Carolina, reported at the meeting. "This goes against what you would think," says Frank Fish, a biomechanicist at West Chester University in Pennsylvania. "You would expect [suction] to fail" on rough surfaces.

Wainwright, an undergraduate, tested the sticking ability of 22 freshly killed *Gobiosox maeandricus* on eight surfaces mimicking the range of sandpaper grades and found that the fish adhered to them all with an average force 180 times their body weight. (In contrast, rubber suction cups fell off rougher surfaces, sticking only to the three smoothest ones.) Scanning electron microscopy of the clingfish's belly fins revealed that the secret to its staying power may be a rim of microscopic hairs akin to what geckos utilize on their toes to enable them to walk upside down on ceilings (*Science*, 9 June 2000, p. 1717). Wainwright suspects that clingfish hairs help the edge of the suction cup conform to uneven surfaces and provide more surface area in which weak attractive forces between molecules in the cup and the surface can operate.

—E.P.

Dickinson, a neurobiologist at the University of Washington, Seattle.

This schooling wasn't simply a learned behavior, Wark and Greenwood showed. Marine fish brought up among benthic Paxton Lake fish still schooled with the plastic counterparts, while benthic fish raised with marine fish did not, indicating that schooling was an inherited behavior.

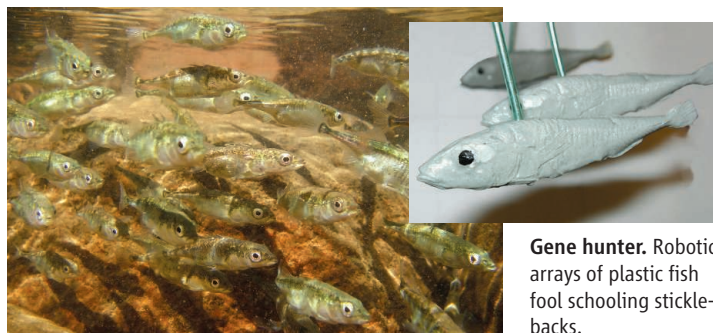
To home in on the genes involved, Greenwood and Wark bred Lake Paxton

more or less schooling behavior and point to *Eda* as a key gene in that behavior. "They have found the needle in the haystack," says Douglas Altshuler, an integrative biologist at the University of British Columbia, Vancouver, in Canada.

The lateral line may explain how *Eda* can be involved in both behavior and physical appearance. The marine stickleback version of *Eda* results in the development of bony plates and a lateral line with two rows of hair cells, not one as in the Paxton Lake swimmers, Greenwood suggested. "The thing that boggles the mind is that this gene controlling this body property ends up controlling behavior," Robertson says. "It is really interesting because it is a social behavior."

Greenwood and Wark have more hybrids to analyze to confirm *Eda*'s role in schooling and to identify additional genes driving the behavior. And they are putting the marine stickleback's version of *Eda* into loner lake fish to see if the resulting transgenic fish have improved schooling behavior. "That will really put the nail in the coffin," Greenwood says.

—E.P.



Gene hunter. Robotic arrays of plastic fish fool schooling sticklebacks.

fish with marine fish and used their robotic array to assess the schooling behavior of the resulting hybrids. Tank testing and DNA studies of these hybrids—250 fish to date—have allowed the researchers to identify chromosomal regions associated with



Archaeologist of Sound

With near-obsessive determination, audio historian Patrick Feaster tracks down remnants of long-vanished voices and noises—and in some cases resurrects them against the odds

WASHINGTON, D.C.—In a quiet storage room three floors above the din of the exhibit halls at the Smithsonian Institution's National Museum of American History, sound historian Patrick Feaster is in nirvana. Donning latex gloves, he shows a visitor some of the ancient audio treasures he had discovered among a stack of more than 200 carefully wrapped glass plates, hollow wax cylinders, and flat metal records.

The collection dates from the 1880s, just after Thomas Edison invented the phonograph, when the idea of capturing and playing back a human voice or the toot of a trumpet seemed nothing short of magical.

Inventors during that early era experimented with glass, cardboard, cardboard covered with wax, tin foil, and mixtures of paraffin and wax as their recording mediums. They shouted into a mouthpiece, causing a vibrating needle to cut grooves into a record; some used photoengraving and vari-

able beams of light to imprint a pattern.

And now Feaster, a friendly but intense 40-year-old with a slender build and a photographic memory for anything phonographic, had first crack at helping bring back to life the lost sounds of 130 years ago. His 2-month stint in the "nation's attic" had turned up undreamed-of finds, including long-lost cylinders recorded at the 1889 World's Fair in Paris and what may be the first-ever sound recording on a disk. Archives and artifacts, however, are only part of Feaster's chosen work. Just as important, he says, is his mission of using modern technology to resurrect long-vanished voices and sounds—some of them never intended to be revived.

Listening backward

Feaster has been obsessed with sound recordings for as long as he can remember. Growing up an only child in Valparaiso, Indiana, in the 1970s, Feaster became fascinated with

Found sound. Wax cylinders Feaster discovered on Smithsonian shelves (*top right*) were recorded at the 1889 World's Fair in Paris, where Thomas Edison was demonstrating the phonograph (*above*).

his parents' vinyl 33-rpm records and started making paper cutouts of his own LPs at age 4. (His mother still has a few.) When his father started frequenting outdoor auctions and swap meets in search of parts for restoring a 1930 Model A Ford pickup, Patrick tagged along, marveling at the old phonographs and records that were on display.

In 1993, Feaster joined the master's degree program in history at Indiana University, Bloomington, but switched to the folklore and ethnomusicology department, where he found an outlet for his love of 19th and early 20th century recorded sound. The research for his 2007 thesis on how the phonograph affected the performances of Victorian musicians, vaudevillians, and orators could have filled several books, recalls his adviser and collaborator, Richard Bauman.

CREDITS (LEFT TO RIGHT): RONDA L. SEWALD; STEVE BARRETT; THE RON COWEN COLLECTION

By then, Feaster and colleagues David Giovannoni, Richard Martin, and Meagan Hennessey had formed FirstSounds.org, a group devoted to finding and disseminating the earliest sound recordings. The team had been nominated for a Grammy for its CD *Actionable Offenses*, a compilation of bawdy wax-cylinder recordings from the 1890s. Another CD, *Debate '08*, reissued 22 recordings by presidential candidates William Howard Taft and William Jennings Bryan during the 1908 campaign—the first time sound bites were used in a presidential election, Feaster says.

In 2007, FirstSounds embarked on a much more daring quest: unearthing and playing back transcribed sounds that predate by 17 years Edison's phonograph and his needle-cut tin foil records. It began over beers at an Italian restaurant near Union, Illinois—the site of a large antique phonograph show—when Feaster and his colleagues began brainstorming about what might be the world's oldest sound recordings. Feaster mentioned the Parisian typesetter and amateur inventor Édouard-Léon Scott de Martinville, who in the 1850s designed and built a machine that used a horn and stylus modeled on the human ear to pick up vibrations from the air and trace them onto paper coated with soot (see figure, above). The inventor had no interest in playing the sounds back; rather, he hoped that people could learn to read the “phonautograms” and mentally reproduce words, songs, and theatrical recitations exactly as originally performed.

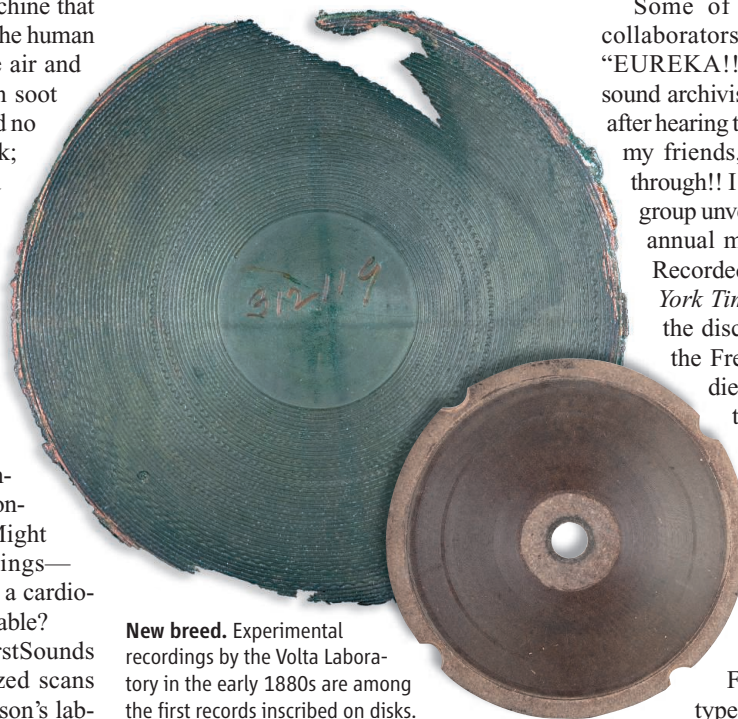
Feaster had come across Scott's work while reading over Edison's papers. He also remembered a rare, self-published book in which Scott, who claimed credit for the idea of recording sound, mentioned having deposited several phonautograms at institutes in Paris. Might those ghostly 150-year-old tracings—undulating scratchings resembling a cardiogram—still be legible, or even playable?

To test that possibility, the FirstSounds team took high-resolution, digitized scans of similar phonautograms that Edison's laboratory had made in 1878 to help New York City officials reduce the din of the newly built elevated railway on Manhattan's Sixth Avenue. After processing the scanned images, FirstSounds sent them to two physicists at Lawrence Berkeley National Laboratory in California who had developed software that reproduces sound from high-resolution scans of the grooves of wax cylinders and disk records too fragile or misshapen to be played

with a stylus. Adapting the software, the Berkeley Lab scientists, Carl Haber and Earl Cornell, succeeded in playing the Edison phonautogram. After 133 years, the ghostly rumblings of a New York City train track rang out once more.

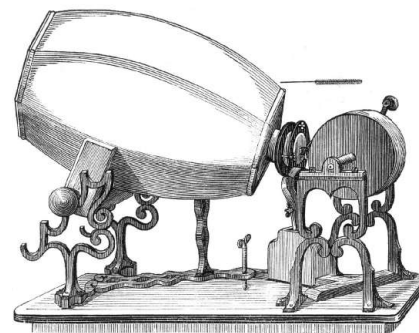
Sound from soot

In late 2007, Giovannoni of FirstSounds flew to Paris and took digital scans of some of Scott's phonautograms the team had tracked down in the French patent office. At first, the wiggly lines seemed unplayable. The traces seemed a mess, and there was no way to tell how fast Scott had turned his hand-cranked machine or how the speed had varied. On some of the other phonautograms Giovannoni examined in early 2008, however, Scott had included what turned out to be a Rosetta stone: a second trace due to the vibration of a tuning fork, its frequency noted on the sheet. By getting the vibration of the tuning fork right and holding it steady, Feaster and his colleagues realized, they could decipher the primary sound print as well.



New breed. Experimental recordings by the Volta Laboratory in the early 1880s are among the first records inscribed on disks.

Haber and Cornell at the Berkeley Lab had produced a raw audio file from some of the tracings, but variations in the speed of Scott's cranking caused the sound to waver unintelligibly, Feaster recalls: “I stayed up into the wee hours of the morning adjusting the [sound of the] tuning fork to a consistent frequency, and bit by bit the recording gradually resolved itself.” About 5:30 a.m., lis-



Before Edison. French “phonautograph” from the 1850s (above) traced sound waves onto paper (right) for sight-reading, not playback.

tening through headphones plugged into his computer, Feaster heard the muffled strains of what sounded like a young girl in 1860 singing the French lullaby *Au Clair de la Lune*. Later that morning, he e-mailed his parents: “After a few hours of audio restoration work last night, I was (I believe) the first person now living to hear a vocal music performance from before the American Civil War.”

Some of Feaster's FirstSound collaborators were less restrained. “EUREKA!!!!!!!!!!!!!!!!!!!!!!!!!!!!!!!!!!!!” sound archivist René Rondeau e-mailed him after hearing the sound file. “Congratulations, my friends, you have made THE breakthrough!! I am beyond stunned.” When the group unveiled the file a month later at the annual meeting of the Association for Recorded Sound Collections, *The New York Times* ran a front-page story on the discovery, and TV crews mobbed the French patent office. Scott, who died believing he might never get the credit he deserved, posthumously got his due.

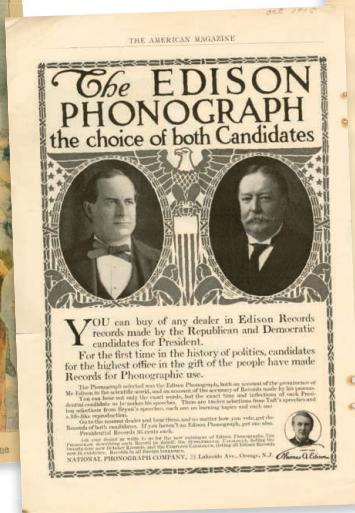
Follow-up work revealed further surprises. In early 2009, Giovannoni scanned a trove of Scott's phonautograms that Feaster's research had turned up at the French Academy of Sciences in Paris. Feaster had adapted a different type of software, designed to convert optical film soundtracks into digital audio files, to play them.

One of the newfound phonautograms—a passage from *Aminta*, a pastoral drama by the 16th century Italian poet Torquato Tasso—also included a trace from a tuning fork. But when Feaster played back the recording, it was too fast. “It sounded like the Chipmunks—unquestionably wrong,” he recalls. “I wondered if I'd miscalculated





Spinning the news. The 1908 Bryan-versus-Taft race marked the first use of sound recordings in a U.S. presidential campaign, to satirists' delight.



Scouring the attic

In comparison, Feaster's sleuthing at the Smithsonian Institution seems

almost contemporary. The little-publicized Smithsonian collection of 1880s recordings is the largest repository of its kind in the world. When Feaster first visited it in December 2010, an old catalog card with the obscure inscription "WJH—damaged record" caught his eye.

He leapt to the conclusion that "WJH" might be William J. Hammer, Thomas Edison's agent at the Paris Exhibition of 1889. That was the world's fair for which the Eiffel Tower was built and the first time that most Europeans heard Edison's talking machine. If Feaster's hunch was correct, the records could contain the only sounds known to exist from the 1889 fair.

But when Feaster returned to the Smithsonian in October 2011 on a 2-month fellowship, he found that a renovation several years earlier had forced the collection to be moved to several temporary storage units. He and Smithsonian curators Carlene Stephens and Shari Stout combed the shelves for anything resembling a box of wax-cylinder records.

In the next-to-last cabinet, Feaster found a closed wooden box stamped "WJH—Newark, N.J." Inside were 28 hollow wax cylinders, some broken, many discolored, each on its own wooden peg. A torn piece of paper describes 16 of the recordings. Among the inscriptions: "Violin recorded on Eiffel Tower, Nov. 6, 1889." The 12 untitled cylinders may include recordings Hammer is reported to have made of native American Indians visiting the fair as part of the Buffalo Bill show, officials from Africa speak-

ing in their native tongues, and prominent French politicians of the day.

Because the records are so fragile—some literally held together by a core of string—it will take time and patience to remove them from the pegs and find out whether any sound can be coaxed out of the 122-year-old grooves, he notes. But the condition of the cylinders looks promising, Giovannoni says.

One of Feaster's latest discoveries sprang from a painstaking perusal of the laboratory notebooks of 1880s sound pioneers in the Washington, D.C.-based

Volta Laboratory, which included Alexander Graham Bell, his cousin Chichester Bell, and Charles Sumner Tainter. In 1881, Tainter described his attempts to record sound on a flat metal record incised with a spiral pattern of grooves and then play it back with a magnet after filling the grooves with a mixture of iron filings and wax. As part of the ultimately unsuccessful work, he cut two ridges along the narrow circular edge of the same record. On one ridge he recorded the word "potato"; on the other, a trilled "r."

Then Feaster had a eureka moment. One of the records he examined in the Smithsonian collection bore an odd, two-ridge pattern on its edge. He had a match. "There's no doubt in my mind that this is the record that Tainter had referred to," he says, cradling a metal record in gloved hands. If so, it is the earliest known recording on disk.

When Feaster isn't contemplating sounds from past generations, he's thinking about those from the newest—in particular his son Perrin. Before Perrin was born last February, Feaster and his wife, Ronda Sewald—a sound archivist whom he met in graduate school—recorded him in the womb and sang to him, putting their own lyrics to a catchy but unknown tune the couple had heard on a century-old wax cylinder. (Their wedding, in June 2006, featured a wax-cylinder procession, vows recorded and played back on a 1906 Edison wind-up phonograph, a century-old recording of Felix Mendelssohn's "Wedding March" as the recessional, and a Victrola-shaped cake.) In the delivery room, the couple banned cameras during the birth but kept the sound recorders rolling. "Perrin is likely to have strong feelings, one way or the other, about old records," Feaster says.

—RON COWEN

Ron Cowen is based in Silver Spring, Maryland, and writes about physics, astronomy, and the history of technology.

somewhere." Scott's notes on the sheet suggested that he had dictated the recording himself. Feaster concluded that Scott's marking of "500" for the tuning fork's frequency must refer to the number of half-cycles, not the full oscillations researchers measure today. In that case, the recording would be an octave lower than he had been assuming. Returning to *Au Clair de la Lune*, he slowed the playback down to the proper speed. The "girl's" voice became that of a man—almost certainly Scott himself.

In 2009, Feaster traveled to Paris to examine some of the phonautograms Scott had deposited at a French scholarly society in 1857. There he met Laurent Scott, a descendent of the inventor. Through headphones attached to Feaster's laptop, Laurent heard his great-grandfather's voice for the first time.

Inspired by the success with Scott's phonautograms, Feaster began exploring other visual recordings that he could attempt to convert into sound. "Today, we can listen—with a little work—to virtually any waveform we can see on paper," he says. Two years ago, in some of his most far-ranging efforts to date, he applied his software to the musical notation found in a 10th century manuscript of the *Enchiriadis* treatise, a medieval work on music theory. The result was a 7-minute sound file that Feaster calls "the closest thing you're likely to hear to a 1000-year-old phonautogram." Feaster has also applied software to "play" other historic musical notations—"as though a sound synthesizer were being programmed directly by medieval monks," he says.

Online
sciencemag.org
Links to sound files and other material.

AUTOPHAGY

Explaining Exercise

Cellular “self-eating” may account for some benefits of exercise

Few would contest that exercise is a healthy habit. It strengthens muscles, keeps weight down, and, population studies suggest, protects against diabetes, cancer, and Alzheimer’s disease. Still, the mechanisms behind exercise’s many benefits remain murky.

Beth Levine of the University of Texas Southwestern Medical Center in Dallas had a hunch that her research interest might help solve the mystery of exercise. Since 1998, Levine has studied autophagy, the “self-eating” process by which cells recycle used or flawed organelles, membranes, and other internal structures. She has largely focused on its role in cancer and infectious diseases, but elevated autophagy can, at least in animal models, produce widespread health benefits, including protection from diabetes, cancer, and neurodegenerative disease.

Because autophagy’s recycling helps cells meet energy demands, Levine began to wonder whether exercise triggers autophagy and if that could somehow account for exercise’s benefits. The exercise-autophagy parallel, Levine says, is “one of those things that’s so obvious that it got overlooked.”

No longer. In the December issue of *Autophagy*, an Italian research team reported the first evidence that exercise induces autophagy in the skeletal muscles of mice. This week in *Nature*, Levine, her Dallas colleague Congcong He, and others confirm that observation and extend it much further, documenting that autophagy is required for exercise’s beneficial metabolic effects. “This paper shows that autophagy really plays a critical role in response to exercise,” says Reuben Shaw, a cancer and diabetes researcher at the Salk Institute for Biological Studies in San Diego, California. “It’s a stronger effect than I would have personally imagined.”

In autophagy, a double membrane encircles target material inside a cell, forming a sphere that then spills its contents into another compartment, the lysosome, where enzymes chop them up so the cell can use it all again (*Science*, 25 November 2011, p. 1048). Organisms from yeast to humans

maintain a background level of autophagy, then boost it under stress.

Exercise is one such stress, Levine found. Running mice for short periods on a treadmill sharply elevated autophagy in many organs, her group reports. The Italian group documented a similar effect in skeletal muscle of



Outrunning diabetes. Obese mice, similar to this one on a treadmill, can reverse their diabetes symptoms with exercise, but only if they can induce autophagy, a process by which cells recycle their contents.

“I’ve always known exercise is good for you, but when we found that it increases autophagy, I finally got a treadmill.”

—BETH LEVINE, UTSW

healthy mice as part of a study of mice with a form of muscular dystrophy.

To isolate downstream effects of this exercise-induced autophagy, Levine compared normal mice with mutant mice that have typical background autophagy but don’t induce more when stressed or stimulated. “A very elegant approach,” says exercise physiologist Zhen Yan of the University of Virginia in Charlottesville, who has unpublished mouse data showing that exercise training leads to more autophagy.

In subsequent work, Levine focused on skeletal muscle. Muscle soaks up about 85% of the glucose derived from food. Strenuous exercise normally lowers glucose and insulin in the bloodstream, but autophagy-impaired mice couldn’t do this nearly as well. On the cellular level, following exercise, the autophagy-impaired mice didn’t relocate a glucose transporter to the cell membrane as do normal mice. Levine’s conclusion: Autophagy is necessary for the short-term metabolic benefits of exercise.

To examine exercise’s long-term effects,

Levine fattened normal mice and the autophagy mutants, which gave both groups a form of diabetes, then put them through 2 months of daily treadmill workouts. Only the normal were able to reverse their diabetes through physical training. Such exercise also brought down elevated cholesterol and triglyceride levels in these mice, but not in the autophagy-impaired mice. Autophagy may also be required to produce the lasting beneficial effects of exercise in diabetes, Levine concludes.

How do exercise and autophagy cooperate? Levine found that, after short-term exercise, normal mice activate in muscle the enzyme AMP-activated protein kinase (AMPK) but the autophagy-defective rodents don’t. AMPK reprograms cells to boost energy production, and its induction by autophagy, Levine says, could explain how exercise training reverses diabetes.

Exercise training also causes lasting adaptations in muscle, including the replacement of old mitochondria, organelles where cellular energy is generated, with new, fuel-efficient ones—what Yan calls a “cash for clunkers” response. Yan believes autophagy following exercise training contributes to the mitochondrial upgrade, and Levine doesn’t rule that out. “We’re not trying to claim that AMPK activation is the only beneficial effect of exercise-induced autophagy on muscle metabolism, or on other organs, and other aspects of health,” she says. “This is probably the tip of the iceberg.” Indeed, Levine is now investigating whether exercise-induced autophagy can slow or prevent cancer and neurodegenerative disease.

Marco Sandri, a researcher at the University of Padova in Italy and an author of the December *Autophagy* paper, suggests that autophagy activators could treat forms of muscular dystrophy. Might such drugs even act as “exercise pills” for otherwise healthy people? Scientists may have trouble demonstrating safety of such drugs, Levine says, because autophagy is a tightly regulated process, and too much can lead to cell death. But exercise itself seems to safely boost autophagy, and for the first time since college, Levine has started to work out. “I’ve always known exercise is good for you,” she says, “but when we found that it increases autophagy, I finally got a treadmill.”

—KEN GARBER

Ken Garber is a science writer in Ann Arbor, Michigan.

CLINICAL TRIALS

Experimental Cancer Therapies Move to the Front Line

It's standard to test drugs in advanced cancer; now, some doctors are using experimental drugs earlier in disease and juggling the challenges that come with doing so

On a Wednesday in mid-March nearly 2 years ago, an unusual cancer trial opened its doors. The study, called I-SPY2, was looking for at least 800 women recently diagnosed with a high-risk form of breast cancer willing to try something new. Before surgery to excise their tumors, they would receive experimental drugs along with the usual chemotherapy. In these women, cancer hadn't spread beyond the lymph nodes, but the tumors they harbored were aggressive and their chance of eventually dying from the cancer was 40%.

A remarkable feature of I-SPY2, one that engendered much behind-the-scenes debate before it launched, was that these women were at an early stage of the disease and standard treatments were at least modestly successful. Patients like these aren't normally recipients of untried therapies. Trials typically follow a well-worn path: Test the drugs in those who have exhausted their options and whose bodies are riddled by disease. The most remarkable successes might add an extra 6 months of life; many drugs are approved for accomplishing much less. Virtually no one expects these volunteers to be cured.

There are good reasons for this paradigm. Novel drugs carry risks and could kill patients faster than the disease itself. It's also easier, researchers say, to measure the effectiveness of new therapies in people at death's door. Tumors can shrink rapidly, and a modest improvement in survival—even in patients with weeks or months to live—means the treatment is working. But this approach also means that patients with, say, early-stage breast cancer, melanoma, or lung cancer don't have access to new treatments for years after testing begins.

A rush of new treatments that attack molecular vulnerabilities in tumors and may be less toxic than traditional chemotherapies has prompted some oncologists, pharmaceutical companies, and drug regulators to recon-

sider how cancer drugs are tested. While new drugs are often tried in patients whose disease is curable, this tends to happen later in development, frequently after the treatment has been under study for 10 years or been approved based on data in those with terminal cancer. Meanwhile, some doctors are wearying of therapies whose ability to extend life is measured in weeks.



Get in early. Breast surgeon Laura Esserman helps lead a study that matches experimental drugs with molecular targets in early-stage, high-risk breast cancer.

“There’s now a fork in the road,” says Razelle Kurzrock, an oncologist who heads the department of investigational cancer therapeutics at M. D. Anderson Cancer Center in Houston, Texas. “We can break our heads over advanced disease, or we can learn from newly diagnosed disease. . . . When the patient comes in with a 1-centimeter tumor, that’s the time to figure out the molecular profile and eradicate the cancer.”

Wake-up call

For oncologist José Baselga, this shift in strategic thinking started with the drug Herceptin, which nails breast tumors that overexpress

the HER2 protein. Baselga was a young doctor at Memorial Sloan-Kettering Cancer Center in the early 1990s when he began working with Herceptin’s maker, the California company Genentech, leading the first study to test Herceptin’s effectiveness in patients with advanced disease. “The response rate was 12%,” with tumors shrinking in roughly one in 10 women, he says. It was a disappointing outcome and didn’t bode well for the drug’s future, says Baselga, now chief of oncology at Massachusetts General Hospital (MGH) in Boston. “Genentech had a big discussion, I was involved in that, and they almost, almost dropped the whole program.”

But instead of relegating Herceptin to the dustbin of history, Baselga says, Genentech gave it another chance. It launched a larger trial in advanced disease and later had Baselga lead a study in which Herceptin was the first treatment patients received instead of one of the last; here, the response rate was dramatically higher, about 40%. Women received it before surgery, and when physicians went in to operate, often there was nothing to take out. Those results, Baselga says, were a “wake-up call for me.” He’s now working with the drug company Novartis on trials of other experimental therapies in early-stage breast cancer.

But testing new drugs in disease that hasn’t spread far is easier said than done. The weightiest questions are ethical: What if giving a new therapy causes side effects that delay surgery or radiation in patients who might be saved by the standard approaches? “You cannot in any way jeopardize the chance of cure in these patients,” Baselga says.

Melanoma poses an interesting challenge. About three-quarters of newly diagnosed patients have disease that appears localized to the skin, and surgery is the treatment of choice. But doctors know that a subgroup already harbor tiny metastases, invisible to imaging machines, elsewhere in the body. Those people will likely die, while the rest will be cured. “We’re not smart enough to figure out” who falls into which group, says Keith Flaherty, a melanoma specialist at MGH.

Deciding whether to test a new drug in patients like these means considering risk from two angles: “It’s a spectrum of risk from the disease side”—how likely disease is to kill, Flaherty says—and “it’s a spectrum of risk from the therapy side,” meaning the severity of a drug’s side effects. In advanced disease, patients are virtually 100% certain to die, making that calculus relatively easy: Gamble on a drug and see what happens. If “you swing to the 15% risk scenario, you better have a safe therapy,” Flaherty says.

But what qualifies as a reasonable risk is a matter of debate. A case in point is a drug Flaherty was intimately involved in testing, called vemurafenib. Approved by the U.S. Food and Drug Administration (FDA) in August for metastatic or inoperable melanoma, it targets the roughly 50% of melanoma tumors that carry *BRAF* mutations.

While testing of vemurafenib continues, no trials so far have included patients with early-stage disease that can be surgically removed. One reason is that *BRAF* inhibitor drugs have a dark side: While they shrink *BRAF*-positive tumors, they can also fuel the growth of *BRAF*-negative tumors.

Online
sciencemag.org
Podcast with
author Jennifer
Couzin-Frankel.

Patients getting vemurafenib sometimes develop *BRAF*-negative squamous cell skin cancers that are easily treated. But doctors worry about something more insidious: whether the drug might nourish virulent *BRAF*-negative cancers elsewhere in the body, such as an undetected tumor in the pancreas unrelated to a patient's melanoma. "You really want to be cautious," says David Solit, an oncologist at Memorial Sloan-Kettering Cancer Center in New York City, who has studied vemurafenib. "The drug can in fact be dangerous."

For Flaherty, it's all about the numbers. Some subsets of melanoma patients with localized disease, treated only by surgery because there is nothing else, have a 50% chance of being cured. "That risk is solid, you know it's there," Flaherty says. Yes, a handful will have a dormant pancreatic tumor, too, but the chance that the drug will make it grow is unknown. "If we were to say, 'We are not willing to take any risk in this population of patients, these people who have a 50–50 chance of dying,' ... then we'll just never make any progress."

When to treat

Reworking the cancer trial paradigm also means rethinking at what point in therapy a new drug is offered. At Johns Hopkins University in Baltimore, Maryland, Charles Rudin, a lung cancer specialist, recently launched a trial in patients with early (stage I) lung cancer, for whom the standard of care is surgery and then no other treatment. Forty percent of this group will see a resurgence of their cancer and likely will die of it.

Last year, Rudin reported on a small trial of two experimental drugs that modify gene

expression in tumors; that trial in advanced lung cancer showed hints of efficacy, so Rudin and doctors at five other centers are recruiting 258 patients with early-stage disease in hopes the drug combination will be more effective. They will offer drugs to half the patients after surgery. The trial is funded by a nonprofit organization, Stand Up To Cancer, with drugs supplied by a program at the U.S. National Cancer Institute that collaborates with drug companies to test experimental and approved drugs. Right now, "the patients get surgery and then are told, 'We're going to watch your CAT scans and hope for the best,'" Rudin says. Joining a trial when there's no evidence of disease is "somewhat easier," he says, when it involves a "decision to get something versus just watching."

Because patients often relapse within a year, Rudin will use the time to relapse as a measure of how well the drugs work. In a disease like breast cancer, women might go 5 years before relapsing. For that reason, breast cancer trials can be "very large and very expensive because you have to [include] so many patients and follow them for such a long time," says Barbara Weber, senior vice president for Oncology Translational Medicine at the Novartis Institutes for Biomedical



Better odds? Lung cancer specialist Charles Rudin recently launched a trial of drugs in stage 1 disease, where cancer recurs in 40% of patients.

called "pathologic complete response," essentially a tumor's disappearance before surgery. This is what Baselga saw in his early-stage Herceptin trial.

A burning question is whether these endpoints—a tumor's disappearance presurgery, or, in Rudin's study, a longer time to relapse—really mean a better shot at a cure. "It's obviously something we and everybody else talk about and struggle with all the time," Weber says.

FDA is considering this issue as well, because companies are unlikely to commit to early-stage cancer trials unless they can use them for drug approval. Last month, Janet Woodcock, who heads FDA's Center for Drug Evaluation and Research, co-authored a paper in *The Journal of the American Medical Association* with Laura Esserman, a breast cancer surgeon at the University of California, San Francisco, and a leader

of I-SPY2. They wrote that in certain breast cancers, pathologic complete response does predict the risk of relapse and that FDA considers this a reasonable basis for approving a drug. The agency plans to issue guidance to companies and scientists spelling out how to use endpoints in early-stage cancer trials.

"Just because we've always done it [one] way doesn't mean we have to do it that way," Esserman says. More than anything, she says she's motivated by a concern for her patients. Efforts to permanently erase metastatic disease haven't worked. More women, she believes, could be saved if trials chased after earlier disease. "The results may turn out to be curative," Esserman says. And that would be something to celebrate.

—JENNIFER COUZIN-FRANKEL

SELECTED EARLY-STAGE CANCER TRIALS

Cancer type	Cancer stage	Number of participants	Drug given when
Breast*	Stage II and III, high-risk	At least 800	Before surgery
Lung	Stage I	258	After surgery
Prostate	Localized, high-risk	58	Before surgery
Breast**	Stage II and III	200	Before surgery

*I-SPY2 trial **Still in planning stage

Research in Cambridge, Massachusetts. "The path to registering a drug"—gaining regulatory approval—"in metastatic disease is much faster" than in less advanced cancer because you get data sooner, Weber says. "Virtually any company will pick the fastest path to registration."

In part because of this, I-SPY2, which is currently testing four different experimental drugs made by several companies, is taking a different tack: giving drugs presurgery. This has the added benefit of providing critical information about a therapy's effect on a tumor, which doctors can glean once the tissue is surgically removed. What researchers are hoping, though, is that there won't be much tumor to find: I-SPY2's success will be measured based on something

LETTERS

edited by Jennifer Sills

Good News for European Vultures

SINCE THE OUTBREAK OF BOVINE SPONGIFORM ENCEPHALOPATHY (BSE) IN 2001, THE CONSERVATION of European scavengers has been the subject of a legal dilemma: Either we can strictly protect scavenger species (1) or we can destroy livestock carcasses, the scavengers' main source of food (2–5). In 2009, Donázar *et al.* (3) remarked that it was time for new regulations and that “encouraging fallen stock to be left in situ is the most ecologically harmonious, inexpensive, and efficient management method for the conservation of scavengers.” Fortunately, recommendations became reality. A broad consensus among scientists, conservationists, and managers (5) led to new EU regulations approved in March 2011 (6, 7). Now, the Spanish government has approved a disposition allowing farmers to abandon the remains of their animals in the field and/or feeding stations (8). Although the



application will be subject to some sanitary and administrative restrictions, the new scenario is grounds for optimism about the future of the Spanish vulture populations (which represent about 95% of European vultures).

With the application of this new measure, Spanish vultures will continue to provide valuable ecosystem services. In Spain alone, avian scavengers are capable of removing 9.9 million tons of carcasses per year. This in turn saves costs for farmers (about €20 per animal). The industrial destruction of carcasses carries costs between €66 and €96 per ton, in addition to the emission of greenhouse gases derived from transport and incineration (5). Overall, these events demonstrate that scientific arguments can indeed trigger positive political action and help to reconcile biodiversity conservation and human activities (9).

ANTONI MARGALIDA,^{1*} MARTINA CARRETE,² JOSÉ A. SÁNCHEZ-ZAPATA,³ JOSÉ A. DONÁZAR⁴

¹Division of Conservation Biology, Institute of Ecology and Evolution, University of Bern, 3012 Bern, Switzerland. ²Department of Physical, Chemical and Natural Systems, University Pablo de Olavide, 41013 Sevilla, Spain. ³Department of Applied Biology, University Miguel Hernández, 33012 Orihuela, Alicante, Spain. ⁴Department of Conservation Biology, Estación Biológica de Doñana, CSIC, 41092 Sevilla, Spain.

*To whom correspondence should be addressed. E-mail: antoni.margalida@iee.unibe.ch

References

1. Directive 2009/147/CE of the European Parliament and of the Council of 30 November 2009 on the conservation of wild birds (<http://eur-lex.europa.eu/LexUriServ/LexUriServ.do?uri=OJ:L:2010:020:0007:0025:EN:PDF>).
2. Regulation CE 1774/2002 of the European Parliament and of the Council of 3 October 2002 laying down health rules concerning animal by-products not intended for human consumption (<http://eur-lex.europa.eu/LexUriServ/LexUriServ.do?uri=CONSLEG:2002R1774:20070724:EN:PDF>).
3. J. A. Donázar *et al.*, *Science* **326**, 664 (2009).
4. A. Margalida *et al.*, *J. Appl. Ecol.* **47**, 931 (2010).
5. J. A. Donázar, A. Margalida, D. Campión, Eds., *Vultures, Feeding Stations and Sanitary Legislation: A Conflict and Its Consequences from the Perspective of Conservation Biology* [Munibe 29 (Suppl.), Sociedad de Ciencias Aranzadi, Donostia, Spain, 2009].
6. Regulation CE 1069/2009 of the European Parliament and of the Council of 21 October 2009 laying down health rules as

regards animal by-products and derived products not intended for human consumption and repealing Regulation (EC) No. 1774/2002 (Animal by-products Regulation) (<http://eur-lex.europa.eu/LexUriServ/LexUriServ.do?uri=OJ:L:2009:300:0001:0033:EN:PDF>).

7. Regulation CE 142/2011 of 25 February 2011 implementing Regulation (EC) No. 1069/2009 of the European Parliament and of the Council laying down health rules as regards animal by-products and derived products not intended for human consumption and implementing Council Directive 97/78/EC as regards certain samples and items exempt from veterinary checks at the border under that Directive (<http://eur-lex.europa.eu/LexUriServ/LexUriServ.do?uri=OJ:L:2011:054:0001:0254:EN:PDF>).
8. Royal Decree 1632/2011 of 14 November, regulating the feeding of certain wildlife species with animal by-products not intended for human consumption (www.boe.es/boe/consultas/bases_datos/doc.php?id=BOE-A-2011-18536) [in Spanish].
9. W. J. Sutherland *et al.*, *TREE* **19**, 305 (2004).

Global Endemism Needs Spatial Integration

UNDERSTANDING THE REASONS WHY certain regions of the world have a high number of endemic species (i.e., species with a limited geographic distribution) is important because it is frequently used in prioritizing biodiversity conservation at both regional and global scales. B. Sandel and colleagues (“The influence of Late Quaternary climate-change velocity on species endemism,” Reports, 4 November 2011, p. 660) concluded that sites where climate is changing at a slower rate (low-velocity) are more likely to harbor endemic species than high-velocity sites. Sandel *et al.*'s endemism maps are quite different from previous maps of endemism (1–3). Their analysis would benefit from the study of regional variation and spatial patterns, particularly for mountain and glacial ranges such as the Asian Himalayas.

The European and Asian continents, although located at almost the same latitude, have experienced different glacial histories (4); many European species expanded in the post–Last Glacial Maximum Quaternary period (5), whereas Asian species such as

those in the eastern Himalayas of China were established before the Last Glacial Maximum (6, 7). The high endemism detected in the southeast mountain subregion of the southeastern Tibetan plateau was caused by geological events that acted as historical and ecological barriers, preventing population gene flow and promoting speciation (2, 3). The uplift of the Tibet Plateau and Quaternary glacial movements are key factors in shaping the distribution pattern of high endemism in the southwestern China mountains. The high-latitude regions of Europe and North America were covered by heavy ice during much of the Pleistocene, but glaciations in southwestern mountains were restricted to relatively high altitudes and did not affect the lower slopes or valleys, leading

to the “sky island” distribution pattern (8, 9).

Regional differences such as these could augment the results of Sandel *et al.*'s study. Geographical, geological (glacial movements), and climate factors must be integrated to form a comprehensive model of endemism (10–13).

FU-MIN LEI

Key Laboratory of Zoological Systematics and Evolution, Institute of Zoology, Chinese Academy of Sciences, Beijing, 100101, China. E-mail: leifm@ioz.ac.cn

References

1. N. Myers *et al.*, *Nature* **403**, 853 (2000).
2. F. M. Lei *et al.*, *Biodivers. Conserv.* **16**, 1119 (2007).
3. X. L. Huang *et al.*, *Int. J. Mol. Sci.* **11**, 2097 (2010).
4. G. Hewitt, *Nature* **405**, 907 (2000).
5. G. Hewitt, *Philos. Trans. R. Soc. B* **359**, 183 (2004).
6. S. Li *et al.*, *Mol. Ecol.* **18**, 622 (2009).
7. G. Song *et al.*, *BMC Evol. Biol.* **9**, 143 (2009).
8. S. Zhou *et al.*, *Quat. Int.* **154**, 44 (2006).

9. Y. H. Qu *et al.*, *BMC Evol. Biol.* **11**, 174 (2011).
10. A. Gómez *et al.*, *Proc. R. Soc. London Ser. B* **267**, 2189 (2000).
11. A. C. Carnaval, C. Moritz, *J. Biogeogr.* **35**, 1187 (2008).
12. A. C. Carnaval *et al.*, *Science* **323**, 785 (2009).
13. L. Excoffier *et al.*, *Annu. Rev. Ecol. Evol. Syst.* **40**, 481 (2009).

Response

LEI ARGUES FOR BETTER INTEGRATION ACROSS different spatial scales in the study of endemism patterns. Detailed glacial histories, for example, may improve understanding of endemism at regional scales. At a global scale, however, our results were insensitive to the inclusion or exclusion of glaciated regions; we ultimately excluded these regions because of difficulties calculating and interpreting their velocities.

There are differences between our endemism map and others produced recently. It is unsurprising that our endemism map does not exactly match previous hotspot maps, especially considering that they may use other species groups, spatial scales of assessment, and additional criteria, such as threat [e.g., (1)]. It is well established from large-scale studies of biodiversity that environmental models for a particular region



Readers' Poll Results

The Well-Behaved Scientist

On 2 December 2011, the special section on Data Replication and Reproducibility discussed ways to incentivize scientists both to fully disclose their own raw data and methods and to spend time replicating others' work. We asked you to weigh in by answering this question: What would best ensure this good behavior?*

More than 1000 of you responded, from dozens of countries around the world. Here are your results.

A selection of your thoughts:

Most readers felt that journals and the peer-review process hold the most sway:

"Journals should be required to publish papers contradicting findings they themselves published."

—reader Björn Brembs

"Online supplementary space ... often turns into a morass of difficult-to-follow, useless information.... I am in favor of publishing supporting material but it needs to be consistently held to high standards."

—reader Chris

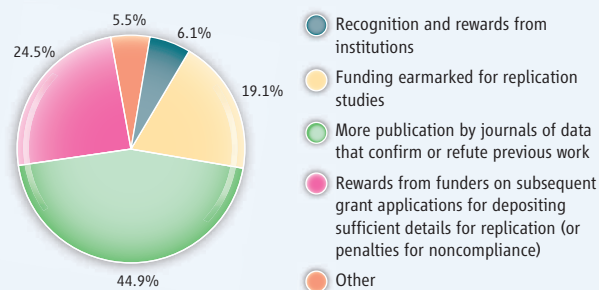
"I propose more reward for conscientious (and constructive) reviewing."

—reader Colin Wraight

Others felt that the science community's priorities should be reevaluated:

"A published data set, properly documented and reviewed, should have the same status and rewards as any other formal scientific publication."

—reader Donald Strebel



"Deemphasize publication and citation record and emphasize successful application."

—reader HCPotter

A few readers feel that this is primarily a practical challenge:

"Researchers may be reluctant to publish a data set that they haven't finished with, as someone else might publish an analysis they themselves were planning to do in the future. Dealing with this will be important to convince researchers to publish data."

—reader Thomas Chesney

"No one needs rewards to put specimens in herbaria or sequences in GenBank. These are cultural norms.... So start with creation of discipline-appropriate sites where one could deposit data."

—reader Darlene Southworth

*See the poll at <http://scim.ag/rGWlxA>.

Polling results reflect those who chose to participate; they do not represent a random sample of the population. Results may not add up to 100% due to rounding.

differ not only from global models, but from models for other regions, and historical contingency is one explanation offered for this. In approaching our study of the global distribution of amphibians, birds, and mammals, we favored generality over specificity, an opportunity afforded by global analysis. Having established the general importance of past climate-change velocity, we hope that more detailed regional studies, such as those suggested by Lei, will add further insight into its importance.

B. SANDEL,^{1,2*} L. ARGE,²

B. DALSGAARD,³ R. G. DAVIES,⁴ K. J. GASTON,⁵

W. J. SUTHERLAND,³ J.-C. SVENNING¹

¹Ecoinformatics and Biodiversity Group, Department of Bioscience, Aarhus University, Aarhus 8000 C, Denmark.

²Center for Massive Data Algorithmics (MADALGO), Department of Computer Science, Aarhus University, Aarhus 8000 C, Denmark. ³Conservation Science Group, Department of Zoology, University of Cambridge, Cambridge CB2 3EJ, UK.

⁴School of Biological Sciences, University of East Anglia, Norwich NR4 7TJ, UK. ⁵Environment and Sustainability Institute, University of Exeter, Cornwall TR10 9EZ, UK.

*To whom correspondence should be addressed. E-mail: brody.sandel@biology.au.dk

Reference

1. N. Myers *et al.*, *Nature* **403**, 853 (2000).

TECHNICAL COMMENT ABSTRACTS

Comment on "Probing the Ultimate Limit of Fiber-Optic Strain Sensing"

Geoffrey A. Cranch and Scott Foster

Gagliardi *et al.* (Reports, 19 November 2010, p. 1081) described an ultra-high-resolution fiber-optic strain sensor. This comment addresses an error in the calculation of the fundamental thermodynamic noise in optical fiber resonators and shows that the actual thermodynamic noise level is lower by a factor of at least 11 than that calculated.

Full text at www.sciencemag.org/cgi/content/full/335/6066/286-a

Response to Comment on "Probing the Ultimate Limit of Fiber-Optic Strain Sensing"

G. Gagliardi, M. Salza, S. Avino, P. Ferraro, P. De Natale

Cranch and Foster argue that the strain resolution of our fiber resonator sensor is not limited by thermal noise. However, extension of common theoretical models to high-finesse passive resonators at low frequency needs further attention. Our findings are consistent with noise of thermodynamic nature for which no experimental evidence in the infrasonic range was available until recently.

Full text at www.sciencemag.org/cgi/content/full/335/6066/286-b

CORRECTIONS AND CLARIFICATIONS

News Focus: "Unraveling the obesity-cancer connection" by G. Taubes (6 January, p. 28). The article incorrectly states that Robert Weinberg referred to a 2004 *Nature Reviews* article by Eugenia Calle and Rudolph Kaaks as directing researchers' attention to the obesity-cancer link. Weinberg was referring to a 2003 article by Calle and collaborators from the American Cancer Society: E. E. Calle, C. Rodriguez, K. Walker-Thurmond, M. J. Thun, *N. Engl. J. Med.* **348**, 1625 (2003).

News Focus: "America's lost city" by A. Lawler (23 December 2011, p. 1618). On p. 1618, Thomas Emerson was described as being affiliated with ITARP. The correct affiliation is Illinois State Archaeological Survey (ISAS). A subsequent ITARP reference on p. 1622 should also be ISAS. These changes have been made to the HTML version online.

Letters to the Editor

Letters (~300 words) discuss material published in *Science* in the past 3 months or matters of general interest. Letters are not acknowledged upon receipt. Whether published in full or in part, Letters are subject to editing for clarity and space. Letters submitted, published, or posted elsewhere, in print or online, will be disqualified. To submit a Letter, go to www.submit2science.org.

A Journal with Impact from AAAS, the publisher of *Science* *Science Translational Medicine* Integrating Medicine and Science

A recent journal article features the sequencing of fetal DNA from plasma of a pregnant woman to permit prenatal, noninvasive genome-wide screening to diagnose fetal genetic disorders.

Sci Transl Med 8 December 2010:
Vol. 2, Issue 61, p. 61ra91
DOI: 10.1126/scitranslmed.3001720

**Recommend an
institutional subscription
to your library today!**

ScienceOnline.org/recommend



ScienceTranslationalMedicine.org



Comment on “Probing the Ultimate Limit of Fiber-Optic Strain Sensing”

Geoffrey A. Cranch^{1*} and Scott Foster^{2*}

Gagliardi *et al.* (Reports, 19 November 2010, p. 1081) described an ultrahigh-resolution fiber-optic strain sensor. This comment addresses an error in the calculation of the fundamental thermodynamic noise in optical fiber resonators and shows that the actual thermodynamic noise level is lower by a factor of at least 11 than that calculated.

Gagliardi *et al.* (1) reported a fiber-optic resonator capable of achieving a strain resolution approaching $10^{-13} \text{ } \epsilon \text{ Hz}^{-1/2}$ at infrasonic frequencies below 10 Hz. The system demonstrated the highest-resolution strain sensitivity at frequencies less than ~ 10 Hz published to date, and we commend the author on an excellent achievement. However, the calculated level of fundamental thermal noise exhibited by such an optical cavity is incorrect and not consistent with previously published theoretical models and experimental measurements. The method used by Gagliardi *et al.* to calculate thermodynamically induced phase fluctuations, employing an effective cavity length for a high-quality factor (high-Q) optical cavity, is not valid because the thermal-noise-limited sensitivity is unaffected by the cavity storage time and is only dependent on fiber length and material properties. We believe that this error may lead to the misconception that fundamentally limited strain resolution is readily achievable in short-length, passive fiber-optic resonators. We show that, in view of the actual thermodynamic noise level, this limit is very difficult to attain in a passive resonator, at frequencies below ~ 10 Hz, with current laser technology.

Thermodynamically induced phase fluctuations can affect many applications, such as fiber-optic sensors (2, 3) and laser stabilization (4, 5). Glenn (6) presented the first rigorous theoretical study of thermal noise in single-mode fiber. An alternative formulation leading to a simplified expression for thermal noise in optical fiber was later presented by Wanser (7), who subsequently provided strong experimental evidence to support the validity of the proposed model (8) and which has been widely applied since. More recent theoretical work has provided a further formulation for equilibrium thermal noise in passive optical fibers and fiber lasers (9), which agrees within a few percent with Wanser’s formulation.

Assuming insulating boundary conditions at the outer cladding interface and taking parameters typical for conventional single-mode fiber, a cavity length of 0.13 m yields thermal phase fluctuations in a fiber Fabry-Perot cavity of $(2S_\phi)^{1/2} = 3.4 \times 10^{-8} \text{ rad/Hz}^{1/2}$ at 1 Hz. This corresponds to a strain resolution, $\delta\epsilon_{\text{th}} = 28 \times 10^{-15} \text{ } \epsilon \text{ Hz}^{1/2}$, a value lower by a factor of ~ 11 than the lowest value calculated by Gagliardi *et al.* To resolve phase fluctuations of this order requires a laser frequency noise less than $\sim 5 \text{ Hz/Hz}^{1/2}$, which is lower by a factor of at least 4 than that achieved by the stabilized semiconductor laser used in (1). The thermal-noise-limited strain resolution is shown in Fig. 1 alongside the strain resolution achieved in (1). At low frequency, the theoretical thermal noise is quite sensitive to the boundary conditions at the interface of the fiber cladding, where we assume ideal insulating conditions (solid line in Fig. 1). However, even if one assumes an infinite cladding, the theoretical thermal noise limit at 1 Hz is still close to an order of magnitude lower than that calculated in (1) (dotted line in Fig. 1).

Thermodynamically induced phase fluctuations in optical fiber are indistinguishable from mechanically induced phase fluctuations. Therefore, the assertion by Gagliardi *et al.* that the thermal-noise-limited strain resolution is de-

pendent on cavity storage time (i.e., finesse) has no physical basis and leads to a large error in the calculated thermal-noise-limited strain sensitivity. It should be noted that variability in material parameters is not sufficient to account for the discrepancy between the thermal noise calculations presented here and those presented in (1). Experimentally measured thermal noise spectra in optical fiber interferometers by Wanser (8) are more than an order of magnitude lower than noise spectra reported in (1) at frequencies above 1 kHz, taking into account the differences in fiber length.

Because of a lack of sufficiently stable lasers, measurement of equilibrium thermal noise has been achieved only in balanced, long path length (>50 m) interferometers (8) and fiber laser strain sensors (9–11), albeit at frequencies typically extending beyond 100 Hz. No studies, to date, have characterized equilibrium thermal noise at frequencies below 100 Hz in passive optical cavities because of the exceptional stability requirements of the probing laser. However, recent work has demonstrated a single-frequency fiber laser locked to a high quality factor (Q) cavity (12) with frequency stability below $1 \text{ Hz/Hz}^{1/2}$ above 1 Hz. It is interesting to note that thermal-noise-limited strain resolution is found to scale as $L_{\text{eff}}^{-1/2}$, as illustrated in the inset of Fig. 1. In the current work, it follows that thermal noise in a fiber Fabry-Perot cavity is more readily resolved with a shorter cavity.

Measurements of thermal noise at low frequencies in passive optical-fiber cavities would establish the validity of current theories over these frequency ranges. In single-frequency fiber lasers, frequency fluctuations are found to be limited by equilibrium thermal noise above ~ 1 kHz with a $1/f^{1/2}$ noise contribution observed at lower frequencies (9). Strong evidence suggests this $1/f^{1/2}$ noise to be associated with radiative transitions (spontaneous emission) in the gain medium (13, 14) and, as such, is referred to as nonequilibrium thermal noise. Experimental evidence

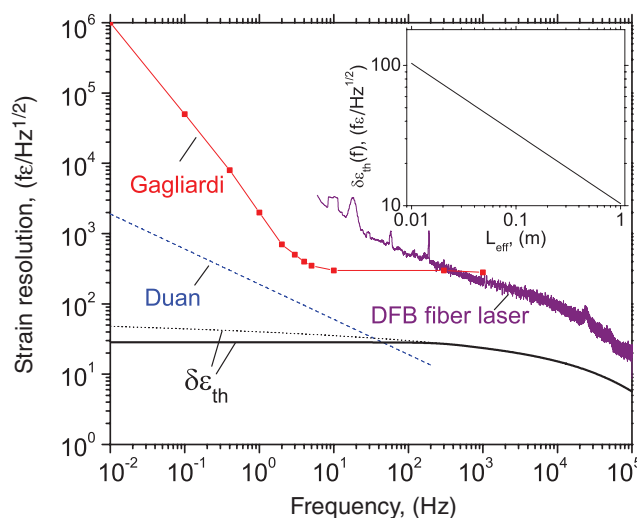


Fig. 1. Theoretical thermal-noise-limited strain sensitivity, $\delta\epsilon_{\text{th}}$, for 0.13-m fiber Fabry-Perot cavity: (solid line) insulating boundary condition and (dotted line) infinite cladding. Also shown is the measured strain resolution according to (1) (red line), the measured strain resolution of a distributed feedback (DFB) fiber laser (9), and a possible $1/f^{1/2}$ noise contribution according to (15) (dashed line). (Inset) The dependence of the thermal-noise-limited strain resolution versus the effective cavity length.

¹Naval Research Laboratory, 4555 Overlook Avenue, SW, Washington, DC 20375, USA. ²Defence Science and Technology Organisation, Post Office Box 1500, Edinburgh, SA, Australia 5111.

*To whom correspondence should be addressed. E-mail: geoff.cranch@nrl.navy.mil (G.A.C.); scott.foster@dsto.defence.gov.au (S.F.)

confirms the absence of this noise mechanism in passive optical fiber (11). More recent theoretical work has proposed a fundamental source of $1/f^{1/2}$ noise in passive optical fiber due to mechanical dissipation (15). A $1/f^{1/2}$ dependence is predicted with a magnitude exceeding equilibrium thermal noise at frequencies below ~ 50 Hz. An estimate of the magnitude of this noise source in a 0.13-m fiber Fabry-Perot cavity is also illustrated in Fig. 1 (dashed line). It is evident from the data obtained by Gagliardi that, if present, this noise source may not be resolvable without further environmental isolation to reduce the $1/f^n$ ($n \sim 1$) noise observed below 1 Hz.

Reaching thermal-noise-limited strain resolution in passive optical fiber at very low frequencies is thus a formidable challenge. At present, thermal-noise-limited strain sensitivity can only be achieved

in short, active optical cavities based on fiber lasers (3). Both the absence of probing lasers with sufficient frequency stability at frequencies below 1 Hz and attaining sufficient environmental isolation may present major obstacles to achieving the full aspiration of (1).

References and Notes

1. G. Gagliardi, M. Salza, S. Avino, P. Ferraro, P. De Natale, *Science* **330**, 1081 (2010).
2. C. K. Kirkendall, A. Dandridge, *J. Phys. D Appl. Phys.* **37**, R197 (2004).
3. G. A. Cranch, G. M. H. Flockhart, C. K. Kirkendall, *IEEE Sens.* **8**, 1161 (2008).
4. B. S. Sheard, M. B. Gray, D. E. McClelland, *Appl. Opt.* **45**, 8491 (2006).
5. J. Alnis *et al.*, *Phys. Rev. A* **84**, 011804 (2011).
6. W. H. Glenn, *IEEE J. Quantum Electron.* **25**, 1218 (1989).
7. K. H. Wanser, *Electron. Lett.* **28**, 53 (1992).
8. K. H. Wanser, A. D. Kersey, A. Dandridge, *Opt. Photonics News* **4**, 37 (1993).

9. S. Foster, A. Tikhomirov, M. Milnes, *IEEE J. Quantum Electron.* **43**, 378 (2007).
10. K. P. Koo, A. D. Kersey, *Electron. Lett.* **31**, 1180 (1995).
11. G. A. Cranch, G. A. Miller, *Opt. Lett.* **36**, 906 (2011).
12. H. Jiang, F. Kéfélian, P. Lemonde, A. Clairon, G. Santarelli, *Opt. Express* **18**, 3284 (2010).
13. S. Foster, *Phys. Rev. A* **78**, 013820 (2008).
14. S. Foster, G. A. Cranch, A. Tikhomirov, *Phys. Rev. A* **79**, 053802 (2009).
15. L. Z. Duan, *Electron. Lett.* **46**, 1515 (2010).

Acknowledgments: G.A.C. was funded by the Naval Research Laboratory 6.2 base program.

Supporting Online Material

www.sciencemag.org/cgi/content/full/335/6066/286-a/DC1

SOM Text

Table S1

References

10 March 2011; accepted 5 December 2011
10.1126/science.1205452

Response to Comment on “Probing the Ultimate Limit of Fiber-Optic Strain Sensing”

G. Gagliardi,* M. Salza, S. Avino, P. Ferraro, P. De Natale

Cranch and Foster argue that the strain resolution of our fiber resonator sensor is not limited by thermal noise. However, extension of common theoretical models to high-finesse passive resonators at low frequency needs further attention. Our findings are consistent with noise of thermodynamic nature for which no experimental evidence in the infrasonic range was available until recently.

Thermally induced phase fluctuations in optical fibers have long been studied because they set a fundamental limit to strain resolution of sensors as well as frequency stability of fiber lasers (1, 2). In our original paper (3), we reported an unprecedented resolution level in strain sensing using a high-finesse fiber Bragg-grating (FBG) resonator interrogated by an optical-frequency-comb (OFC) stabilized diode laser. The OFC minimizes noise contribution from the laser, which is usually dominant in similar systems, particularly in the infrasonic frequency range (4, 5). Taking into account the laser-frequency noise when locked to the OFC, we estimated the ultimate limit of our technique to be $120 \text{ f}\epsilon/\sqrt{\text{Hz}}$ at 2 Hz (3). Despite that, the strain resolution was found to be above the expected value.

Cranch and Foster (6) compare our strain noise with that predicted by their model with an effective fiber length equal to twice the FBGs distance (analogous to fiber lasers) (7). We remark that the definition of effective length given in (7) is difficult to match with the popular Wanser’s model (8). Wanser’s theory provides the only analytical expression of thermal phase fluctuations for finite-cladding fibers. Over the past two decades, few experiments have confirmed this model for long-fiber interferometers—and those have been only in the acoustic range—whereas strong deviations were found at low frequency (9, 10). A similar theory was developed for fiber lasers, but a discrepancy with Wanser’s expression was pointed out, and the measured low-frequency noise was far from the predicted level as well (7). To explain this behavior, a different theoretical model was proposed for fiber lasers, based on the introduction of source terms in the stochastic heat diffusion equation (11). However, the extrapolation of the predictions of these models at low frequencies is still questionable. To our knowl-

edge, no theory or experiment has been reported to date for high-finesse passive fiber resonators, which leaves open the question of which theoretical approach better describes the observed noise. In the absence of other models, we used Wanser’s formula with a finesse-dependent length to account for the power storage inside the cavity due to multiple reflections. Although the use of this scaling factor is arguable, it leads to a factor 8 in the noise calculation compared with the original Wanser’s formulation, and it describes well the observed noise. Finally, we note that the OFC noise-limited strain resolution is about a factor 6 below the measured noise floor, thereby indicating that we were approaching the thermal fluctuation level predicted by Wanser’s expression (8), even considering the actual length of our fiber sensor. On the other hand, very recently a new model for low-frequency thermally induced length fluctuations in optical fibers was proposed by Duan (12, 13), following an approach based on the fluctuation-dissipation theorem (14). A comparison with our data is already shown by Cranch and Foster (6), but a deeper analysis reveals that the expression derived from (12) is much closer to experimental findings than others.

The formula is based on the calculation of the dissipated elastic energy in a bar of finite length. The dissipation is expressed by the structure damping model through a loss angle ϕ , whose value for acrylic-coated silica fibers is only available in the 75- to 200-kHz range (15). In Fig. 1, we show the noise spectrum re-calculated from (12), using the real part of Young’s modulus recently measured in (16) and the lowest-frequency ϕ obtained from (15). Actually, there is no direct evidence that this value is valid at frequencies below 1 kHz, and it is suggested that, in principle, the loss angle is a function of frequency (17). Nonetheless, the resulting theoretical curve resembles our data between 1 Hz and 10 Hz. In Fig. 1, we also show the root mean square (RMS) sum between the comb-induced laser-frequency noise and the thermal noise spectrum derived from (12), which agrees well with our data for $f > 1$ Hz. It is interesting to note that the noise spectrum calculated from (12) is markedly different from that obtained by Cranch and Foster over the same frequency range. Furthermore, the model developed in (12) is the only one that accounts for a noise roll-up at low frequencies in passive fibers.

We fully investigated all known noise sources in (3). The locked laser-frequency noise calculated from local oscillator (LO) phase-noise multiplication in the OFC was found to be well below the measured strain noise level. Extra phase noise was injected in the system via the LO as a countercheck, and the resulting strain spectrum demonstrated that the observed detection limit was not due to the residual laser-frequency stability [supporting online material for (3)]. Environmental disturbances were minimized by careful thermal, acoustic, and seismic insulation. Shielding from low-frequency vibrations was provided by a long elastic suspension, with resonance around 0.7 Hz: Neither seismic noise ($\propto 1/f^2$) below 1 Hz nor low-pass filtering from the suspension ($\propto 1/f^2$) above 1 Hz were visible in the measured RMS strain spectral densities. In our opinion, all the above sources can be ruled out from the noise

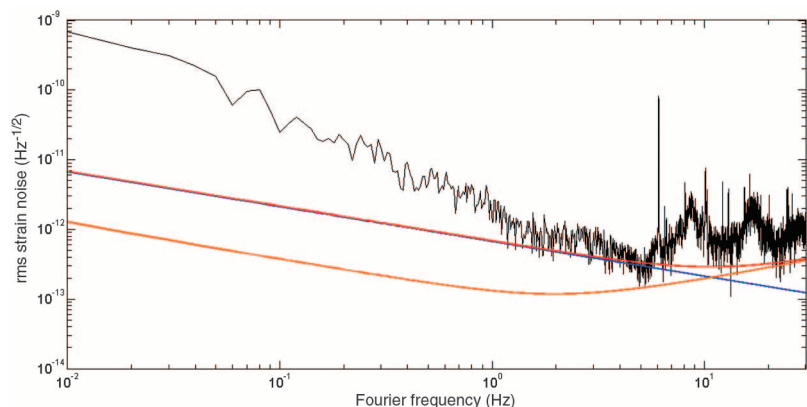


Fig. 1. Strain noise measured by the FBG resonator in (3). The blue line is the noise calculated from Duan’s model (12), the orange line is the comb-stabilized strain noise, and the red line is the RMS sum of them.

Consiglio Nazionale delle Ricerche—Istituto Nazionale di Ottica (INO) and European Laboratory for Non-Linear Spectroscopy (LENS), Comprensorio A. Olivetti, Via Campi Flegrei 34 I-80078 Pozzuoli (Naples), Italy.

*To whom correspondence should be addressed. E-mail: gianluca.gagliardi@ino.it

budget. Accordingly, we stand by our conclusion that the measured excess noise can be of thermal origin.

A more general theory of phase noise of optical fiber resonators should consider all thermally induced noise sources. Actually, neither the model in (12) nor the more popular theories in (7, 8) considered thermal effects due to light storage in fiber resonators. Photothermal effect caused by the optical loss in photosensitive fibers and Bragg gratings has to be taken into account as a source term for calculating thermal fluctuations in the fiber. That would justify a dependence on the cavity finesse that may influence the overall assessment of thermodynamic noise. Also, thermally excited vibrations in the fiber cavity may add extra noise in the acoustic frequency range (9).

Cranch and Foster remark that thermally induced strain noise is very difficult to observe below 100 Hz. We agree that sophisticated laboratory experiments are required to observe these phenomena. However, we note that ours is the first sensor that is capable of detecting sub-

picostrain signals in the infrasonic range. We believe that the diverse theories proposed so far to describe thermal noise really need experimental validations to provide a meaningful description of physical systems. For instance, the theory proposed in (12) yields a frequency response of the type $1/\sqrt{f}$, and the temperature dependence is \sqrt{T} . This is in evident disagreement with other models (7, 8), which predict, for passive fibers, an almost flat frequency response and a temperature dependence on T .

In conclusion, we thank Cranch and Foster for opening with their comment a debate on present models and laboratory experiments. Although a validation of theoretical models was beyond the scope of our original paper as well as of this response, we are confident that our contribution can stimulate novel approaches in this field.

References and Notes

1. W. H. Glenn, *IEEE J. Quantum Electron.* **25**, 1218 (1989).
2. E. Ronnekleiv, *Opt. Fiber Technol.* **7**, 206 (2001).
3. G. Gagliardi, M. Salza, S. Avino, P. Ferraro, P. De Natale, *Science* **330**, 1081 (2010).

4. G. Gagliardi, S. De Nicola, P. Ferraro, P. De Natale, *Opt. Express* **15**, 3715 (2007).
5. D. Gatti, G. Galzerano, D. Janner, S. Longhi, P. Laporta, *Opt. Express* **16**, 1945 (2008).
6. G. A. Cranch, S. Foster, *Science* **335**, 286 (2012); www.sciencemag.org/cgi/content/full/335/6066/286-a.
7. S. Foster, A. Tikhomirov, M. Milnes, *IEEE J. Quantum Electron.* **43**, 378 (2007).
8. K. H. Wanser, *Electron. Lett.* **28**, 53 (1992).
9. K. H. Wanser, A. D. Kersey, A. Dandridge, *Opt. Photonics News* **4**, 37 (1993).
10. S. Knudsen, A. B. Tveten, A. Dandridge, *IEEE Photon. Technol. Lett.* **7**, 90 (1995).
11. S. Foster, G. A. Cranch, A. Tikhomirov, *Phys. Rev. A* **79**, 053802 (2009).
12. L. Z. Duan, *Electron. Lett.* **46**, 1515 (2010).
13. The Duan paper (12) was published on 28 October 2010, after acceptance and online publication of our paper (3).
14. Y. Levin, *Phys. Rev. D Part. Fields* **57**, 659 (1998).
15. B. M. Beadle, J. Jarzynski, *Opt. Eng.* **40**, 2115 (2001).
16. P. Antunes, H. Lima, J. Monteiro, P. S. André, *Microw. Opt. Technol. Lett.* **50**, 2467 (2008).
17. K. Numata, A. Kemery, J. Camp, *Phys. Rev. Lett.* **93**, 250602 (2004).

7 April 2011; accepted 5 December 2011
10.1126/science.1205516

HEALTHCARE

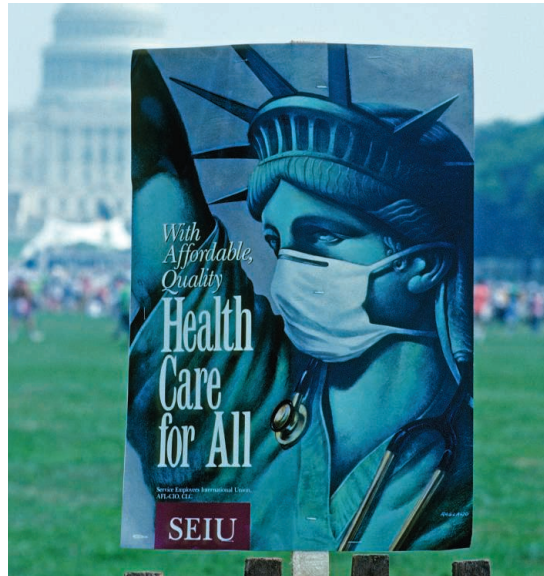
The Long and Winding Road

Jonathan Oberlander

In the summer of 2009, President Barack Obama's plan to secure enactment of major healthcare reform legislation appeared to be in serious jeopardy. In town hall meetings with members of Congress, Tea Party activists protested vociferously against the proposed expansion (real and imagined) of federal power. Buffeted by false accusations that the law would create "death panels," public support for reform was fading. Meanwhile, Republican resistance had sharpened, extinguishing any prospects of a bipartisan deal in the Senate. Anxious Democrats wondered if the push for healthcare reform should be scaled back in favor of more limited, less politically risky action.

Historians of U.S. health policy had seen this story unfold before. Since 1915, Americans have periodically engaged in fierce debates over overhauling the nation's healthcare system. And with the important exception of the 1965 law creating Medicare and Medicaid, efforts to move the United States closer to a system of universal health insurance have ended in failure or with only incremental change. But the 2009–10 episode of this long-running drama at last produced a different ending: Congress enacted the 2010 Patient Protection and Affordable Care Act (ACA), a landmark reform that provided Barack Obama with a signature achievement of his presidency. And yet, going into the 2012 elections that achievement remains embroiled in controversy, its fate uncertain as legal and political challenges mount.

Paul Starr's *Remedy and Reaction* explores why healthcare reform is so difficult to enact in the United States and how the ACA beat the odds to become law in 2010. The book's sweeping scope covers seemingly every major milestone in U.S. health policy during the past century: battles over national health insurance, the enactment of Medicare and Medicaid, the Clinton Administration's ill-fated campaign for universal insurance, Republi-



Remedy and Reaction
The Peculiar American
Struggle over Health
Care Reform

by Paul Starr

Yale University Press,
New Haven, CT, 2011. 336 pp.
\$28.50. ISBN 9780300171099.

can attempts in the past two decades to overhaul Medicare, and much more. As a work of policy history *Remedy and Reaction* excels, offering an accessible and indispensable introduction to the development of the U.S. healthcare system. Starr skillfully traces the origins of our crazy-quilt patchwork of private insurance and government programs, using that history to "make sense of a healthcare system that, from the perspective of its results, makes very little sense at all."

Given the long-standing problems in American healthcare—we have the world's most expensive system while still leaving 17% of the nation without insurance—why has meaningful reform proven so elusive? Starr argues that following World War II, the United States "ensnared itself in a policy trap" that generated a powerful "bias against change." The establishment of employer-sponsored private insurance for most working-age Americans and of Medicare for elderly Americans complicated reform by giving the "protected public," as well as stakeholders who profit from current arrangements, a stake in preserving a status quo replete with inequities and inefficiencies.

There is no question that the United States developed a complicated nonsystem of health insurance that made major change difficult—

indeed, this argument is widely accepted among health policy scholars. But there are limits to the explanatory power of Starr's policy trap. Canada, too, developed a system of employer-based insurance coverage but still managed to break away from that model and enact single-payer national health insurance. And the enactment of Medicare had little to do with the failure of U.S. reformers in the early 1970s to agree to a legislative compromise for universal insurance. These episodes underscore the crucial role that American political institutions—which fragment power, create numerous veto points that legislation must pass through, and generate divisions in Congress and between Congress and the presidency—have played in stopping comprehensive healthcare reform and weakening the incremental measures that survived the legislative gauntlet.

The Obama Administration and congressional Democrats pulled off a political miracle by circumventing—just barely—the enduring barriers to healthcare reform in 2010. Luck played a substantial role: if Pennsylvania Senator Arlen Specter had not switched political parties in 2009 in an ultimately unsuccessful effort to secure his reelection, Senate Democrats would have been deprived of the 60-vote supermajority they needed to pass healthcare legislation in the Senate. Yet their legislative triumph also reflected political skill and strategic adaptation—the defeat of the Clinton Administration's healthcare reform plan in 1993–94 produced painful lessons that they applied, such as the importance of crafting a "minimally invasive" reform plan that did not change too much for well-insured Americans.

As Starr notes, the ACA actually drew on ideas that have a long Republican lineage and that were adopted with broad bipartisan support by Massachusetts in 2006—an individual mandate to obtain health insurance, regulated marketplaces to help the uninsured buy private insurance, and tax credits to make coverage affordable for lower-income persons. While the ACA represents a substantial step forward, it has serious shortcomings, including leaving many U.S. residents uninsured and not creating a reliable system for controlling costs. Starr rightly emphasizes that the ACA "calls for major changes, but it is also notable for what it leaves unchanged."

Yet this centrist reform triggered an extreme reaction as critics alleged that the law consti-

The reviewer is at the Department of Social Medicine and Department of Health Policy and Management, University of North Carolina, Chapel Hill, NC 27599–7240, USA. E-mail: jonathan_oberlander@med.unc.edu

tuted a “government takeover” of healthcare, echoing the historic cries of “socialized medicine” heard in previous conflicts. Never mind that the ACA leaves employer-sponsored private insurance in place or that medical care delivery will remain largely in private hands. Not a single congressional Republican voted for the final version of the ACA, reflecting the rightward turn of the Republican party in recent years and historic levels of partisan and ideological polarization in Congress.

The partisan divide means that the fate of healthcare reform is unsettled. Much depends on the outcome of the 2012 elections and a forthcoming decision by the Supreme Court regarding the constitutionality of the individual mandate. *Remedy and Reaction* chronicles just how difficult a struggle it has been to make the U.S. healthcare system more equitable and efficient and how far we still have to go.

10.1126/science.1215773

ENVIRONMENT

Deploying a Powerful Pesticide

Frederick R. Davis

Silent Spring, Rachel Carson’s controversial critique of the indiscriminate use of chemical insecticides in agriculture and public health campaigns (1), was published 50 years ago. “Miss Carson’s book,” as President John F. Kennedy referred to it, galvanized the American environmental movement and fueled the hearings and litigation that would lead to the ban on uses of the pesticide DDT in the United States late in 1972. Over the past decade, Carson’s legacy and her role in the DDT ban have come under fire as pundits have questioned the wisdom of restricting the use of an important (and inexpensive) insecticide while malaria claims the lives of many victims around the globe. Meanwhile, others fear the ecological risks posed by a return to DDT.

Those seeking to understand the deep historical roots of the DDT debates need look no farther than David Kinkela’s *DDT and the American Century*. To frame his topic, Kinkela (a historian at the State University of New York–Fredonia) deftly employs Henry Luce’s concept of the “American Century,”

which justified U.S. expansionism in altruistic terms, placing Americans at the center of the global economy and efforts to control threats to health around the world. In this context, DDT served as a critical tool in the Green Revolution and in campaigns against insect-borne diseases.

In the winter of 1943–44, the Allied military government in Naples, Italy, called on the Rockefeller Foundation to stave off a typhus epidemic by delousing the populace. Kinkela argues that Americans discovered the promise of DDT through news coverage of this typhus campaign, which featured numerous paternalistic images of public health officers spraying Neapolitans with the powerful new insecticide. Once World War II ended, the foundation sought to eradicate malaria on Sardinia. After the spraying of more than 10,000 tons of DDT on the island, malaria rates dropped precipitously from more than 75,000 cases in 1946 to just 9 in 1951. Rockefeller officials celebrated DDT’s role in both campaigns despite local concerns regarding unintended consequences. DDT, Kinkela claims, became the foundation’s preferred weapon in fights against insects and disease.

DDT also played an important role in the development of the Green Revolution. Through its Mexican Agricultural Program, which began in the 1940s, the Rockefeller Foundation sought a complete modernization of Mexican farming. Rockefeller’s substantial presence allayed concerns regarding the availability of DDT in Mexico as well as worries about the viability of the new insecticide in agriculture. Norman Borlaug, the chief architect of Rockefeller’s wheat program, developed a hybrid wheat that dramatically enhanced Mexican wheat production. Kinkela, however, argues that Borlaug’s wheat required enormous amounts of water, chemical fertilizers, and pesticides, like DDT, which offset the harvest gains of the new strain.

Their ambitions fueled by local successes, entomologists began to imagine global eradication of certain insect pests, particularly malarial mosquitoes. However, Kinkela notes, the American Century created paradoxes that undermined the logic of eradication. Whereas the humanitarian goals of eradication were clear, unintended consequences for societies and ecosystems remained unknown. Yet, proponents of the American Century viewed global eradication efforts as an opportunity to generate good will, and

the World Health Organization continued to press for global eradication and required the full commitment of its member nations (more than 100 by 1965). Kinkela recounts the mounting concerns of ecologists as it became clear that DDT posed environmental threats, but eradicators ignored such concerns as they imagined that former disease-plagued areas of the world would emerge as vibrant capitalist economies.

Silent Spring appeared against this backdrop of hubristic hopes for global eradication of insect vectors of disease. Kinkela sees Carson’s book as having changed the DDT story in that she indicted the logic of eradication

and showed Americans how dangerous chemicals such as DDT had permeated many aspects of their lives. Still, her account revealed more nuance than her critics acknowledged. Far from calling for the abandonment of chemical insecticides in agriculture and public health, Carson, according to Kinkela, counseled

judicious use. Nevertheless, chemical companies launched a full-scale attack on *Silent Spring*, arguing for the continued role of pesticides in producing solutions to population growth, international food production, and the threat of communism.

In the aftermath of *Silent Spring*, American legislators debated the roles of DDT in agriculture and public health. The global fight against malaria and the struggle to feed a rapidly growing global population served as critical elements of the arguments by DDT’s defenders. Even after ecological concerns drove the United States to ban DDT, pesticide use exploded overseas, with consequences for ecosystems and human health. Moreover, Kinkela argues, the U.S. action signaled a rejection of its global presence, which notably undermined belief in the American Century.

DDT and the American Century skillfully juxtaposes DDT with American aspirations abroad. This meticulous study reveals the many historical complexities of DDT use and clarifies the pesticide’s role in U.S. global relations. While Kinkela wisely deflects questions regarding global malaria control today, his account will enrich debates surrounding the future of DDT.

References

1. R. Carson, *Silent Spring* (Houghton Mifflin, Cambridge, MA, 1962).

DDT and the American Century
Global Health, Environmental
Politics, and the Pesticide
That Changed the World

by David Kinkela

University of North Carolina Press,
Chapel Hill, 2011. 272 pp. \$39.95.
ISBN 9780807835098.

The reviewer is at the Department of History, Florida State University, Tallahassee, FL 32306–2200, USA. E-mail: fdavis@fsu.edu

AGRICULTURE

What Next for Agriculture After Durban?

J. R. Beddington,^{1*} M. Asaduzzaman,² M. E. Clark,³ A. Fernández Bremauntz,⁴ M. D. Guillou,⁵ D. J. B. Howlett,⁶ M. M. Jahn,^{7†} E. Lin,⁸ T. Mamo,⁹ C. Negra,¹⁰ C. A. Nobre,¹¹ R. J. Scholes,¹² N. Van Bo,¹³ J. Wakhungu¹⁴

Global agriculture must produce more food to feed a growing population. Yet scientific assessments point to climate change as a growing threat to agricultural yields and food security (1–4). Recent droughts and floods in the Horn of Africa, Russia, Pakistan, and Australia affected food production and prices. The Intergovernmental Panel on Climate Change predicts that the frequency of such extreme weather events will increase (5), which, when combined with poverty, weak governance, conflict, and poor market access, can result in hunger and famine. At the same time, agriculture exacerbates climate change when greenhouse gases (GHGs) are released by land clearing, inappropriate fertilizer use, and other practices (6).

Alternative agricultural practices, tailored to different regions, show promise for reducing net GHG emissions and maintaining or improving yields despite extreme weather (7). In Niger, agroforestry on 5 million hectares has benefited >1.25 million households, sequestered carbon, and produced an extra 500,000 metric tons of grain per year (8). In Denmark, agricultural emissions have been reduced by 28%, while productivity increased (9).

Agriculture, the FCCC, and Durban

Despite growing support for an integrated approach to agricultural adaptation to, and mitigation of, climate change, financial and policy actions have been slow to materialize in most countries and at the global level, including the United Nations Framework Convention on Climate Change (FCCC). At the 15th

FCCC Conference of the Parties (COP-15) in Copenhagen, negotiators developed text on agriculture, but no agreement was reached. In the lead-up to COP-17 in Durban in late 2011, political momentum grew for a work program on agricultural adaptation and mitigation within the FCCC's Subsidiary Body for Scientific and Technological Advice (SBSTA). This included a common position by African Ministers (10), the scientific Wageninngen Statement (11), a joint letter from the United Nations and other agencies (12), and public statements by South African President Jacob Zuma and former UN Secretary-General Kofi Annan.

COP-17 produced the “Durban Platform for Enhanced Action” (13), which commits parties to reach a legal framework for reducing global emissions by 2015. The only specific agreement on agriculture was to consider adopting a framework for sectoral actions, which could include agriculture, and for the SBSTA to “exchange views on agriculture,” with a 5 March deadline for parties and observers to provide evidence (13). This modest progress, without adoption of a formal work program on agriculture, can be attributed to the following issues:

- Views on inclusion of agriculture depend on the degree to which agriculture features in national economies. Countries vary in their vulnerability to climate change, their GHG emissions from agriculture, and their opportunities to reduce emissions from changes in agricultural practice. Forested nations that may benefit from Reducing Emissions from Deforestation and Forest Degradation (REDD+) policies may see the inclusion of agriculture as delaying or competing for climate finance.

- Actions agreed in Durban were in the mitigation track of FCCC negotiations, which are separate from adaptation discussions. This obscures opportunities for agriculture, which can deliver benefits for both, and has led to concern that the focus on agricultural adaptation—a priority for developing countries—will be reduced. Others worry that inclusion of agriculture under the mitigation track could lead to mandatory

Despite obstacles in the UN climate talks, modest progress and opportunities for scientific input on agriculture arose.

commitments and/or that possible mechanisms (e.g., carbon trading) will not benefit smallholder farmers. Some countries do not welcome potential restrictions on conversion of land to agricultural use. Export-focused agricultural producers worry that mitigation measures for agriculture could restrict trade from “high-emission agriculture.”

- Some negotiators are concerned that technical challenges (e.g., carbon monitoring by millions of farmers and pastoralists) are too great to develop agriculture agreements.

In general, higher-income countries, farmers' organizations, UN and agricultural agencies, and some nongovernmental organizations (NGOs) supported a SBSTA work program on agricultural adaptation and mitigation. Other nations, primarily low and middle income, supported by a different set of NGOs, resisted a work program and called for emphasis on agricultural adaptation to climate change.

What Now on Agriculture?

The Commission on Sustainable Agriculture and Climate Change was set up in early 2011 to synthesize evidence into policy actions to help achieve a food-secure world in the face of climate change. The Commission encouraged policy action inside the FCCC, as well as through other global processes (e.g., the UN Conference on Sustainable Development and the G-20) and bilateral, national, public-private, and “bottom-up” initiatives (14). Seven priority actions were identified:

1. Integrate food security and sustainable agriculture into global and national policies, including adaptation and mitigation;
2. Increase global investment in sustainable agriculture and food systems;
3. Sustainably intensify agricultural production while reducing emissions and other environmental impacts;
4. Target programs and policies to assist vulnerable populations;
5. Reshape food access and consumption to ensure that basic nutritional needs are met and to foster healthy and sustainable eating habits;

¹Government Office of Science, UK. ²Bangladesh Institute of Development Studies. ³Commonwealth Scientific and Industrial Research Organisation, Australia. ⁴Universidad Autónoma Metropolitana, Mexico. ⁵INRA, French National Institute for Agricultural Research. ⁶UK Department for International Development and University of Leeds, UK. ⁷University of Wisconsin–Madison, USA. ⁸Chinese Academy of Agricultural Sciences. ⁹Ministry of Agriculture, Ethiopia. ¹⁰Secretariat, Commission on Sustainable Agriculture and Climate Change. ¹¹Ministry of Science, Technology and Innovation, Brazil. ¹²Council for Scientific and Industrial Research, South Africa. ¹³Vietnam Academy of Agricultural Science. ¹⁴African Center for Technology Studies, Kenya.

*Complete addresses are available in the SOM.

†Author for correspondence. E-mail: mjahn@wisc.edu

6. Reduce food loss and waste across supply chains; and

7. Create comprehensive information systems on human and ecological dimensions.

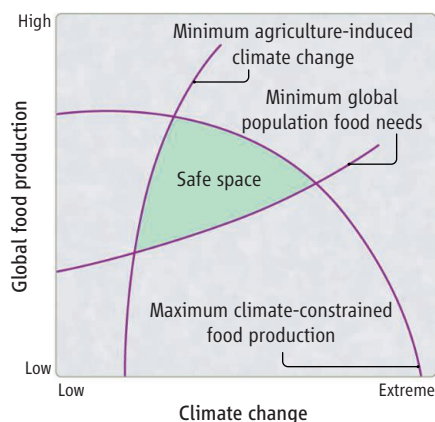
In light of these recommendations and the obstacles and opportunities highlighted in Durban, and acknowledging the many factors beyond science, we suggest areas for scientific contribution to policy progress under the FCCC:

•Common definitions. Terms like “climate-smart agriculture” (CSA) and “sustainable intensification” are widely used in relation to FCCC; however, common understandings of how these terms address adaptation and mitigation is needed. The following elements are essential to defining these terms: maintains or increases production of food, fodder, fiber, and fuel; supports livelihoods and builds prosperity; sustains environmental resources and ecosystems; adapts to existing and future climate; and, sequesters carbon and/or reduces GHG emissions. Through efforts like the CSA source book (15), led by the UN Food and Agriculture Organization, scientists can develop objectively grounded “standards” and can address concerns about an unbalanced focus on mitigation.

•Forestry and agriculture. Although agreements reached at Durban for REDD+ did not explicitly mention agriculture, it is implicitly recognized as a driver of deforestation. Scientists can more clearly describe adaptation and mitigation strategies that span agriculture and forestry and improve food security and livelihoods.

•New information systems. To help countries evaluate potential policies and practices for agricultural adaptation and mitigation, geographically explicit estimates of risks and benefits are needed. These should better describe and manage tradeoffs and synergies among the biophysical and human dimensions of systems affected by agriculture and emissions from agriculture. We need to assess who has benefited from actions in agricultural landscapes and food systems and to develop and test a broad range of potential mechanisms for both mitigation and adaptation (i.e., not just market-based approaches). This must be supported by a global, public-domain system of repeated observations of terrestrial systems at scales suitable for small-holder agriculture.

•Scaling up to “safe operating space.” The Commission emphasized that the world is already outside a safe operating space with respect to agriculture, climate change, and food security, as defined by three theoretical limits: the maximum amount of food that



A schematic of an integrated conceptual framework for the scientific community to define and test limits, thresholds, and dynamics that affect food security in the face of climate change. Modified from (14).

can be produced under a given climate; the minimum quantity of food needed by a growing population; and the minimum effects of food production on the climate (see the figure) (14). To mobilize increased investment, scientists must document ways that farmers, industry, consumers, and government can move toward, expand, or shift the safe space and achieve multiple benefits from sustainable farming practices (1, 7–9, 12, 14). More integrated research and improved knowledge systems on what works in different regions, farming systems, and landscapes is needed, especially in the most vulnerable socio-ecological systems.

•Climate financing. We are already seeing investments in agriculture through the Adaptation Fund of the Kyoto Protocol. There are two other opportunities: the Green Climate Fund (13), which is to invest \$100 billion per year for mitigation and adaption to climate change in developing countries, and the Clean Development Mechanism (13). For both, we need processes that allow investments in integrated agricultural adaptation and mitigation.

•National action. Linked to the FCCC are national plans for adaptation and mitigation that should consider agriculture (13). For developed countries, this means transforming incentives and markets to steer public and private investments toward efficient, sustainable agricultural practices. For developing countries, this means increasing investment in agricultural development emphasizing “climate-smart” practices and food security.

Conclusions

Converging trends in climate change, population growth, and use of resources threaten

global food security and environmental sustainability. Widespread use of sustainable agricultural practices can help by reducing risks to food production and farmer incomes and by decreasing GHG emissions and resource degradation. Investments and policy changes are needed from local to global scales. A SBSTA work program on agriculture, looking at adaptation and mitigation, and an agreement on a framework for agriculture are needed at COP-18 in Qatar in late 2012. By expanding understanding of agricultural practices that deliver multiple benefits and of the links between agriculture and forestry, scientists can make critical contributions to these initiatives.

References and Notes

1. Foresight, *The Future of Food and Farming: Final Project Report: Futures* (Government Office for Science, London, 2011).
2. INRA and Agricultural Research for Development (CIRAD), *Agrimonde: Scenarios and Challenges for Feeding the World in 2050* (Editions Quae, Versailles, France, 2011).
3. B. D. McIntyre, H. R. Herren, J. Wakhungu, R. T. Watson, Eds., *Agriculture at a Crossroads: A Synthesis of the Global and Sub-Global IAASTD Reports* [International Assessment of Agricultural Knowledge, Science and Technology for Development (IAASTD), Island Press, Washington, DC, 2009].
4. D. B. Lobell et al., *Science* **333**, 616 (2011).
5. IPCC, *Summary for Policy Makers: Special Report on Managing the Risks of Extreme Events and Disasters to Advance Climate Change Adaptation* (Cambridge Univ. Press, Cambridge, 2011).
6. P. Smith et al., in *Climate Change: Mitigation. Contribution of Working Group III to Fourth Assessment Report of the Intergovernmental Panel on Climate Change*, B. Metz, O. R. Davidson, P. R. Bosch, R. Dave, L. A. Meyer, Eds. (Cambridge Univ. Press, Cambridge, 2007), chap. 8.
7. J. Pretty et al., *Int. J. Agric. Sustain.* **9**, 5 (2011).
8. C. Reij, G. Tappan, M. Smale, *Agroenvironmental transformation in the Sahel: Another kind of “Green Revolution”* (IFPRI Discussion Paper 914, International Food Policy and Research Institute, Washington, DC, 2009); www.ifpri.org.
9. Decline in Danish agricultural greenhouse gases (Danish Food and Agriculture Council, Copenhagen, 2011); www.agricultureandfood.dk.
10. The Johannesburg Communiqué—“Africa: A Call to Action,” African Ministerial Conference on Climate-Smart Agriculture, Johannesburg, South Africa, 13 to 14 September 2011; <http://climatechange.worldbank.org/sites/default/files/documents/CSACommunique14.09.11.pdf>.
11. Global Science Conference on Climate-Smart Agriculture, Wageningen Statement; www.gscsa2011.org/LinkClick.aspx?fileticket=eDlto5l7E0E%3d&tabid=2871.
12. Agriculture and Rural Development Day, www.agricultureday.org/openletter.
13. UN Climate Change Conference, Durban, November–December 2011, <http://unfccc.int/2860.php>.
14. J. Beddington et al., *Achieving Food Security in the Face of Climate Change, Summary for policy makers from the Commission on Sustainable Agriculture and Climate Change* [Consortium of International Agricultural Research (CGIAR) Research Program on Climate Change, Agriculture and Food Security (CCAFS), Copenhagen, Denmark, 2011]; <http://ccafs.cgiar.org/commission/>.
15. Climate-Smart Agriculture: Managing Ecosystems for Sustainable Development, www.fao.org/climatechange/climatesmart/en/.

Supporting Online Materials

www.sciencemag.org/cgi/content/full/335/6066/289/DC1

10.1126/science.1217941

PSYCHOLOGY

Bird-Brained Illusionists

Barton L. Anderson

Our perceptual experience is constructed from the cues extracted about the content of the world by our senses. In vision, any source of image variation that is predictive of a property about the world is a potential cue. But which cues are actually used, and how do they affect our experience and behavior? If we understand what cues are used to make inferences about the world, then we should be able to manipulate our perceptual experience by manipulating the cue, even if—and most impressively when—this manipulation gives rise to experiences that appear to differ from physical reality (1). On page 335 of this issue, Kelley and Endler (2) show that humans may not be alone in this perceptual manipulation game. In terms of concrete rewards, we may even be trumped by the architectural craftsmanship of male great bowerbirds.

The males of avenue-species bowerbirds—including great bowerbirds—construct elaborate bowers composed of two stick walls (see the figure, panel A). The bowers are aligned to run from north to south, and the ends are filled with “gesso” (a collection of gray to white shells, stones, and bones), upon which colored objects are placed and thrown. These elaborate bowers have only one purpose: to lure female mates. Females enter bowers from their south end and watch the male at the north end carry on a display that includes vocalizations, movements, and the tossing of colored objects in front of the gesso. Many males never succeed in attracting females to their bowers, and only a select few do most of the mating after females visit and inspect their bower. The reproductive stakes are therefore high, and the quality of the bower plays a key role in separating the successful from the unsuccessful male. Kelley and Endler now show that one of the measures of bower quality is literally in the eye of the beholder—specifically, the female’s view of the gesso from within the bower (see the figure, panel B).

In a previous report, Endler *et al.* (3) discovered that the arrangement of the gesso is not random: Smaller objects are arranged near the opening of the display court, and larger ones more distant from the opening.

School of Psychology, University of Sydney, Sydney, NSW 2006, Australia. E-mail: barta@psych.usyd.edu.au



How to attract a mate. The bachelor bower (A) of a male great bowerbird serves to attract females to mate. Kelley and Endler show that the males arrange the gradients in the rocks such that from the vantage point of the female in the bower, larger objects are placed farther away, making the projected texture appear more uniform (B). This arrangement results in an optical illusion, but it remains to be shown whether the birds construct these illusions intentionally.



When the researchers reversed the gradient, the bowerbirds rapidly restored it to its initial distribution (but not the individual objects, just the gradient). This study showed that male bowerbirds, for whatever reason, care about the gradient. The interesting observation was that the bower creates a condition conducive to creating experiences of “forced perspective,” a term used to describe size and/or distance illusions in photography, filmmaking, and vision science laboratories.

Kelley and Endler provide insight into why the males care so much about the gradient. They report that the males most adept at crafting forced-perspective illusions are most likely to achieve mating success. In other words, not only the males care about the distribution of gesso; the females also care, and appear to make mating decisions based on perceived properties of the gesso. The projected gradients, as seen from within the bower, are more predictive of mating success than the actual physical gradients.

The bowers constructed by great bowerbirds to attract mates create optical size and distance illusions.

These intriguing results suggest that male bowerbirds manipulate the perceptual experience of prospective mates, which appear to create illusions of forced perspective. But do these results actually demonstrate that bowerbirds use illusions to promote mating success? Have male bowerbirds mastered the laws of perspective and learned to manipulate them to achieve lascivious ends?

Although this possibility is intriguing, the current data are not yet sufficiently rich to sustain this remarkable hypothesis. The data provide compelling evidence that the quality of the gradient, from the vantage point of the female, predicts mating success, but the visual fact of the more uniform texture, not an illusion, may be the only factor determining her preference. Indeed, it has been previously reported that males with more symmetrical bower avenues have a higher mating success rate (4). Constructing a bower that appears as orderly as possible from the female viewpoint is in itself a remarkable feat, but it does not entail the construction of illusions.

The authors list seven possible consequences of their findings, most of which involve speculations about the role that visual illusions might play in shaping females' mating choices. Although intriguing, there are currently no data to support these speculations, as the authors appropriately note. Indeed, some of the proposed effects may be perceptually nonexistent or even in the opposite direction to that proposed by the authors.

For example, the authors suggest that the manipulated gradients might cause male bowerbirds or their display objects to appear larger. But if bowerbirds experience the same illusion as humans, then the positive texture gradients in the bower should cause more distant objects to appear closer in depth than

they truly are, which should, in turn, cause them, or objects placed or displayed in front of these regions, to appear smaller. There is also no evidence that bowerbirds use texture gradients as a cue to depth, or if they do, how strongly they weight this cue in comparison to others. Any attempt to ascribe bowerbird mating success to their capacity to construct visual illusions requires a much more extensive assessment of their visual sensitivities than currently available.

Another interpretation of the data is that there is some other behavior that is highly correlated with the males who produce the best forced-perspective displays, and that it is this other behavior that is responsible for the mating choices made by females.

So the question remains: Do male bow-

erbirds craft illusions to attract mates? The answer is currently unknown. Kelley and Endler's data suggest that male bowerbirds appear to consider the viewpoint of their potential mates when constructing their bower courtyards, and the ones who do this best are rewarded with a higher rate of mating success. Just what matters, and why it matters, remain open and intriguing questions.

References

1. B. L. Anderson, J. O'Vari, H. Barth, *Curr. Biol.* **21**, 492 (2011).
2. L. A. Kelley, J. A. Endler, *Science* **335**, 335 (2012).
3. J. A. Endler, L. C. Endler, N. R. Doerr, *Curr. Biol.* **20**, 1679 (2010).
4. G. Borgia, *Am. Sci.* **83**, 542 (1995).

10.1126/science.1217451

CANCER

Taking a Back Door to Target Myc

Gerard Evan

The transcription factor Myc coordinates the expression of a vast and functionally diverse repertoire of thousands of genes that, together, are required for the orderly proliferation of somatic cells within the body. These include genes that govern processes within the cell, such as the cell division cycle, cell metabolism and biosynthesis, cell architecture, and cell survival, as well as the multitude of processes that proliferating cells need to engage in their surrounding microenvironment, such as the generation of blood vessels, tissue remodeling, and the recruitment of cells loaded with enzymes and growth factors needed to do this. Myc is functionally nonredundant and absolutely required for the efficient proliferation of normal and cancer cells. Its expression depends on growth signals in normal cells, ensuring that its growth-promoting activities are unleashed only in cells instructed to proliferate. Control of Myc expression in cancer cells is almost always compromised. Mutations that cause Myc to become hyperactivated cause uncontrollable cell proliferation and tumor formation. However, Myc has proven to be an elusive target for drug development. On page 348 of this issue, Kessler *et al.* (1) provide insight into how Myc's oncogenic activity might be suppressed by targeting nononcogenic proteins whose functions help

Myc to transform cells.

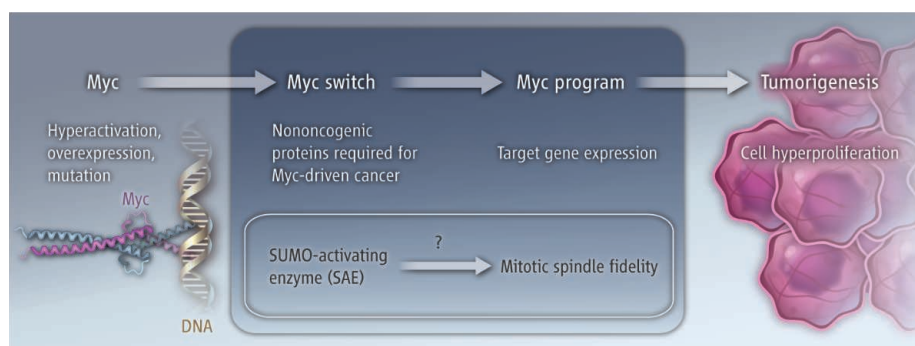
Myc is thought to act as a "driver" of cancer, but in many cancers, the *Myc* genes (there are three isofunctional genes) appear untainted. In these situations, Myc expression is deregulated due to its relentless induction by oncogenic mutations in upstream signaling molecules. Whether this occurs by direct or indirect mechanisms, the outcome locks cells into a continuously proliferating state.

Experiments in which a switchable transgenic form of oncogenic Myc is used to drive tumor formation in mice have shown that inactivation of transgenic Myc in such tumors triggers dramatic regression. This is mediated by a variety of mechanisms, but typically involves terminal differentiation, tumor cell death, and collapse of the tumor microenvironment (2–5). Further mouse

The oncogenic activity of the transcription factor Myc might be blocked by targeting nononcogenic proteins that Myc depends on to cause cancer.

studies have also demonstrated that inhibition of endogenous Myc function also elicits a therapeutic effect in diverse tumor types in which Myc is not itself mutated and where the oncogenic driver mutations lie in other signaling pathways (6, 7). Moreover, indirect pharmacological inhibition of Myc triggers tumor regression (8). These studies have strengthened Myc's candidacy as a promising cancer drug target and also intimate that Myc inhibition might be therapeutic in many or most cancer types, irrespective of the driving oncogenic mechanism. Unfortunately, we have as yet no clue how to develop drugs that inhibit Myc function.

If Myc can't be targeted, what can be done? One intriguing idea is that the oncogenic mutations that drive cancers necessarily impose novel dependencies on other, collat-



Myc-driven cancer. Many genes implicated in Myc-driven cancer encode proteins that are not oncogenic and may affect a specific genetic program regulated by Myc that promote tumorigenesis.

Department of Biochemistry, University of Cambridge, Cambridge CB2 1QW, UK. E-mail: gie20@cam.ac.uk

The authors list seven possible consequences of their findings, most of which involve speculations about the role that visual illusions might play in shaping females' mating choices. Although intriguing, there are currently no data to support these speculations, as the authors appropriately note. Indeed, some of the proposed effects may be perceptually nonexistent or even in the opposite direction to that proposed by the authors.

For example, the authors suggest that the manipulated gradients might cause male bowerbirds or their display objects to appear larger. But if bowerbirds experience the same illusion as humans, then the positive texture gradients in the bower should cause more distant objects to appear closer in depth than

they truly are, which should, in turn, cause them, or objects placed or displayed in front of these regions, to appear smaller. There is also no evidence that bowerbirds use texture gradients as a cue to depth, or if they do, how strongly they weight this cue in comparison to others. Any attempt to ascribe bowerbird mating success to their capacity to construct visual illusions requires a much more extensive assessment of their visual sensitivities than currently available.

Another interpretation of the data is that there is some other behavior that is highly correlated with the males who produce the best forced-perspective displays, and that it is this other behavior that is responsible for the mating choices made by females.

So the question remains: Do male bow-

erbirds craft illusions to attract mates? The answer is currently unknown. Kelley and Endler's data suggest that male bowerbirds appear to consider the viewpoint of their potential mates when constructing their bower courtyards, and the ones who do this best are rewarded with a higher rate of mating success. Just what matters, and why it matters, remain open and intriguing questions.

References

1. B. L. Anderson, J. O'Vari, H. Barth, *Curr. Biol.* **21**, 492 (2011).
2. L. A. Kelley, J. A. Endler, *Science* **335**, 335 (2012).
3. J. A. Endler, L. C. Endler, N. R. Doerr, *Curr. Biol.* **20**, 1679 (2010).
4. G. Borgia, *Am. Sci.* **83**, 542 (1995).

10.1126/science.1217451

CANCER

Taking a Back Door to Target Myc

Gerard Evan

The transcription factor Myc coordinates the expression of a vast and functionally diverse repertoire of thousands of genes that, together, are required

The oncogenic activity of the transcription factor Myc might be blocked by targeting nononcogenic proteins that Myc depends on to cause cancer.

eral pathways (9, 10). For example, individual oncogenic mutations may engage growth-inhibitory tumor suppressor pathways that curb the devastating potential of rogue cells. Indeed, Myc triggers programmed cell death (apoptosis), a self-defeating propensity that must be blocked by cooperating oncogenic mechanisms before its oncogenic capacity can be manifest. Given Myc's prodigious diversity of downstream targets, it seems likely that other such acquired dependencies exist.

To find such "synthetic lethalties," Kessler *et al.* employed an unbiased screening approach in which a genome-wide library of small hairpin interfering RNAs (shRNAs) was used to block expression of genes in human mammary epithelial cells engineered to express oncogenic Myc. By comparing the abundance of shRNAs in control versus Myc-expressing cells that survive, the authors identified shRNAs (and their complementary gene targets) that confer selective disadvantage only in the presence of oncogenic Myc. This approach identified several genes already implicated in survival of Myc-driven cancer cells, including MDM2, a negative regulator of the p53 tumor suppressor pathway. Unexpectedly, however, the screen also identified a specific SUMO-activating enzyme (the heterodimer SAE1/2) (see the figure). Such enzymes covalently attach small SUMO proteins to specific target proteins, thereby modifying their target's behavior. In this way, SAEs function as general purpose, context-dependent switches. Inhibition of SAE2 triggered mitotic spindle defects in Myc-expressing cells, eliciting missegregation of chromosomes. Consistent with this, breast cancer patients with high Myc-expressing tumors but low amounts of SAE1/2 fared substantially better than patients whose cancers expressed high amounts of SAE1/2. It might appear as no surprise that interference with processes necessary for successful completion of the cell division cycle provokes unrecoverable problems. However, the unbiased approach adopted by Kessler *et al.* is profound in its capacity to unearth components of such necessary processes irrespective of how indirectly or circuitously they are involved.

Why do Myc-driven cells die when SAE1/2 function is ablated? Although it may be a consequence of the mitotic defects that SAE1/2 inhibition elicits, there is no direct evidence for this. Oncogenic Myc reduces the threshold for triggering apoptosis and thereby sensitizes cells to many stresses, including DNA damage, growth factor or nutrient privation, matrix detachment, and hypoxia (11, 12). So it remains possible that cell death induced by a decrease in SAE1/2

arises from interference with some other, as yet unknown, SAE1/2 function. Another nagging problem is why modest expression of deregulated Myc should elicit such remarkable synthetic lethalties at all. Endogenous Myc is already expressed at appreciable levels in proliferating cells such as human mammary epithelial cells and this amount is barely doubled upon expression of ectopic Myc. Is it the increased amount of Myc that confers vulnerability or is it because ectopic Myc, unlike normal endogenous Myc, is expressed in a constitutive unregulated manner? If the former, then the synthetic lethality observed arises from some type of novel process born of excessive Myc—perhaps the engagement of novel target genes via lower-affinity Myc-binding DNA elements—and would presumably be progressively more evident in those cancer cells expressing yet greater amounts of Myc. If the latter, then the synthetic vulnerability must have its roots in the anomalous persistence of some or other Myc effector function.

In the end, the key question is whether it is best to target a collateral Myc dependency or bite the bullet and target Myc itself. Targeted therapies frequently fail because cancer cells compensate for, and evolve around, the drug-induced blockage (13). Such relapses are a tragic by-product of the fact that biological "wetwear" is inherently

noisy and works reliably only because signaling networks have evolved to be robust, self-correcting, and functionally degenerate. Hence, the therapeutic durability of targeting a pharmacologically tractable synthetic lethal function like SAE1/2 will depend not only on how tight its initial interdependency with Myc is, but how easy such interdependency is to adapt or evolve around. By contrast, Myc is functionally nonredundant and essential for tumor cell survival, so the opportunities for circumventing Myc inhibition are greatly restricted and, perhaps, absent altogether. Most likely, successful, durable, and safe cancer therapies will exploit both types of approach.

References

1. J. D. Kessler *et al.*, *Science* **335**, 348 (2012); 10.1126/science.1212728.
2. D. W. Felsher, J. M. Bishop, *Mol. Cell* **4**, 199 (1999).
3. M. Jain *et al.*, *Science* **297**, 102 (2002).
4. S. Pelengaris, M. Khan, G. I. Evan, *Cell* **109**, 321 (2002).
5. S. Pelengaris, T. Littlewood, M. Khan, G. Elia, G. Evan, *Mol. Cell* **3**, 565 (1999).
6. L. Soucek *et al.*, *Nature* **455**, 679 (2008).
7. N. M. Sodir *et al.*, *Genes Dev.* **25**, 907 (2011).
8. J. Zuber *et al.*, *Nature* **478**, 524 (2011).
9. R. Brough, J. R. Frankum, S. Costa-Cabral, C. J. Lord, A. Ashworth, *Curr. Opin. Genet. Dev.* **21**, 34 (2011).
10. W. G. Kaelin Jr., *Nat. Rev. Cancer* **5**, 689 (2005).
11. G. I. Evan *et al.*, *Cell* **69**, 119 (1992).
12. S. W. Lowe, E. Cepero, G. Evan, *Nature* **432**, 307 (2004).
13. Z. Zhang, A. L. Stiegler, T. J. Boggon, S. Kobayashi, B. Halmos, *Oncotarget* **1**, 497 (2010).

10.1126/science.1217819

PHYSICS

Moving Beyond Trust in Quantum Computing

Vlatko Vedral

A protocol that allows users and operators of a quantum computer to avoid revealing their methods has implications for the need of classical ideas in quantum mechanics.

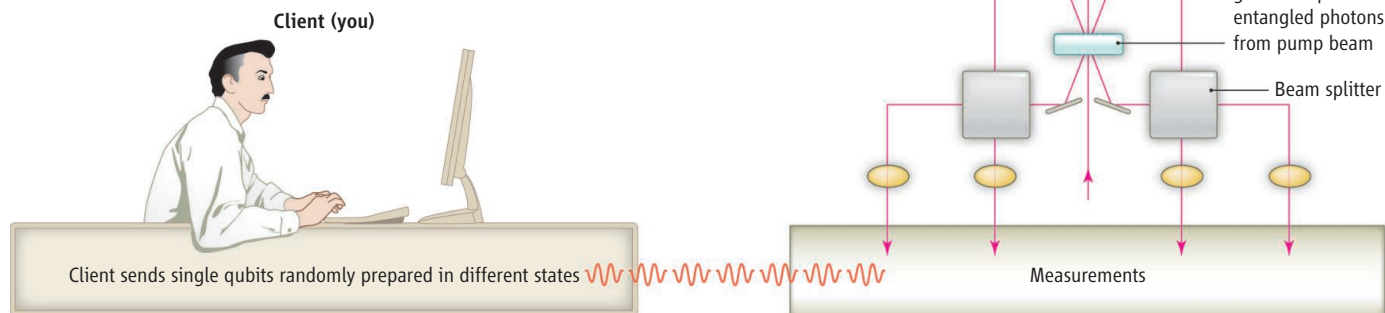
Suppose you have just come up with a killer application for a quantum computer and, by a stroke of amazing luck, a company announces that they have made the world's first large-scale quantum computer. You want them to run your app, but you don't want to disclose the code, your input, or the output. The company, on the other hand, would like to convince you—and the rest of the world—that they have a genuine quantum computer, but they don't trust you enough

to show it to you (you might be a spy for a competitor). Neither of you trusts the other—can anything be done to break the impasse? Amazingly, the answer is "yes." On page 303 of this issue, Barz *et al.* (1) show experimentally that neither of you has to reveal anything, if you can manipulate single quantum bits (qubits).

The resolution to the problem described above is generally known as "blind" quantum computation, a term introduced by Broadbent *et al.* (2). Its classical analog, first espoused by Rivest, Adleman, and Dertouzos in 1978 (3), relies on some computations

Department of Atomic and Laser Physics, University of Oxford, Oxford OX1 3PU, UK. E-mail: vlatko.vedral@gmail.com

Not passing secrets. An artist's impression of the photon-based blind quantum computation protocol. You, the client, prepare a state of a photon unknown to the server, the company running the computer. It is then passed on to the server, who, depending on the photon state, creates an entangled state of four photons. These are manipulated to execute a particular computation whose results are communicated back to the client. This way, the client can learn the result of a computation (unknown to the server) and can verify if the server can do genuine quantum computations. Note that the experiment of Barz *et al.* was performed differently for reasons of convenience (namely, the generation of entangled photons was done on the client's premises).



being thought to be intrinsically more difficult to run backward than forward (multiplying the factors of a number is simpler than finding prime factors of a given number). The quantum protocol, however, is more secure because it relies on two key features of quantum physics: the genuine randomness arising from quantum measurements, and quantum entanglement, or “spooky action at a distance” in Einstein’s language. Quantum entanglement is a form of correlation between quantum bits that exceeds any classical correlations. It is this form of super-correlation that allows quantum computers to be more efficient than classical ones.

For the particular problem posed above, if the company has a quantum computer, then they could create a large entangled state of many qubits. In the protocol for blind quantum computation, which particular state they prepare is decided by you, the user, who supplies single qubits randomly prepared in different states. All the company does is execute an entangling gate between these qubits, so they do not know which entangled state they possess (nor can they investigate the state, without changing it in a way that you could later detect). Then, they run a sequence of single qubit measurements (specified by you) and report the output of your algorithm to you. This way of executing quantum computation, by making measurements on an entangled state, is known as measurement-based quantum computation. The company cannot decipher your algorithm because it is run on a random entangled state (as far as the company is concerned) by making measurements whose outcomes are random.

However, to you, the entangled state is known (because you supplied the qubits) and the random measurement outcomes can be

streamed (meaning that a sequence of transformations can be done to account for different measurement outcomes) into a deterministic outcome (because you know the entangled state on which this is supposed to be run if the company’s claim is indeed genuine). Thus, by inspecting the output, you can know if the company really has a quantum computer, without disclosing your algorithm, the input, or indeed the output. The computation is thus “doubly” blind.

The idea behind this protocol combines quantum cryptography with the measurement-based quantum computation (4). Blind quantum computation is more secure than the classical version for the same reason that quantum cryptography is more secure than classical cryptography. The double blindness is guaranteed by the laws of quantum physics, instead of the assumed difficulty of computational tasks as in classical physics.

Experimentally, Barz *et al.* show how simple two-qubit computations can be executed in the blind way. Their method relies on being able to manipulate two polarization-entangled pairs of photons, which are generated with crystals that exhibit nonlinear optical properties (5). Various phase shifters are then applied to create different entangled states, technically known as cluster states (the phase shifts are the ones that remain unknown to the company and are generated by interacting with qubits that you supply). Barz *et al.* ran two different quantum algorithms in a blind fashion, Deutsch’s algorithm and Grover’s search. The former is a specialized algorithm aimed at detecting specific regularities in evaluating a given function, while the latter is a quantum version of searching through an unsorted database (and gives a quadratic speedup over its classical analog).

Building a large-scale quantum computer is equivalent to confirming quantum mechanics at the macroscopic level. If the quest to build a quantum computer fails, it means that quantum physics must fail at the macroscopic level, which would be a great discovery. Blind testing of quantum computation is equivalent to blind testing of macroscopic quantum mechanics (with the company being Mother Nature, reluctant to give up her secrets). Barz *et al.* show that we need to be able to manipulate a quantum bit in order to do this. Thus, in order to convince ourselves that the universe is fully quantum mechanical, we need to execute quantum mechanics at the level of individual qubits.

It might be inconsistent to think of the world as partly classical and partly quantum (6). Bohr thought that in order to talk about quantum physics and test it, we need concepts from classical physics, and we need to discuss the setting of our experiments necessarily using classical information. In blind quantum computation, we require a little bit of quantum information in order to verify a lot of quantum information. Thus, even quantum physics requires quantum physics to test its validity.

References

1. S. Barz *et al.*, *Science* **335**, 303 (2012).
2. A. Broadbent, J. Fitzsimons, E. Kashefi, in *Proceedings of the 50th Annual IEEE Symposium on Foundations of Computer Science (FOCS, 2009)*, pp. 517–526.
3. R. Rivest, L. Adleman, M. Dertouzos, in *Foundations of Secure Computation* (Academic Press, New York, 1978), pp. 169–178.
4. R. Raussendorf, H. Briegel, *Phys. Rev. Lett.* **86**, 5188 (2001).
5. P. Walther *et al.*, *Nature* **434**, 169 (2005).
6. W. H. Zurek, *Phys. Today* **44**, 36 (1991).

10.1126/science.1216922

ASTRONOMY

The Final Flight of a Sun-Diving Comet

Carey M. Lisse

Over the past decade, solar monitoring observatories have detected and discovered more than 1600 discrete members of the Kreutz family of comets. These comets are associated by common orbits and their propensity to come within a few solar radii (R_{sun}) of the Sun. They can be detected as they evaporate and disintegrate, throwing out huge amounts of fine dust and gas, which can be seen even against the Sun's glare. Thought to be the fragmented remnants of the passage of a giant (~10 to 50 km radius) parent comet several thousand years ago, the Kreutz family has been the subject of intense study by both amateur and professional astronomers using a plethora of optical and ultraviolet instrumentation onboard a number of spacecraft designed to study the Sun. On page 324 of this issue, Schrijver *et al.* (1) report combined observations from the Solar Dynamics Observatory (SDO), the Solar Heliospheric Observatory (SOHO), and Solar-Terrestrial Relations Observatory (STEREO) detailing the path of comet C/2011 N3 (SOHO) as it passes through and disintegrates in the Sun's lower corona. Such a method of cometary study may provide insight into the makeup of the parent body as well as the constituent material of the early solar system.

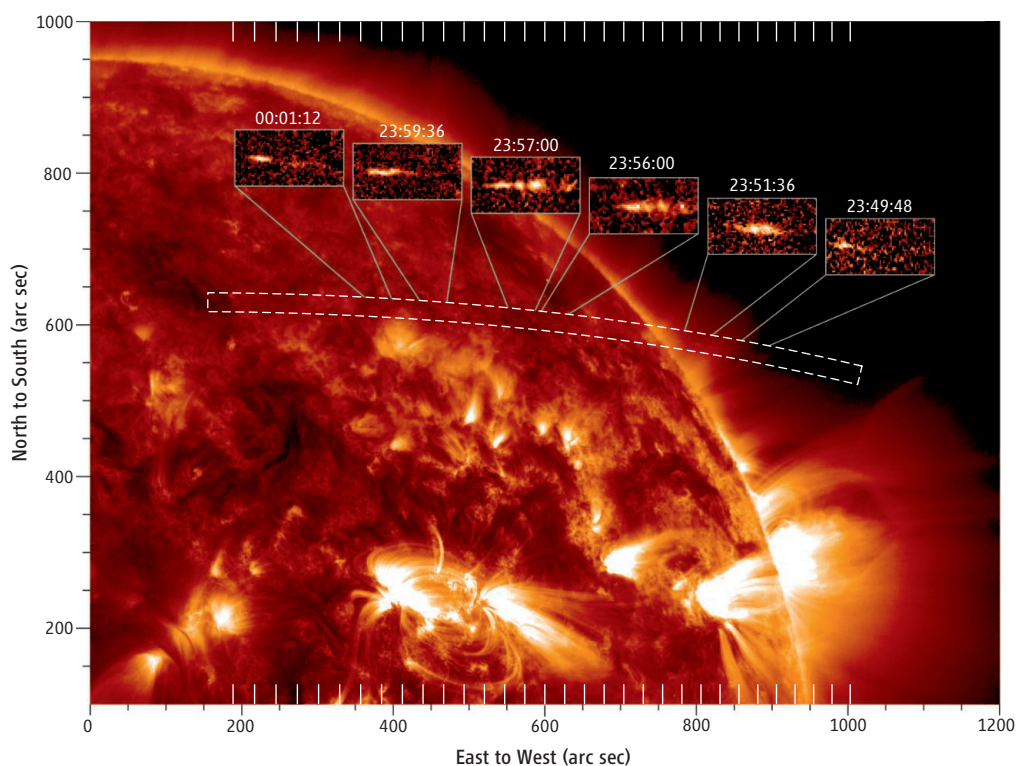
Some of the brightest comets ever seen have been large Kreutz sungrazers—the Great Comets of 1106, 1843, 1882, and C/1965 Ikeya-Seki (2, 3); and there is a steady stream of smaller Kreutz fragments arriving more or less continuously. The various pieces of the original Kreutz comet are estimated (4) to be roughly the same size (~10 to 1000 m in radius) as the fragments produced by disrupting comets D/1999 S4 (LINEAR) (5) and 73P/Schwassmann-Wachmann 3 (6, 7) and, like

those fragments, may reveal details about the sizes of the constituents from which the comets were formed.

Schrijver *et al.* tracked comet C/2011 N3 (SOHO) and monitored its optical and extreme-ultraviolet (EUV) emissions and absorptions as it passed at tremendous speed (~650 km/s) through the solar corona on 6 July 2011 UT (Universal Time) only 100,000 km (~0.15 R_{sun}) above the Sun's photosphere (see the figure). The first observations of their kind, the results pave the way for future measurements of sungrazer cometary disintegration times, length scales, masses and

A suite of space-based observatories has captured the details of a comet as it disintegrates in the solar corona.

mass loss rates. The exact physical details of the process are still to be worked out—i.e., exactly what happens to a chunk of cometary matter once it breaks off or is ejected from the nucleus—but it is highly likely, as the authors argue, that the dominant mechanisms are related to coronal plasma collisions. By studying more passages of comets through the corona, both in new events [e.g., the recent sun-diving passage of comet C/Lovejoy on 16 December 2011 (8)] and by searching through the archival SOHO, STEREO, and SDO records, we will increase our understanding of how comets fall apart and are put



A flight path to destruction. Extreme-ultraviolet image of the solar corona (in SDO's 171 Å channel, most sensitive to emission from coronal plasma near 10^6 K), on 6 July 2011 00:00:01 UTC (coordinated UT). Overlaid (dashed-white box) is the projected orbit of the comet C/2011 N3 between 5 July 2011 23:46 UTC and 6 July 2011 00:06 UT. Insets (with UTC times) show a subframe region containing the comet nucleus, coma, and debris trail, after subtraction of the same region imaged 36 s earlier to remove the background corona. The nucleus and coma region were found to be consistently dark and EUV absorptive in all images; the trail was found to be EUV bright, likely due to energy deposition and heating from collisions with the solar coronal plasma. Detailed modeling shows that the comet passed at perihelion through the closed-field solar corona rather than through the solar wind, although the EUV-bright tail does not align with the observed coronal magnetic field lines. The comet is moving from right to left across the face of the Sun in this image, and the nucleus is on the extreme left of each subframe; the debris trail is becoming fainter with time, as the comet dissipates and disintegrates in the corona. One arc sec equals ~740 km.

John Hopkins University, Applied Physics Laboratory, Laurel, MD 20723, USA. E-mail: carey.lisse@jhuapl.edu

together. The results from comet C/2011 N3 (SOHO) are thus pioneering a new method of cometary study.

Understanding the physical construction of comets sheds important light on how matter accreted from tiny, micrometer-sized specks of dust and molecules of gas to build kilometer-sized ice and rock-rich bodies, the comets, in the first million years of the solar system's existence (9). This is still a great mystery—most studies of the aggregation of protoplanetary gas and dust, using their known physical parameters (bulk modulus, porosity, surface cohesion, dielectric constant, etc.) at the expected interaction speeds of a few kilometers per second or more, show that particles should build up to millimeter- to centimeter-sized objects quite easily along the plane of the early solar system, but larger-sized particles disintegrate upon impact, creating an “aggregational barrier” to planetesimal formation (10, 11). (On the other hand, once billions of kilometer-sized comet bodies were formed, accretion into the known planetary-sized objects was relatively straightforward.) Since comets are weak bodies formed relatively gently, it is likely they fragment and disrupt into pieces similar to those from which they were assembled. Thus, the size-

frequency distribution of sun-grazing comet fragments may be able to provide important information about the formation mechanisms of comets.

Sun-grazing comets also probe a local temperature regime, from 1000 to 4000 K, that is not otherwise encountered in the solar system, emitting material via sublimation and thermal desorption as they do so. Thus, from remote spectroscopic studies of sungrazers, we can learn about the least-volatile components that make up comets (and presumably the rest of the bodies in the solar system), like the rocky silicates and metal sulfides that are some of the first materials to condense out of the protosolar nebula and protoplanetary disk and make up the bulk of Earth and the other terrestrial planets.

The work of Schrijver *et al.* also holds great promise for improving our understanding of the solar corona. By using comets as standard test particles and “running” them through the corona, observations of the passage of many comets at different heights above the photosphere, at different times, and in different solar latitudes and longitudes, will also help us to map out the three-dimensional density structure of the corona in a completely new way, independent of the

quasi-static magnetohydrodynamic models used in the past. Understanding how the roiling 5780 K convective surface of the present-day Sun, perfused with magnetic field lines extending out into interplanetary space, creates the $\sim 10^6$ K tenuous corona exosphere is not only the prime goal of NASA's next big solar mission, Solar-Probe Plus, but is also vital to our existence as human beings living 93 million miles away, as this is the region of space where the giant solar flares and coronal mass ejections are created and launched toward the planets.

References

1. C. J. Schrijver *et al.*, *Science* **335**, 324 (2012).
2. B. G. Marsden, *Astron. J.* **98**, 2306 (1989).
3. Z. Sekanina, P. W. Chodas, *Astrophys. J.* **607**, 620 (2004).
4. M. M. Knight *et al.*, *Astron. J.* **139**, 926 (2010).
5. H. A. Weaver *et al.*, *Science* **292**, 1329 (2001).
6. H. A. Weaver *et al.*, *Bull. Am. Astron. Soc.* **38**, 490 (2006).
7. W. T. Reach, J. Vaubaillon, M. S. Kelley, C. M. Lisse, M. V. Sykes, *Icarus* **203**, 571 (2009).
8. http://science.nasa.gov/science-news/science-at-nasa/2011/16dec_cometlovejoy
9. C. M. Lisse, *Bull. Am. Astron. Soc.* **42**, 965 (2010).
10. K. Wada, H. Tanaka, T. Suyama, H. Kimura, T. Yamamoto, *Astrophys. J.* **702**, 1490 (2009).
11. A. Zsom, C. W. Ormel, C. Güttler, J. Blum, C. P. Dullemond, *Astron. Astrophys.* **513**, A57 (2010).

10.1126/science.1217168

GEOPHYSICS

Transforming Earthquake Detection?

Richard M. Allen

Earthquakes are a collective experience. Citizens have long participated in earthquake science through the reporting, collection, and analysis of individual experiences. The value of citizen-generated status reports was clear after the 1995 Kobe, Japan, earthquake (1). Today's communications infrastructure has taken citizen engagement to a new level: Earthquake-related Twitter messages can outrun the shaking (2), Internet traffic detects earthquakes (3–7) and maps the distribution of shaking in minutes (8–10), and accelerometers in consumer electronic devices record seismic waveforms (11–16). What are we learning from this flood of data, and what are the limitations? How do we harness these new capabilities for scientific

discovery, and what is the role of education?

Modern geophysical instruments can record a magnitude 5 (M5) earthquake from the other side of the world. However, to map, track, and analyze the details of large destructive earthquake ruptures, and to elucidate how the rupture process links to earthquake impacts, requires detailed data from close to the event. Currently, the best traditional geophysical networks only have stations every ~ 10 km and cover limited areas. Contributions of citizens have the potential to provide much higher resolution, especially in residential areas.

The best-developed citizen-based earthquake science project today is the U.S. Geological Survey's (USGS) “Did You Feel It?” (DYFI) (8–10). After an earthquake, individuals can go online and answer questions designed to capture the data necessary to estimate shaking intensity. The location infor-

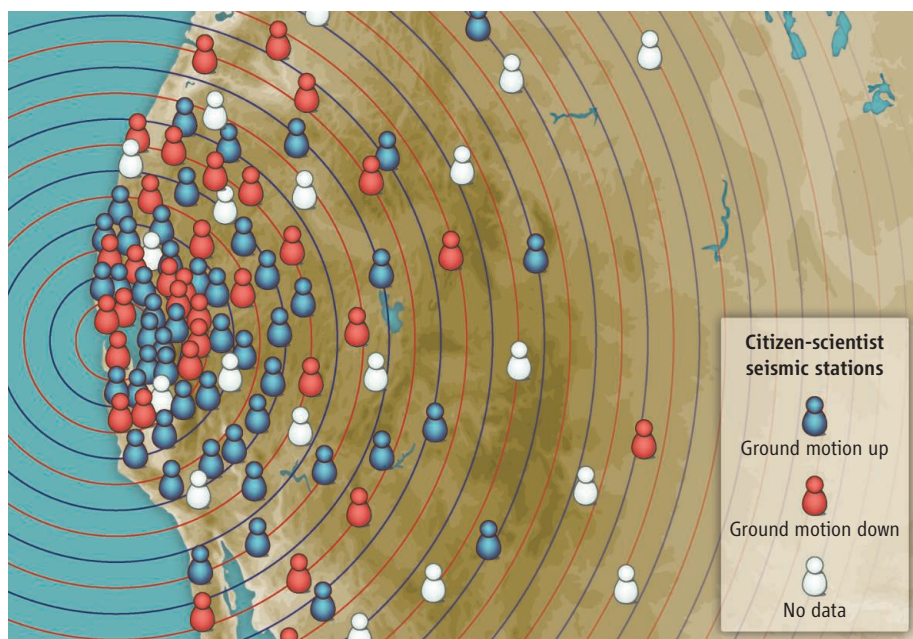
Citizen science projects have the potential to transform earthquake science if data quality standards are maintained.

mation of each report is converted to latitude-longitude coordinates and the data are mapped. Online tools allow users to explore the data set that includes their contribution. The project also has an educational component explaining earthquake phenomena.

The DYFI database now contains nearly 2 million entries available for download (8–10). The DYFI data are used to complement the traditional network data. Combined with reports of building damage, they can also help to determine how well building infrastructure can withstand earthquake shaking in different locations.

An individual's reaction to an earthquake can also be tracked for scientific purposes without that individual's active participation. The European-Mediterranean Seismological Center (EMSC) tracks the hits on its Web site and uses the hit rate and Internet protocol (IP) addresses to extract information about earth-

Seismological Laboratory and Department of Earth and Planetary Science, University of California, Berkeley, CA 94720, USA. E-mail: rallen@berkeley.edu



The value of citizen science. New networks allow citizen-scientists to host seismic stations and provide detailed waveform recordings. This instantaneous view of ground shaking looks like ripples on a pond propagating away from the earthquake source. In the future, such data may provide detailed observations of seismic wave propagation and earthquake source processes. The challenge is to maintain data quality and ensure that citizen networks are still active when the next big earthquake occurs.

quake occurrence and the likely affected areas (6, 7). Similarly, the USGS monitors Twitter messages containing the word “earthquake” to detect events (3–5). This approach detects earthquakes that are broadly felt but provides no accurate location or magnitude information. Research continues into whether intensity information can be extracted from tweets.

Reports of individual experiences are valuable sources of data, but instrumental time series of ground motion contain much more information. Accelerometers that record such data are now embedded in many laptop computers and smart phones. The “iShake Cal” iPhone application records seismic waveforms and transmits them to a central server when it detects an earthquake (15, 16). The Quake-Catcher Network (QCN) uses the accelerometers in laptop computers to collect data in a similar way (11, 12). The accelerometers in both the iShake phones and the QCN laptops are orders of magnitude less sensitive than the instruments in traditional networks, and earthquake signals must be separated from everyday movements. However, for events of M5 and greater, the signals are strong enough to be clearly recorded, provided that the laptop or phone is within tens of kilometers of the epicenter and is stationary at the time of the quake.

USB accelerometers that plug into desktop computers and cost tens of dollars are an improvement on embedded instruments.

The sensor can be glued to a basement or the wall of a building, providing better coupling to ground or building motion and allowing detection of M3 earthquakes. Both the Community Seismic Network (CSN) and the QCN deploy such sensors in citizens’ homes in earthquake-prone regions (11–14). The USGS NetQuakes project uses a more robust system with a higher-quality sensor. An engineer bolts the ~\$6000 sensor package to the concrete basement of a home; the instrument is largely autonomous, needing only periodic connections to the citizen-host’s wireless Internet. Online tools allow the citizen-scientist to look at the recorded data and compare recordings across the region (17).

This new age of networks has the potential to increase the density of instruments by an order of magnitude or more. Data from a recent deployment of 5000 sensors in a 5 km by 7 km area in Long Beach, California, by NodalSeismic Inc. show that as the seismic energy from nearby earthquakes radiates across the array, it deviates from the simple waves-on-a-pond pattern, indicating the complexities of the subsurface structure (18). Dense data like this across swaths of earthquake-prone regions could substantially advance understanding of wave propagation effects and the earthquake source (see the figure). In addition, sensors can be placed in different types of locations, such as multiple stories of different types of buildings.

Finally, this approach provides one of the best opportunities to engage citizens to learn about earthquakes.

However, the challenges are substantial. First, how good are the data? Some sensors may record true ground or building motion, whereas others record the oscillations of a wobbly tabletop. Second, how robust will the networks be? How many will lose power or data in a large earthquake? And will they still be running by the time a large earthquake occurs? Long-term operation requires continued interest of the citizen-hosts to ensure that both hardware and software remain operational. Finally, privacy concerns may limit data use if individuals are not prepared to release precise sensor locations.

Despite these challenges, citizen-based projects have the potential to transform earthquake science if two conditions are met. First, amateur scientists must be able to explore the data and draw conclusions. Online educational tools such as those at DYFI allow individuals to see how their data are used and how they contribute to scientific discovery. This is crucial for maintaining continued participation. Second, the citizen-generated data must conform to high data management standards with accurate location and instrument type information. It must also be archived alongside traditional data in order to be useful to professional scientists and thereby drive fundamental discovery.

References and Notes

1. E. M. Noam, H. Sato, *Science* **274**, 739 (1996).
2. See www.youtube.com/watch?v=XJ1EQbmj_LQ.
3. P. S. Earle, D. C. Bowden, M. Guy, *Ann. Geophys.* **54**, 10.4401/ag-5364 (2011).
4. P. S. Earle, *Nat. Geosci.* **3**, 221 (2010).
5. To follow the USGS tweet-derived earthquake information, subscribe to @USGSed on twitter.com.
6. R. Bossu et al., *Ann. Geophys.* **54**, 10.4401/ag-5265 (2011).
7. R. Bossu et al., in *Comparative Emergency Management: Examining Global and Regional Responses to Disasters*, D. M. Miller, J. Rivera, Eds. (Auerbach/Taylor and Francis, New York, 2011), pp. 235–257.
8. D. J. Wald et al., *Ann. Geophys.* **54**, 10.4401/ag-5354 (2011).
9. G. M. Atkinson, D. J. Wald, *Seismol. Res. Lett.* **78**, 362 (2007).
10. See <http://earthquake.usgs.gov/dyfi>.
11. A. I. Chung et al., *Seismol. Res. Lett.* **82**, 526 (2011).
12. See <http://qcn.stanford.edu>.
13. R. W. Clayton et al., *Ann. Geophys.* **54**, 10.4401/ag-5269 (2011).
14. See <http://map.communityseismicnetwork.org>.
15. S. Dashti et al., “iShake: Using Personal Devices to Deliver Rapid Semi-Quantitative Earthquake Shaking Information,” USGS Final Technical Report, G10AP00006 (2011).
16. See <http://ishake.berkeley.appspot.com/>.
17. See <http://earthquake.usgs.gov/monitoring/netquakes>.
18. See www.gps.caltech.edu/~clay/EQmovies/EQmovies.html.

Supporting Online Material

www.sciencemag.org/cgi/content/full/335/6066/297/DC1
Movie S1

10.1126/science.1214650

GENETICS

Sowing the Seeds of Centromeres

Lars E. T. Jansen

The centromere is a chromatin-based platform that accumulates microtubule-binding proteins that drive chromosome segregation during cell division. Despite their size (on the order of megabases of DNA in mammals) and conserved role, centromeres have the remarkable capacity to leave their usual comfort zone and to reform at a new chromosomal site (1). Although found rarely, these so-called neocentromeres are by most measures bona fide and segregate chromosomes with high fidelity. What accounts for this nomadic behavior?

A clue came from the identification of a variant of the histone protein H3 called centromere protein A (CENP-A), which is incorporated into nucleosomes specifically at the centromere region (2, 3). Histones (the protein constituent of nucleosomes) bind DNA in a non-sequence specific manner, yet can heritably differentiate genomic regions. This is achieved either by the local decoration of canonical histones with chemical modifications or by replacement with variant histones. As such, histones are ideal candidates to epigenetically maintain chromatin identity. This notion led to the proposal that instead of a unique DNA sequence signature, it is the presence of CENP-A nucleosomes that identifies the position of the centromere (4). Consistent with this, CENP-A nucleosomes are not turned over except by dilution on newly replicated centromeres during cell division (5) and appear to evade epigenetic reprogramming in the germ line (6).

A strong predictor of the behavior of an epigenetic system is the ability to nucleate a structure or “mark” that in turn

is propagated independently of the initial trigger, much like a seed that triggers subsequent autonomous growth of a crystal. Until very recently, such direct evidence for the epigenetic nature of the centromere was lacking. Although we’ve known that centromeres can move, they have yet to be caught in the act. Two recent studies provide plausible solutions for how neocentromeres form, going beyond phenomenology by experimentally inducing the formation of a new centromere (7, 8).

Both studies, one in cultured fruit fly cells (*Drosophila melanogaster* S2 cells) (7) and one in human tissue culture cells

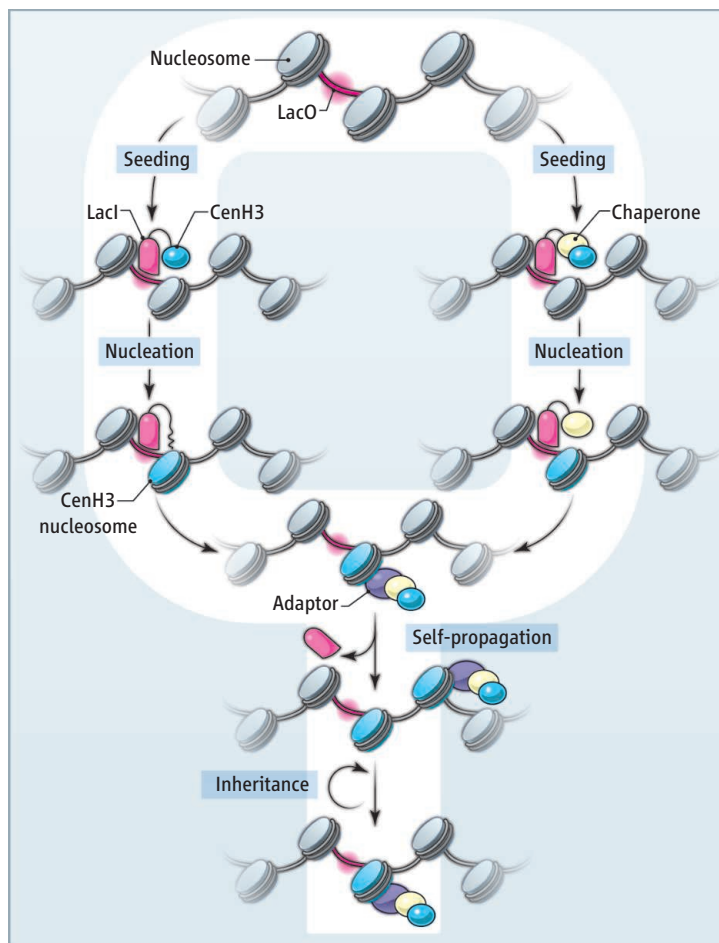
How can a centromere relocate to a new chromosomal position?

(8), employed arrays of bacterial Lac operator (LacO) DNA sequences integrated into a defined chromosomal site to form a recruitment platform for the ectopically expressed Lac repressor protein (LacI). The *Drosophila* study by Mendiburo *et al.* (7) simply fused *Drosophila* centromeric histone H3 (CenH3, the fly homolog of CENP-A; also called CID) directly to LacI and tethered the fusion protein to a LacO DNA site, far removed from endogenous centromeres (see the figure). Although highly artificial, these hybrid CenH3 molecules, literally dragged in by their tails, assembled locally into

nucleosomes. Critically, they in turn recruited endogenous CenH3 that was not pulled in by LacI but rather as a consequence of the initial pool of CenH3-LacI fusion protein; recruitment expanded laterally beyond the LacO DNA sites to which the initial pool bound. Analogous to the template-directed duplication of genetic information in DNA, a protein structure (CenH3 nucleosome) is “replicated” based on the initial template, a cycle that is a central feature of epigenetic mechanisms.

Barnhart *et al.* (8) took a slightly different approach—it was not CENP-A that was forced onto the LacO domain but rather Holliday junction-recognizing protein (HJURP), a chaperone for CENP-A. The authors show that HJURP acts as an assembly factor for CENP-A nucleosomes in vitro. Indeed, creating a local concentration of HJURP at the LacO array was sufficient to nucleate CENP-A chromatin. Thus, HJURP is the seed that sows the epigenetic centromere; it is not a part of the stable centromere structure but its transient presence kick-starts the process.

An earlier report (9) used the same powerful LacO technique to tether both CENP-C



Seeding and propagation. CenH3 is targeted to a naïve chromatin locus either by direct fusion to locally bound LacI (7) or through recruitment by the LacI-tethered chaperone HJURP (8). This results in the nucleation of CenH3 nucleosomes, which in turn triggers the propagation of CenH3 chromatin in a self-templating manner (likely through an adaptor intermediate) without the need for the initial LacI seed. CenH3 chromatin propagation and turnover through cell divisions reach an equilibrium, which results in stable inheritance of the epigenetic centromere mark.

and CENP-T, two centromere components acting downstream of CENP-A, onto an ectopic chromosomal site. Remarkably, this was sufficient to trigger the recruitment of other centromere constituents (but not CENP-A), as well as the kinetochore, the microtubule-binding complex that drives chromosome segregation during cell division. Indeed, at least transiently, this naïve locus became a site that powered chromosome movement, which suggests that a key role of CENP-A-containing nucleosomes is to recruit CENP-C and CENP-T to the centromere. These findings were further extended by the demonstration that a defined array of CENP-A nucleosomes is sufficient to nucleate a functional kinetochore in extracts from *Xenopus laevis* oocytes (10).

Previous attempts to generate neocentromeres in cells by simple CenH3/CENP-A overexpression were successful in *Drosophila* (11) but failed in human cells (9, 12). However, as observed in the earlier CENP-C/T tethering experiments, artificial nucleation of CENP-A or its chaperone HJURP results in efficient recruitment of kinetochore components that capture spindle microtubules and mediate chromosome movement (7, 8). In these experiments, a new centromere was created in addition to the original one, and this led to mitotic failure and cell death. Although this highlights

the detrimental consequences of such dicentric chromosomes, it precludes determining whether these “new-born” centromeres are heritable. Mendiburo *et al.* addressed this by analyzing ectopic, plasmid-based artificial chromosomes that are not essential for cell viability. These can replicate but have no means for active segregation, which leads to their rapid loss from a dividing population of cells. As on chromosomal sites, tethering of CenH3 to LacO-containing plasmids led to the recruitment of kinetochore proteins and microtubule binding. Seeding of such centromeres required LacI-bound CenH3 to be present only transiently. This pool was subsequently replaced by endogenous self-replicating pools of CenH3 nucleosomes, which allowed the ectopic plasmid-based centromeres to be maintained for over a month in cultured cells. Thus, centromeric chromatin is not only required for centromere function, but its creation is sufficient to nucleate a centromere and render it heritable.

Although seeding of CenH3/CENP-A allows small episomal plasmids to be propagated for some time, it is unclear whether it can support heritable centromeres on chromosomal sites and how natural neocentromeres form. Forced expression of CENP-A can trigger neocentromere function primarily adjacent to preexisting heterochromatin (regions of the genome where gene expres-

sion is generally suppressed) (11, 13, 14). Although naturally occurring human neocentromeres appear to lack heterochromatin (15), this suggests that a particular local chromatin environment permissive for CENP-A assembly is required for neocentromere formation. The experimental seeding and subsequent inheritance of the centromere implies that CENP-A is central to a self-templating positive-feedback loop. What remains is to demonstrate the components that are part of such a loop and how it works.

References

1. P. E. Warburton, *Chromosome Res.* **12**, 617 (2004).
2. W. C. Earnshaw, B. R. Migeon, *Chromosoma* **92**, 290 (1985).
3. K. F. Sullivan, M. Hechenberger, K. Masri, *J. Cell Biol.* **127**, 581 (1994).
4. P. E. Warburton *et al.*, *Curr. Biol.* **7**, 901 (1997).
5. L. E. T. Jansen, B. E. Black, D. R. Foltz, D. W. Cleveland, *J. Cell Biol.* **176**, 795 (2007).
6. D. K. Palmer, K. O'Day, R. L. Margolis, *Chromosoma* **100**, 32 (1990).
7. M. J. Mendiburo, J. Padeken, S. Fülöp, A. Schepers, P. Heun, *Science* **334**, 686 (2011).
8. M. C. Barnhart *et al.*, *J. Cell Biol.* **194**, 229 (2011).
9. K. E. Gascoigne *et al.*, *Cell* **145**, 410 (2011).
10. A. Guse, C. W. Carroll, B. Moree, C. J. Fuller, A. F. Straight, *Nature* **477**, 354 (2011).
11. A. M. Olszak *et al.*, *Nat. Cell Biol.* **13**, 799 (2011).
12. A. A. Van Hooser *et al.*, *J. Cell Sci.* **114**, 3529 (2001).
13. H. D. Folco, A. L. Pidoux, T. Urano, R. C. Allshire, *Science* **319**, 94 (2008).
14. K. Ishii *et al.*, *Science* **321**, 1088 (2008).
15. A. Alonso, D. Hasson, F. Cheung, P. E. Warburton, *Epigenetics Chromatin* **3**, 6 (2010).

10.1126/science.1218162

BIOCHEMISTRY

Enzymes in Coherent Motion

H. Peter Lu

Subtle conformational changes often play a crucial role in enzyme functions, and enzyme conformations are highly dynamic. The use of only a static structural characterization from an ensemble-averaged measurement at equilibrium is therefore often inadequate for predicting dynamic conformations and understanding correlated enzyme functions. Single-molecule approaches (1), which investigate individual molecules under specific physiological conditions, are a powerful tool for characterizing and analyzing complex enzymatic reaction dynamics and correlated conformational dynamics. On page 319 of this

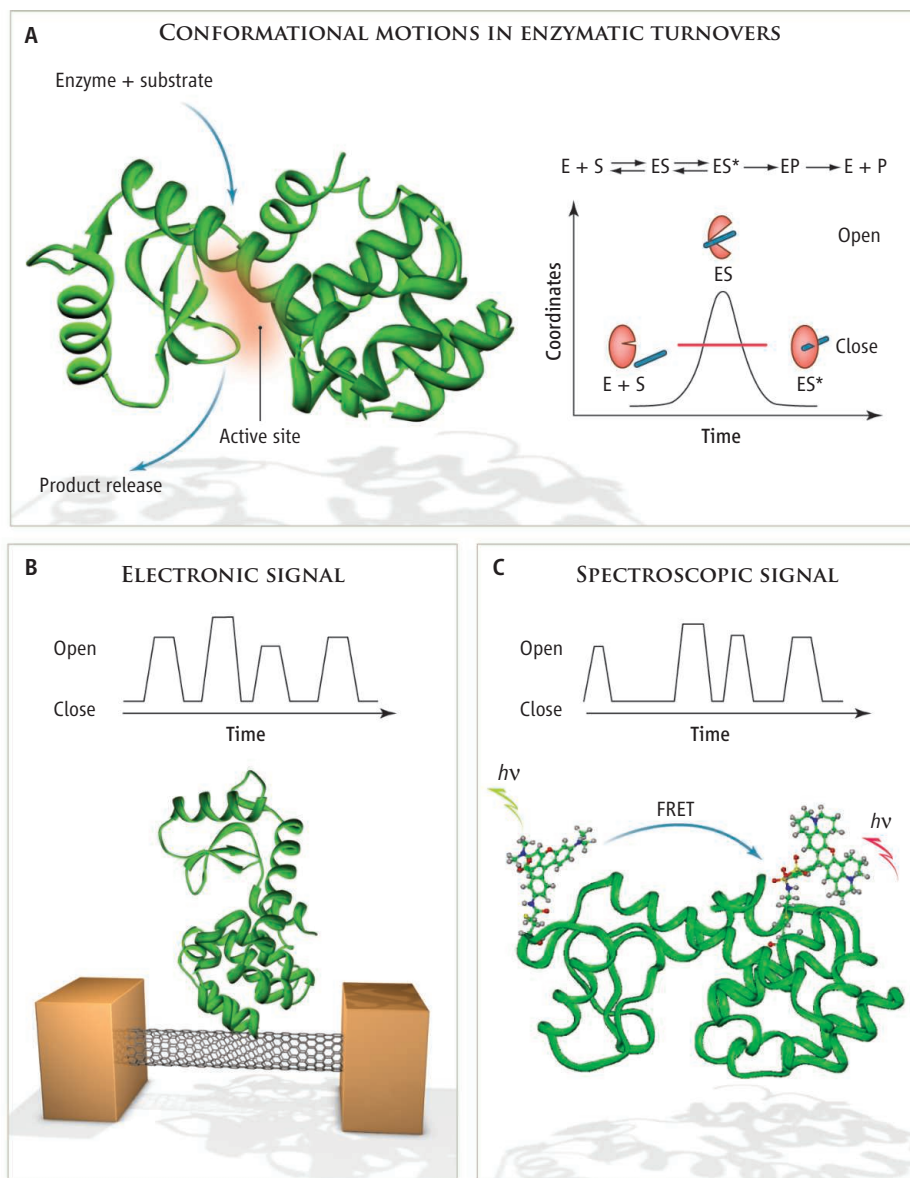
issue, Choi *et al.* (2) report a novel approach to probing single-molecule conformational dynamics that reveals the conformational motions of the enzyme's active site during enzymatic reaction turnovers.

The authors studied T4 lysozyme, an enzyme that catalyzes the hydrolysis of the glycosidic bonds in the polysaccharide found in bacterial cell walls (3). During the enzymatic reaction, an active substrate-enzyme complex forms, followed by chemical transformation and product release (see the figure, panel A). Choi *et al.* attached the T4 lysozyme molecule to a single-walled carbon nanotube (SWNT) device (see the figure, panel B). In their single-molecule enzymatic reaction assay, enzyme molecular motions create changes in electrostatic potentials that can be converted and ampli-

fied into dynamically changing electron fluxes. Using this approach, the authors were able to record hinge-bending motions of the T4 lysozyme active site under enzymatic reactions with high time resolution and signal clarity.

The authors detected two different electronic signals caused by the lysozyme hinge-bending motions: Slow signal oscillations result from the transduction of catalytic turnover events at ~15 Hz, and fast signal oscillations correspond to nonproductive binding events at ~330 Hz. These results are in good agreement with earlier results from single-molecule fluorescence resonance energy transfer (smFRET) spectroscopy under enzymatic reactions (see the figure, panel C) (4–6). This is encouraging, as the conclusions are reached from very different

Department of Chemistry and Center for Photochemical Sciences, Bowling Green State University, Bowling Green, OH 43403, USA. E-mail: hplu@bgsu.edu



Single-molecule enzyme studies. Active-site conformational motions are essential for the catalytic function of T4 lysozyme (A). Through open-close motions, the enzyme adjusts its physical and chemical flexibility toward an active state (ES^*), which consists of the binding complex of an enzyme (E) and a substrate (S) for a specific catalytic reaction. Choi *et al.* now report SWNT electronic measurements of single-molecule T4 lysozyme conformational dynamics (B), which allow longer trajectories to be recorded than with FRET spectroscopic studies (C).

technical approaches that probe electronic and photon signals, respectively.

More intriguingly, both this work (2) and previous single-molecule spectroscopic analyses (5, 6) suggest that the hinge-bending motions in T4 lysozyme show intermittent coherent conformational dynamics. The reported enzyme dynamics imply that active-site conformational motion times tend to bunch in a narrow time window (5–7). The dynamics reported for enzymes (2, 5–10) are likely common in the conformational dynamics of other proteins, especially those that perform conformation-

gated functions. Substrate-enzyme binding and substrate-enzyme complex formation serve as a driving force and negative-entropy source for the coherent dynamics at the single-molecule level. Accordingly, the conformational motions are driven by the local environment, such as electrostatic field, and hydrophobicity at the active site of the enzyme (2, 4–7).

The results reported by Choi *et al.* show that SWNT electronic detection is complementary to smFRET measurements. For example, with their SWNT-based approach, Choi *et al.* were able to overcome signal

bleaching (11), a typical barrier for single-molecule spectroscopic measurements. This enabled them to record trajectories of hundreds of hinge-bending open-close motion events under enzymatic reaction conditions. The same approach could be used to explore the dynamics of other molecules with charged functionalities.

In the future, it will be critical to probe the conformational change dynamics at a time scale of nanoseconds or even picoseconds, because many important protein conformational motions occur at the nanosecond time scale. (The reported results are in the time scale of minutes to microseconds.) Furthermore, a suite of single-molecule experiments will be needed to probe different aspects of the complex reaction dynamics and associated conformational dynamics of enzymes. In recent years, such a combined approach has yielded detailed mechanistic information about enzymatic conformational dynamics, including structures of the intermediate enzyme-substrate complex and the associated energy landscape.

A particularly promising technique uses correlated mechanical force to perturb enzyme conformational dynamics and reactivity, thereby allowing enzyme activities to be manipulated in order to explore new enzyme properties and obtain fundamental understanding of enzymatic dynamics (12–15). The next generation of single-molecule approaches will be capable not only of probing complex single-molecule protein dynamics but also of manipulating protein conformational dynamics and controlling protein activities.

References and Notes

1. *Single Molecule Spectroscopy in Chemistry, Physics and Biology: Nobel Symposium*, A. Gräslund, R. Rigler, J. Widengren, Eds. (Springer, New York, 2009).
2. Y. Choi *et al.*, *Science* **335**, 319 (2012).
3. R. Kuroki, L. H. Weaver, B. W. Matthews, *Science* **262**, 2030 (1993).
4. H. P. Lu, *Acc. Chem. Res.* **38**, 557 (2005).
5. Y. Chen, D. Hu, E. R. Vorpagel, H. P. Lu, *J. Phys. Chem. B* **107**, 7947 (2003).
6. Y. Wang, H. P. Lu, *J. Phys. Chem. B* **114**, 6669 (2010).
7. Y. He *et al.*, *J. Am. Chem. Soc.* **133**, 14389 (2011).
8. H. P. Lu, L. Y. Xun, X. S. Xie, *Science* **282**, 1877 (1998).
9. H. P. Lerch, R. Rigler, A. S. Mikhailov, *Proc. Natl. Acad. Sci. U.S.A.* **102**, 10807 (2005).
10. W. Min *et al.*, *Acc. Chem. Res.* **38**, 923 (2005).
11. In optical signal bleaching, laser excitation with dye probe molecules causes irreversible changes in the chemical structure of the dye molecule, resulting in non-fluorescence molecule products.
12. O. Miyashita, J. N. Onuchic, P. G. Wolynes, *Proc. Natl. Acad. Sci. U.S.A.* **100**, 12570 (2003).
13. M. A. Lomholt, M. Urbakh, R. Metzler, J. Klafter, *Phys. Rev. Lett.* **98**, 168302 (2007).
14. H. Gumpf *et al.*, *Nano Lett.* **9**, 3290 (2009).
15. A. P. Wiita *et al.*, *Nature* **450**, 124 (2007).

10.1126/science.1217170

RETROSPECTIVE

Lynn Margulis (1938–2011)

Moselio Schaechter

Science progresses mainly through experimentation, but to become useful, experimental results have to be scrutinized, interpreted, and placed on a proper intellectual scaffold. These two activities are not always carried out evenly by the same person. Some scientists become known for their impressive experiments, others for innovative theoretical syntheses. Lynn Margulis, who died on 22 November 2011 at the age of 73, was a striking example of the latter group. She is responsible for the transformative idea that eukaryotic cells evolved by the acquisition and exploitation of other, smaller cells, a process known as endosymbiosis. Accordingly, essential components of eukaryotic cells—the organelles mitochondria and, in photosynthetic cells, plastids—are derived from bacteria that some ancestral cell had ingested. These events are thought to have taken place early in the history of life on Earth.

Lynn Margulis grew up in Chicago, Illinois, and graduated from the University of Chicago before going on to earn a master's degree in genetics and zoology from the University of Wisconsin, Madison, and a Ph.D. in genetics from the University of California in 1965. She then moved to Boston University, where she was a neighbor and friend of mine, and after 22 years there, went to the University of Massachusetts, Amherst. In 1967, when she was 29 years old, Margulis presented the thesis of endosymbiosis in a 50-page article published in the *Journal of Theoretical Biology*. In part, she based her arguments on relatively neglected publications, giving credit to authors who had proposed the same notion, but her hypothesis was not taken seriously at first. Margulis recounted that the paper had been rejected by 15 journals. It took some 10 years after her publication for the hypothesis to become one of the central tenets of modern biology. She was recognized for her contributions by being elected to the U.S. National Academy of Sciences (1983) and receiving the U.S. National Medal of Science (1999).

Margulis correctly predicted that, "If an organelle originated as a free-living cell, it is possible that naturally occurring counterparts still can be found among extant organ-



isms." It is now widely accepted that relatives of bacterial ancestors of mitochondria and plastids exist to this day. In support of this idea, both mitochondria and plastids have critical biochemical commonalities with bacteria. The clincher lies in the genomic similarity of the genes that they share. These organelles have a reduced genome, sometimes consisting of only a few dozen genes, yet these demonstrate a common heritage. In the case of mitochondria, the homology is with extant bacteria called rickettsiae (interestingly, themselves obligatory intracellular parasites) and with photosynthetic cyanobacteria for the plastids.

The importance of this notion extends beyond explaining steps early in evolution because it also explains what came later. It empowers the momentous idea that evolution does not proceed by single mutational steps only, but, notably, also occurs by the acquisition of packets of genes simultaneously. The allure here is that it allows one to grasp how complex structures may have arisen not one mutational step at a time, but by acquiring and combining multiple arrays of genes that themselves had evolved for different functions. An example is the prokaryotic flagellum, an elaborate structure of locomotion, which is thought by experts to have arisen by such a process.

In Margulis's weltanschauung, symbiosis was the driving force of evolution. However, symbiosis is not the only way to acquire new genes en masse. Another powerful discovery has been that bacteria acquire such packets through the incorporation of viruses

A biologist's innovative theoretical syntheses provided the intellectual scaffolding for endosymbiotic theory, a cornerstone of mainstream evolutionary biology.

or plasmids—a view that Margulis regarded with some reticence. I never asked her about this, but she could have claimed that, by extension, these entities could also qualify as symbionts. She proposed that evolution by symbiosis or "syntrophogenesis" could explain many specific phenomena. She championed the idea that eukaryotes gained their flagella (which differ from the prokaryotic flagella) by the acquisition of a motile bacterium, a spirochete, a view that has few subscribers today. She also proposed that AIDS is caused by a long-living (hence symbiont-like) spirochete, an even less popular view. Those who actually read her seminal 1967 paper should have seen such idiosyncratic ideas coming, as it is written with the fierce intensity that became her signature.

Her positive contributions extend well beyond proposing scientific theories. Margulis wrote a number of books, some with her son Dorion Sagan, which had a profound effect on readers. Many young people have recalled their pleasure in reading them and have noted that it influenced their decision to pursue a career in science. Moreover, her familiarity with the inner lives of members of certain biological groups was stunning. Much was acquired the old-fashioned way, by going on field trips and collecting material for the lab. She was a master of the protists and through her knowledge and insight made others aware of the importance of this highly diverse group of organisms from which plants, fungi, and animals evolved. Her depth of knowledge in this area included a critical understanding of the pioneering work done in the early 20th century and before. Margulis did science by erudition. Such knowledge is evident in the 1967 paper: It was not just a manifesto on the endosymbiotic theory; it was also a treatise on comparative biochemistry, cytology, and systematics.

On occasion, the notions she espoused caused dismay among her colleagues and friends. But, to those who knew her, this is not her relevant legacy. She should be remembered as a person whose passionate beliefs and creative ideas changed the scientific discourse in several areas. In so doing, she touched many people, scientists and non-scientists alike.

Biology Department, San Diego State University, San Diego, CA 92182, USA. E-mail: mschaech@sunstroke.sdsu.edu

10.1126/science.1218027

Demonstration of Blind Quantum Computing

Stefanie Barz,^{1,2*} Elham Kashefi,³ Anne Broadbent,^{4,5} Joseph F. Fitzsimons,^{6,7} Anton Zeilinger,^{1,2} Philip Walther^{1,2}

Quantum computers, besides offering substantial computational speedups, are also expected to preserve the privacy of a computation. We present an experimental demonstration of blind quantum computing in which the input, computation, and output all remain unknown to the computer. We exploit the conceptual framework of measurement-based quantum computation that enables a client to delegate a computation to a quantum server. Various blind delegated computations, including one- and two-qubit gates and the Deutsch and Grover quantum algorithms, are demonstrated. The client only needs to be able to prepare and transmit individual photonic qubits. Our demonstration is crucial for unconditionally secure quantum cloud computing and might become a key ingredient for real-life applications, especially when considering the challenges of making powerful quantum computers widely available.

Among many quantum-enhanced applications, quantum computing has generated much interest because of the discovery of applications (1–4) that outperform their best-known classical counterparts. Although vast technological developments already allow for small-scale quantum computers with ionic (5–8), photonic (9–16), superconducting (17–21), and solid-state (22–24) systems, the hurdles encountered in realizing quantum devices are enormous. This intrinsic technical complexity may result in, initially, only a few powerful quantum computers, or quantum servers, operating at specialized facilities. A key challenge in using such central quantum computers is enabling a quantum computation on a remote server while keeping the client's data hidden from the server (25–30).

The classical analog of this issue was addressed in 1978 (31) and became one of the most active fields in cryptography. A full solution was over 30 years in the making and enables (32) the evaluation of data-processing circuits over encrypted data without the need for any decryption, but provides only computational security. In analogy to many widely used cryptographic protocols, this means that the security relies on the assumption of a limit to the adversary's compu-

tational power, as well as on the difficulty of the underlying mathematical problem.

Recent theoretical work (29) overcomes this limitation and shows that quantum computers can provide unconditional security in data processing, a hitherto unrecognized potential of quantum computers that is not known to be achievable classically. This new fundamental advantage of quantum computers is manifested in the blind quantum computing (BQC) protocol that combines notions of quantum cryptography and quantum computation to achieve the delegation of a quantum computation from a client with no quantum computational power to an untrusted quantum server, such that the client's data remains perfectly private.

BQC uses the concept of one-way quantum computing (33–37), a measurement-based model of computation (38, 39) that represents a paradigm shift in the understanding of complex data processing by clearly separating the classical and quantum parts of a computation. In the most general case, a one-way quantum computer has its basis in highly entangled multiparticle states, so-called cluster states, which are a resource for universal quantum computing. On these cluster states, adaptive single-qubit measurements alone are sufficient to implement deterministic universal quantum computation. Different algorithms require only a different pattern of single-qubit measurements on a sufficiently large cluster state.

Therefore, a quantum computation is hidden as long as these measurements are successfully hidden. In order to achieve this, the BQC protocol exploits special resources called blind cluster states that must be chosen carefully to be a generic structure that reveals nothing about the underlying computation (Fig. 1). These blind cluster states are multiparticle entangled states created by preparing qubits in $|\theta_j\rangle = 1/\sqrt{2}(|0\rangle + e^{i\theta_j}|1\rangle)$, where $|0\rangle$ and $|1\rangle$ are the computational basis of the physical qubits and θ_j is chosen uniformly at random from $\{0, \pi/4, \dots, 7\pi/4\}$, and then interacting each qubit via controlled-phase (CPhase) gates with its nearest neighbors (here, CPhase $|i\rangle|j\rangle \mapsto (-1)^{\delta_{ij}}|i\rangle|j\rangle$ with $i, j \in \{0, 1\}$). Similar to the one-way quantum computer, a blind computation is described by a pattern of consecutive adaptive single-qubit measurements. Measuring the first qubit, initially in state $|\theta_1\rangle$, of a one-dimensional linear blind cluster in the basis $|\pm_{\delta_1}\rangle = 1/\sqrt{2}(|0\rangle \pm e^{i\delta_1}|1\rangle)$ has the effect of applying a single-qubit rotation $R_z(-\delta_1 + \theta_1)$ on

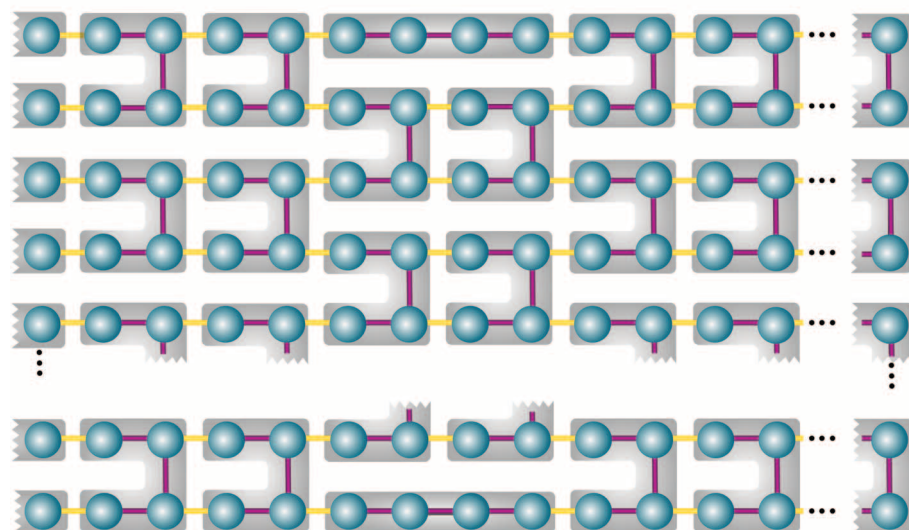


Fig. 1. The universal blind cluster state for BQC. This family of cluster states can be built by joining (yellow edges), for example, using optical fusion operations, smaller cluster states (purple edges, gray background) that are in one of the configurations of $|\Phi^{\delta}\rangle$ as implemented in the laboratory. The resulting state allows universal blind quantum computation when combined with measurements in the basis $|\pm_{\delta}\rangle$, $\delta \in \{0, \pi/4, \dots, 7\pi/4\}$.

¹Vienna Center for Quantum Science and Technology, Faculty of Physics, University of Vienna, Boltzmanngasse 5, A-1090 Vienna, Austria. ²Institute for Quantum Optics and Quantum Information, Austrian Academy of Sciences, Boltzmanngasse 3, A-1090 Vienna, Austria. ³School of Informatics, University of Edinburgh, 10 Crichton Street, Edinburgh EH8 9AB, UK. ⁴Institute for Quantum Computing, University of Waterloo, 200 University Avenue West, Waterloo, Ontario N2L 3G1, Canada. ⁵Department of Combinatorics and Optimization, University of Waterloo, 200 University Avenue West, Waterloo, Ontario N2L 3G1, Canada. ⁶Centre for Quantum Technologies, National University of Singapore, Block S15, 3 Science Drive 2, 117543 Singapore. ⁷School of Physics, University College Dublin, Belfield, Dublin 4, Ireland.

*To whom correspondence should be addressed. E-mail: stefanie.barz@univie.ac.at

the encoded input state $|+\rangle$, followed by a Hadamard, H . Here, $R_z(\phi) = \exp(-i\phi\sigma_z/2)$, $H = (\sigma_x + \sigma_z)/\sqrt{2}$, and σ_x , σ_y , and σ_z denote the usual Pauli matrices. As long as the angle θ_1 of the rotated qubit is unknown, the real rotation remains secret.

This feature of blind cluster states is used to perform a delegated computation on a server such that all data and the whole computation remain hidden. The only quantum power that is required from the client is the preparation of each qubit j in a state $|\theta_j\rangle$ and the transmission of the qubits to the server; in particular, there is no need for any quantum memory (40) or ability to perform quantum gates. From this point on in the protocol, the client communicates only measurement instructions and can be considered completely classical. The quantum server, which can perform universal quantum computation, performs a CPhase gate between qubits received from the client. Then in each round of interaction, the server performs adaptive single-qubit measurements in the $|\pm_{\delta_j}\rangle$ basis, as instructed by the client. The measurement basis is chosen such that $\delta_j = \phi_j + \theta_j + \pi r_j$, where ϕ_j is the desired target rotation and r_j is a randomly chosen value in $\{0, 1\}$ that hides the value of the measurement outcome. These classical measurement angles are set in such a way to compensate for the initial random rotation θ_j and any other Pauli by-products (12, 41) produced by previous measurements.

We present an optimized version of the original protocol that uses photonic qubits. Photons are ideally suited for BQC because they provide the natural choice as quantum information carrier for the client and enable quantum computing for the server. This is a unique feature of photonic systems and so far not realizable in other quantum systems. We experimentally demonstrate the concept of BQC via a series of blind computations on four-qubit blind cluster states. These photonic states can be combined via optical gates to create a universal resource state for BQC (Fig. 1) (29).

Our protocol uses, compared with the original BQC proposal (29), the experimental resources in an optimized way, independent of the physical system and without affecting blindness.

Optimized BQC. It is a conceptual strength of the BQC protocol that perfect security can be established over a subset of computations even if not all of the qubits are unknown to the server. For the four-qubit blind cluster state, it is sufficient for the client to be able to prepare only one or two of the qubits in arbitrary states $|\theta_j\rangle$ for delegating various one- and two-qubit circuits as well as quantum algorithms (Fig. 2). This is a remarkable optimization for the experimental requirements and is demonstrated here [see supporting online material (SOM) section S1 for theoretical details]. Furthermore, this optimization is scalable beyond our four-qubit experimental setting and creates an interesting challenge on the design level to construct a computation such that the sensitive measurements remain hidden.

We thus fix θ_1 and θ_4 equal to zero while varying the choices of θ_2 and θ_3 . The resulting four-qubit linear blind cluster state is

$$|\Phi^{\hat{\theta}}\rangle = \frac{1}{2} \left[|++\rangle_{1234} + e^{i\theta_3} |+-\rangle_{1234} + e^{i\theta_2} |-10\rangle_{1234} - e^{i(\theta_2 + \theta_3)} |-11\rangle_{1234} \right] \quad (1)$$

where $\hat{\theta} = (n_2, n_3)$ and $(\theta_2, \theta_3) = (\frac{n_2\pi}{4}, \frac{n_3\pi}{4})$. Our experimental implementation of BQC has its basis in such a family of four-qubit linear blind cluster states. These are produced by using photon emissions of a non-collinear type-II spontaneous parametric down-conversion process (SPDC) (10, 42) (SOM sections S3 and S4). If four photons are emitted into the output modes of the polarizing beam splitters 1, 2, 3, and 4 (Fig. 3A), they are in a highly entangled state that is equivalent to the state $|\Phi^{\hat{\theta}}\rangle$ under the local unitary operation $H \otimes \mathbf{I} \otimes \mathbf{I} \otimes H$:

$$|\Phi^{\hat{\theta}}\rangle = \frac{1}{2} \left[|0000\rangle_{1234} + e^{i\theta_3} |0011\rangle_{1234} + e^{i\theta_2} |1100\rangle_{1234} - e^{i(\theta_2 + \theta_3)} |1111\rangle_{1234} \right] \quad (2)$$

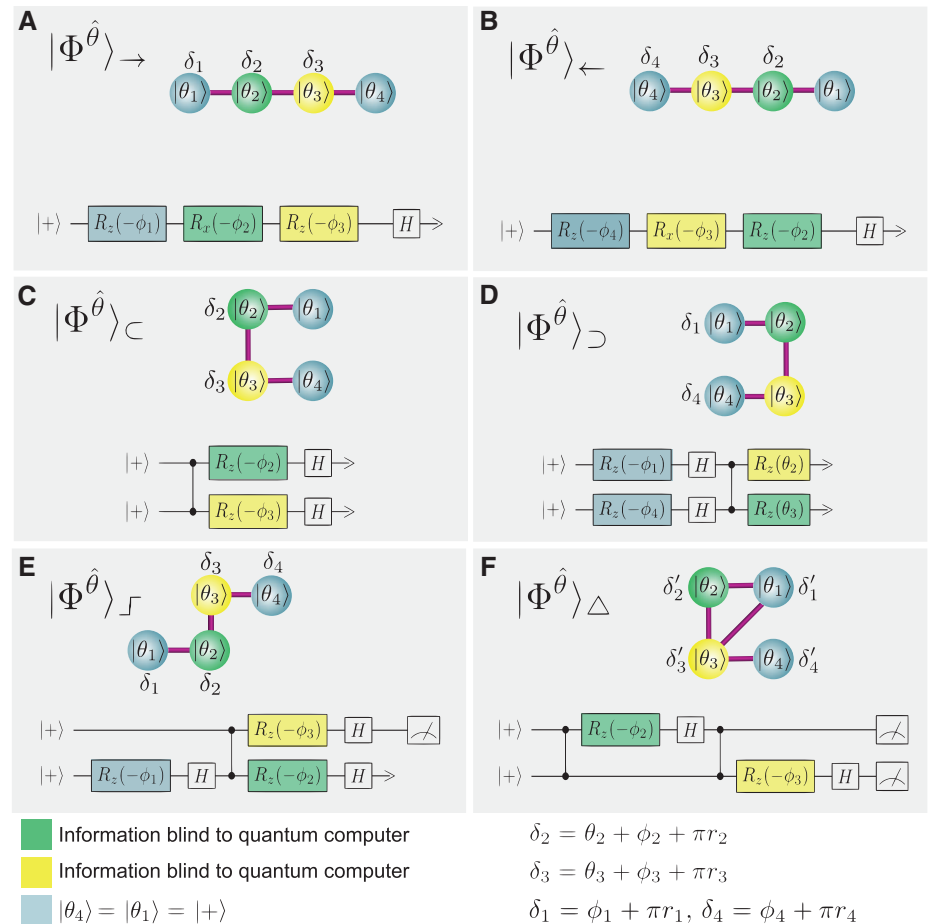


Fig. 2. Blind circuits and corresponding measurement patterns. (A to F) We implement various types of blind computations by using different configurations for $|\Phi^{\hat{\theta}}\rangle$. For all implementations, θ_2 and θ_3 are blind, as has been demonstrated in the experiment. The angles θ_1 and θ_4 are fixed to be zero. The measurement angle δ_j , as instructed by the client, depends on the initial rotation of the qubit θ_j (unknown to the server), the target rotation ϕ_j , and a randomly chosen value r_j in $\{0, 1\}$.

setup, this method allows the client's choice of configuration to also be hidden from the server.

We use an overcomplete state tomography for each of our cluster states in order to reconstruct the four-qubit density matrix (SOM section S5). The most likely physical density matrix for each four-qubit state is extracted by using a maximum-likelihood reconstruction (43) (Fig. 3B). Uncertainties in quantities extracted from these density matrices are calculated by using a Monte Carlo routine and assumed Poissonian errors. Our computed fidelities for the various blind cluster states achieve maximum values of up to $0.679 \pm 0.004\%$ via local unitary transformation. These nonideal fidelities arise because of experimental imperfections (SOM section S4). Experimental influences on the server's side only affect the correctness of the computation, whereas imperfections in the client's qubit preparation might also weaken the assumption of an unbiased state distribution.

Blind single- and two-qubit unitaries. The four-qubit linear blind cluster $|\Phi_L^{(2,3)}\rangle$ (Fig. 2) can be used to implement an arbitrary single-qubit unitary gate. Measuring qubit 1 in the eigenstates of σ_x , σ_y , or σ_z has the effect of preparing the input on qubit 2 in the state $|0\rangle$, $|+_i\rangle$, or $|+\rangle$, respectively, where $|+_i\rangle = 1/\sqrt{2}(|0\rangle + i|1\rangle)$. We are thus left with a three-qubit linear cluster

state that implements a single-qubit rotation gate with rotations determined by the measurements of the second and third qubits; this rotates the input qubit $|\Psi_{in}\rangle$ to the final state $|\Psi_{out}\rangle = R_x(-\phi_3)R_z(-\phi_2)|\Psi_{in}\rangle$, where $R_x(\alpha) = \exp(-i\alpha\sigma_x/2)$. By fixing θ_2 and varying θ_3 , we can demonstrate a blind X rotation. In the same way, a blind Z rotation can be achieved by using the four-qubit linear blind cluster state $|\Phi_L^{(2,3)}\rangle$, which has the order of measurements going from qubit 4 down to qubit 1. Figure 3C depicts a blind Z rotation. By varying θ_3 and averaging over all resulting density matrices, we obtain a totally mixed state with a linear entropy of 0.989 ± 0.010 that is close to the entropy of 1 for a perfectly mixed state (Fig. 3C). Because the experiments include the preparation of all eight blind cluster states $|\Phi_L^{(2,n)}\rangle$, we can quantify the blindness of the single-qubit rotations demonstrated experimentally. The value of the Holevo information χ (see SOM section S2 for details) must then be between 0 (for perfect blindness) and 3 (for no blindness). By using the tomographic measurements performed on these input states, we determine χ of such states to be 0.169 ± 0.074 , far below the three bits necessary to uniquely identify the client's choice of ϕ_2 and ϕ_3 , proving that within the assumptions of our model these experimental implementations of the protocol maintains close to

perfect blindness. The above value of χ assumes the initial state is chosen uniformly at random. However, even when this value is maximized over all possible prior distributions on the choice of states, it increases only slightly to 0.185 ± 0.087 .

Two-qubit gates are required for universal quantum computation; by choosing the order of measurements in a suitable way, the blind cluster $|\Phi_L^{(2,3)}\rangle$ implements blind two-qubit gates (Fig. 2, C to F). One family of two-qubit gates generated in our experiment has its basis in the blind horseshoe cluster $|\Phi_L^{(2,3)}\rangle$, where measuring qubits 2 and 3 of the blind cluster state performs a transformation on the logical input qubits (Fig. 2C). Both implemented rotations are blind, and the entire computation remains hidden. Analyzing the output state, that is, measuring qubits 1 and 4, delivers the result of the computation. Figure 3D shows an example of a two-qubit computation using the blind horseshoe cluster. Consistency with blindness can be seen by averaging over all output states, giving as a result a totally mixed state with a linear entropy of 0.955 ± 0.011 . It is an interesting challenge to demonstrate the consistency with blindness in full generality by producing 64 blind cluster states. Our demonstration uses a selection of four states, which suffices to hide the choice of rotations among four possibilities:

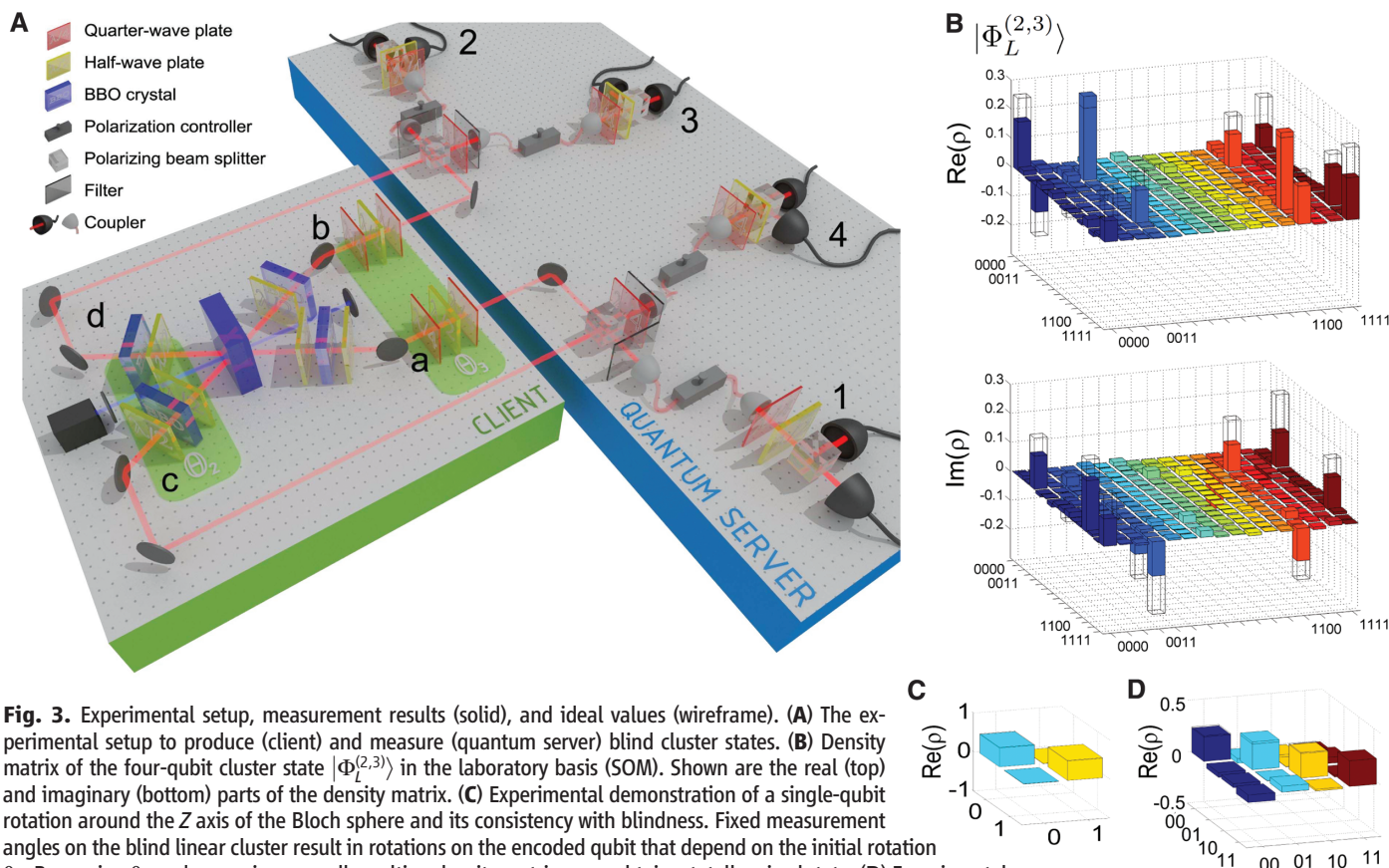


Fig. 3. Experimental setup, measurement results (solid), and ideal values (wireframe). **(A)** The experimental setup to produce (client) and measure (quantum server) blind cluster states. **(B)** Density matrix of the four-qubit cluster state $|\Phi_L^{(2,3)}\rangle$ in the laboratory basis (SOM). Shown are the real (top) and imaginary (bottom) parts of the density matrix. **(C)** Experimental demonstration of a single-qubit rotation around the Z axis of the Bloch sphere and its consistency with blindness. Fixed measurement angles on the blind linear cluster result in rotations on the encoded qubit that depend on the initial rotation θ_3 . By varying θ_3 and averaging over all resulting density matrices, we obtain a totally mixed state. **(D)** Experimental demonstration of a two-qubit gate and its consistency with blindness. Fixing measurements at a subset of all 64 possible states and averaging over all output density matrices results in a totally mixed state. The imaginary part of the density matrices (C and D) is below 0.05 and hence not shown. For details, see figs. S36 and S42.

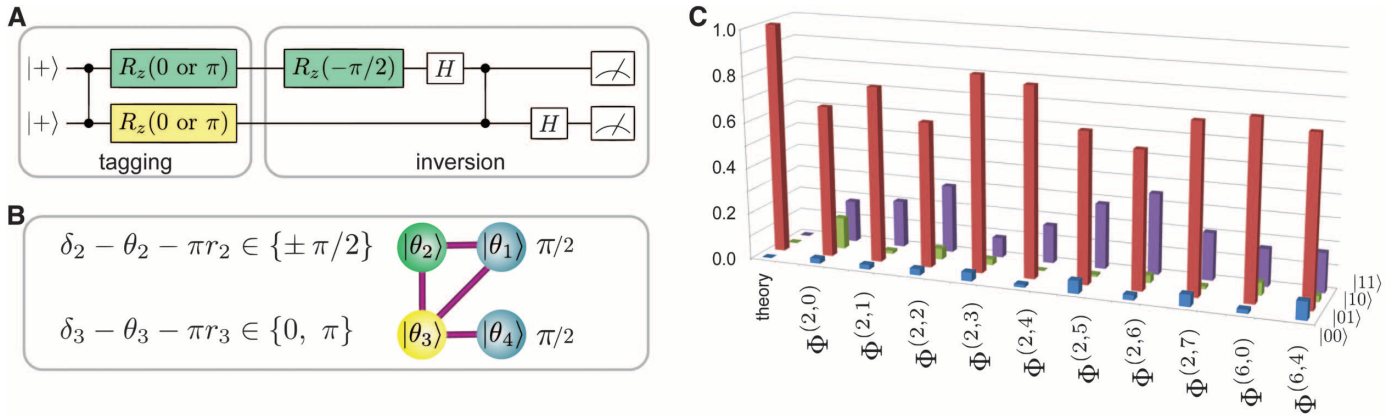


Fig. 4. Blind implementation of Grover's algorithm. **(A)** Quantum circuit. The input to the circuit is $|+\rangle|+\rangle$; the tagging of one of the four input states $|00\rangle$, $|01\rangle$, $|10\rangle$, or $|11\rangle$ applies a phase shift of π to that state. These four states are then mapped to an output that is measured in the basis $(|+_i\rangle, |-_i\rangle)$. **(B)** Corresponding implementation on a triangle cluster $|\Phi^\delta\rangle_\Delta$. Here, the measurement of qubits 2 and 3 corresponds to the tagging of one of the elements,

measuring the output qubits 1 and 4 identifies then which input was tagged. Without the knowledge of the initial rotation of the qubit, the quantum server is unable to distinguish the algorithm from a given family of circuits. **(C)** Measurement outcomes for tagging the $|01\rangle$ element for all states $|\Phi^{(n_2, n_3)}\rangle_\Delta$ are shown. The corresponding error bars are smaller than 0.056 for all results.

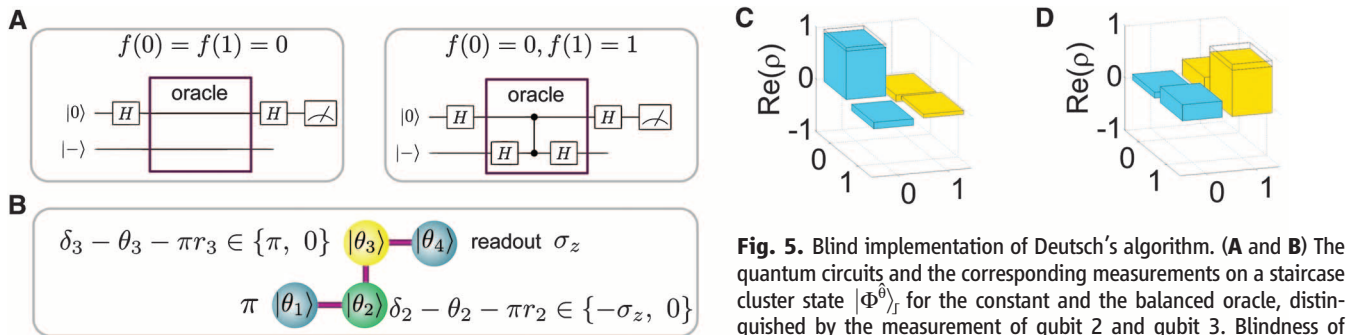


Fig. 5. Blind implementation of Deutsch's algorithm. **(A and B)** The quantum circuits and the corresponding measurements on a staircase cluster state $|\Phi^\delta\rangle_I$ for the constant and the balanced oracle, distinguished by the measurement of qubit 2 and qubit 3. Blindness of qubit 3 guarantees that the quantum server cannot distinguish between the execution of each of these scenarios (constant or balanced oracles) and corresponding families of quantum circuits. **(C and D)** Experimental (solid) and theoretical (wireframe) results for a constant (C) and a balanced (D) oracle for the example of the state $|\Phi^{(6,4)}\rangle_I$.

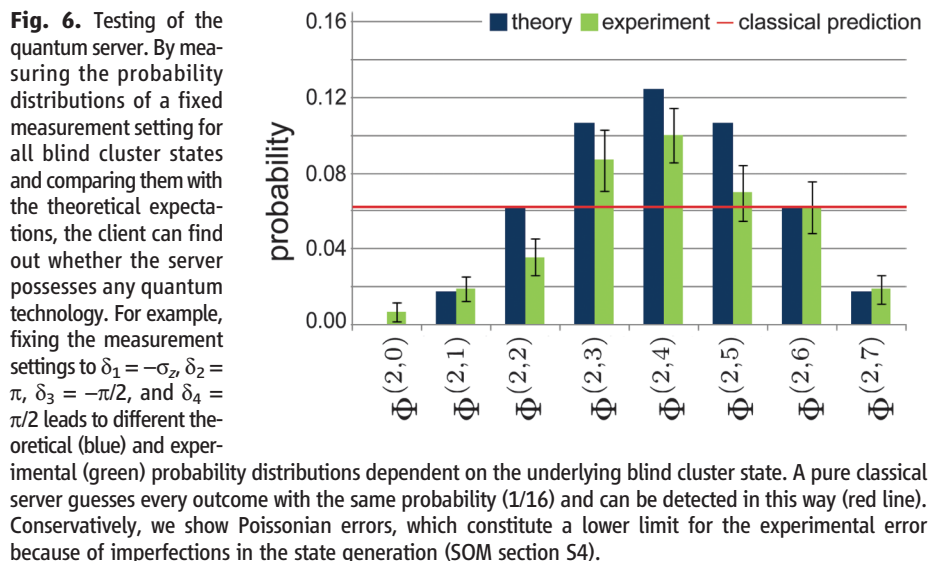
$R_z(\pi/2 \pm \pi) \otimes R_z(\pi/2 \pm \pi)$. In a similar way, the consistency with blindness of the rotated horseshoe cluster $|\Phi^\delta\rangle_\Delta$ (Fig. 2D) can be shown (SOM section S10). We also realize blind computations based on the blind staircase cluster $|\Phi^\delta\rangle_I$ (Fig. 2E) and blind triangle cluster $|\Phi^\delta\rangle_\Delta$ (Fig. 2F). The state $|\Phi^\delta\rangle_\Delta$ is obtained via local complementation (44) on qubit 2 of $|\Phi^\delta\rangle_\Delta$. Thus $U|\Phi^\delta\rangle_\Delta = |\Phi^\delta\rangle_\Delta$, where $U = \sqrt{\sigma_z} \otimes \sqrt{\sigma_x} \otimes \sqrt{\sigma_z} \otimes I$ (with U acting on qubits ordered as 1, 2, 3, and 4), and measuring the qubits of $|\Phi^\delta\rangle_\Delta$ by absorbing the action of U into the measurements yields a computation on $|\Phi^\delta\rangle_\Delta$ as represented by measurement instructions δ' (Fig. 2F). However, blindness on qubit i is guaranteed only if the resulting measurement can be expressed as a basis $|\pm_{\delta'_i}\rangle$. We will show that the blind staircase cluster allows for the blind implementation of Deutsch's algorithm, whereas the blind triangle cluster allows for the blind implementation of Grover's algorithm.

To demonstrate the quality of our gate operations, we performed various single-qubit gates and two-qubit gates with each of the blind cluster states; the resulting density matrices, obtained via quantum state tomography, are shown in SOM sections S6 and S7.

Blind algorithms. One of the most prominent examples where quantum mechanics demonstrates its superiority in computational speedup is Grover's search algorithm (3, 45), which provides a quadratic speedup to the following problem: Given a function $f: \{0,1\}^n \rightarrow \{0,1\}$, find an x such that $f(x) = 1$. We demonstrate a blind implementation of Grover's search for $n = 2$, where blindness ensures that the server is unable to distinguish the actual computation from within a given family of circuits implementing $[I \otimes R_z(\xi)H]$. Whereas previous realizations (10, 12) are not amenable to blind implementations, our computation, embedded into the blind triangle cluster $|\Phi^\delta\rangle_\Delta$ (Fig. 2F), remains blind. The algorithm proceeds as follows: The values of x are represented by the states $|00\rangle$, $|01\rangle$, $|10\rangle$, and $|11\rangle$, respectively. A superposition of all four states is initially created, and the oracle tags one element by applying a phase of π , thus flipping the sign of this term (Fig. 4A). Then each of the four states is mapped to an output such that measuring both qubits in the basis $|\pm_i\rangle$ reveals the tagged item. This computation can be embedded into the blind triangle cluster, $|\Phi^\delta\rangle_\Delta$ (Fig. 2F); the choice of ϕ_2 and ϕ_3 determines which element is tagged.

Figure 4C shows the results of a Grover search for the tagging of the state $|01\rangle$. For each blind cluster state, we show the probability of identifying the tagged state as well as the probabilities of finding the unwanted states, because of the experimental noise. We achieve probabilities of finding these positive events of up to 0.850 ± 0.039 with an average over all blind states of 0.720 ± 0.015 . No classical algorithm can succeed in this scenario with probability higher than 0.5.

Another algorithm that demonstrates the power of quantum computing is the Deutsch-Jozsa algorithm (2) that takes as input an oracle (or black box) for computing an unknown function $f: \{0,1\}^n \rightarrow \{0,1\}$ with the promise that f is either constant, meaning $f(x)$ is the same for all x , or balanced, meaning $f(x) = 0$ for exactly half of the inputs x and $f(x) = 1$ for the other half. The algorithm determines whether f is constant or balanced by making queries to the oracle. Whereas the best possible classical algorithm to solve this problem uses at least $2^{n-1} + 1$ queries in the worst case, the Deutsch-Jozsa algorithm takes advantage of quantum superposition and interference to determine whether f is constant or balanced with only one query. In contrast to previously realized



implementations of Deutsch's algorithm using traditional cluster states (16, 46), we exploit blind staircase cluster states $|\Phi^{(b)}\rangle_f$ for the implementation of this quantum algorithm for the case $n = 1$. Figure 5A shows the quantum circuits that realize oracles corresponding to constant and balanced functions. The corresponding implementation on $|\Phi^{(b)}\rangle_f$ is given in Fig. 5B, where the choice of oracle is done by fixing the measurement on qubits 2 and 3. Blindness of qubit 3 guarantees that the quantum server will not recognize the implementation of a constant oracle from the Grover algorithm or general circuits implementing $R_z(\xi)H \otimes I$ and a balanced oracle from $(I \otimes H)CPhase[R_z(\xi)H \otimes H]$ (Fig. 5). Figure 5, C and D, shows the outcome of our measurement for the case of $|\Phi^{(6,4)}\rangle_f$. A tomography of the state of qubit 4 is performed in order to fully characterize the output of the computation. In this case, the obtained fidelity for the output state is $F = 0.930 \pm 0.025$ for the constant oracle and $F = 0.887 \pm 0.033$ for the balanced oracle, with the algorithm producing the correct result with probabilities 0.899 ± 0.006 for the constant and 0.895 ± 0.022 for the balanced oracle.

Toward verifying the quantumness. Self-testing is a verification process for the operations of a collection of untrusted quantum devices (47, 48); a key application of the blind computing protocol is also toward such verification of quantum devices (29, 30). We demonstrate a notion of verification that can be used as a heuristic probabilistic test for whether the server indeed possesses any quantum technology or is a completely classical device. For this, the client chooses a measurement setting for which, for each measurement outcome, there exists a state with a detection probability of zero. Because of blindness, however, the quantum server has no information about which initial states the client has prepared. If it has no quantum technology in hand, it attempts to use its classical devices and guesses the outcome for the client's computa-

tion wrong with probability at least 1/8. Better bounds can be achieved by using statistics of several rounds and comparing it with the known theoretical statistics to test whether the quantum-computing server is producing the expected outcome or not.

The testing procedure uses statistics of several outcomes for different measurement instructions. Figure 6 shows relevant theoretical predictions as well as experimental outcomes that confirm the quantum nature of the server. By instructing the quantum server to measure, for example, this statistical distribution, the client can see whether the outcomes coincide with the expectations. Our demonstration is a first step toward an efficient verification scheme for quantum technology and acts as an experimental benchmark for future fault-tolerant protocols using more qubits that are expected to enable the detection of a cheating quantum server with probability exponentially close to one.

Discussion. The blind quantum computation protocol demonstrated here is most naturally viewed in the context of measurement-based quantum computation. The required operations, however, can be implemented in any model of computation that is universal for quantum computation on unencoded data and allows intermediate measurements. Finding extensions to other models, such as the adiabatic model, remains an open question.

From our proof-of-principle experiment to a full implementation of the BQC scheme, there are several technical challenges to be faced: Emitted photons that do not contribute to the generation of the cluster state can in principle reveal information about the blind phases. Furthermore, postselection and photon losses decrease the efficiency of the protocol. Therefore, the realization of single-qubit states on demand and the heralded generation of blind cluster states using measurement-induced interactions with high fidelity and low losses will be crucial for future applications. In our experiment, the blind angles were chosen by the human client, and the

measurement settings were selected from a prepared list. Ideally, the source of randomness should be carefully scrutinized to avoid any correlations with the server, and an efficient shot-by-shot randomization should be implemented. Considering the photon rates in our experiment, the realization of full randomization for each measurement is a major challenge. The question of how far imbalances and deviations from the uniform distribution can be acceptable is a topic of current research.

Our experiment is a step toward unconditionally secure quantum computing in a client-server environment where the client's entire computation remains hidden, a functionality not known to be achievable in the classical world. This should present an important privacy-preserving technique in future quantum computing networks or clouds (49). Especially considering the tremendous challenges encountered in making quantum computers widely available, such future networks could consist of a few powerful quantum-computer nodes. The only quantum requirement for the clients would be to communicate with the nodes via quantum links enabling the transfer of arbitrary qubits. Although photonic quantum systems seem to be ideally suited for privacy-preserving quantum computing, we stress that our results are applicable to any physical implementation of qubits and that in the near future the precise quantum control of multiqubit quantum systems (50) will allow for implementing more complex algorithms.

References and Notes

- R. Feynman, *Int. J. Theor. Phys.* **21**, 467 (1982).
- D. Deutsch, R. Jozsa, *Proc. R. Soc. London Ser. A* **439**, 553 (1992).
- L. K. Grover, in *Proceedings of the 28th Annual ACM Symposium on the Theory of Computing*, G. L. Miller, Ed. [Association for Computing Machinery (ACM), New York, 1996], pp. 212–219.
- P. W. Shor, *SIAM J. Comput.* **26**, 1484 (1997).
- J. I. Cirac, P. Zoller, *Phys. Rev. Lett.* **74**, 4091 (1995).
- C. Monroe, D. M. Meekhof, B. E. King, W. M. Itano, D. J. Wineland, *Phys. Rev. Lett.* **75**, 4714 (1995).
- D. Kielpinski, C. Monroe, D. J. Wineland, *Nature* **417**, 709 (2002).
- K. Kim *et al.*, *Nature* **465**, 590 (2010).
- J. L. O'Brien, G. J. Pryde, A. G. White, T. C. Ralph, D. Branning, *Nature* **426**, 264 (2003).
- P. Walther *et al.*, *Nature* **434**, 169 (2005).
- N. Kiesel *et al.*, *Phys. Rev. Lett.* **95**, 210502 (2005).
- R. Prevedel *et al.*, *Nature* **445**, 65 (2007).
- C.-Y. Lu *et al.*, *Nat. Phys.* **3**, 91 (2007).
- Y. Tokunaga, S. Kuwashiro, T. Yamamoto, M. Koashi, N. Imoto, *Phys. Rev. Lett.* **100**, 210501 (2008).
- R. Kaltenbaek, J. Lavoie, B. Zeng, S. Bartlett, K. Resch, *Nat. Phys.* **6**, 850 (2010).
- G. Vallone, G. Donati, N. Bruno, A. Chiuri, P. Mataloni, *Phys. Rev. A* **81**, 50302 (2010).
- Y. Makhlin, G. Schön, A. Shnirman, *Rev. Mod. Phys.* **73**, 357 (2001).
- T. Yamamoto, Y. A. Pashkin, O. Astafiev, Y. Nakamura, J. S. Tsai, *Nature* **425**, 941 (2003).
- M. Neeley *et al.*, *Science* **325**, 722 (2009).
- L. DiCarlo *et al.*, *Nature* **460**, 240 (2009).
- R. Bialczak *et al.*, *Nat. Phys.* **6**, 409 (2010).
- J. Berezovsky, M. H. Mikkelsen, N. G. Stoltz, L. A. Coldren, D. D. Awschalom, *Science* **320**, 349 (2008).
- I. Fushman *et al.*, *Science* **320**, 769 (2008).
- R. Hanson, D. D. Awschalom, *Nature* **453**, 1043 (2008).
- A. Childs, *Quantum Inf. Comput.* **5**, 456 (2005).
- P. Arrighi, L. Salvai, *Int. J. Quantum Inf.* **4**, 883 (2006).

27. V. Giovannetti, S. Lloyd, L. Maccone, *Phys. Rev. Lett.* **100**, 230502 (2008).
 28. F. De Martini *et al.*, *Phys. Rev. A* **80**, 10302 (2009).
 29. A. Broadbent, J. Fitzsimons, E. Kashefi, in *Proceedings of the 50th Annual Symposium on Foundations of Computer Science* (IEEE Computer Society, Los Alamitos, CA, 2009), pp. 517–526.
 30. D. Aharonov, M. Ben-Or, E. Eban, in *Proceeding of Innovations in Computer Science* (Tsinghua Univ. Press, Beijing, 2010), p. 453.
 31. R. Rivest, L. Adleman, M. Dertouzos, in *Foundations of Secure Computation*, R. DeMillo, D. Dobkin, A. Jones, R. Lipton, Eds. (Academic Press, New York, 1978), pp. 169–180.
 32. C. Gentry, in *Proceedings of the 41st Annual ACM Symposium on Theory of Computing*, M. Mitzenmacher, Ed. (ACM, New York, 2009), pp. 169–178.
 33. R. Raussendorf, H. J. Briegel, *Phys. Rev. Lett.* **86**, 5188 (2001).
 34. R. Raussendorf, D. E. Browne, H. J. Briegel, *Phys. Rev. A* **68**, 022312 (2003).
 35. V. Danos, E. Kashefi, P. Panangaden, *J. ACM* **54**, 8 (2007).
 36. D. Gross, J. Eisert, N. Schuch, D. Perez-Garcia, *Phys. Rev. A* **76**, 052315 (2007).
 37. H. Briegel, D. Browne, W. Dür, R. Raussendorf, M. Van den Nest, *Nat. Phys.* **5**, 19 (2009).
 38. D. Gottesman, I. L. Chuang, *Nature* **402**, 390 (1999).
 39. E. Knill, R. Laflamme, G. J. Milburn, *Nature* **409**, 46 (2001).
 40. M. P. Hedges, J. J. Longdell, Y. Li, M. J. Sellars, *Nature* **465**, 1052 (2010).
 41. V. Danos, E. Kashefi, *Phys. Rev. A* **74**, 052310 (2006).
 42. P. G. Kwiat *et al.*, *Phys. Rev. Lett.* **75**, 4337 (1995).
 43. D. F. V. James, P. G. Kwiat, W. J. Munro, A. G. White, *Phys. Rev. A* **64**, 52312 (2001).
 44. M. Van den Nest, J. Dehaene, B. De Moor, *Phys. Rev. A* **69**, 022316 (2004).
 45. M. Boyer, G. Brassard, P. Høyer, A. Tapp, *Fortschr. Phys.* **46**, 493 (1998).
 46. M. S. Tame *et al.*, *Phys. Rev. Lett.* **98**, 140501 (2007).
 47. F. Magniez, D. Mayers, M. Mosca, H. Ollivier, *Automata, Languages and Programming: 33rd International Colloquium, ICALP 2006, Venice, Italy, July 2006, Proceedings, Part I*, M. Bugliesi, B. Preneel, V. Sassone, I. Wegener, Eds. (LNCS 4051, Springer, Berlin, 2006), pp. 72–83.
 48. M. McKague, M. Mosca, in *Theory of Quantum Computation, Communication, and Cryptography: 5th Conference, TQC 2010, Leeds, UK, April 13–15 2010, Revised Selected Papers*, W. van Dam, V. M. Kendon, S. Severini (LNCS 6519, Springer, Berlin, 2011), pp. 113–130.
 49. B. Hayes, *Commun. ACM* **51**, 9 (2008).
 50. T. Monz *et al.*, *Phys. Rev. Lett.* **106**, 130506 (2011).
- Acknowledgments:** The authors are grateful to C. Brukner, V. Danos, and R. Prevedel for discussions and to F. Cipcigan and J. Schmölle for support. We acknowledge support from the European Commission, Q-ESSENCE (no. 248095); European Research Council senior grant (QIT4QAD); John Templeton Foundation; Austrian Science Fund (FWF): [SFB-FOCUS] and [Y585-N20]; Engineering and Physical Sciences Research Council; grant EP/E059600/1; Canada's Natural Sciences and Engineering Research Council; the Institute for Quantum Computing; QuantumWorks; the National Research Foundation and Ministry of Education, Singapore; and the Air Force Office of Scientific Research, Air Force Material Command, U.S. Air Force, under grant no. FA8655-11-1-3004. S.B. designed and performed the experiments, acquired the experimental data, carried out theoretical calculations and the data analysis, and wrote the manuscript. E.K., A.B., and J.F. contributed to the data analysis, carried out theoretical calculations, and wrote the manuscript. A.Z. supervised the project. P.W. contributed to the planning of the experiment, wrote the manuscript, and supervised the project. All authors discussed the results and commented on the manuscript.

Supporting Online Material

www.sciencemag.org/cgi/content/full/335/6066/303/DC1
Materials and Methods
SOM Text
Figs. S1 to S42
Tables S1 to S9

30 September 2011; accepted 30 November 2011
10.1126/science.1214707

An Engineered Microbial Platform for Direct Biofuel Production from Brown Macroalgae

Adam J. Wargacki,^{1*} Effendi Leonard,^{1*} Maung Nyan Win,^{1*} Drew D. Regitsky,¹ Christine Nicole S. Santos,¹ Peter B. Kim,¹ Susan R. Cooper,¹ Ryan M. Raisner,¹ Asael Herman,^{1†} Alicia B. Sivitz,^{1‡} Arun Lakshmanaswamy,¹ Yuki Kashiya,^{1,2,3} David Baker,⁴ Yasuo Yoshikuni^{1§}

Prospecting macroalgae (seaweeds) as feedstocks for bioconversion into biofuels and commodity chemical compounds is limited primarily by the availability of tractable microorganisms that can metabolize alginate polysaccharides. Here, we present the discovery of a 36-kilo-base pair DNA fragment from *Vibrio splendidus* encoding enzymes for alginate transport and metabolism. The genomic integration of this ensemble, together with an engineered system for extracellular alginate depolymerization, generated a microbial platform that can simultaneously degrade, uptake, and metabolize alginate. When further engineered for ethanol synthesis, this platform enables bioethanol production directly from macroalgae via a consolidated process, achieving a titer of 4.7% volume/volume and a yield of 0.281 weight ethanol/weight dry macroalgae (equivalent to ~80% of the maximum theoretical yield from the sugar composition in macroalgae).

Volatile energy costs and pressure to conserve fossil fuel resources have ignited efforts to produce biofuels and renewable commodity chemical compounds via microbial fermentation of biomass. Pursuant to these goals, microbial engineering aims to increase product yields and bioconversion efficiencies. Equally critical, development of scalable and diverse feedstocks will empower sustainable use of this technology and drive the widespread adoption of renewable bio-economies. At present, corn and sugarcane are vetted industrial feedstocks, but “food versus fuel” concerns may preclude their long-term use. Inedible lignocellulosic plant materials are preferable feedstocks, but current mi-

crobial technologies for fermentation of the simple sugars in lignocellulose have yet to overcome the cost of the complex processes needed to release these sugars from recalcitrant polysaccharides (*1*). Therefore, distinct strategies are required to develop scalable and sustainable non-lignocellulosic biomass resources such as marine macroalgae (seaweeds) for use as next-generation feedstocks.

Brown macroalgae exhibit several key features of an ideal feedstock for production of biofuels and renewable commodity chemical compounds. Requiring no arable land, fertilizer, or fresh water resources, cultivation of these crops circumvents economic concerns associated with

land management and avoids adverse impacts on food supplies. Macroalgae are already grown for human consumption, but not as a staple crop. Large-scale cultivation is practiced in several countries, yielding 15 million metric tons per year (*2*); in these countries, macroalgae are also used as animal feeds, agricultural fertilizers, and sources of polymers. Because brown macroalgae does not contain lignin, sugars can be released by simple operations such as milling or crushing. This bio-architectural feature gives macroalgae a distinct advantage over lignocellulosic biomass, facilitates higher yields, and averts the need for energy-intensive pretreatment and hydrolysis processes before fermentation. An analysis prepared for the U.S. Department of Energy (DOE) reports a macroalgae productivity of 59 dry metric tons/ha/year and an ideal ethanol yield from macroalgae of 0.254 weight (wt) ethanol/wt dry macroalgae (*2*). Based on these numbers, an optimum bioethanol productivity of 19,000 liters/ha/year is estimated. This value is approximately two times higher than the ethanol productivity from sugarcane and

¹Bio Architecture Lab, 604 Bancroft Way, Suite A, Berkeley, CA 94710, USA. ²BAL Chile S.A., La Quebrada No. 1005, Puerto Varas 5550658, Chile. ³BAL Biofuels S.A., Alcantara 200, piso 6, Las Condes, Santiago 7550159, Chile. ⁴Bio-molecular Structure and Design (BMSD), Department of Biochemistry, University of Washington, J Wing, Health Sciences Building, Post Office Box 357350, Seattle, WA 98195, USA.

*These authors contributed equally to this work.

†Present address: Biologic Design, Mapo 11, Tel Aviv 63577, Israel

‡Present address: Laboratoire de Biochimie et Physiologie Moléculaire des Plantes, Centre National de la Recherche Scientifique, Unité Mixte de Recherche 5004, Institut de Biologie Intégrative des Plantes, F-34730 Montpellier cedex 2, France.

§To whom correspondence should be addressed. E-mail: yoshikuni@ba-lab.com

5 times higher than the ethanol productivity from corn (3).

The most abundant sugars in brown macroalgae are alginate, mannitol, and glucan (glucose polymers in the form of laminarin or cellulose). Ethanol production from glucan and mannitol yields approximately 0.08 to 0.12 wt ethanol/wt dry macroalgae (2). However, the full potential of ethanol production from macroalgae cannot currently be realized because of the inability of industrial microbes to metabolize the alginate component. For example, fermentation of glucan in *Saccharina latissima* by *Saccharomyces cerevisiae* produced ~0.45% volume/volume (v/v) ethanol (4). Compared with glucose, the catabolism of mannitol generates excess reducing equivalents, causing an unbalanced reduction-oxidation (redox) environment under fermentative conditions. Hence, ethanol production from mannitol is feasible only in the presence of electron shunts (such as micro-aerobic conditions). Semifermentative conditions enabled ethanol production from mannitol by *Zymobacter palmae* with a yield of 0.38 wt ethanol/wt mannitol (5). Additionally, this strain cometabolized glucan and mannitol, producing ~1.6% v/v from these sugar fractions in *Saccharina hyperborea* under micro-aerobic conditions (5, 6). In contrast to mannitol, each mole unit of alginate fermented to ethanol

consumes two reducing equivalents. Therefore, the catabolic pathway of alginate provides both an additional source of sugars and a counterbalance to the excess-reducing equivalents produced by mannitol catabolism, enabling ethanol fermentation from all three sugar components in macroalgae simultaneously.

Alginate is a linear block copolymer of two uronic acids, β -D-mannuronate (M) and α -L-guluronate (G), arranged in varying sequences, with uniform regions of M (poly-M) or G (poly-G), and/or a mixture of M and G (poly-MG) (7). To date, several microorganisms that can metabolize alginate have been characterized. In these microorganisms, a class of enzymes called alginate lyases (Alys) catalyze the depolymerization of alginate into oligomers via an endolytic β -elimination reaction (8). Oligomers are further degraded into unsaturated monomers by an exolytic enzyme known as oligoalginate lyase (Oal). These monomers spontaneously rearrange into 4-deoxy-L-erythro-5-hexoseulose uronic acid (DEH) (9). Subsequently, DEH reductase (DehR) reduces DEH into 2-keto-3-deoxygluconate (KDG), a common metabolite that is fed into the Entner-Doudoroff (ED) pathway. KDG eventually yields pyruvate and glyceraldehyde-3-phosphate via the activities of KDG kinase (KdgK) and KDG-6-phosphate aldolase (Eda) (Fig. 1A) (10, 11).

A recent report described the engineering of a homoethanol pathway in the alginate-metabolizing microbe *Sphingomonas* sp. A1 (12). However, the lack of robustness under standard industrial fermentation conditions, genetic and metabolic intractability, and scarcity of tools for genetic manipulation of such native organisms are likely to prevent their rapid engineering for production optimization or minimization of by-products (13). Here, we sought to circumvent the limitations of native strains and unlock the potential of all major sugar components in brown macroalgae for industrial fermentation by engineering the capacity for alginate degradation, uptake, and metabolism (Fig. 1) into the well-characterized microorganism *Escherichia coli*. We chose this microorganism as a prototype because of its natural ability to metabolize mannitol and glucose. Furthermore, *E. coli* has also been used as a host to produce a wide array of native and heterologous metabolites, including alcohols (14–17), polyketides (18, 19), plant natural products (20–23), fatty acid ethyl esters (24), alkanes (25), 1,3-propanediol (26), and 1,4-butanediol (27).

Engineering a secreted Aly enzyme for alginate degradation in *E. coli*. We first engineered a secreted Aly system to enable efficient and rapid degradation of alginate by our microbial platform. The objective was to couple this

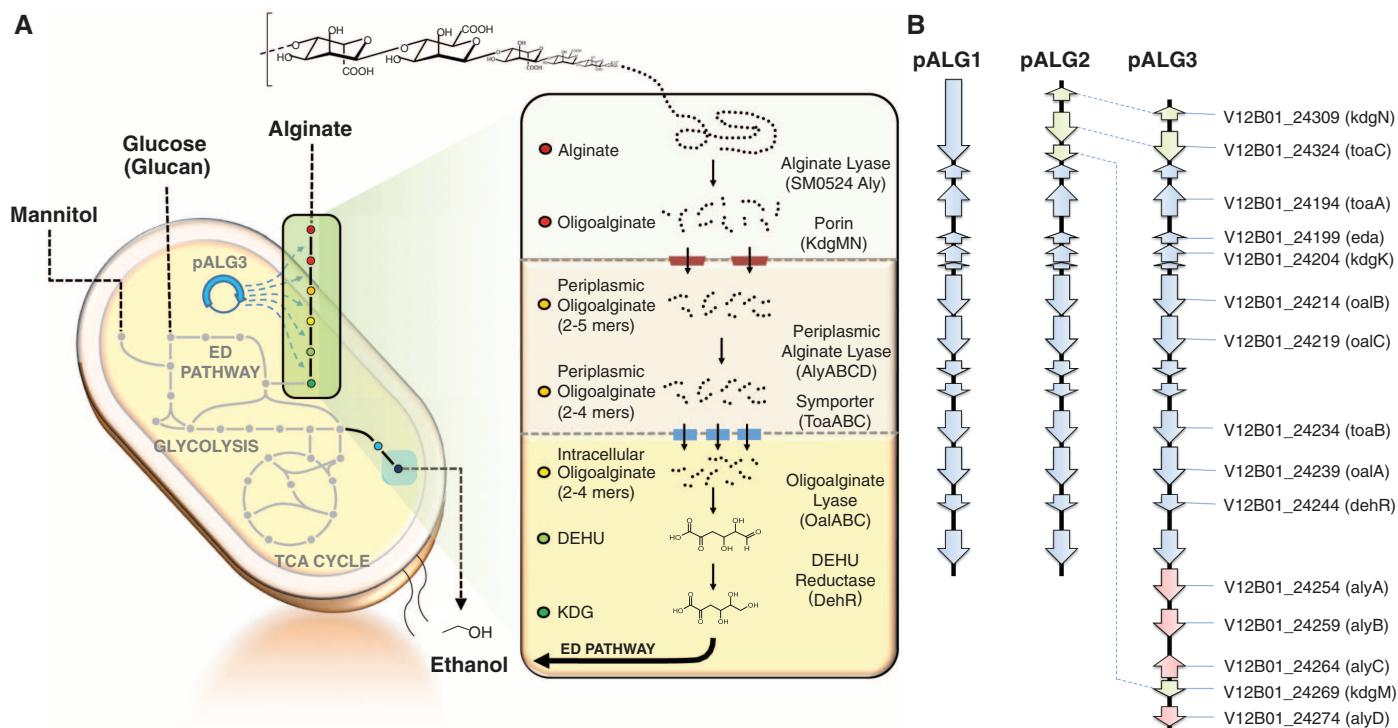


Fig. 1. Design of the microbial platform for production of biofuels and renewable commodity chemical compounds from macroalgae. **(A)** Schematic representation of the engineered *E. coli* platform for alginate degradation, uptake, and metabolism. Alginate polymer is first degraded into oligomers by an alginate lyase. The oligomers are then translocated through the outer-membrane porins (KdgMN) into the periplasmic fraction, where those oligomers with degree of polymerization (DP) > 3 are degraded into di-, tri-, and tetramers by periplasmic alginate lyases (AlyABCD). These subsequent oligomers are

transported into the cytosol via oligoalginate transporters (ToaABC). Oligoalginate lyases (OalABC) then degrade oligomers into monomer units (DEH). DEH is converted by DEH reductase (DehR) to KDG, which enters the ED pathway. This platform can be used to synthesize fuels and chemicals such as ethanol. **(B)** The genetic organization of the synthetic pathway (pALG1, pALG2, and pALG3) containing genes discovered in *V. splendidus* 12B01. Blue, original ORFs found from fosmid library generation (pALG1); pink and green, auxiliary genes that improved *E. coli* growth on alginate (added to pALG2 and pALG3, respectively).

engineered system with the alginate uptake and metabolic pathway, enabling consolidated bioprocessing (CBP) for production of biofuels and renewable commodity chemical compounds directly from macroalgae without thermal and chemical pretreatment or enzymatic saccharification before fermentation. Commonly proposed as a cost-effective strategy, CBP combines enzyme production, feedstock degradation and metabolism, and product formation in a single-process step, thus eliminating the costs of production and purification of feedstock-degrading enzymes (1, 28). Considering that some energy and carbon flux must necessarily be diverted toward Aly synthesis, a single enzyme with a low molecular weight and high, bifunctional (both M- and G-polymer-specific) activity was desirable. The Aly derived from *Pseudoalteromonas* sp. SM0524 (SM0524 Aly) was an attractive candidate because it is a small bifunctional enzyme (32 kD) that mainly produces dimers, trimers, and tetramers from alginate substrates (29). In addition, SM0524 Aly is secreted by its natural producer and is thus functional in the extracellular milieu. Therefore, we chose this enzyme as a model Aly.

Next, we identified a system to be engineered for secretion of SM0524 Aly. Numerous surface-display and medium secretion systems have been developed in *E. coli* for various applications. However, to avoid compromising downstream product synthesis and to ensure the overall efficiency of the CBP process, we established a

number of specific criteria: (i) The system must not require coexpression of complex and multi-component secretion machinery such as Out (30, 31); (ii) secretion must occur constitutively without reliance on further treatment (32); (iii) the enzyme must be secreted into the medium (detached from the cell surface) because faster diffusion and better access to the substrate can provide more efficient degradation; (iv) to ensure economical usage of cellular resources, the major fraction of the enzyme expressed must be deployed into the medium; and (v) secretion of the enzyme must begin at the early stages of fermentation, enabling rapid substrate degradation for subsequent metabolism and chemical production by the fermenting cell.

We found antigen 43 (Ag43) to be an excellent candidate that could potentially satisfy all of these criteria. It is an autotransporter protein native to most *E. coli* strains that contains within itself all the information required for membrane localization and extracellular secretion (33). Ag43 is produced as a pre-protein composed of an N-terminal signal peptide that directs membrane translocation, a succeeding passenger or α domain, and a C-terminal carrier or β domain (Fig. 2A) (34). Maturation of the pre-protein into Ag43 α and Ag43 β subunits arises from removal of the 52-amino acid signal peptide by a signal peptidase and an internal cleavage between amino acids D551 and P552, presumably through autocatalysis. (Single-letter abbrevia-

tions for the amino acid residues are as follows: A, Ala; C, Cys; D, Asp; E, Glu; F, Phe; G, Gly; H, His; I, Ile; K, Lys; L, Leu; M, Met; N, Asn; P, Pro; Q, Gln; R, Arg; S, Ser; T, Thr; V, Val; W, Trp; and Y, Tyr.) This cleavage mechanism is supported by the presence of an aspartyl protease active site within Ag43 α (35). Ag43 α is naturally secreted outside the cell yet remains bound to the cell surface via noncovalent interaction with Ag43 β , which forms an integral outer-membrane protein (35). This indicates the presence of residues within Ag43 α responsible for such binding interaction.

Although Ag43 has been previously engineered to display epitopes and protein domains on the cell surface of bacteria (36), we wanted our system to release Aly beyond the cell surface and into the surrounding medium. To this end, we implemented two important design specifications in engineering our Ag43-mediated Aly secretion system (Fig. 2A). First, to prevent surface attachment we removed a substantial portion of Ag43 α , from amino acid A52 to N455. We replaced this region of the passenger domain with a truncated SM0524. This truncated SM0524 (tSM0524 Aly), containing the catalytic domain for alginate degradation, begins at amino acid D168 of the full-length lyase (GenBank no. ACB87607). Second, we added the aspartyl protease active site, previously removed from the region between A52 and N455, back at a location C-terminal to tSM0524 Aly and immediately

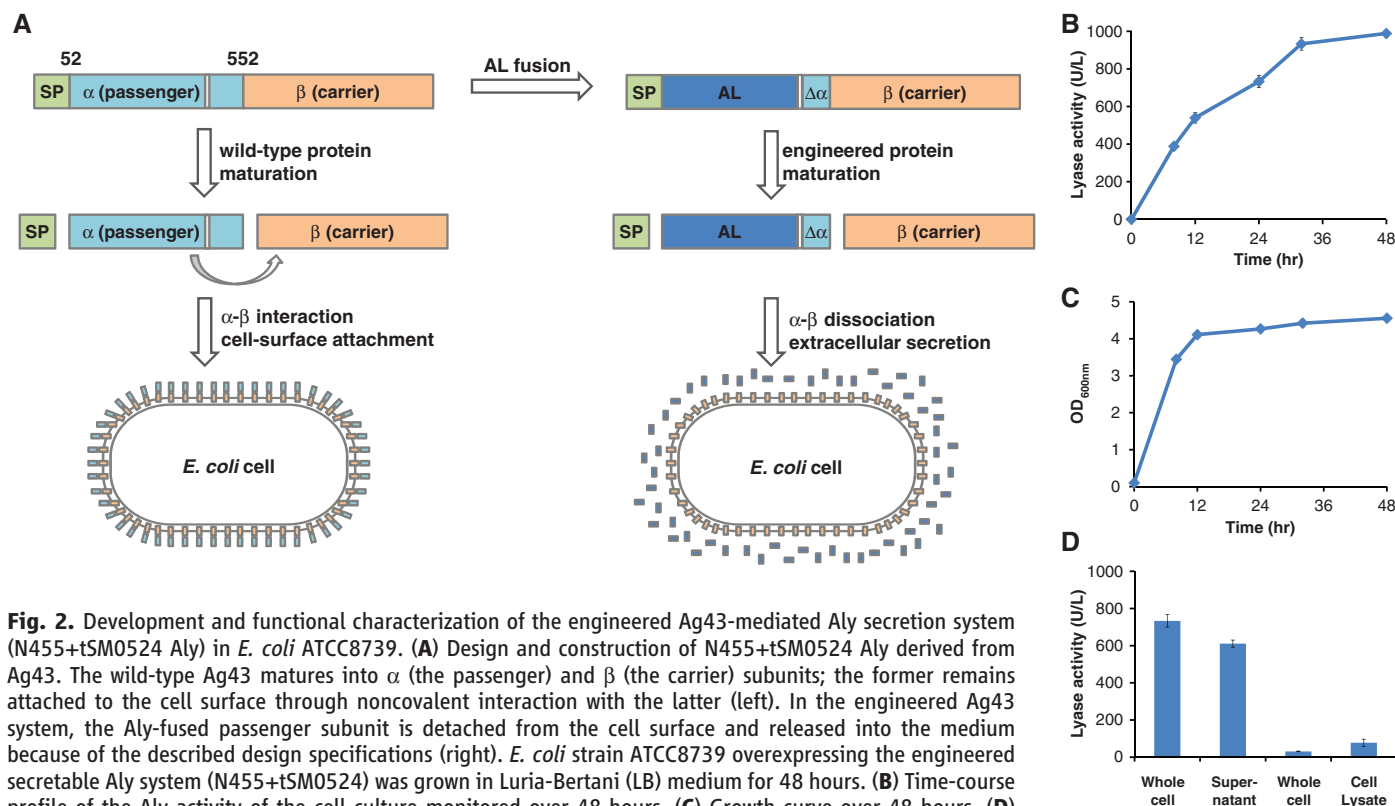


Fig. 2. Development and functional characterization of the engineered Ag43-mediated Aly secretion system (N455+tSM0524 Aly) in *E. coli* ATCC8739. **(A)** Design and construction of N455+tSM0524 Aly derived from Ag43. The wild-type Ag43 matures into α (the passenger) and β (the carrier) subunits; the former remains attached to the cell surface through noncovalent interaction with the latter (left). In the engineered Ag43 system, the Aly-fused passenger subunit is detached from the cell surface and released into the medium because of the described design specifications (right). *E. coli* strain ATCC8739 overexpressing the engineered secretable Aly system (N455+tSM0524) was grown in Luria-Bertani (LB) medium for 48 hours. **(B)** Time-course profile of the Aly activity of the cell culture monitored over 48 hours. **(C)** Growth curve over 48 hours. **(D)** Distribution profile of the Aly activities in whole-cell culture, supernatant, whole-cell pellet, and cell lysate samples prepared from the 24-hour cell culture. SD of the triplicate measurements is shown in error bars.

N-terminal to N455. We expected that with these two design specifications, the passenger fusion protein consisting of the Aly would be released to the medium from the carrier. Using a single-copy plasmid vector, we expressed this engineered Aly secretion construct (N455+tSM0524 Aly) in an *E. coli* strain (ATCC8739) under the control of

a constitutive promoter ($P_{D/E20}$) derived from bacteriophage T5.

We examined the functional performance of our Aly secretion system by applying samples of interest to an alginate solution and monitoring their alginate-degrading activities. A 48-hour time-course of the cell culture medium showed

Aly activities as high as 1000 U/liter. Forty percent of the Aly activity was detected within the first 10 hours of cell growth, indicating that tSM0524 Aly can be rapidly secreted for effective substrate degradation in the early stages of fermentation (Fig. 2B). Analysis of the whole-cell culture, supernatant, whole-cell pellet, and cell lysate prepared from the cell culture growing at 24 hours revealed that the Aly activity in the supernatant was significantly higher than the activities in the cell pellet or lysate and similar to that in the whole-cell culture. This result indicated that tSM0524 Aly was efficiently secreted into the medium, with little remaining on the cell surface or inside the cell (Fig. 2C).

Engineering the metabolic pathway for transport and metabolism of alginate oligomers in *E. coli*. We engineered functional alginate transport and metabolic systems into our host strain via expression of genes from a heterologous DNA fragment (Fig. 1A). The enzymes responsible for alginate metabolism in several bacteria have been described, but the only known alginate transport system is found in *Sphingomonas* sp. A1. This transport system comprises an unusual outer-membrane protein complex and inner-membrane adenosine 5'-triphosphate (ATP)-binding cassette (ABC) transporter, which together can directly incorporate alginate polymer into the cytosol (37). Functional expression of such a large and complicated alginate transport system in *E. coli* is daunting and has never been demonstrated. However, other systems such as the *Erwinia chrysanthemi* oligopectin ABC transporter TogMNAB and symporter TogT (38) are much simpler. Considering the similarities between pectin and alginate, as well as the widespread occurrence of the Tog system in pectinolytic

Table 1. ORFs in pALG1, pALG2, and pALG3 and their annotated functions. Dashes substitute for the gene name when the function is not established.

Locus tag	Gene size (bp)	Annotated function based on conserved domain	Assigned gene name
V12B01_24189	762	Solute-binding protein	—
V12B01_24194	1764	Sodium/solute symporter	<i>toaA</i>
V12B01_24199	624	KDGPA/eda	<i>eda</i>
V12B01_24204	930	KDGK	<i>kdgK</i>
V12B01_24209	333	Unknown	—
V12B01_24214	2205	Heparinasell/III-like protein and alginate lyase	<i>oalB</i>
V12B01_24219	2151	Heparinasell/III-like protein and alginate lyase	<i>oalC</i>
V12B01_24224	822	Fumaryl-acetoacetate hydrolase, 4-hydroxyphenylacetate decarboxylase	—
V12B01_24229	714	GntR transcriptional repressor	—
V12B01_24234	1776	Sodium/solute symporter	<i>toaB</i>
V12B01_24239	2076	Heparinasell/III-like protein	<i>oalA</i>
V12B01_24244	879	NADPH/NADH dehydrogenase	<i>dehR</i>
V12B01_24249	1869	Signaling protein/chemoreceptor	—
V12B01_24269	858	Oligogalacturonate-specific porin	<i>kdgM</i>
V12B01_24309	723	Oligogalacturonate-specific porin	<i>kdgN</i>
V12B01_24324	1656	Sodium/solute symporter	<i>toaC</i>
V12B01_24254	1740	Alginate lyase	<i>alyA</i>
V12B01_24259	1566	Alginate lyase	<i>alyB</i>
V12B01_24264	1230	Alginate lyase	<i>alyC</i>
V12B01_24274	1038	Alginate lyase	<i>alyD</i>

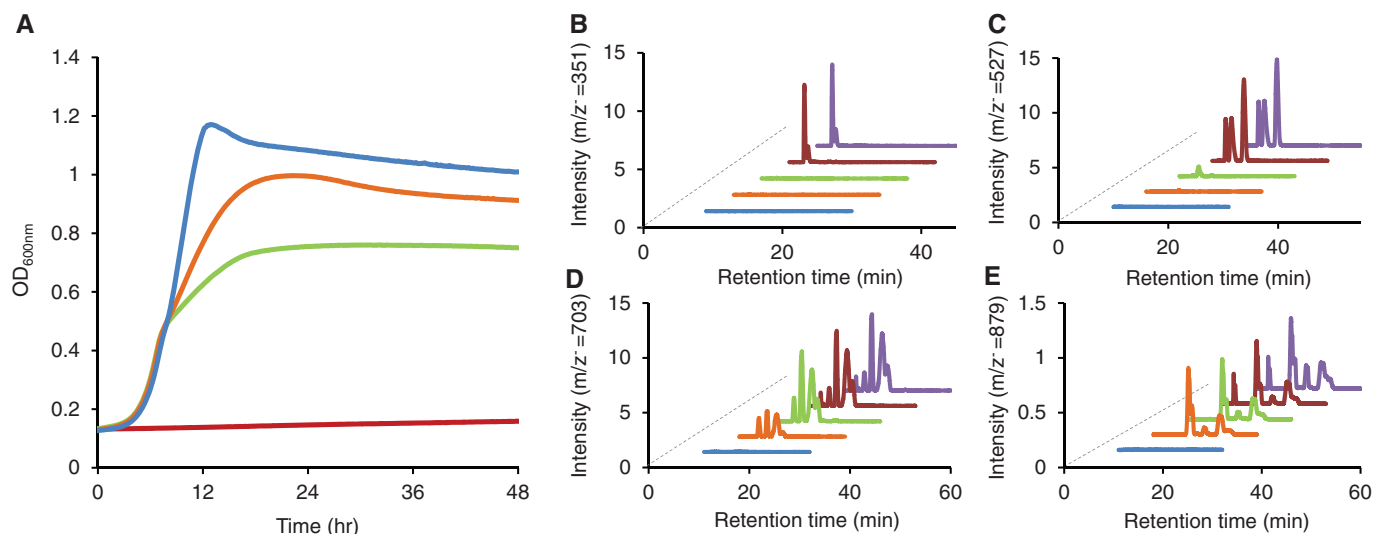


Fig. 3. *E. coli* growth on alginate predegraded by SM0524 Aly after sequential incorporation of auxiliary transporters and Alys into pALG1. (A) Growth phenotypes of *E. coli* strain ATCC8739 harboring pBeloBAC11 (red), pALG1 (green), pALG2 (orange), and pALG3 (blue) on M9 salt medium containing 1% alginate predegraded with SM0524 Aly. An average of three independent growth curves is shown in each case. SD of these

triplicate measurements was smaller than 2%. The mass spectrometric analyses of the growth medium for residual (B) dimer [mass/charge ratio (m/z) = 351], (C) trimer (m/z = 527), (D) tetramer (m/z = 703), and (E) pentamer (m/z = 879) after a 48-hour culture. Starting medium (purple), negative control pBeloBAC11 (red), pALG1 (green), pALG2 (orange), and pALG3 (blue).

bacteria, we postulated that a gene cluster encoding similar transport machineries and metabolic enzymes might be found within the genome of some alginate-degrading bacteria.

In searching the genomes of bacteria available in the National Center for Biotechnology Information database, we recognized a 30-kilo-base pair (kbp) fragment that might contain all necessary genes for alginate degradation, transport, and metabolism within the genome of *Vibrio splendidus* 12B01 (V12B01_24199 to V12B01_24274 in the Gene Identification AAMR00000000). However, direct cloning of a 30-kbp DNA fragment is technically challenging, and reconstruction of the pathway with the targeted genes was even more difficult because the function and regulation of these genes had not been characterized. We overcame these challenges by creating a fosmid library of random DNA fragments using the genomic DNA of this microbe. *E. coli* transformants harboring this library were then screened for growth on minimal-salt medium containing alginate oligomers. We found that colonies that grew on this carbon source contained a fosmid with the insertion of a ~40-kbp genomic fragment. The fosmid, designated pALG1, consisted of intact open reading frames (ORFs) V12B01_24189 to V12B01_24249 (Fig. 1B). This fragment contains the same genes putatively responsible for alginate metabolism located in our original search (Table 1). No other fragments were found in positive transformants, suggesting a lack of alginate metabolism variation in *V. splendidus*. pALG1 comprised several intact ORFs. Assignment of protein function showed that the ORFs in pALG1 encode for enzymes exclusive to *V. splendidus*—with the exception of KDGK and KDGPA, the enzymes in the ED pathway, which are also present in *E. coli* (Table 1).

To probe the function and necessity of each gene in conferring this growth phenotype, we individually deleted each corresponding ORF (predicted to be responsible for alginate metabolism) in pALG1. Growth was assessed on alginate predegraded by SM0524 Aly. As shown in fig. S1, individual deletion of the ORFs in pALG1 encoding for V12B01_24189, V12B01_24224, V12B01_24229, V12B01_24234 (a putative sodium/solute symporter we termed ToaB), and V12B01_24239 (a putative heparinaseII/III-like protein) (fig. S1, C and G to J) did not affect *E. coli* growth, indicating that they are not essential in conferring alginate oligomer metabolism. The rest of the ORFs, when individually deleted, reduced the ability of the *E. coli* host to grow on predegraded alginate. Deletion of ORF V12B01_24194, which encodes for another putative sodium/solute symporter (which we termed ToaA), completely abolished the growth phenotype of our strain (fig. S1D). We have thus identified an essential transport system of alginate oligomers that has not been previously described.

Deletion of three ORFs that encode for putative heparinaseII/III-like protein/alginate lyases impaired growth of the *E. coli* host (figs. S1,

E, F, and J, and S2). On the basis of the model pathway for alginate metabolism, we speculated that these three enzymes function as oligo-alginate lyases (Oal), similar to the recently characterized A1-IV from *Sphingomonas* sp. A1, and Atu3025 from *A. tumefaciens* C58 (40 to 45% primary sequence identity) (39, 40). We designated the enzymes encoded by the V12B01_24239, V12B01_24214, and V12B01_24219 ORFs OalA, OalB, and OalC, respectively. Deletion of ORFs encoding for OalB and OalC resulted in limited impact on degradation of oligomers in vitro, but deletion of the ORF encoding for OalA dramatically reduced degradation of alginate oligomers (fig. S3). It is not clear why the OalA deletion had minimal impact on the growth of *E. coli*, whereas deletion of OalB and OalC delayed cell growth on oligoalginate (fig. S2). However, taken together these results suggest that degradation of the various alginate oligomers proceeded most effectively when all three putative Oal enzymes were present (figs. S1 to S3).

We also found that deletion in pALG1 of ORF V12B01_24244, which encodes for a putative NADPH/NADH-dependent alcohol dehydrogenase (NADPH, reduced form of nicotinamide adenine dinucleotide phosphate; NADH, reduced form of nicotinamide adenine dinucleotide), seriously impaired the growth of our strain (fig. S1K). This enzyme exhibits ~40% DNA sequence identity with the recently characterized NADPH-dependent uronate reductase from *Sphingomonas* sp. strain A1 that catalyzes conversion of DEH into KDG (11). However, biochemical assays demonstrated a preference of this gene's enzyme product for NADH as a cofactor rather than NADPH (fig. S4). These results describe a distinct NADH-dependent DehR. Altogether, we identified the minimum genetic prerequisites for alginate oligo-

mer utilization including a symporter (ToaA) and an NADH-dependent DehR.

Expression of auxiliary genes to improve alginate utilization. We next explored other ORFs (Table 1) in the flanking regions of the isolated 36-kbp fragment from *V. splendidus* 12B01 that may be involved in alginate metabolism. Because they are similar to the outer membrane oligopeptide porins in *Erwinia* sp. (41), we hypothesized that ORFs V12B01_24269 and V12B01_24309 encode for transport systems (termed KdgM and KdgN, respectively) important for channeling alginate oligomers through the outer membrane. We also recognized that ORF V12B01_24324 exhibited high sequence identity to ToaA (64%) and ToaB (88%); hence, we named it ToaC. To investigate the effect of expressing these putative auxiliary transporters, we cloned the ORFs into pALG1 to yield pALG2 (Fig. 1B). We also recognized other ORFs (V12B01_24254, V12B01_24259, V12B01_24264, and V12B01_24274) with a high degree of similarity to the previously discovered Alys. These ORFs encode for enzymes we designated AlyA, AlyB, AlyC, and AlyD, respectively. To test the effect of expressing these additional putative Alys, we cloned the corresponding genes along with genes encoding KdgMN and ToaC into pALG1 to create pALG3 (Fig. 1B). We tested the growth of *E. coli* harboring these new constructs on predegraded alginate (Fig. 3A) and showed that the final cell-culture density of strains harboring pALG2 and pALG3 increased as compared with those expressing pALG1 (Fig. 3A). Compared with *E. coli* strains expressing pALG1, *E. coli* strains expressing pALG2 greatly reduced populations of alginate tetramers in the medium, and only traces of alginate trimers remained (Fig. 3, B to D). With expression of AlyABCD, *E. coli*

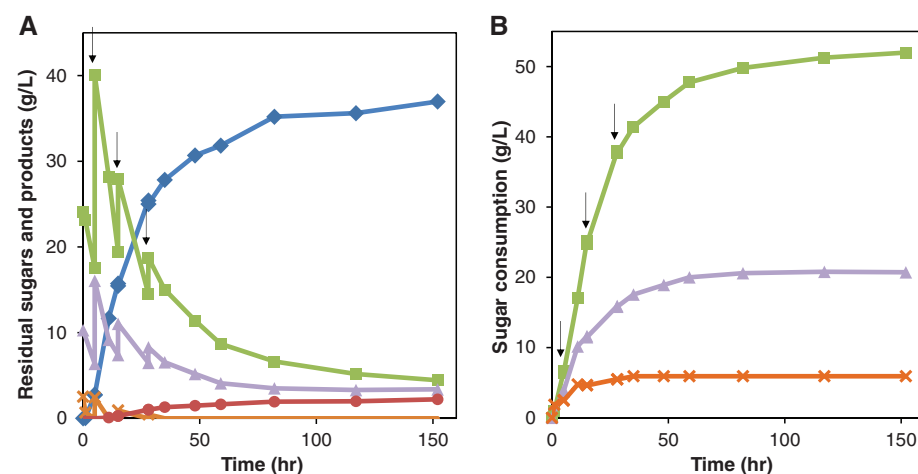


Fig. 4. Fed batch fermentation of macroalgae *S. japonica* to ethanol using BAL1611. (A) Ethanol production and carbohydrate consumption profiles. (B) Total carbohydrate consumption. Ethanol (blue), mannitol (green), alginate (purple), glucose (orange), and succinate (red). The starting medium contains 50 g of dry milled macroalgae. The arrows denote the time points when dry milled macroalgae (50, 20, and 10 g at 5, 15, and 28 hours, respectively) was added to the fermentation to make the final working volume of 1 liter. These data are representative of nine independent fermentation runs, ranging in final ethanol titer from 35 to 41 g/liter (average, 37.8 g/liter; SD = 2.4 g/liter) in the same timeframe.

harboring pALG3 consumed all oligomer populations. These auxiliary genetic components thus help enable complete alginate oligomer utilization (Fig. 3, B to E).

Ethanol fermentation from macroalgae using the engineered *E. coli*. After installation of the alginate metabolism pathway genes from pALG3 into the *E. coli* chromosome, we evaluated the performance of this platform for producing ethanol directly from macroalgae. To engineer an efficient ethanol-production phenotype (17), we introduced a heterologous homo-ethanol pathway consisting of *Zymomonas mobilis* pyruvate decarboxylase (Pdc) and alcohol dehydrogenase B (AdhB). To divert carbon flux away from fermentative by-products, we deleted *pflB-focA*, *frdABCD*, and *ldhA* from the genome of the host strain. We first confirmed the ability of the resultant strain (BAL1366) to secrete alginate lyase (fig. S5A) and grow on alginate without an enzymatic saccharification step (fig. S5B). We then incorporated the engineered secretable alginate lyase system, N455+SM0524 Aly, into the chromosome of this strain. The resulting strain (BAL1611) was tested for its ability to ferment a 5% sugar mixture consisting of alginate, mannitol, and glucose at a ratio of 5:8:1, simulating a typical sugar ratio in brown macroalgae (fig. S6). To explore the engineered strain's fermentation performance at different temperatures, we tested BAL1611 at 25°, 30°, and 37°C (fig. S6). We found that higher ethanol titers were achieved (up to approximately 20 g/liter or 2.4% v/v) when the operating temperature was maintained at 25° to 30°C. This temperature range was therefore chosen for subsequent laboratory-scale fermentation experiments.

We used *Saccharina japonica* (kombu), a common and widely available brown macroalgae, as a model fermentation substrate. Using our microbial platform, we demonstrated macroalgae fermentation producing ethanol at a final titer of ~4.7% v/v, which is comparable with the recently reported benchmark ethanol titer derived from lignocellulosic biomass fermentation using *S. cerevisiae* (42). This ethanol titer corresponds to a bioconversion value of ~0.281 wt ethanol/wt biomass with yield of ~0.41 wt ethanol/wt total sugars (alginate, mannitol, and glucan). This fermentation achieved over 80% of the maximum theoretical yield. Additionally, 83% of this titer was achieved within the first 48 hours of fermentation, corresponding to an overall rate of 0.64 g/liter/hour (Fig. 4A), with a sugar consumption ratio of approximately 2.5 mol mannitol/mol alginate (Fig. 4B).

The common fermentation by-product lactate was present at a final concentration of approximately 2 g/liter, a relatively small amount. This lactate formation may be due to a function of the methylglyoxylate pathway (43). Acetate, succinate, and formate concentrations were extremely low and could not be accurately quantified. These results indicate that carbon flux from pyruvate was efficiently channeled toward ethanol synthe-

sis. Moreover, although *E. coli* can naturally assimilate mannitol and glucose, our engineered strain substantially increased the rate of mannitol fermentation and the resulting ethanol titer relative to the native process (fig. S7). These results support our hypothesis that the alginate pathway plays an important role in balancing the intracellular redox environment by consuming the excess-reducing equivalents generated from mannitol catabolism. Overall, by facilitating simultaneous alginate degradation and assimilation, we demonstrated that our tractable, engineered microbial platform can efficiently ferment all sugars in macroalgae into ethanol.

Catabolism of alginate, mannitol, and glucose in our engineered microbe generates the common metabolic intermediate pyruvate, from which a plethora of fuels and commodity chemical compounds could be synthesized. Hence, our CBP-enabling microbial platform for conversion of marine biomass would be complementary to and synergistic with microbial platforms that will be developed for lignocellulosic feedstocks, contributing toward a broad effort to realize production of renewable fuels and commodity chemical compounds from sustainable biomass resources.

References and Notes

- G. Stephanopoulos, *Science* **315**, 801 (2007).
- G. Roessijadi, S. B. Jones, L. J. Snowden-Swan, Y. Zhu, "Macroalgae as a Biomass Feedstock: A Preliminary Analysis," prepared for the U.S. Department of Energy under contract DE-AC05-76RL01830 by Pacific Northwest National Laboratory (2010).
- C. Somerville, H. Youngs, C. Taylor, S. C. Davis, S. P. Long, *Science* **329**, 790 (2010).
- J. M. Adams, J. Gallagher, I. S. Donnison, *J. Appl. Phycol.* **21**, 569 (2008).
- I. M. A. S. J. Horn, K. Ostgaard, *J. Ind. Microbiol. Biotechnol.* **24**, 51 (2000).
- S. J. Horn, I. M. Aasen, K. Ostgaard, *J. Ind. Microbiol. Biotechnol.* **25**, 249 (2000).
- K. I. Draegt, O. Smidsrod, G. Skjak-Braek, in *Polysaccharides and Polyamides in the Food Industry. Properties, Production, and Patents*, A. Steinbuechel, S. K. Rhee, Eds. (Wiley-VCH Verlag GmbH KGaA, Weinheim, 2005), pp. 1–30.
- T. Y. Wong, L. A. Preston, N. L. Schiller, *Annu. Rev. Microbiol.* **54**, 289 (2000).
- A. Ochiai, M. Yamasaki, B. Mikami, W. Hashimoto, K. Murata, *Acta Crystallogr. Sect. F Struct. Biol. Cryst. Commun.* **62**, 486 (2006).
- J. Preiss, G. Ashwell, *J. Biol. Chem.* **237**, 317 (1962).
- R. Takase, A. Ochiai, B. Mikami, W. Hashimoto, K. Murata, *Biochim. Biophys. Acta* **1804**, 1925 (2010).
- H. Takeda, F. Yoneyama, S. Kawai, W. Hashimoto, K. Murata, *Energy Environ. Sci.* **4**, 2575 (2011).
- H. Alper, G. Stephanopoulos, *Nat. Rev. Microbiol.* **7**, 715 (2009).
- S. Atsumi, T. Hanai, J. C. Liao, *Nature* **451**, 86 (2008).
- B. B. Bond-Watts, R. J. Bellerose, M. C. Chang, *Nat. Chem. Biol.* **7**, 222 (2011).
- C. Dellomonaco, J. M. Clomburg, E. N. Miller, R. Gonzalez, *Nature* **476**, 355 (2011).
- K. Ohta, D. S. Beall, J. P. Mejia, K. T. Shanmugam, L. O. Ingram, *Appl. Environ. Microbiol.* **57**, 893 (1991).
- H. Y. Lee, C. J. Harvey, D. E. Cane, C. Khosla, *J. Antibiot. (Tokyo)* **64**, 59 (2011).
- B. A. Pfeifer, S. J. Admiraal, H. Gramajo, D. E. Cane, C. Khosla, *Science* **291**, 1790 (2001).
- P. K. Ajikumar et al., *Science* **330**, 70 (2010).
- H. Alper, K. Miyaoku, G. Stephanopoulos, *Nat. Biotechnol.* **23**, 612 (2005).
- E. Leonard et al., *Mol. Pharm.* **5**, 257 (2008).
- V. J. Martin, D. J. Pitera, S. T. Withers, J. D. Newman, J. D. Keasling, *Nat. Biotechnol.* **21**, 796 (2003).
- E. J. Steen et al., *Nature* **463**, 559 (2010).
- A. Schirmer, M. A. Rude, X. Li, E. Popova, S. B. del Cardayre, *Science* **329**, 559 (2010).
- F. A. Skraly, B. L. Lytle, D. C. Cameron, *Appl. Environ. Microbiol.* **64**, 98 (1998).
- H. Yim et al., *Nat. Chem. Biol.* **7**, 445 (2011).
- L. R. Lynd, W. H. van Zyl, J. E. McBride, M. Laser, *Curr. Opin. Biotechnol.* **16**, 577 (2005).
- J. W. Li et al., *Mar. Drugs* **9**, 109 (2011).
- S. Y. He, M. Lindeberg, A. K. Chatterjee, A. Collmer, *Proc. Natl. Acad. Sci. U.S.A.* **88**, 1079 (1991).
- N. Kazemi-Pour, G. Condemine, N. Hugouvieux-Cotte-Pattat, *Proteomics* **4**, 3177 (2004).
- K. Fujiyama, H. Maki, S. Kinoshita, T. Yoshida, *FEMS Microbiol. Lett.* **126**, 19 (1995).
- P. Klemm, L. Hjerrild, M. Gjermansen, M. A. Schembri, *Mol. Microbiol.* **51**, 283 (2004).
- M. W. van der Woude, I. R. Henderson, *Annu. Rev. Microbiol.* **62**, 153 (2008).
- I. R. Henderson, P. Owen, *J. Bacteriol.* **181**, 2132 (1999).
- K. Kjaergaard, H. Hasman, M. A. Schembri, P. Klemm, *J. Bacteriol.* **184**, 4197 (2002).
- W. Hashimoto, S. Kawai, K. Murata, *Bioeng. Bugs* **1**, 97 (2010).
- N. Hugouvieux-Cotte-Pattat, S. Reverchon, *Mol. Microbiol.* **41**, 1125 (2001).
- W. Hashimoto, O. Miyake, K. Momma, S. Kawai, K. Murata, *J. Bacteriol.* **182**, 4572 (2000).
- A. Ochiai, W. Hashimoto, K. Murata, *Res. Microbiol.* **157**, 642 (2006).
- N. Blot, C. Berrier, N. Hugouvieux-Cotte-Pattat, A. Ghazi, G. Condemine, *J. Biol. Chem.* **277**, 7936 (2002).
- M. W. Lau, B. E. Dale, *Proc. Natl. Acad. Sci. U.S.A.* **106**, 1368 (2009).
- L. P. Yomano, S. W. York, K. T. Shanmugam, L. O. Ingram, *Biotechnol. Lett.* **31**, 1389 (2009).

Acknowledgments: This work is supported by the DOE under Advanced Research Projects Agency–Energy (ARPA-E) award DE-AR0000006 and by the CORFO INNOVA CHILE (código 09CTEI-6866). We thank M. Polz (Department of Civil and Environmental Engineering, Massachusetts Institute of Technology) for the kind gift of the *V. splendidus* strain. We thank R. Bailey for important discussion on microbial engineering. We also thank A. Wahler for critical review and editing of the manuscript. The assistance of A. Gill for in vitro characterization of Oal enzymes is greatly appreciated. Patents describing components of this work can be found under U.S. patent application nos. 12/245537, 12/361293, 12/899419, 61/427077, and 61/436173. This report was prepared as an account of work sponsored by an agency of the U.S. government. Neither the U.S. government nor any agency thereof, nor any of their employees, makes any warranty, express or implied, or assumes any legal liability or responsibility for the accuracy, completeness, or usefulness of any information, apparatus, product, or process disclosed, or represents that its use would not infringe privately owned rights. Reference herein to any specific commercial product, process, or service by trade name, trademark, manufacturer, or otherwise does not necessarily constitute or imply its endorsement, recommendation, or favoring by the U.S. government or any agency thereof. The views and opinions of authors expressed herein do not necessarily state or reflect those of the U.S. government or any agency thereof.

Supporting Online Material

www.sciencemag.org/cgi/content/full/335/6066/308/DC1
Materials and Methods
Figs. S1 to S7
References (44, 45)

27 September 2011; accepted 15 November 2011
10.1126/science.1214547

Synthetic Partial Waves in Ultracold Atomic Collisions

R. A. Williams,¹ L. J. LeBlanc,¹ K. Jiménez-García,^{1,2} M. C. Beeler,¹ A. R. Perry,¹ W. D. Phillips,¹ I. B. Spielman^{1*}

Interactions between particles can be strongly altered by their environment. We demonstrate a technique for modifying interactions between ultracold atoms by dressing the bare atomic states with light, creating an effective interaction of vastly increased range that scatters states of finite relative angular momentum at collision energies where only *s*-wave scattering would normally be expected. We collided two optically dressed neutral atomic Bose-Einstein condensates with equal, and opposite, momenta and observed that the usual *s*-wave distribution of scattered atoms was altered by the appearance of *d*- and *g*-wave contributions. This technique is expected to enable quantum simulation of exotic systems, including those predicted to support Majorana fermions.

Interactions can be generally understood as arising from collisions between particles that exchange energy and momentum. For an interacting gas at the lowest temperatures T , the thermal de Broglie wavelength λ_{dB} can vastly exceed the characteristic range ℓ of the interparticle potential; the interactions can then be cast in terms of an effective contact potential that couples states with zero relative angular momentum (*s*-wave interactions). Only at higher collision energies, when $\lambda_{dB} \lesssim \ell$, do the details of the potential become important.

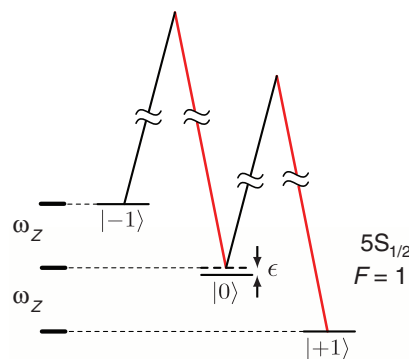
For alkali atomic gases at degenerate temperatures ($T \lesssim 1 \mu\text{K}$), $\lambda_{dB} \geq 100 \text{ nm}$ is much larger than the characteristic range of the interatomic van der Waals potential (I), $\ell_{vdW} = 1.5$ to 5 nm , and *s*-wave interactions dominate. Collisional Fano-Feshbach resonances (I), which are used to modify the strength of atomic interactions, do not change the characteristic range of the potential, and only *s*-wave interactions are usefully modified (2).

Interactions with higher-order partial waves are critical for creating systems whose elementary excitations are Majorana fermions, enigmatic particles that are their own antiparticles. Some many-body systems, including two-dimensional (2D) *p*-wave superfluids (3) and 1D Fermi gases with spin-orbit coupling (4), have been theoretically shown to support Majorana fermions among their elementary excitations. Ultracold Fermi gases could realize these systems by using laser-induced *p*-wave interactions (5, 6), the fermionic analog to the bosonic *d*-wave interactions we demonstrate here.

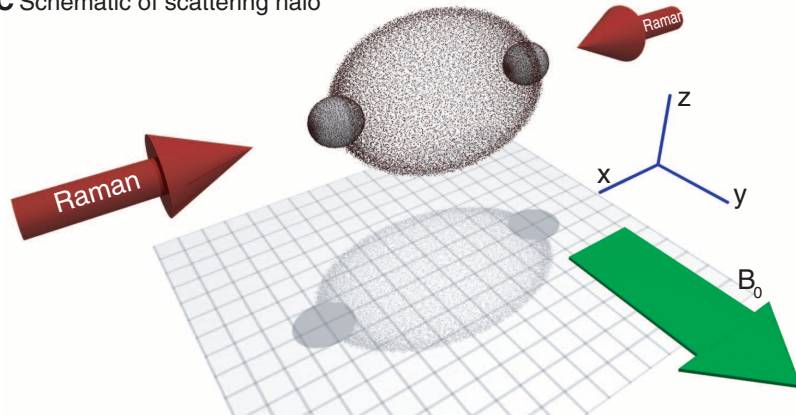
We effectively screened the native atomic interaction with light, which is reminiscent of effects familiar in condensed matter systems, such

as the screening of the Coulomb interaction between a pair of electrons by the collective response of the remaining electrons (7). Similarly,

A Three-level coupling scheme



C Schematic of scattering halo



the laser dressing modifies collisions between dressed atoms, producing effective higher-order partial waves, even though atoms still microscopically collide in the *s*-wave channel. The interaction potential between a pair of particles located at positions \mathbf{r} and \mathbf{r}' can often be described as a function of their separation, $V(\mathbf{r} - \mathbf{r}')$. The two-body term

$$\hat{H}_{\text{int}} = \frac{1}{2} \int \frac{d^3 \mathbf{k}_1}{(2\pi)^3} \cdots \frac{d^3 \mathbf{k}_4}{(2\pi)^3} \hat{\phi}^\dagger(\mathbf{k}_4) \hat{\phi}^\dagger(\mathbf{k}_3) \times \tilde{V}(\mathbf{k}_3 - \mathbf{k}_1) \hat{\phi}(\mathbf{k}_2) \hat{\phi}(\mathbf{k}_1) \times \delta^{(3)}(\mathbf{k}_3 + \mathbf{k}_4 - \mathbf{k}_1 - \mathbf{k}_2) \quad (1)$$

in the Hamiltonian describing this interaction is expressed in terms of the Fourier-transformed potential $\tilde{V}(\Delta \mathbf{k})$, which describes the transition amplitude for a collision that changes the wave vector of a particle by $\Delta \mathbf{k} = \mathbf{k}_3 - \mathbf{k}_1$. The field operator $\hat{\phi}(\mathbf{k})$ denotes the annihilation of a particle with momentum $\hbar \mathbf{k} = \hbar(k_x, k_y, k_z)$,

B Energy-momentum dispersion

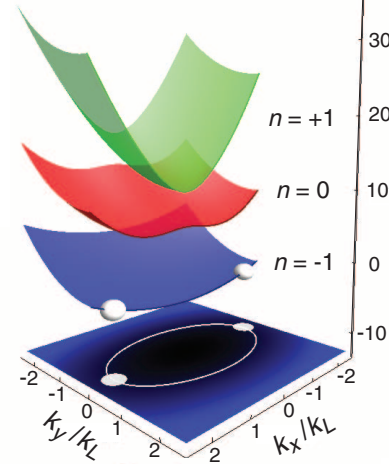


Fig. 1. Creation and detection of synthetic higher-order partial waves. **(A)** Two Raman laser beams couple the three hyperfine Zeeman states comprising the $F = 1$ ground state manifold of ^{87}Rb . **(B)** Energy-momentum dispersion relations for Raman-dressed atoms with Raman lasers counterpropagating along $\pm \mathbf{e}_x$. **(C)** Schematic of two Raman-dressed BECs with atomic momenta $\hbar \mathbf{k}_x = \pm 2 \hbar k_L$ after their collision, indicating the scattering halo as imaged after TOF. A magnetic bias field, $B_0 \mathbf{e}_z$, generates the linear (ω_z) and quadratic (ϵ) Zeeman shifts. In this figure and throughout the manuscript, we use the natural units of momentum $\hbar k_L = 2\pi \hbar / \lambda$ and energy $E_L = \hbar^2 k_L^2 / 2m$ defined by the Raman laser's wavelength.

¹Joint Quantum Institute (JQI), National Institute of Standards and Technology (NIST), and University of Maryland, Gaithersburg, MD 20899, USA. ²Departamento de Física, Centro de Investigación y Estudios Avanzados del Instituto Politécnico Nacional, México Distrito Federal 07360, México.

*To whom correspondence should be addressed. E-mail: ian.spielman@nist.gov

and the Dirac δ -function ensures conservation of momentum. The bare interaction between ultracold atoms is well described by a contact potential $V(\mathbf{r} - \mathbf{r}') \approx g\delta^{(3)}(\mathbf{r} - \mathbf{r}')$, with Fourier transform $\tilde{V}(\Delta\mathbf{k}) = g = 4\pi\hbar^2 a_s/m$, where a_s is the scattering length, and m is the atomic mass. Because $\tilde{V}(\Delta\mathbf{k})$ is independent of $\Delta\mathbf{k}$, low-energy scattering is isotropic. The modification of interactions by an environment (screening) can be characterized in terms of a response function (7) χ , producing the screened interaction $\tilde{V}' = \chi(\mathbf{k}_1, \mathbf{k}_2, \mathbf{k}_3, \mathbf{k}_4) \tilde{V}(\mathbf{k}_3 - \mathbf{k}_1)$.

To modify the effective atomic interactions, we illuminated a Bose-Einstein condensate (BEC) of ^{87}Rb atoms with a two-photon Raman field, producing dressed atoms (spin and momentum superpositions). Two $\lambda = 790.1$ nm Raman laser beams counterpropagating along $\pm\mathbf{e}_x$ coupled the three Zeeman states comprising ^{87}Rb 's $F = 1$ ground state manifold with strength $\hbar\Omega_R$ (Fig. 1A). The dispersion relations of laser-dressed

atoms (Fig. 1B) are altered from those of free particles and consist of three distinct bands labeled by $n = \{-1, 0, +1\}$ with energies $E_{0,\pm 1}(\mathbf{k})$. These altered single-particle dispersions lead to synthetic magnetic (8) and electric fields (9) and spin-orbit coupling (10). The current work reveals how Raman-dressing modifies the interaction between atoms. For atoms in the $n = -1$ (ground) band, we demonstrate higher-order effective d - and g -wave scattering between ultracold atoms at collision energies orders of magnitude below those traditionally required to depart from the s -wave regime. Odd partial waves are absent when elastically scattered atoms lie in the same band and are hence indistinguishable, whereas inelastic (band-changing) transitions can have contributions from all partial waves.

We first considered the elastic interactions between dressed atoms in the $n = -1$ band when the relevant energies (kinetic, interaction, and thermal) are less than the $\sim\hbar\Omega_R$ energy gap

between bands. The dressed states are related to the bare atomic spin states by a momentum-dependent unitary transformation, $\tilde{U}(\mathbf{k})$ (a 3 by 3 matrix that depends on k_x , not k_y or k_z), that links the spin character of an atom to its momentum. To a very good approximation, interactions between ^{87}Rb atoms in the $F = 1$ manifold are spin-independent (11) and cannot change the spin; hence, the scattering amplitude from one pair of momentum states to another depends on the overlap of the spin wave functions associated with the initial and final momentum states. Although microscopically the atoms still collide in the s -wave channel, the result of this momentum-dependent overlap is that atoms experience an interaction altered (12) by a response function

$$\chi = \langle n = -1 | \tilde{U}(\mathbf{k}_4) \tilde{U}^\dagger(\mathbf{k}_2) | n = -1 \rangle \times \langle n = -1 | \tilde{U}(\mathbf{k}_3) \tilde{U}^\dagger(\mathbf{k}_1) | n = -1 \rangle \quad (2)$$

leading to scattering described by effective higher-order partial waves. The modified scattering can be described by an effective real-space potential (determined by the momentum-dependence of χ) that is finite-ranged along the direction of the Raman beams, as discussed in detail in (12).

We investigated interactions between Raman-dressed atoms by observing the scattering halo formed by the collision of two BECs in the lowest-energy Raman-dressed band (Fig. 1C). The experiments started with a nearly pure ^{87}Rb BEC of around 5×10^5 atoms in a crossed optical-dipole trap with frequencies of $\{\omega_x, \omega_y, \omega_z\}/2\pi = \{13, 45, 90\}$ Hz. That BEC was then prepared in the $n = -1$ band, with coupling strength Ω_R , and split into two (initially spatially overlapping) condensates with momenta $\hbar\mathbf{k}_x = \pm 2\hbar\mathbf{k}_L$ per atom (12). After this preparation, the dipole trap was immediately turned off ($t_{\text{off}} < 1 \mu\text{s}$), allowing the dressed condensates to collide in the absence of any confining potential. The scattering halos formed in ~ 2 ms, during which time Ω_R was held constant, and the colliding BECs separated and expanded. After this initial 2-ms stage, we transferred the atoms from the ground dressed state into the bare $|F = 1, m_F = +1\rangle$ spin state (9, 12) and imaged the atomic distribution after a 36.2-ms time of flight (TOF).

Representative scattering halos from colliding BECs are shown in Fig. 2, with (Fig. 2, A to D) and without (Fig. 2E) Raman dressing. Both the absorption images of the scattering halos (which record the atomic column density in the $\mathbf{e}_x\text{-}\mathbf{e}_y$ plane) and the radial density distributions $n(k_p, k_x)$, reconstructed using the inverse Abel transform (12), are depicted. A striking difference between the images in Fig. 2, A to D, and that of Fig. 2E is the shape of the scattering halo. The halo represents a constant energy surface on which the scattered particles lie as a consequence of conservation of energy and momentum in the collision process. For atoms with an isotropic dispersion relation, the scattering halo is approximately spherical in TOF (Fig. 2E). However, the Raman lasers break the spherical symmetry of the system

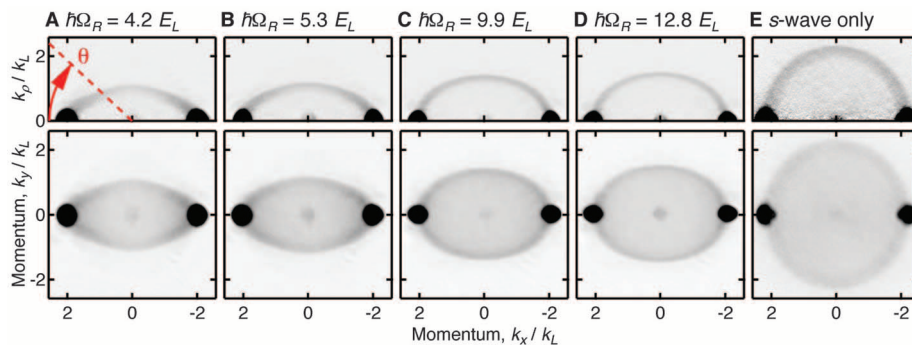


Fig. 2. Scattering halos produced by colliding Raman-dressed BECs. 2D momentum distributions—projections of the scattering halo onto the $\mathbf{e}_x\text{-}\mathbf{e}_y$ plane—are shown along with the radial momentum distributions, $n(k_p, k_x)$, reconstructed by using the inverse Abel transform, where $k_p = (k_y^2 + k_x^2)^{1/2}$. Darker colors correspond to regions of higher atomic density. (A to D) The halos produced by colliding dressed condensates are nearly ellipsoidal and have a nonisotropic angular density distribution. For reference, (E) depicts the s -wave scattering halo from a pair of colliding BECs without Raman coupling in the $|F = 1, m_F = +1\rangle$ spin state. Each image represents the average of ~ 50 experimental shots.

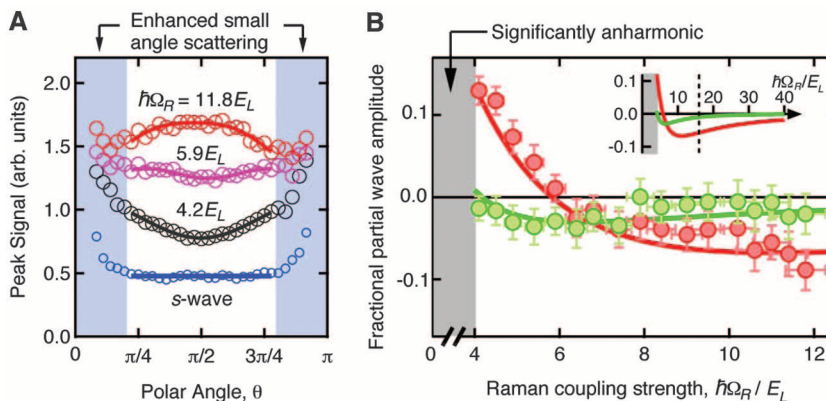


Fig. 3. Beyond s -wave scattering. (A) Peak signal of the radial momentum distribution (after normalizing to the anisotropic density of states) as a function of θ (circles) and fits to a partial wave expansion containing s -, d -, and g -wave contributions (solid lines). (B) d -wave amplitude (red circles) and g -wave amplitude (green circles) as a fraction of the s -wave amplitude together with the respective theoretical values (solid lines). (Inset) Theoretical fractional partial wave amplitudes plotted over a larger range of Ω_R . For $\hbar\Omega_R/E_L > (\delta k_x/k_L)^2$ (dashed vertical line), the response function $\chi \rightarrow 1$ and the interactions return to pure s -wave.

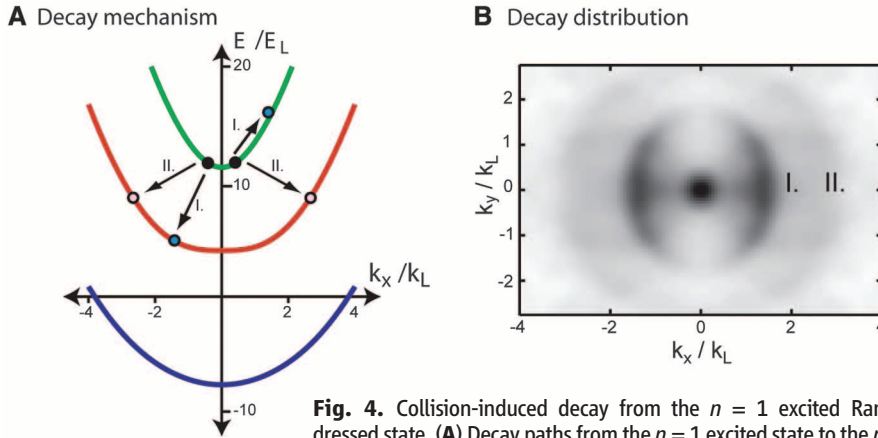


Fig. 4. Collision-induced decay from the $n = 1$ excited Raman-dressed state. **(A)** Decay paths from the $n = 1$ excited state to the $n = 0$ state (here, $\hbar\Omega_R = 13E_L$). **(B)** Momentum distribution of decay products in the $n = 0$ state. After loading into the $n = 1$ band, the atoms were held in the dipole trap for 1 ms before release, allowing a substantial fraction to decay to the lower-energy bands. An adiabatic deloading technique transferred $n = 0$ dressed atoms into the $m_F = 0$ spin state (12), and the atoms were subsequently imaged after 7 ms TOF.

by modifying the dispersion relation along \mathbf{e}_x , $E_{-1}(\mathbf{k}) = E_{-1}(k_x) + \hbar^2(k_y^2 + k_z^2)/2m$, resulting in an approximately ellipsoidal equipotential surface.

As Ω_R increases, $E_{-1}(\mathbf{k})$ tends to the isotropic $\hbar^2\mathbf{k}^2/2m$ free-particle dispersion, and the scattering halo becomes spherical (seen in the progression in Fig. 2, A to D). A quantitative analysis of the scattering halos' shape is considered in (12). We restricted our measurements to $\hbar\Omega_R \geq 4E_L$; for smaller coupling strengths, the lowest band is substantially anharmonic. The deviations from sphericity result from a single-particle effect—the altered dispersion relations—and are not a signature of beyond s -wave scattering.

Along with the modification of scattering halo shape, the distribution of atoms on the scattering surface is also changed. Two main effects determine the distribution of atoms: (i) the anisotropic final density of states (DOS) $\rho_f(\mathbf{k})$ and (ii) effective higher-order partial waves in the binary collision process. The first effect, resulting from the shape of the scattering halo as determined by $E_{-1}(\mathbf{k})$, would occur in an identical scattering experiment with spinless bosons subject to the same energy-momentum dispersion relation. The second effect, described by the response function χ of Eq. 2, is a consequence of the momentum-dependent spin structure of Raman-dressed atoms leading to effective beyond- s -wave interactions and is the central result of this paper.

These independent effects may be quantified with Fermi's golden rule (FGR). For two colliding atoms, the scattering rate from the initial state $|i\rangle = \hat{\phi}_{-1}^\dagger(2k_L\mathbf{e}_x)\hat{\phi}_{-1}^\dagger(-2k_L\mathbf{e}_x)|\text{vac}\rangle$ into the final state $|f\rangle = \hat{\phi}_{-1}^\dagger(\mathbf{k}_f)\hat{\phi}_{-1}^\dagger(-\mathbf{k}_f)|\text{vac}\rangle$ is $\Gamma(\mathbf{k}_f) = 2\pi\langle f|\hat{H}_{\text{int}}|i\rangle^2\rho_f(\mathbf{k}_f)/\hbar$, dependent on both the final DOS ρ_f and the transition matrix element $\langle f|\hat{H}_{\text{int}}|i\rangle$ describing the screened potential \tilde{V} . Here, $|\text{vac}\rangle$ is the many-body vacuum, and $\hat{\phi}_{\mathbf{k}}^\dagger(\mathbf{k})$ describes the annihilation of a Raman-dressed atom with wave vector \mathbf{k} . The dependence of the matrix element on the re-

sponse function χ gives rise to effective higher-order partial wave scattering (12). The contributions of the DOS and the matrix element to the anisotropic nature of the scattering rate $\Gamma(\mathbf{k}_f)$ are of comparable magnitude.

The peak signal as a function of polar angle θ extracted from the inverse Abel transform for several different Ω_R , normalized to the anisotropic DOS (12), is shown in Fig. 3A. This normalization removes all anisotropies except those resulting from beyond s -wave scattering, which we quantify by fitting the data with the partial-wave expansion (13) $p(\theta) = A|\sum_{l=0,2,4}(2l+1)(\exp 2i\eta_l - 1)P_l(\cos\theta)|^2/k^2$, where the fit parameter η_l is the phase shift of the l^{th} partial wave, $P_l(\cos\theta)$ is the Legendre polynomial of order l , and A is an overall scaling factor (for example, dependent on the initial condensate densities and their interaction time). The peak signal $p(\theta)$ is proportional to $\Gamma(\mathbf{k}_f)$. The fit was restricted to the angular range $\pi/5 \leq \theta \leq 4\pi/5$, which excluded the regions close to the unscattered clouds. These regions showed an increase in atom number beyond that expected, even for pure s -wave scattering between bare spin states, possibly because of multiple scattering events or Bose stimulation.

The d - and g -wave amplitudes (normalized to the s -wave amplitude) are shown in Fig. 3B as a function of Ω_R , obtained from fits as in Fig. 3A, where the fractional amplitude of the l^{th} partial wave is $(2l+1)\text{sign}(\eta_l)\exp 2i\eta_l - 1/|\exp 2i\eta_l - 1|$. At $\hbar\Omega_R = 4.1E_L$, we found a fractional d -wave amplitude of 13% for collision temperature $T_{\text{col}} = \mu v_{\text{rel}}^2/2k_B \approx 0.7\mu\text{K}$, where μ is the reduced mass of the colliding particles, and v_{rel} is their relative velocity. By comparison, two previous experiments (14, 15), which studied the scattering of ^{87}Rb in a bare spin state, did not find comparable d -wave magnitudes until $T_{\text{col}} \geq 100\mu\text{K}$. The solid lines show the theoretical prediction for the fractional partial wave amplitudes, calculated from a

partial wave expansion of the matrix element $\langle f|\hat{H}_{\text{int}}|i\rangle$. As highlighted in Fig. 3B, the engineered effective interaction potentials are not only long-ranged but also tunable; by changing Ω_R , we controlled both the magnitude and sign of the d -wave phase shift.

We then considered collisions between atoms in the highest-energy $n = 1$ Raman-dressed band. Although spin-changing collisions of bare atoms hardly occur in ^{87}Rb , strong band-changing transitions of dressed atoms are in general permitted (16, 17). To study this effect, we investigated the (energetically allowed) collision-induced transitions of atoms to lower bands. We considered collisions in a single BEC (so that atoms collided at extremely low relative momenta) and observed the spatial distribution of the collision products after TOF.

We prepared a BEC in the highest-energy dressed state with zero momentum (12). Shown in Fig. 4B are atoms in the $n = 0$ (intermediate energy) band that have decayed from the excited band by the processes indicated in Fig. 4A. Scattered atoms exhibited a node in the $k_x = 0$ plane—a dramatic manifestation of beyond s -wave scattering. The inner halo (I) is due to a process in which one atom in a colliding pair undergoes an inelastic transition to the $n = 0$ band, while the other scattered atom remains in the $n = 1$ band. Because the scattering products are distinguished by their band index, the spatial wave function need not be symmetric with respect to exchange, and the scattered wave function can in principle have contributions from all partial waves. However, only effective p -wave and higher odd partial wave components are permitted because of the underlying symmetry of the Hamiltonian.

Our technique for modifying atomic interactions has substantial ramifications for systems of ultracold atoms, bosons, and fermions alike. Possible new effects induced by synthetic higher-order partial wave interactions in a harmonically trapped BEC could include roton features in the excitation spectrum (16), crystalline ordering (18), supersolidity (19), or even the support of 2D solitons (20). In addition, collisions in this experiment are subject to a new kind of resonance phenomenon. As the collision energy approaches the interband spacing, virtual excitations to the higher band can greatly modify the collisional properties beyond the effects described here.

References and Notes

- C. Chin, R. Grimm, P. Julienne, E. Tiesinga, *Rev. Mod. Phys.* **82**, 1225 (2010).
- The large inelastic loss rates generally associated with p -wave Feshbach resonances (21) significantly limit their utility.
- C. Nayak, S. H. Simon, A. Stern, M. Freedman, S. D. Sarma, *Rev. Mod. Phys.* **80**, 1083 (2008).
- J. Allica, *Phys. Rev. B* **81**, 125318 (2010).
- C. Zhang, S. Tewari, R. M. Lutchyn, S. Das Sarma, *Phys. Rev. Lett.* **101**, 160401 (2008).
- L. Jiang *et al.*, *Phys. Rev. Lett.* **106**, 220402 (2011).
- A. L. Fetter, J. D. Walecka, *Quantum Theory of Many-Particle Systems* (Courier Dover Publications, Mineola, NY, 2003).

8. Y. J. Lin, R. L. Compton, K. Jiménez-García, J. V. Porto, I. B. Spielman, *Nature* **462**, 628 (2009).
9. Y.-J. Lin *et al.*, *Nat. Phys.* **7**, 531 (2011).
10. Y.-J. Lin, K. Jiménez-García, I. B. Spielman, *Nature* **471**, 83 (2011).
11. A. Widera *et al.*, *New J. Phys.* **8**, 152 (2006).
12. Materials and methods are available as supporting material on Science Online.
13. J. J. Sakurai, *Modern Quantum Mechanics (Revised Edition)* (Addison Wesley, Boston, 1993).
14. N. R. Thomas, N. Kjaergaard, P. S. Julienne, A. C. Wilson, *Phys. Rev. Lett.* **93**, 173201 (2004).
15. Ch. Buggle, J. Léonard, W. von Klitzing, J. T. M. Walraven, *Phys. Rev. Lett.* **93**, 173202 (2004).
16. D. M. Stamper-Kurn, *New J. Phys.* **5**, 50 (2003).
17. I. B. Spielman, *Phys. Rev. A* **79**, 063613 (2009).
18. I. Romanovsky, C. Yannouleas, U. Landman, *Phys. Rev. Lett.* **93**, 230405 (2004).
19. V. W. Scarola, S. Das Sarma, *Phys. Rev. Lett.* **95**, 033003 (2005).
20. I. Tikhonenkov, B. A. Malomed, A. Vardi, *Phys. Rev. Lett.* **100**, 090406 (2008).
21. C. A. Regal, C. Ticknor, J. L. Bohn, D. S. Jin, *Phys. Rev. Lett.* **90**, 053201 (2003).

Acknowledgments: We thank C. Sa de Melo, J. V. Porto, and V. Galitski for useful conversations. This work was partially supported by the Office of Naval Research; by Army Research Office with funds from the Defense Advanced Research Projects Agency Optical Lattice Emulator program and the Atomtrons Multidisciplinary University Research

Initiative; and by the NSF through the Physics Frontier Center at JQI. L.J.L. acknowledges National Sciences and Engineering Research Council of Canada, K.J.-G. acknowledges CONACYT (Consejo Nacional de Ciencia y Tecnología), and M.C.B. acknowledges NIST–American Recovery and Reinvestment Act.

Supporting Online Material

www.sciencemag.org/cgi/content/full/science.1212652/DC1
Materials and Methods
SOM Text
Figs. S1 to S3
References (22–27)

15 August 2011; accepted 18 November 2011

Published online 8 December 2011;

10.1126/science.1212652

Visualizing Gas Molecules Interacting with Supported Nanoparticulate Catalysts at Reaction Conditions

Hideto Yoshida,^{1*} Yasufumi Kuwauchi,^{2*} Joerg R. Jinschek,³ Keju Sun,⁴ Shingo Tanaka,⁴ Masanori Kohyama,⁴ Satoshi Shimada,⁵ Masatake Haruta,⁵ Seiji Takeda^{1†}

Understanding how molecules can restructure the surfaces of heterogeneous catalysts under reaction conditions requires methods that can visualize atoms in real space and time. We applied a newly developed aberration-corrected environmental transmission electron microscopy to show that adsorbed carbon monoxide (CO) molecules caused the {100} facets of a gold nanoparticle to reconstruct during CO oxidation at room temperature. The CO molecules adsorbed at the on-top sites of gold atoms in the reconstructed surface, and the energetic favorability of this reconstructed structure was confirmed by ab initio calculations and image simulations. This atomic-scale visualizing method can be applied to help elucidate reaction mechanisms in heterogeneous catalysis.

Visualizing atoms and molecules that are involved in chemical reactions and material syntheses is indispensable in sci-

ence and technology. Transmission electron microscopy (TEM) has markedly advanced in recent years because of an aberration corrector

used in electromagnetic lenses (1). Individual atoms such as lithium (2), carbon (3), and heavier atoms (4–6), as well as molecules (7, 8), are readily visible. One of the challenges in TEM is to visualize gas molecules that interact with a solid surface under various reaction conditions. Here, we report on the imaging of CO molecules adsorbed on the surfaces of supported gold nanoparticles (GNPs) by means of aberration-corrected environmental TEM (ETEM) (9–16).

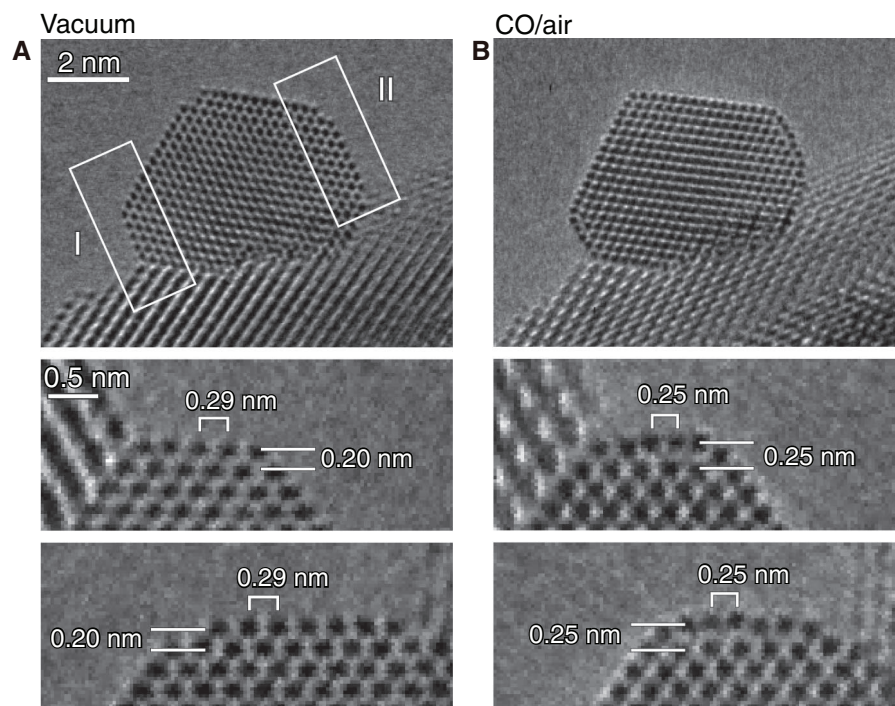
¹The Institute of Scientific and Industrial Research, Osaka University, 8-1 Mihogaoka, Ibaraki, Osaka 567-0047, Japan.

²Department of Physics, Graduate School of Science, Osaka University, 1-1 Machikaneyama, Toyonaka, Osaka 560-0043, Japan. ³FEI Company, 5651 GG Eindhoven, Netherlands. ⁴Research Institute for Ubiquitous Energy Devices, National Institute of Advanced Industrial Science and Technology (AIST), Midorigaoka, Ikeda, Osaka 563-8577, Japan. ⁵Department of Applied Chemistry, Graduate School of Urban Environmental Sciences, Tokyo Metropolitan University, 1-1 Minami-osa, Hachioji, Tokyo 192-0397, Japan.

*These authors contributed equally to this work.

†To whom correspondence should be addressed. E-mail: takeda@sanken.osaka-u.ac.jp

Fig. 1. Au{100}-hex reconstructed surface under catalytic conditions. GNP supported on CeO₂ in (A) a vacuum and (B) a reaction environment (1 volume % CO in air gas mixture at 45 Pa at room temperature). Two {100} facets are present in the rectangular regions indicated by I and II in (A). The enlarged images of these regions in vacuum and in the CO in air gas mixture are shown at the bottom of (A) and (B), respectively. In vacuum, the distance between the topmost and the second topmost {100} surface layers of 0.20 nm was the same as the interplanar distance of the {200} planes in crystalline bulk gold. The average distance of the adjoining Au atomic columns on the topmost surface layer of 0.29 nm was the same as the corresponding distance in a {100} plane in crystalline bulk gold. In the reaction environment, both the average distance of the adjoining Au atomic columns and the interplanar distance changed to 0.25 nm. These changes in positions of the Au atomic columns correspond well to those of the Au{100}-hex reconstructed surface structure. To reduce random noise, the images in (A) and (B) were obtained by averaging four successively acquired images.



We examined a catalyst composed of GNPs supported on CeO_2 . Inactive gold becomes active for the oxidation of CO, even below room temperature, when it is supported in the form of nanoparticles on metal oxides such as TiO_2 and CeO_2 that have reducible metal cations (17–19). Many studies of catalysis by GNPs have dealt with the adsorption sites of CO molecules on the surfaces of GNPs. CO molecules have been postulated to adsorb preferentially onto specific sites such as steps, edges, and corners on the surfaces of GNPs (20–23). Our observations by aberration-corrected ETEM show that an unpredicted structural reconstruction is induced onto the {100} facets of the GNPs in various reaction environments and that CO molecules are adsorbed at the on-top sites of the gold atoms in the well-extended reconstructed {100} facets. An analysis of the observed images was confirmed by image simulations based on ab initio electronic theory.

A Au/ CeO_2 powder catalyst, which exhibited high catalytic activity for the oxidation of CO at room temperature, was observed by ETEM. The catalyst was prepared by a deposition precipitation method (17), and its activity was measured by using a fixed-bed flow reactor (24). Figure 1 shows that structural reconstruction was induced onto the {100} facets under the catalytic reaction. The aberration-corrected ETEM images shown in Fig. 1 were obtained with 300 keV electrons

that travelled parallel to the $\langle 110 \rangle$ zone axis of a crystalline GNP under the optimum under-defocus condition. Each Au atomic column was present as a dark dot (24). As shown in the enlarged images in Fig. 1A, the {100} facets remained unreconstructed in vacuum [see movie S1]. Under a specific reaction environment (1 volume % CO in air at 45 Pa at room temperature), as shown in Fig. 1B, the Au atomic columns on the topmost and second topmost {100} layers shifted to positions they do not normally occupy on the clean surface (see movie S2). These reconstructed positions of the Au atomic columns agree with those derived by density functional theory calculations (25, 26) and TEM observations (27) of the Au{100}-hex reconstructed surface structure (28). In the reconstructed surface, the Au atoms on the topmost surface layer form an undulating hexagonal lattice, whereas those on the second topmost surface layer form a normal square lattice with slight distortion. The reconstruction was also observed when using other GNPs in 1 volume % CO in air of 100 to 2000 Pa, as shown in fig. S1 and fig. S2. The majority (at least 75%) of the GNPs among the 20 that were evaluated exhibited reconstruction in CO in air gas. In sharp contrast to the surface of thin Au foils (27), the reconstructed surface structure appeared in the GNPs preferentially under specific reaction environments.

To improve the image contrast of light-element atoms such as carbon and oxygen (3, 8, 29), we observed the catalyst samples using lower energy electrons (24). Figure 2, A and B, shows aberration-corrected ETEM images of a {100} facet of a GNP in vacuum and under a specific reaction environment (1 volume % CO in air at 100 Pa) that were obtained with 80 keV electrons. Images and a movie of the whole GNP are given in fig. S3 and in movie S3, respectively (24). The direction of view in Fig. 2, A and B, is parallel to the {100} facet and it is off the $\langle 110 \rangle$ zone axis, which decreased the image contrast of the crystalline GNP and enhanced that of the light-element atoms such as carbon and oxygen. Under the specific reaction environment, an unusual contrast appeared on the reconstructed facet (Fig. 2B). Bright and dark contrast features were found that extruded from the reconstructed facet of GNPs (Fig. 2, B and C, and figs. S3 and S4).

An image simulation was performed in combination with ab initio electronic calculations with regard to CO adsorption on the Au{100}-hex reconstructed surface (24) (fig. S5). A simulated image (Fig. 2D) based on an energetically favorable model for CO adsorption (Fig. 2, E and F) fit well with the observed image (Fig. 2C). TEM images are becoming more quantitatively useful than ever before through image simula-

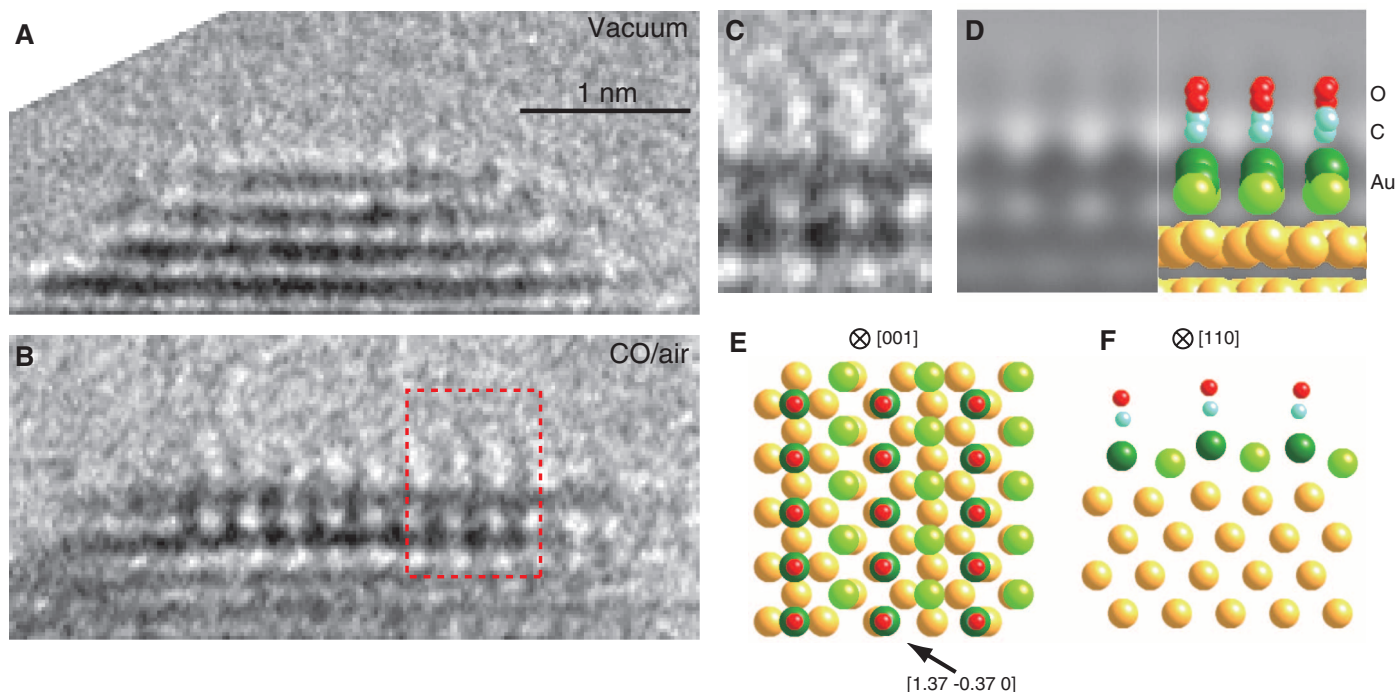


Fig. 2. Adsorbed CO molecules on a Au{100}-hex reconstructed surface under catalytic conditions. Aberration-corrected ETEM images in (A) a vacuum and (B) a reaction environment (1 volume % CO in air at 100 Pa at room temperature) taken using 80 keV electrons using an under-defocus condition. (C) The observed image in the rectangular region in (B) at higher magnification. (D) A simulated image based on an energetically favorable model. The model is superimposed on the simulated image. The model in (E) plan view along the [001] direction of crystalline gold and (F) cross-sectional view along the [110] direction of crystalline gold to show the undulating topmost Au layer. C atoms,

blue colored balls; O atoms, red colored balls; CO adsorbed Au atoms within the surface hexagonal lattice, darker green colored balls; the other Au atoms within the surface hexagonal lattice, brighter green colored balls; the Au atoms within and below the second topmost surface layer, gold colored balls. By fitting the simulated images with the observed images, the viewing direction in (A) to (C) was determined to be the $[1.37, -0.37, 0]$ direction of the crystalline GNP. As shown in models (D) and (E), the $[1.37, -0.37, 0]$ direction is nearly parallel to one side of the surface hexagonal lattice. To reduce random noise, the images in (A), (B), and (C) were obtained by averaging four successively acquired images.

tion with the advent of aberration correctors. The aberration-corrected ETEM images in Fig. 2, B and C, were therefore analyzed quantitatively as summarized in fig. S6. The imaging of adsorbed molecules of CO was thus further supported (24). As shown in a plan view (Fig. 2E) and a cross-sectional view (Fig. 2F) of this model, the CO molecules were adsorbed at the on-top sites of half the Au atoms in the undulating hexagonal lattice. The adsorption energy per CO molecule for this model was estimated to be 0.26 eV. Surface coverages exceeding 50% in the undulating hexagonal lattice were energetically unfavorable.

Previous theoretical studies (22, 23, 30) examined the adsorption of CO molecules onto unreconstructed GNP surfaces. CO molecules adsorb more strongly than oxygen molecules onto the surface of GNPs. Unlike ordinary Pd and Pt catalysts, it was thought that a flat facet of a GNP cannot accommodate CO molecules in high density (20, 21) because of the intrinsic weak adsorption of a CO molecule and the repulsive interactions between CO molecules. CO molecules were thought to be adsorbed onto low-coordination sites such as steps, edges, and corners more strongly than a flat facet. However, the present aberration-corrected ETEM observation combined with ab initio calculations revealed that the surface structure of the {100} facets undergoes modifications that allow CO molecules to adsorb at higher surface coverages. In the Au{100}-hex reconstructed surface, the Au atoms on the topmost layer have unusual bonding configurations with the Au atoms on the second surface layer (24). The adsorption of CO molecules in high density can be sustained on the reconstructed surface. Reconstruction was not observed on the {111} facet of GNPs during our observations. According to theoretical studies, tensile stress is known to be induced onto the

{100} facet more strongly than the {111} facet (31, 32). In addition, the surface energy is higher in the {100} facet than in the {111} facet. Correspondingly, only long-range reconstruction is observed experimentally on the {111} facet (33–35). Therefore, a high affinity for CO adsorption is induced on the {100} facet of GNPs through reconstruction, whereas the stable {111} surface is considered to be oblivious to the presence of CO gas. Hence, along with previous studies, we have now obtained an atomistic view about the adsorption of CO molecules onto the supported GNP catalysts. Accumulated experimental data (36, 37) indicate that the active sites of the GNP catalysts are located at the particle-support periphery where gas species such as O₂ or -OH probably react with CO. The methodology demonstrated in this study has opened an experimental route toward the elucidation of GNP catalytic mechanisms by direct observation of metal atoms and gas species at the particle-support periphery.

References and Notes

- M. Haider et al., *Nature* **392**, 768 (1998).
- Y. Oshima et al., *J. Electron Microsc.* **59**, 457 (2010).
- J. C. Meyer et al., *Nano Lett.* **8**, 3582 (2008).
- C. L. Jia, M. Lentzen, K. Urban, *Science* **299**, 870 (2003).
- Y. Oshima et al., *Phys. Rev. B* **81**, 035317 (2010).
- J. E. Allen et al., *Nat. Nanotechnol.* **3**, 168 (2008).
- M. Koshino et al., *Science* **316**, 853 (2007).
- Z. Liu, K. Yanagi, K. Suenaga, H. Kataura, S. Iijima, *Nat. Nanotechnol.* **2**, 422 (2007).
- E. D. Boyes, P. L. Gai, *Ultramicroscopy* **67**, 219 (1997).
- P. L. Hansen et al., *Science* **295**, 2053 (2002).
- H. Yoshida, S. Takeda, *Phys. Rev. B* **72**, 195428 (2005).
- H. Yoshida, S. Takeda, T. Uchiyama, H. Kohno, Y. Homma, *Nano Lett.* **8**, 2082 (2008).
- R. Wang, P. A. Crozier, R. Sharma, J. B. Adams, *Nano Lett.* **8**, 962 (2008).
- P. L. Gai, E. D. Boyes, *Microsc. Res. Techn.* **72**, 153 (2009).
- T. W. Hansen, J. B. Wagner, R. E. Dunin-Borkowski, *Mater. Sci. Technol.* **26**, 1338 (2010).
- H. Yoshida et al., *Appl. Phys. Express* **4**, 065001 (2011).
- M. Haruta, N. Yamada, T. Kobayashi, S. Iijima, *J. Catal.* **115**, 301 (1989).
- M. Haruta, *Catal. Today* **36**, 153 (1997).
- S. D. Gardner et al., *Langmuir* **7**, 2135 (1991).
- F. Bocuzzi et al., *J. Catal.* **202**, 256 (2001).
- M. Haruta, *CATTECH* **6**, 102 (2002).
- M. Mavrikakis, P. Stoltze, J. K. Nørskov, *Catal. Lett.* **64**, 101 (2000).
- L. M. Molina, B. Hammer, *Phys. Rev. B* **69**, 155424 (2004).
- Materials and methods are available as supporting material on Science Online.
- Y. J. Feng, K. P. Bohnen, C. T. Chan, *Phys. Rev. B* **72**, 125401 (2005).
- T. Jacob, *Electrochim. Acta* **52**, 2229 (2007).
- H. W. Zandbergen, C.-W. Pao, D. J. Srolovitz, *Phys. Rev. Lett.* **98**, 036103 (2007).
- D. G. Fedak, N. A. Gjostein, *Surf. Sci.* **8**, 77 (1967).
- T. Sasaki et al., *J. Electron Microsc. (Tokyo)* **59** (suppl. 1), S7 (2010).
- K. P. McKenna, P. V. Sushko, A. L. Shluger, *J. Chem. Phys.* **126**, 154704 (2007).
- V. Fiorentini, M. Methfessel, M. Scheffler, *Phys. Rev. Lett.* **71**, 1051 (1993).
- V. Zólyomi, L. Vitos, S. K. Kwon, J. Kollár, *J. Phys. Condens. Matter* **21**, 095007 (2009).
- M. A. Van Hove et al., *Surf. Sci.* **103**, 189 (1981).
- K. Takayanagi, Y. Tanishiro, K. Yagi, K. Kobayashi, G. Honjo, *Surf. Sci.* **205**, 637 (1988).
- J. V. Barth, H. Brune, E. Ertl, R. J. Behm, *Phys. Rev. B* **42**, 9307 (1990).
- I. X. Green, W. Tang, M. Neurock, J. T. Yates Jr., *Science* **333**, 736 (2011).
- T. Fujitani, I. Nakamura, *Angew. Chem. Int. Ed.* **50**, 10144 (2011).

Acknowledgments: This study was supported by a Grant-in-Aid for Specially Promoted Research, grant 19001005, from the Ministry of Education, Culture, Sports, Science and Technology, Japan.

Supporting Online Material

www.sciencemag.org/cgi/content/full/335/6066/317/DC1
Materials and Methods
Figs. S1 to S6
Movies S1 to S3
References (38–53)

25 August 2011; accepted 22 November 2011
10.1126/science.1213194

Single-Molecule Lysozyme Dynamics Monitored by an Electronic Circuit

Yongki Choi,^{1,2*} Issa S. Moody,^{3*} Patrick C. Sims,² Steven R. Hunt,² Brad L. Corso,² Israel Perez,² Gregory A. Weiss,^{3,4†} Philip G. Collins^{1,2†}

Tethering a single lysozyme molecule to a carbon nanotube field-effect transistor produced a stable, high-bandwidth transducer for protein motion. Electronic monitoring during 10-minute periods extended well beyond the limitations of fluorescence techniques to uncover dynamic disorder within a single molecule and establish lysozyme as a processive enzyme. On average, 100 chemical bonds are processively hydrolyzed, at 15-hertz rates, before lysozyme returns to its nonproductive, 330-hertz hinge motion. Statistical analysis differentiated single-step hinge closure from enzyme opening, which requires two steps. Seven independent time scales governing lysozyme's activity were observed. The pH dependence of lysozyme activity arises not from changes to its processive kinetics but rather from increasing time spent in either nonproductive rapid motions or an inactive, closed conformation.

Numerous experimental techniques have been developed to probe the dynamics of single molecules (*1*) and overcome the

averaging effects of ensemble measurements. The most common experimental techniques use fluorescence, encoding molecular motions and/or

chemical reactions into a highly amplified photon flux that can be monitored and analyzed (*2, 3*). We show that single-molecule dynamics can be monitored by attaching the molecule of interest to a field-effect transistor (FET) device (Fig. 1A). Signal amplification was achieved by allowing the charged functionalities on the surface of the protein to electrostatically gate the underlying FET. By exploiting the low dimensionality and extreme local gate sensitivity of single-walled carbon nanotube (SWNT) FETs, molecular motions create changes in electrostatic potentials that can be converted into dynamically changing elec-

¹Institute for Surface and Interface Science, University of California Irvine, Irvine, CA 92697–2375, USA. ²Department of Physics and Astronomy, University of California Irvine, Irvine, CA 92697–4576, USA. ³Department of Molecular Biology and Biochemistry, University of California Irvine, Irvine, CA 92697–4292, USA. ⁴Department of Chemistry, University of California Irvine, Irvine, CA 92697–2025, USA.

*These authors contributed equally to this work.

†To whom correspondence should be addressed. E-mail: gweiss@uci.edu (G.A.W.); collinsp@uci.edu (P.G.C.)

tron fluxes. Such signals are similar to the photon fluxes in fluorescence experiments, but with advantageous bandwidth and shot noise limitations.

The general concept of electronic transduction by low-dimensional FETs has been explored with SWNT (4–7), silicon nanowire (8–11), nanocluster (12, 13), and graphene (14–16) devices. In most cases, slow changes in DC conductance have been suggestive of single-molecule detection, but the absence of dynamic responses undermined the general premise of high bandwidth detection. Recently, high-bandwidth dynamic transduction has been achieved in two single-molecule electronic architectures. In the first, DNA molecules threading through solid state pores have generated high-fidelity electronic signals that offer opportunities for DNA sequencing (15, 16). Separately, a more traditional FET architecture has leveraged amplification at SWNT point defects (17) to demonstrate kinetic binding and unbinding, both for molecules interacting directly with the defect site (18) and indirectly through an attached biomolecule (19, 20).

Here, we accomplished single-molecule transduction very similar to the work of Sorgenfrei *et al.* (19, 20), but using a noncovalent bioconjugation strategy that provides a high device-fabrication yield. Rather than introducing a defect, tailoring its chemistry, and then conjugating that site to the target molecule, our method used noncovalent immobilization based on pyrene linkers (21). The pyrenes adhered to SWNTs through pi-pi stacking, and could provide dilute anchor points for further derivatization of the surface (22–24). In our particular implementation, a thiol from a single cysteine variant of T4 lysozyme (S90C) was covalently conjugated to a pyrene-maleimide anchor site [see figs. S1 and S2 for characterization details (25)]. Similar site-specific conjugation of lysozyme to a solid surface has previously been shown to have no effect on the catalytic activity of lysozyme (26). Used here as a template for introducing the S90C substitution, the pseudo-wild-type mutant of lysozyme (C54T, C97A) has activity and stability identical to that of wild-type lysozyme (27). To minimize potential perturbations to the enzyme, lysozyme was not conjugated to a His₆ epitope, and was instead purified to >95% homogeneity by cation exchange followed by size exclusion chromatography. Standard biochemical conjugation protocols, followed by a strict rinsing protocol to minimize non-specific binding, readily produced lysozyme attachments with a mean separation of 0.5 μm along the SWNT. Matching this empirical spacing to the SWNT channel length is a surprisingly simple method that produced active single-molecule devices in 8 out of 10 fabrication attempts.

Atomic force microscopy (AFM) before functionalization and after completion of the measurements (Fig. 1B) confirmed the presence of a single attached lysozyme. Lysozyme is ~ 7 nm in size, which made it easily distinguishable when attached to a 1- to 2-nm-diameter SWNT [see fig. S3 for additional examples and height

profiles (25)]. In addition to microscopy, electrical characterization was performed at each fabrication stage. Figure 1C shows the gate dependence of the source-drain current $I(V_g)$ in a completed lysozyme device, measured with aqueous electrolyte (phosphate-buffered saline) in direct contact with the SWNT sidewall (28). The shape of this curve reflects SWNT band structure, contact resistance effects, and the role of scattering induced by the pyrenes and attached lysozyme; these issues are discussed in greater detail in the supporting online material (SOM) (25). In general, the coating technique added 1 to 2 megohms of series resistance to the SWNT conductor and shifts its $I(V_g)$ curve, in accord with previous reports (4, 29, 30). Finally, Fig. 1D displays the typical device response $I(t; V_g = 0)$ upon introduction of the lysozyme substrate, peptidoglycan (Sigma-Aldrich). A polysaccharide found in bacterial cell walls, peptidoglycan consists of *N*-acetylmuramate (NAM)-*N*-acetylglucosamine (NAG) repeating units, and lysozyme catalyzes the hydrolysis of its glycosidic bonds (31). Chemoresistive responses of this nature are widely reported for nanodevices, and SWNT conductance can be quite sensitive to slight environmental changes, even when they are not decorated with proteins (32–34).

The time-averaged, DC response depicted in Fig. 1D underlies the classification of such devices as chemical or biological “sensors.” How-

ever, analysis of the dynamic response, not the DC level, can provide insights into conformational changes of the attached single protein. The magnitude of $I(t)$ fluctuations increased immediately when peptidoglycan substrate was added, and, after one or more seconds of equilibration, these fluctuations developed into a two-level, random telegraph signal (RTS) that can be statistically analyzed. Control experiments probing bare SWNTs [fig. S4 (25)] and lysozyme-free, pyrene-coated SWNTs [fig. S5 (25)] revealed no RTS response to peptidoglycan substrate; further controls included 12 devices fabricated with either of two, inactive variants of lysozyme [fig. S6 (25)], none of which exhibited RTS signals. In every experiment, the presence or absence of RTS fluctuations was a reliable predictor of the simultaneous presence of the peptidoglycan substrate and a SWNT-bound, catalytically functional variant of lysozyme.

Figure 2A shows 30 s of raw data collected from a single lysozyme device, along with the time-varying mean computed with a 10-Hz digital filter. The lowest-frequency fluctuations had a $1/f$ spectral dependence and were indistinguishable from the noise incurred by a pristine SWNT in solution. Removing this slowly changing component, as shown in Fig. 2B, greatly simplified further analysis. The higher-frequency components were revealed to be a two-level RTS with a constant amplitude distribution but two dis-

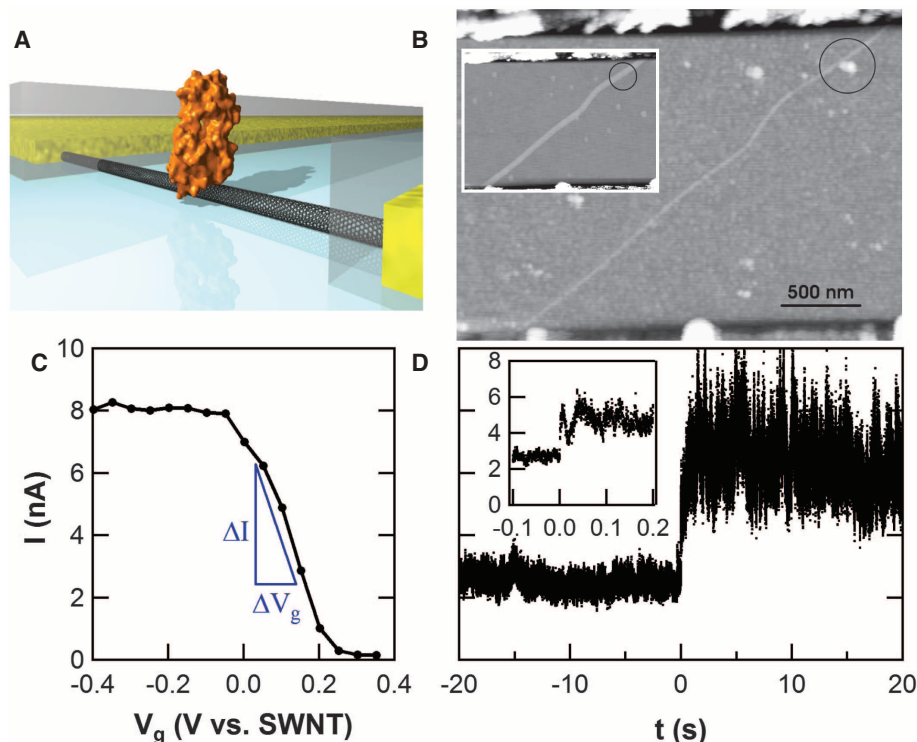


Fig. 1. (A) Schematic diagram of the single lysozyme being interrogated by a carbon nanocircuit. The partial poly(methyl methacrylate) coating is depicted in gray. (B) AFM topography of a SWNT FET before (inset) and after coating with the pyrene linker, lysozyme incubation, and washing to reduce nonspecific binding. The circle highlights the point of lysozyme attachment. (C) Response of current in a lysozyme device to electrolytic gating. (D) $I(t)$ measured in phosphate buffer, with peptidoglycan substrate (25 $\mu\text{g}/\text{ml}$) added to the solution at $t = 0$. The inset with a magnified time axis indicates a rapid response of < 50 ms (inset).

tinct RTS fluctuation rates. During some time periods, the RTS oscillated with a “fast” mean frequency of 316 Hz (Fig. 2C). At other times, the RTS oscillated with a “slow” mean frequency of 15.4 Hz (Fig. 2D). The data in Fig. 2C are colored to differentiate the two types of RTS response and to emphasize their typical durations. Both the fast and the slow RTS segments lasted many seconds, suggestive of a long-term, two-state “memory” that was independent of the RTS itself. Accurate determination of the mean duration of this memory effect ($\langle\tau_{\text{mem}}\rangle$) required that measurements be conducted for at least 600 s.

The sequences of fast and slow RTS oscillations could be separated for independent analysis. Each type of oscillation had a high and a low current state characterized by durations τ_{hi} and τ_{lo} , respectively. Probability distributions for τ_{hi} and τ_{lo} are shown for a sequence of fast RTS fluctuations in Fig. 3A and for slow RTS fluctuations in Fig. 3B; the color scheme corresponds to the data in Fig. 2, B to D. All four distributions were well fit by single exponential time constants for periods of analysis shorter than $\langle\tau_{\text{mem}}\rangle$. Analysis of much longer time periods resulted in biexponential distributions (Fig. 3, C and D) and reflected the presence in data sets extending over hundreds of seconds of many sequences of both fast and slow RTS fluctuations. However, the fast and slow rates were sufficiently different that they appeared as two distinguishable slopes in Fig. 3, C and D. As a guide, blue and green colors have been applied to portions of the distribution that correspond to the fast and slow fluctuations, respectively.

Figure 3, C and D, further provide a comparison of the probability distributions acquired at different pH values. The stability of the lysozyme devices allowed statistics to be accumulated for many minutes at each pH, all from the same attached enzyme. Figure 3C shows that

τ_{hi} was nearly independent over a pH range from 5 to 11; outside this pH range, lysozyme was no longer catalytically active (35–37). Figure 3D, however, shows that τ_{lo} is much faster at pH 7 than at pH 5 or 11. The pH dependence of τ_{lo} in the long-duration, slow-switching region of the histogram, being much longer than the other three time constants, dominates the time-averaged properties of the lysozyme molecule.

Two important physical parameters could be calculated from the mean values of $\langle\tau_{\text{lo}}\rangle$ and $\langle\tau_{\text{hi}}\rangle$. Their sum represents one complete oscillation and defines a mean turnover rate for the activity, $k = (\langle\tau_{\text{lo}}\rangle + \langle\tau_{\text{hi}}\rangle)^{-1}$. The calculation of enzymatic reaction rates from single-molecule data has been reviewed by Xie (38). The ratio of $\langle\tau_{\text{lo}}\rangle$ and $\langle\tau_{\text{hi}}\rangle$ also determines an energy separation, ΔE , between the two physical states responsible for the high and low $I(t)$ values. Boltzman statistics provides the relative thermodynamic probability of being in one state versus the other as $\Delta E = k_{\text{B}}T \ln(\langle\tau_{\text{hi}}\rangle / \langle\tau_{\text{lo}}\rangle)$. In total, we identified five independent parameters $\langle\tau_{\text{hi}}\rangle$, $\langle\tau_{\text{lo}}\rangle$, $\langle\tau_{\text{mem}}\rangle$, k , and ΔE , all of which change when the lysozyme switches from its fast RTS state to its slow RTS state. Table 1 summarizes these parameters and their pH dependence for a single lysozyme molecule.

Table 1 further lists the overall percentage of time spent in the fast or slow RTS states. This percentage is yet another independent parameter, being a nontrivial combination of the duration $\langle\tau_{\text{mem}}\rangle$ and the regularity with which each behavior is observed. At pH 7, $\langle\tau_{\text{mem}}\rangle$ was nearly equal for the fast and the slow RTS state, and the time in either state approached 50%. At non-neutral pH values, however, multiple changes skewed this balance. First, the number of inactive periods in which no switching was observed nearly doubled. This doubling, amplified by a modest increase in $\langle\tau_{\text{mem}}\rangle$ of the inactive duration, resulted in a rapidly growing proportion of total inactive time. Moreover, we observed that inactive periods always interrupted sequences of fast RTS oscillations and doubled the number of fast RTS intervals observed while only modestly decreasing their duration $\langle\tau_{\text{mem}}\rangle$. The increased time spent in inactive or fast RTS intervals both came at a cost to the percentage of time spent in the slow-switching RTS state, which was reduced to 19.7% at pH 11 and 15.7% at pH 5. This decrease occurred despite a substantial increase in $\langle\tau_{\text{mem}}\rangle$, which considered in isolation would indicate an improving stability of the slow RTS state. We further note that the fast and slow RTS oscillation rates k both decreased by 25 to 35% away from pH 7; because they both decreased proportionally, the k values only minimally contributed to the pH dependence of the time spent in the fast or slow RTS states.

The conductance signal of a single lysozyme device allowed us to directly determine multiple independent parameters, including seven independent time constants and their pH dependence, all without foreknowledge of the properties of either the enzyme or the SWNT. Out of 50 single-

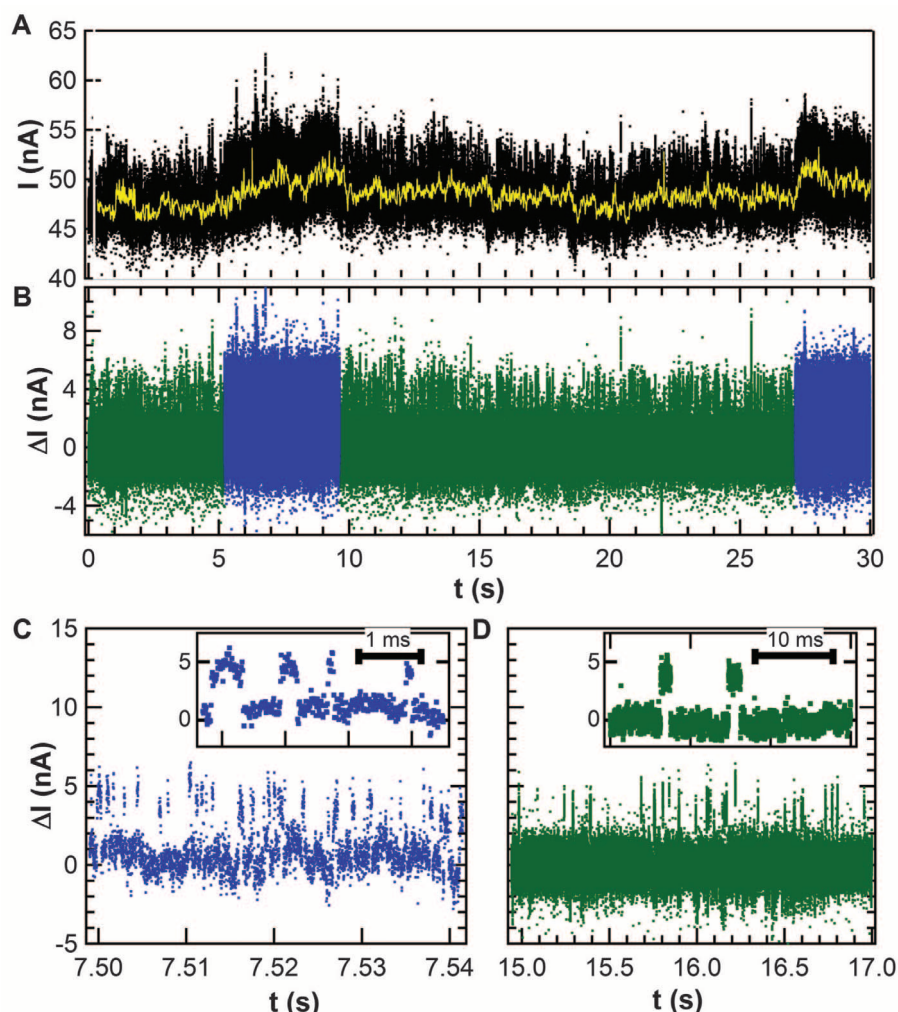


Fig. 2. (A) Long-duration $I(t)$ sequences exhibit dynamic noise on top of low-frequency fluctuations (yellow line) having a $1/f$ distribution. (B) Subtracting the meandering mean produces a filtered data set that clarifies the fluctuations as two-level, simplifies further analysis, and reveals that the two-level switching rates vary over 5- to 15-s periods. (C) The faster RTS oscillates about 300 times per second, whereas (D) the slower RTS oscillates 15 times per second. The insets show individual switching events for each case.

molecule devices, the presence of fast and slow RTS components was very reproducible, although there were variations in the numerical rates observed. For example, among seven lysozyme devices with high-quality signal-to-noise ratios, the rates of the slow RTS state at pH 7 varied from 10 to 50 Hz, with a mean $k = 24 \pm 15$ Hz. The rate of the fast RTS state varied from 127 to 461 Hz, with a mean $k = 284 \pm 127$ Hz.

Next, we applied these empirical observations to examine the mechanism and catalytic activity of lysozyme, through detailed analysis of the electronic device signal from lysozyme-tethered nanocircuits. As noted above and demonstrated in figs. S4 to S6 (25), the RTS can be ascribed to the presence of protein-substrate interactions. By comparing the $I(t)$ signal to lysozyme dynamics known from ensemble and single-molecule fluorescence resonance energy transfer (FRET) experiments (39–42), we can draw several parallels (e.g., lysozyme remains static in the absence of substrate). During substrate processing, lysozyme undergoes an 8 Å, hinge-like mechanical motion with two domains closing around the substrate (41–45). FRET observations reveal that this motion occurs at two different rates: a slow hinge oscillation of 20 to 90 Hz corresponding to enzymatic turnover events, or else a more rapid, nonproductive movement at 200 to 400 Hz (37, 41, 42).

These FRET rates are in excellent agreement with our fast RTS and slow RTS oscillations, and

the interconversion rate matches our $\langle\tau_{\text{mem}}\rangle$ values. Thus, we conclude that the two-level electronic signal is caused by the lysozyme hinge motion, with slow RTS oscillations resulting from the transduction of catalytic turnover events and fast RTS oscillations corresponding to lysozyme's nonproductive binding events. These kinetic rates obtained with surface-bound lysozyme might differ from bulk rates, but FRET measurements with freely diffusing lysozyme and surface-bound peptidoglycan (40) yield the same range of rates, suggesting that the consequences of tethering the lysozyme to a surface are minor.

The agreement demonstrates the equivalence of the lysozyme device data with FRET measurements, but in other ways the SWNT-lysozyme device data are more informative. Fluorophore bleaching and quenching limit the duration of FRET measurements on a single molecule and constrain the ability to observe slow conformational interconversions by FRET (37). The $I(t)$ measurement duration is not similarly limited, and the $\langle\tau_{\text{mem}}\rangle$ values in Table 1 represent hundreds of such events by the same single molecule. Using such long time scales, we directly observed the same molecule changing from its productive conformation to its unproductive one. We also obtained the average percentage time spent in the slow RTS state, which when multiplied by k gave a time-averaged, effective catalytic rate for the single molecule. By collecting a true average over many conformational

changes, this single-molecule rate approached the kinetics of an ensemble (Table 1). Furthermore, our $I(t)$ records extend this single-molecule insight to different pH conditions.

Measurements of a long-duration $\langle\tau_{\text{mem}}\rangle$ support a processive catalytic mechanism in which each lysozyme hydrolyzes on average 100 glycosidic bonds before dissociation and reassociation of the substrate (40). During the slow RTS state, no breaks in activity were observed, and so no product dissociation and substrate rebinding occurred. Furthermore, the substrate remained bound during both nonproductive fast RTS and the substrate-bound inactive state before returning to processing.

Our long-duration data sets also enable analysis of the statistical variance of the τ_{lo} and τ_{hi} values. Any single-step Poisson process has a statistical variance $\sigma^2 = \langle\tau\rangle^2$, and the normalized variance

$$r = \frac{\sigma^2}{\langle\tau\rangle^2} = \frac{\sum_i (\tau_i - \langle\tau\rangle)^2}{\sum_i \tau_i^2}$$

is a powerful tool in single-molecule studies for distinguishing hidden intermediate steps along a reaction coordinate (46–48). As shown in Table 2, analysis of individual τ_{lo} durations concludes that $r \approx 1$, indicating that the physical processes underlying the transition from I_{lo} to I_{hi} is in fact governed by a simple, single-step Poisson pro-

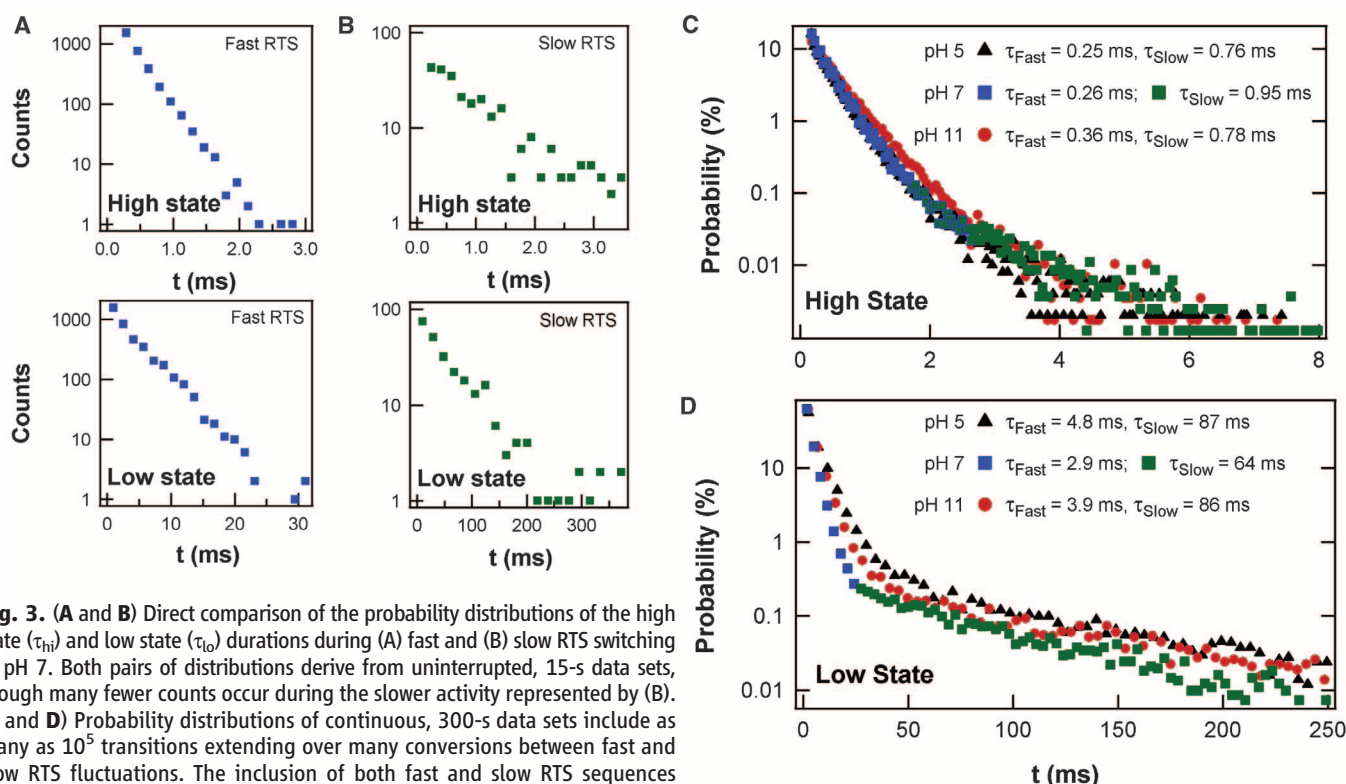


Fig. 3. (A and B) Direct comparison of the probability distributions of the high state (τ_{hi}) and low state (τ_{lo}) durations during (A) fast and (B) slow RTS switching at pH 7. Both pairs of distributions derive from uninterrupted, 15-s data sets, though many fewer counts occur during the slower activity represented by (B). (C and D) Probability distributions of continuous, 300-s data sets include as many as 10^5 transitions extending over many conversions between fast and slow RTS fluctuations. The inclusion of both fast and slow RTS sequences produces distinct, double-exponential distributions. Color has been applied to portions of the distributions in (A) to (D) to highlight correspondences with Fig. 2. Measurements at three different pH values show that the high-current state has almost no pH dependence (C). By contrast, the low-current state is at least 25% faster at pH 7 than at pH 5 or 11 (D).

cess. This conclusion remains true for both fast and slow RTS data at the different pH values tested, even though τ_{lo} differs by a factor of 20. By contrast, the physical process underlying the I_{hi} to I_{lo} transition has values of $r < 1$, indicating more complex processes. For example, n identical Poisson processes in succession will produce a distribution of durations τ that have a variance $r = 1/n$ (47, 49). Thus, lysozyme forms a closed conformation in a single step, but the transition back to its open configuration requires at least two steps. Although this finding is the same for both fast and slow RTS oscillations, the extra intermediate step required for opening is not necessarily the same in both cases. During processive sequences, the intermediate step could play a role in the catalysis and substrate turnover (50). During fast sequences of nonproductive binding, it might be involved in repositioning the substrate within the active site in an attempt to find a reactive bond for hydrolysis. Notably, the inactive state of lysozyme occurs when the enzyme closes around the substrate.

Finally, we conclude with a brief discussion of the device's transduction mechanism. The current step that occurs with each opening and closing of the lysozyme is surely not additional carriers flowing into the SWNT from the protein or the electrolyte. The entire current $I(t)$ flows from source to drain electrode, with variability

introduced by lysozyme's hinge-bending motion. The change from open to closed conformations moves lysozyme's charge residues (51). The surrounding electrolyte, which has a Debye length of 0.8 nm, screens most of the residues but not two, positively charged residues, Lys⁸³ and Arg¹¹⁹, that are located on the protein surface within 1.0 to 1.2 nm of the SWNT attachment site. Both of these residues lie close enough to the SWNT that their movement can electrostatically gate the channel conductance (52–54), according to the mechanism most often attributed to similar sensing experiments (6, 29, 55).

To test the applicability of this mechanism, we compared the transduction by different SWNT devices. Using the average slope dI/dV_g indicated in Fig. 1C, one can convert the RTS magnitude ΔI of a fluctuation into an effective swing in the applied gate, $\Delta V_g = \Delta I (dI/dV_g)^{-1}$. For the device in Fig. 2, for example, $\Delta I = 5$ nA and $\Delta V_g = 0.20$ V. Table S2 summarizes device properties of five semiconducting SWNT devices and five metallic ones, each having a different contact resistance and mean current (25). For these 10 devices, the switching magnitudes ΔI vary from 3 to 300%, but the calculated values ΔV_g are all narrowly clustered around $\Delta V_g = 0.19 \pm 0.02$ V. This reproducibility in ΔV_g demonstrates that the signal transduction mechanism is indeed electrostatic, with every protein-pyrene attachment modu-

lating its underlying SWNT channel with the same effective field. Metallic SWNTs display the smallest ΔI signals, but only because of their modest sensitivity to gating.

It would be a mistake, however, to infer that the lysozyme is gating the entire SWNT, or to convert ΔV_g into a carrier concentration. The pyrene-protein attachment site is a highly localized scattering center that, because the SWNT is quasi-one dimensional, can modulate the entire channel conductance. The resistance increase that occurs upon conjugation (table S2) is believed to be concentrated primarily at the attachment site, similar to the case of a defect being introduced (17–19). Scanning probe measurements prove these local scattering sites to be strongly gate-dependent conduction barriers (56). During substrate binding and release, the charged side chains of Lys⁸³ and Arg¹¹⁹ move by 1 to 2 Å relative to the SWNT (41–44, 57). This motion is sufficient to modulate the local chemical potential in the SWNT and account for our observed ΔI (56).

This nanocircuit architecture is complementary to more traditional fluorescence techniques, but with the advantages that fluorescent labels are not required, the transduction mechanism does not bleach, and electronic bandwidths extend temporal resolution into the single-microsecond regime. These advantages provide a framework for exploring dynamics of other molecules with charged functionalities.

Table 1. Lysozyme activity rates.

Parameter	pH 5	pH 7	pH 11
<i>Processing (slow)</i>			
$\langle\tau_{hi}\rangle$ (ms)	0.76 ± 0.05	0.95 ± 0.08	0.78 ± 0.09
$\langle\tau_{lo}\rangle$ (ms)	87 ± 3.0	64 ± 2.0	86 ± 3.0
ΔE (kcal/mol)	2.84	2.53	2.82
k (Hz)	11.4	15.4	11.5
$\langle\tau_{mem}\rangle$ (s)	9.3 ± 5.1	8.0 ± 3.0	12.0 ± 4.4
% time in state	16.3%	41.1%	21.1%
Time-averaged catalytic rate (Hz)	1.8	6.3	2.4
<i>Nonproductive (fast)</i>			
$\langle\tau_{hi}\rangle$ (ms)	0.25 ± 0.01	0.26 ± 0.01	0.36 ± 0.01
$\langle\tau_{lo}\rangle$ (ms)	4.80 ± 0.35	2.90 ± 0.10	3.90 ± 0.17
ΔE (kcal/mol)	1.77	1.45	1.43
k (Hz)	198	316	235
$\langle\tau_{mem}\rangle$ (s)	6.2 ± 4.0	7.9 ± 2.3	5.4 ± 1.8
% time in state	72.4%	52.1%	63.8%
<i>Inactive</i>			
$\langle\tau_{mem}\rangle$ (s)	0.83 ± 0.63	0.72 ± 0.25	0.96 ± 0.53
% time in state	11.3%	6.8%	15.0%

Table 2. Normalized variances of lysozyme rates.

Parameter	pH 5	pH 7	pH 11
<i>Processing (slow)</i>			
r_{hi}	0.68 ± 0.15	0.74 ± 0.12	0.60 ± 0.15
r_{lo}	1.00 ± 0.18	1.06 ± 0.15	1.11 ± 0.23
<i>Nonproductive (fast)</i>			
r_{hi}	0.48 ± 0.10	0.43 ± 0.06	0.61 ± 0.08
r_{lo}	0.97 ± 0.13	0.99 ± 0.09	1.00 ± 0.10

References and Notes

- S. A. Claridge, J. J. Schwartz, P. S. Weiss, *ACS Nano* **5**, 693 (2011).
- W. Min et al., *Acc. Chem. Res.* **38**, 923 (2005).
- R. Roy, S. Hohng, T. Ha, *Nat. Methods* **5**, 507 (2008).
- A. Star, J. C. P. Gabriel, K. Bradley, G. Gruner, *Nano Lett.* **3**, 459 (2003).
- A. Star et al., *Org. Lett.* **6**, 2089 (2004).
- K. Besteman, J. O. Lee, F. G. M. Wiertz, H. A. Heering, C. Dekker, *Nano Lett.* **3**, 727 (2003).
- G. Gruner, *Anal. Bioanal. Chem.* **384**, 322 (2006).
- Y. Cui, Q. Q. Wei, H. K. Park, C. M. Lieber, *Science* **293**, 1289 (2001).
- F. Patolsky et al., *Proc. Natl. Acad. Sci. U.S.A.* **101**, 14017 (2004).
- F. Patolsky et al., *Science* **313**, 1100 (2006).
- F. Patolsky, G. F. Zheng, C. M. Lieber, *Anal. Chem.* **78**, 4260 (2006).
- S. J. Park, T. A. Taton, C. A. Mirkin, *Science* **295**, 1503 (2002).
- Y. Xiao, F. Patolsky, E. Katz, J. F. Hainfeld, I. Willner, *Science* **299**, 1877 (2003).
- F. Schedin et al., *Nat. Mater.* **6**, 652 (2007).
- S. Huang et al., *Nat. Nano* **5**, 868 (2010).
- M. Tsutsui et al., *Sci. Rep.* **1**, 1 (2011).
- B. R. Goldsmith et al., *Science* **315**, 77 (2007).
- B. R. Goldsmith, J. G. Coroneus, A. A. Kane, G. A. Weiss, P. G. Collins, *Nano Lett.* **8**, 189 (2008).
- S. Sorgenfrei et al., *Nat. Nano* **6**, 126 (2011).
- S. Sorgenfrei, C. Y. Chiu, M. Johnston, C. Nuckolls, K. L. Shepard, *Nano Lett.* **11**, 3739 (2011).
- R. J. Chen, Y. Zhang, D. W. Wang, H. J. Dai, *J. Am. Chem. Soc.* **123**, 3838 (2001).
- A. B. Artyukhin, O. Bakajin, P. Stroeve, A. Noy, *Langmuir* **20**, 1442 (2004).
- Y. L. Zhao, L. B. Hu, J. F. Stoddart, G. Gruner, *Adv. Mater.* **20**, 1910 (2008).
- D. J. Perello et al., *J. Appl. Phys.* **105**, 124309 (2009).

25. Materials, methods, and additional control data are available as supporting material on Science Online.
26. K. L. Heredia *et al.*, *J. Am. Chem. Soc.* **127**, 16955 (2005).
27. M. Matsumura, B. W. Matthews, *Science* **243**, 792 (1989).
28. S. Rosenblatt *et al.*, *Nano Lett.* **2**, 869 (2002).
29. R. J. Chen *et al.*, *Proc. Natl. Acad. Sci. U.S.A.* **100**, 4984 (2003).
30. R. J. Chen *et al.*, *J. Am. Chem. Soc.* **126**, 1563 (2004).
31. S. O. Meroueh *et al.*, *Proc. Natl. Acad. Sci. U.S.A.* **103**, 4404 (2006).
32. J. Kong *et al.*, *Science* **287**, 622 (2000).
33. P. G. Collins, K. Bradley, M. Ishigami, A. Zettl, *Science* **287**, 1801 (2000).
34. T. Zhang, S. Mubeen, N. V. Myung, M. A. Deshusses, *Nanotechnology* **19**, 332001 (2008).
35. A. Tsugita, M. Inouye, E. Terzaghi, G. Streisin, *J. Biol. Chem.* **243**, 391 (1968).
36. H. B. Jensen, K. Kleppe, *Eur. J. Biochem.* **28**, 116 (1972).
37. Y. Chen, D. Hu, E. R. Vorpapel, H. P. Lu, *J. Phys. Chem. B* **107**, 7947 (2003).
38. S. N. Xie, *Single Molecules* **2**, 229 (2001).
39. H. P. Lu, L. Y. Xun, X. S. Xie, *Science* **282**, 1877 (1998).
40. D. Hu, H. P. Lu, *Biophys. J.* **87**, 656 (2004).
41. H. P. Lu, *Curr. Pharm. Biotechnol.* **5**, 261 (2004).
42. Y. Wang, H. P. Lu, *J. Phys. Chem. B* **114**, 6669 (2010).
43. G. E. Arnold, J. I. Manchester, B. D. Townsend, R. L. Ornstein, *J. Biomol. Struct. Dyn.* **12**, 457 (1994).
44. B. L. de Groot, S. Hayward, D. M. F. van Aalten, A. Amadei, H. J. C. Berendsen, *Proteins* **31**, 116 (1998).
45. H. R. Faber, B. W. Matthews, *Nature* **348**, 263 (1990).
46. K. Svoboda, P. P. Mitra, S. M. Block, *Proc. Natl. Acad. Sci. U.S.A.* **91**, 11782 (1994).
47. M. J. Schnitzer, S. M. Block, *Cold Spring Harb. Symp. Quant. Biol.* **60**, 793 (1995).
48. W. L. Xu, J. S. Kong, P. Chen, *J. Phys. Chem. C* **113**, 2393 (2009).
49. M. J. Schnitzer, S. M. Block, *Nature* **388**, 386 (1997).
50. G. Bhabha *et al.*, *Science* **332**, 234 (2011).
51. H. S. Mchaourab, K. J. Oh, C. J. Fang, W. L. Hubbell, *Biochemistry* **36**, 307 (1997).
52. E. Stern *et al.*, *Nano Lett.* **7**, 3405 (2007).
53. I. Heller *et al.*, *Nano Lett.* **8**, 591 (2008).
54. L. Prisbrey, G. Schneider, E. Minot, *J. Phys. Chem. B* **114**, 3330 (2010).
55. C. Li *et al.*, *J. Am. Chem. Soc.* **127**, 12484 (2005).
56. S. R. Hunt, D. Wan, V. R. Khalap, B. L. Corso, P. G. Collins, *Nano Lett.* **11**, 1055 (2011).
57. B. Brooks, M. Karplus, *Proc. Natl. Acad. Sci. U.S.A.* **82**, 4995 (1985).

Acknowledgments: This work was sponsored by the National Cancer Institute of the NIH (R01 CA133592-01 and T32CA009054) and NSF (DMR-0801271, ECCS-0802077, and the Center for Chemical Innovation on Chemistry at the Space-Time Limit CHE-0802913).

Supporting Online Material

www.sciencemag.org/cgi/content/full/335/6066/319/DC1
Materials and Methods
SOM Text
Figs. S1 to S6
Tables S1 and S2
References (58–74)

4 October 2011; accepted 5 December 2011
10.1126/science.1214824

Destruction of Sun-Grazing Comet C/2011 N3 (SOHO) Within the Low Solar Corona

C. J. Schrijver,^{1*} J. C. Brown,² K. Battams,³ P. Saint-Hilaire,⁴ W. Liu,^{1,5}
H. Hudson,^{2,4} W. D. Pesnell⁶

Observations of comets in Sun-grazing orbits that survive solar insolation long enough to penetrate into the Sun's inner corona provide information on the solar atmosphere and magnetic field as well as on the makeup of the comet. On 6 July 2011, the Solar Dynamics Observatory (SDO) observed the demise of comet C/2011 N3 (SOHO) within the low solar corona in five wavelength bands in the extreme ultraviolet (EUV). The comet penetrated to within 0.146 solar radius (~100,000 kilometers) of the solar surface before its EUV signal disappeared. Before that, material released into the coma—at first seen in absorption—formed a variable EUV-bright tail. During the final 10 minutes of observation by SDO's Atmospheric Imaging Assembly, $\sim 6 \times 10^8$ to 6×10^{10} grams of total mass was lost (corresponding to an effective nucleus diameter of ~10 to 50 meters), as estimated from the tail's deceleration due to interaction with the surrounding coronal material; the EUV absorption by the comet and the brightness of the tail suggest that the mass was at the high end of this range. These observations provide evidence that the nucleus had broken up into a family of fragments, resulting in accelerated sublimation in the Sun's intense radiation field.

During its 15 years of operation, the Large Angle and Spectrometric Coronagraph (LASCO) (*1*) onboard the Solar and Heliospheric Observatory (SOHO) has observed more than 2000 comets as they approached the

Sun. The population of Sun-grazing comets is dominated by the Kreutz group, which orbit to within one to two solar radii from the solar surface with orbital periods of 500 to 1000 years. More than 1400 of the comets seen by SOHO are members of this group, making it the largest known group of comets, likely originating from the breakup of a progenitor body as recently as 2500 years ago (*2*). Only the largest of the Kreutz-group comets [with diameters up to ~100 m (*2*)] have survived closest approach (perihelion), and SOHO never witnessed such a survival (*3*) until sungrazing comet Lovejoy emerged after its perihelion passage on the Sun's far side on 15–16 December 2011. Most of the destructions occurred well before perihelion, but some

occurred after the comet disappeared behind the occulting disk of the coronagraph. None could be followed into the Sun's lower atmosphere.

Here, we report on the observed destruction of comet C/2011 N3 (SOHO) within the solar atmosphere. We use EUV images obtained with the Atmospheric Imaging Assembly [AIA (*4*)] on the Solar Dynamics Observatory (SDO), which show different parts of the comet in absorption and in emission against the background EUV emission from the hot (1×10^6 to 3×10^6 K) outer solar atmosphere (the corona). AIA images the entire visible hemisphere of the Sun, including its off-disk corona, at 12-s intervals for sets of eight distinct (E)UV channels, at a resolution of ~1.2 arc sec, and with a high signal-to-noise ratio achieved with exposures no longer than 2.3 s. The comet's speed of ~600 km/s caused blurring in the AIA exposures that is only slightly in excess of the instrumental resolution. This detailed view of the solar corona enabled us to track the comet's tail and to determine the comet's orbit across much of the solar disk until it faded within 20 min of its first appearance. From Fig. 1 and movies S1 and S2, it appears that the comet's nucleus had fragmented.

The comet C/2011 N3 (SOHO) was first seen in AIA's 171 Å EUV channel while it was ~0.2 solar radii in projection off the solar limb, roughly at 5 July 2011 23:46 UTC (all times are given in UTC for photon arrival times at SDO, in geosynchronous orbit). The comet could be tracked in AIA images until approximately 6 July 2011 00:05:50, when it faded from all five EUV channels in which it was visible (131, 171, 193, 211, and 335 Å). Observations made by the Extreme-Ultraviolet Imager (EUVI) on the Solar-Terrestrial Relations Observatory [STEREO (*5*)] B show a faint signal of the comet high above the solar surface from its near-quadrature view relative to the Sun-Earth line (and thus against a background coronal emission weaker than from AIA's perspective by nearly a factor of 10) up to

¹Lockheed Martin Advanced Technology Center, 3251 Hanover Street, Palo Alto, CA 94304, USA. ²School of Physics and Astronomy, University of Glasgow, Glasgow G12 8QQ, UK. ³Naval Research Laboratory, Code 7663, 4555 Overlook Avenue, SW, Washington, DC 20375, USA. ⁴Space Sciences Laboratory, University of California, Berkeley, CA 94720, USA. ⁵W. W. Hansen Experimental Physics Laboratory, Stanford University, Stanford, CA 94305, USA. ⁶Code 671, NASA Goddard Space Flight Center, Greenbelt, MD 20771, USA.

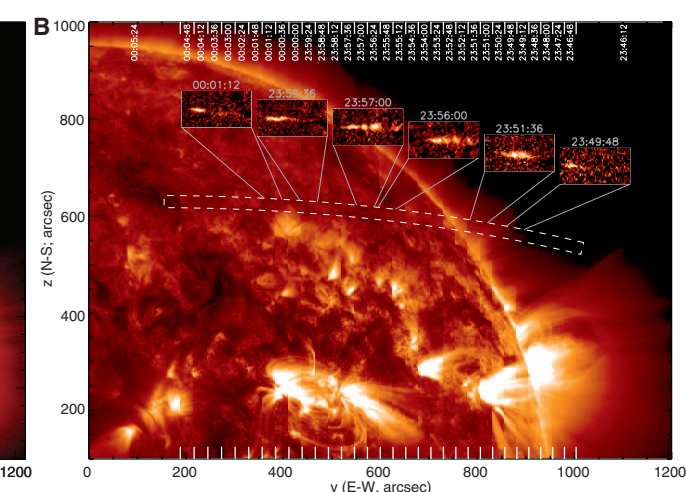
*To whom correspondence should be addressed. E-mail: schrijver@lmsal.com

Fig. 1. (A) EUV image of the solar corona (in AIA's 171 Å channel, most sensitive to coronal emission near 10^6 K) at 6 July 2011 00:00:01 UTC. Overlaid (in black) is the projected orbit of the comet C/2011 N3 between 5 July 2011 23:46 UTC and 6 July 2011 00:06 UTC. Orbital positions marked by plus signs were used as the three-dimensional starting points to trace the Sun's magnetic field through a potential field source surface (PFSS) approximation (9); all of the traced fields lead to the solar surface in both directions, showing that the comet in this time interval moved through the closed-field corona rather than through the solar wind. **(B)** Composite AIA 171 Å images in which vertical strips (marked on the axes, with UTC time stamps) are concatenated as the comet (moving within the dashed outline) is within

00:11:28 UTC, but the comet is not visible in the next image at 00:12:43 UTC. The AIA observations during this later phase of STEREO observations have intensity upper limits at least an order of magnitude lower than the average intensity during AIA visibility (see below), so that the comet's mass loss in that late phase observed by STEREO was probably much smaller than when it was visible to AIA.

The trajectory of the comet (Fig. 2) determined from our observations agrees well with the orbit determined from observations with the SOHO/LASCO and STEREO/SECCHI (Sun Earth Connection Coronal and Heliospheric Investigation) (5) coronagraphs. The match of the projected orbit is better than ~ 3 arc sec and ~ 15 s, implying that there was no significant deceleration of the nuclear body or major fragments within the solar corona (consistent with the estimate of the cross section) (6, 7). This close match gives us confidence that we know the height of the comet's trajectory above the solar surface to within a few thousand kilometers. The orbit of the comet (8), determined by the IAU Minor Planet Center, shows an orbital perihelion time of 6 July 2011 6.00232 TT (corresponding to a photon-arrival time at SDO of 6 July 2011 00:11:11 UTC) and an orbital perihelion parameter of $q = 0.0052986$ (corresponding to a height above the solar surface of 97,200 km).

After manually tracing the comet's bright tail (extending over $\sim 10^4$ km) in the AIA images, we slid a box along a parabolic fit to the traced positions to determine the intensity variations during the comet's final phase as it moved through the solar corona (Fig. 3). The light curves in all but one of the coronal emission lines (i.e., excluding the low-signal 94 Å channel as well as the He⁺ 304 Å channel with a high background from the low solar atmosphere) show that the total signal varied on a 100-s time scale by up to a factor of ~ 4 . The various wavelengths show



that strip (see movie S1 for a sequence of unaltered images). Insets (with UTC times) show intensity differences for images containing the comet and images taken 36 s earlier, thus removing the background corona. Note that the EUV-bright tail does not align with the field lines. In both panels, 1 arc sec \approx 740 km.

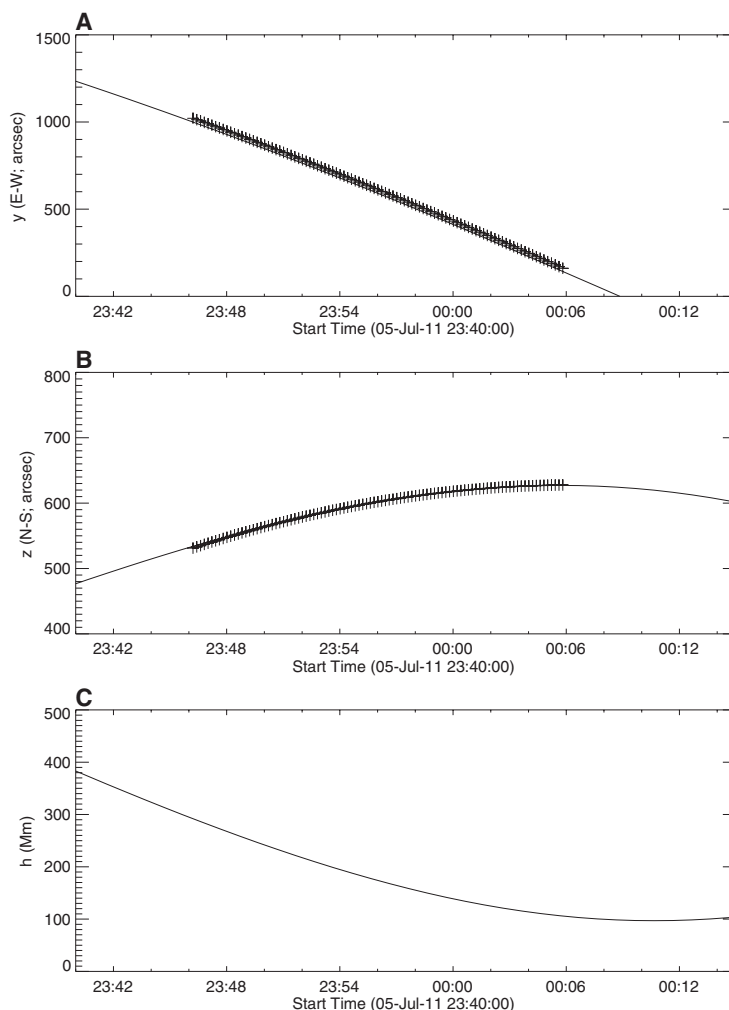


Fig. 2. (A to C) Orbital details of the comet nucleus derived from the orbital parameters for the comet from the Minor Planet Center (16), converted to photon-arrival times at Earth in UTC [(A) and (B)] and the corresponding height above the solar surface (C). The y coordinate is positive to solar west and the z coordinate positive to solar north; 1 arc sec \approx 740 km. The plus signs show the tracked positions in the SDO/AIA images (Fig. 1) interpolated from a smooth parabolic fit to the original measurements.

near-synchronous changes, implying that this variability was real. Variations in the solar magnetic field at the height of the comet above the surface are expected to be small. A model potential magnetic field (9) (Fig. 1A) shows closed fields that increase in field strength from 0.4 to 0.8 G along

the trajectory marked in the figure. The observed variability likely reflects varying rates of sublimation of the comet nucleus, possibly owing to a combination of rotation, heterogeneous nuclear structure, and sequential fragmentation events; we see evidence in the images of several fragments

(Fig. 1B) and have indirect evidence for multiple fragments (7). The positive and negative intensity variations in the He II 304 Å channel partly reflect the high background emission, resulting in a lower signal-to-noise ratio, possibly compounded by opacity effects in the cometary tail.

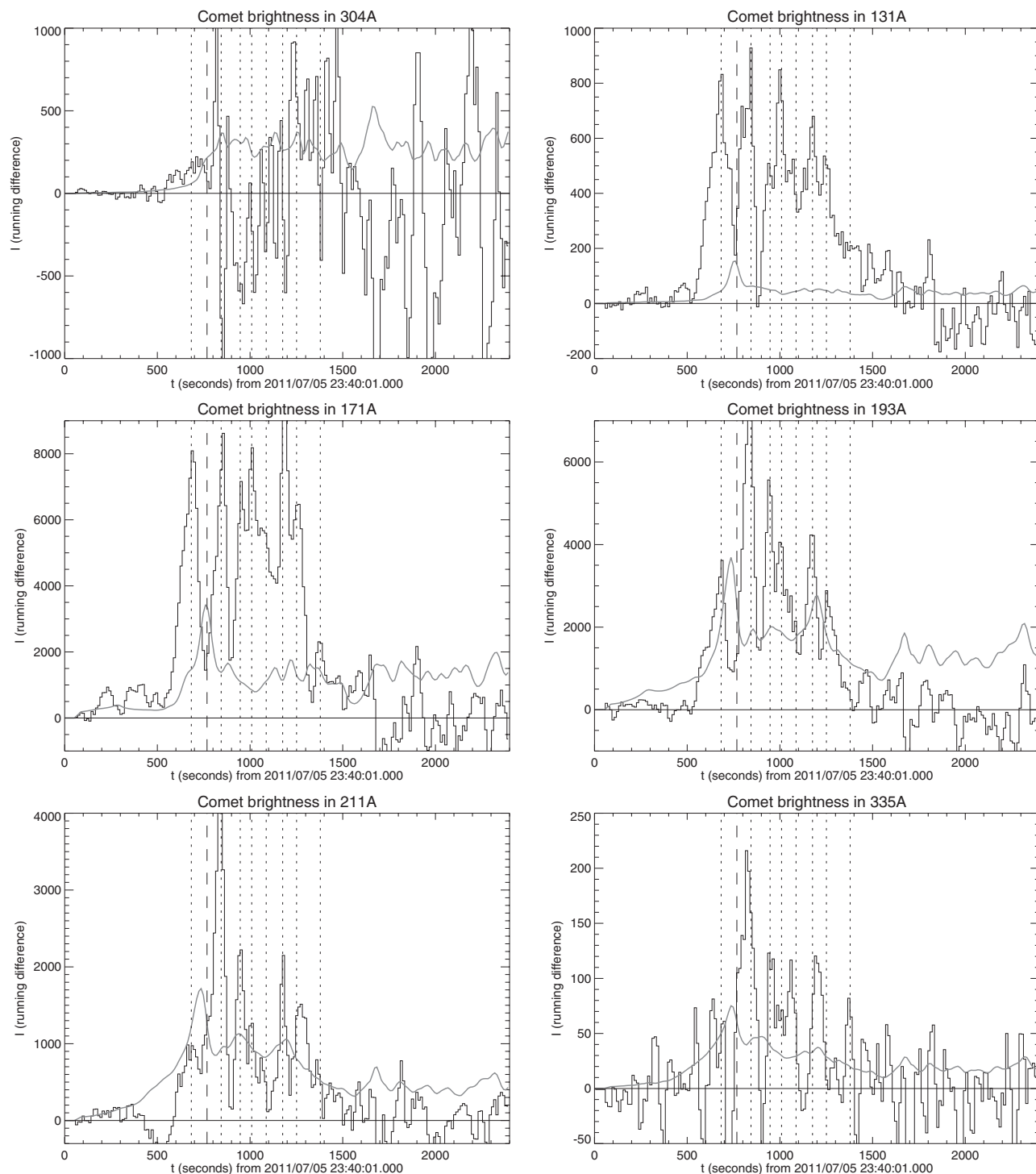


Fig. 3. Brightness I as a function of time for six EUV channels of SDO/AIA for the comet (304, 131, 171, 193, 211, and 335 Å) after subtraction of the coronal background brightness I_b in the same locations 36 s earlier. The brightness is measured by summing over a box 30 pixels wide by 15 pixels high (or 13,300 km by 6700 km) that moves with the comet,

starting behind the absorption feature of the inner, dense part of the coma (at $x = 0$ in Fig. 4). Dotted lines mark times of peak comet brightness in 171 Å; dashed lines mark the edge of the Sun. For comparison, the scaled coronal background brightness, $I_b/100$, is shown by the gray curves.

The AIA observations show an absorption signature in a region just ahead of the tail's EUV emission. This feature, seen most strongly when the comet crossed the solar limb, reveals the densest inner part of the comet's coma. A series of space-time diagrams (Fig. 4) (7) show that this region was typically 7 arc sec (~ 5000 km) ahead of the EUV-bright tail. The diameter of the coma's absorption feature as seen in the 193 Å channel at the half-intensity point is $d_{193} \approx 1700 \pm 300$ km, which exceeds the resolution of $\ell_{193} = 1000$ km for the 193 Å AIA channel derived from ray-tracing modeling (10); the observed radius of the coma's dense inner region can thus be estimated from the combined effect of intrinsic width and instrumental resolution through $d_{193}^2 - \ell_{193}^2$ to be 1400 ± 600 km. This value is comparable to the motion blurring during the 2.3-s exposure, so it constitutes an upper limit. If the coma were completely opaque, the intensity contrast of $\sim 1\%$ against the background corona (with most of the corona behind it) would require a radius of ~ 50 km; hence, we can set a range for the coma's radius $r_{\text{coma}} = 50$ to 700 km.

During the ~ 600 s when the tail was brightest in the EUV, the time-distance diagram (Fig. 4) shows a series of arches behind the nucleus. We

interpret these as tracks of variable amounts of released material decelerating behind the nucleus as that material interacted with the hot ($\sim 10^6$ K) coronal plasma, with relative kinetic energy of 2 keV per nucleon. The inertia of the sublimated and subsequently ionized material must therefore have sufficed, at least within much of the EUV-bright tail, to largely outweigh the Lorentz force induced by motion through the coronal field (distorting the magnetic field, rather than allowing that field to determine the plasma motion). The decelerated tail was deflected only weakly to the north as the comet traveled across the solar disk (7).

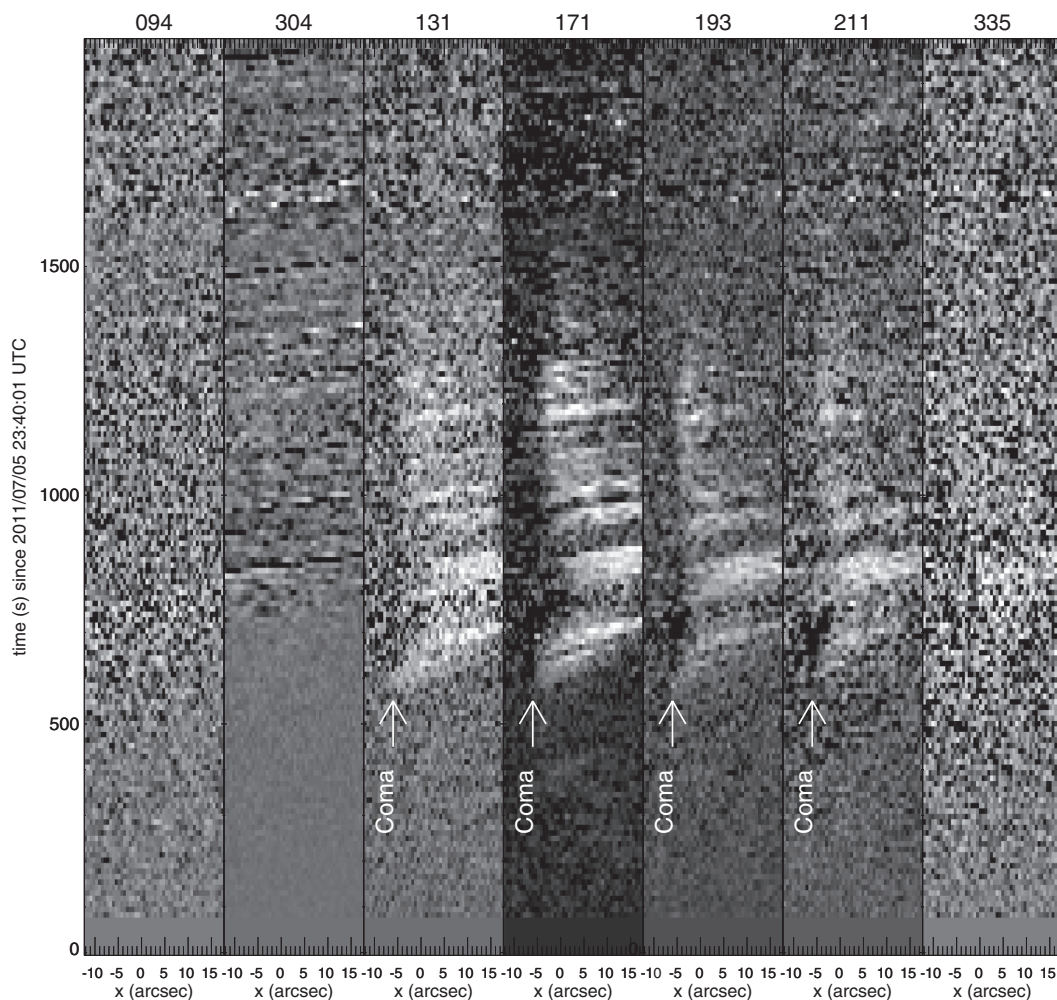
We were able to measure the deceleration of the material lost from the nucleus only because the sublimation rate was highly variable, producing discrete episodes of enhanced mass loss. The variability in the tail's brightness was not caused by density contrasts in the background corona; the coronal emission just before the time when the nucleus passed over a given location exhibited much smaller variations. Because we know the comet's orbital trajectory and speed, know the time scale for the deceleration of the tail, and have an approximate knowledge of the plasma density in the quiet-Sun corona (11) along that trajectory, we can estimate the mass

loss rate and total mass lost during the visibility in the AIA images (7): 10^6 to 10^8 g/s and 6×10^8 to 6×10^{10} g, respectively.

The mass loss rate estimated from the tail deceleration can be compared to the mass lost by insolation during the same period (12) on the basis of the relationship between heat input and the latent heat of vaporization of cometary materials, the specific heat of sublimation, and the mean mass density of the nucleus (7). This comparison suggests that the comet's nuclear material was contained in a number of fragments, because a single nuclear body would have had too small a cross section to capture the insolation energy needed to sublimate the total mass in the available time. About one to two dozen of these fragments must have been larger than 10 m in diameter. We see direct observational evidence for fragmentation in the AIA observations (7).

Deexcitation after ionizing collisions should be the main mechanism by which the tail of C/2011 N3 becomes visible in the EUV. A comet moving at ~ 600 km/s through the solar corona releases grains, molecules, and atoms with energies of 2 keV per nucleon in the coronal rest frame. The deceleration of these particles through collisions with the coronal plasma excites and

Fig. 4. Intensity profiles along east-west cuts (9 AIA pixels or 3600 km high) comoving with the comet, stacked into a grayscale display of time versus distance (1 arc sec \approx 740 km, with arbitrary offset). AIA channel identifications (mean wavelengths, in angstroms) are shown at the top. The 131, 171, 193, and 211 Å channels exhibit bright arcs that reveal the deceleration of the material in the comet's tail behind the nucleus. A very faint arc in the 171 Å channels at $t \approx 400$ s (black arrow) suggests that this process already occurs there (at $h \approx 300,000$ km; Fig. 2) but is much more visible later on, closer to the insulating solar surface.



ionizes the cometary material, both by direct collisional excitation and by charge-exchange collisions. For comets far from the Sun, charge-exchange collisions of the cometary material with the solar wind flowing by at relative speeds of ~300 to 800 km/s excite electrons into highly excited states of solar-wind minor ions that subsequently emit EUV or even x-ray photons as they transition to lower-energy states (13, 14).

However, one possible explanation for the EUV-bright tail of C/2011 N3, consistent with our mass estimate from the tail's time-distance behavior (7), is that the ionization and excitation states of the material lost from the nuclear bodies are equilibrated with those of the surrounding coronal plasma. One important aspect in estimating the tail's EUV brightness in the AIA observations is that the comet released a mix of elements very rich in heavy ions relative to the mixture of the solar plasma, which is strongly dominated by hydrogen and helium. Efficient heat conduction into this metal-rich mixture could thus explain why the contrast of tail to coronal brightness is comparable in all of the coronal AIA channels (see Fig. 3). Other emission mechanisms, including collisional ionization (direct or charge-exchange) and emis-

sion from elements other than iron, might also be important; we merely argue that at least one mechanism is consistent with the observed tail brightness for the mass estimate based on the observed tail deceleration, provided it lies near the high end of that range (7).

Prior to these observations, cometary masses were generally derived from light curves during their orbits, assumed albedos, and estimated mass densities, or by direct imaging for the few comets that have been visited by spacecraft. SOHO/LASCO observes a Sun-grazing comet roughly once every 3 days, and although most fade well before perihelion, several per year should reach the solar corona and be available for further study of cometary properties, as well as probes of the solar corona.

References and Notes

1. G. E. Brueckner *et al.*, *Sol. Phys.* **162**, 357 (1995).
2. M. M. Knight *et al.*, *Astron. J.* **139**, 926 (2010).
3. M. Iseli, M. Küppers, W. Benz, P. Bochsler, *Icarus* **155**, 350 (2002).
4. J. R. Lemen *et al.*, *Sol. Phys.* 10.1007/s11207-011-9776-8 (2011).
5. R. A. Howard *et al.*, *Space Sci. Rev.* **136**, 67 (2008).
6. J. C. Brown, H. E. Potts, L. J. Porter, G. le Chat, <http://arxiv.org/abs/1107.1857> (2011).
7. See supporting material on Science Online.

8. www.minorplanetcenter.net/mpec/K11/K11N41.html; MPEC 2011-N41: COMET C/2011 N3 (SOHO).
9. C. J. Schrijver, M. L. DeRosa, *Sol. Phys.* **212**, 165 (2003).
10. P. Boerner *et al.*, *Sol. Phys.* 10.1007/s11207-011-9804-8 (2011).
11. M. Guhathakurta, R. R. Fisher, R. C. Alcock, *Astrophys. J.* **414**, L145 (1993).
12. At heights above 0.01 solar radii, collisional heating and ablative mass loss by atmospheric impacts are negligible (6).
13. T. E. Cravens, *Science* **296**, 1042 (2002).
14. C. M. Lisse, T. E. Cravens, K. Dennerl, in *Comets II*, M. C. Festou, H. U. Keller, H. A. Weaver, Eds. (Univ. of Arizona Press, Tucson, AZ, 2004), pp. 631–643.

Acknowledgments: Supported by NASA SDO/AIA contract NNG04EA00C to Lockheed Martin's Solar and Astrophysics Laboratory. The SDO/AIA data can be accessed at <http://aia.lmsal.com>; the STEREO/SECCHI data can be accessed at http://stereo-ssc.nascom.nasa.gov/data/ins_data/secchi. We thank the four reviewers and the editor for their help in improving the manuscript.

Supporting Online Material

www.sciencemag.org/cgi/content/full/335/6066/324/DC1
Materials and Methods
Fig. S1
References (15–21)
Movies S1 and S2

25 July 2011; accepted 22 November 2011
10.1126/science.1211688

Polymerase Exchange During Okazaki Fragment Synthesis Observed in Living Cells

Giuseppe Lia,^{1,2,3*} Bénédicte Michel,^{1,2} Jean-François Allemand^{3,4,5*}

DNA replication machineries have been studied extensively, but the kinetics of action of their components remains largely unknown. We report a study of DNA synthesis during replication in living *Escherichia coli* cells. Using single-molecule microscopy, we observed repetitive fluorescence bursts of single polymerase IIIs (Pol IIIs), indicating polymerase exchange at the replication fork. Fluctuations in the amount of DNA-bound single-stranded DNA-binding protein (SSB) reflect different speeds for the leading- and lagging-strand DNA polymerases. Coincidence analyses of Pol III and SSB fluctuations show that they correspond to the lagging-strand synthesis and suggest the use of a new Pol III for each Okazaki fragment. Based on exchanges involving two Pol IIIs, we propose that the third polymerase in the replisome is involved in lagging-strand synthesis.

DNA replication is carried out in all organisms by a multiprotein complex called the replisome. Owing to the high level of functional similarity of replication proteins in

different species from bacteria and phages to eukaryotes, bacterial replication is used as a model system. In *Escherichia coli*, the replisome consists of 13 proteins that participate in the synchronized DNA synthesis of the leading strand (synthesized continuously) and the lagging strand, made discontinuously as ~1- to 2-kb Okazaki fragments (OF) (1–10). The DNA polymerase III holoenzyme (hPol III) is composed of a clamp loader that interacts with three copies of the core polymerase Pol III, two of which act on the two DNA strands (Pol_{lead} and Pol_{lag}) (11, 12). Pol III contains a catalytic subunit, DnaE, and a proofreading subunit, DnaQ. Active Pol IIIs are stabilized on DNA by interactions with the sliding clamp. The DNA helicase DnaB unwinds the

template DNA by progressing on the lagging-strand template; it interacts with the hPol III through the clamp loader subunit τ and with a primase that synthesizes RNA primers for each OF. Single-stranded (ss) DNA-binding proteins (SSB) bind the exposed ssDNA on the lagging-strand template.

A single fluorescent protein can be detected in living *E. coli* cells when its diffusion is reduced (13–15). The replication fluorescent proteins will diffuse slowly enough to be detected only when bound to the replisome. We implemented a version of the detection by localization technique (13–15) with stroboscopic illumination. This limited illumination duration reduces photobleaching, allowing us to probe the dynamics of Pol III in vivo for long periods. We used a dual view system to measure the simultaneous binding times of two differentially labeled replisome components. We expressed fluorescent fusions of the DNA polymerase DnaE, the proofreading subunit DnaQ, and the SSB protein, labeled with either a yellow [enhanced yellow fluorescent protein (eYFP) or yellow fluorescent protein for energy transfer (Ypet)] or red fluorescent protein (mCherry). *dnaQ*-Ypet and *dnaE*-eYFP were fully functional under our experimental conditions (16) [supporting online material (SOM)]. *ssb*-mCherry and Ypet fusions were functional only in the presence of the wild-type (wt) *ssb* gene, but 20 to 50% of SSB proteins could be labeled, enough to ensure the labeling of most tetramers without causing any defect in cell growth (figs. S1 and S3 and tables S1 and S2).

As expected, measures of the relative position of DnaQ-Ypet and DnaE-eYFP in growing

¹CNRS, Centre de Génétique Moléculaire, UPR3404, Gif-sur-Yvette F-91198, France. ²Université Paris-Sud, Orsay F-91405, France. ³Laboratoire de Physique Statistique, Ecole Normale Supérieure (ENS), UMR 8550 CNRS, Universités Pierre et Marie Curie and Paris Diderot, Département de Physique, 24 rue Lhomond, 75231 Paris Cedex 05, France. ⁴Département de Biologie, Institut de Biologie de l'Ecole Normale Supérieure, UMR 8542 CNRS, 46 rue d'Ulm, 75231 Paris Cedex 05, France. ⁵Institut Universitaire de France (IUF), 103, bd Saint-Michel 75005 Paris, France.

*To whom correspondence should be addressed. E-mail: allemand@lps.ens.fr (J.-F.A.); lia@cgm.cnrs-gif.fr (G.L.)

cells showed cells with one spot in the center and cells with two spots near the $\frac{1}{4}$ and $\frac{3}{4}$ positions along the cell length (Fig. 1A and fig. S17A). In the latter, each spot is known to correspond to an individual replisome (11, 16). The fluorescence intensity of a spot is proportional to the number of localized fluorophores it contains (11). Consistent with the finding of Reyes-Lamothe *et al.*

(11), we observed initial intensity levels corresponding to three DnaQ-YPet and three DnaE-eYFP proteins per spot, hence per replisome (fig. S17, B and C), as confirmed by the observation of three photobleaching steps (Fig. 1C and figs. S11 and S12). Figure 1B shows a representative temporal montage of DnaQ-YPet fluorescence in a single replisome (frame rate of 5 images per s

and 20-ms integration time); such a montage can be converted into a temporal trace and analyzed (SOM, Fig. 1C, and figs. S11 and S12 obtained with DnaE-eYFP). We analyzed 73% of the DnaQ-YPet and 90% of the DnaE-eYFP traces. They correspond to all the traces (fig. S32) starting from a fluorescence level corresponding to three DnaQ-YPet (or DnaE-eYFP) proteins, or

Fig. 1. Polymerase exchange dynamics. **(A)** Representative images of a cluster of bacteria showing the localization of DnaQ-YPet protein within individual replisomes. **(B)** Representative example of a montage showing the localization of DnaQ-YPet over time. Each localization spot is imaged at a frame rate of 200 ms. **(C)** Representative example of an integrated fluorescence trace of DnaQ-YPet localization at an individual replisome (a.u., arbitrary units). The trace was converted into equivalent YPet molecules. **(D)** Tail distributions of time on (1069 events) and time off (1193 events) of individual DnaQ-YPet molecules. The time on distribution was fitted with a linear combination of two exponential functions [orange line, $A1 \cdot \exp(-x/\tau_1) + A2 \cdot \exp(-x/\tau_2)$, $A1 = 0.42 \pm 0.04$ (SE), $A2 = 0.58 \pm 0.05$, $\chi^2/\text{df} = 1.40$]. Average decay times (τ_{on}) are $\tau_{1\text{on}} = 230 \pm 40$ ms and $\tau_{2\text{on}} = 926 \pm 48$ ms. $\tau_{1\text{on}}$ was attributed to YPet photophysics, whereas $\tau_{2\text{on}}$ corresponds to time bound to DNA. The time off distribution was fitted with a linear combination of two exponential functions (red line, $A1 = 0.78 \pm 0.02$, $A2 = 0.36 \pm 0.05$, $\chi^2/\text{df} = 1.36$). Average decay times (τ_{off}) are $\tau_{1\text{off}} = 984 \pm 34$ ms and $\tau_{2\text{off}} = 6.8 \pm 0.4$ s. $\tau_{2\text{off}}$ was attributed to the competition time for binding bleached and unbleached proteins, whereas $\tau_{1\text{off}}$ corresponds to DNA unbound time. Error bars are statistical errors.

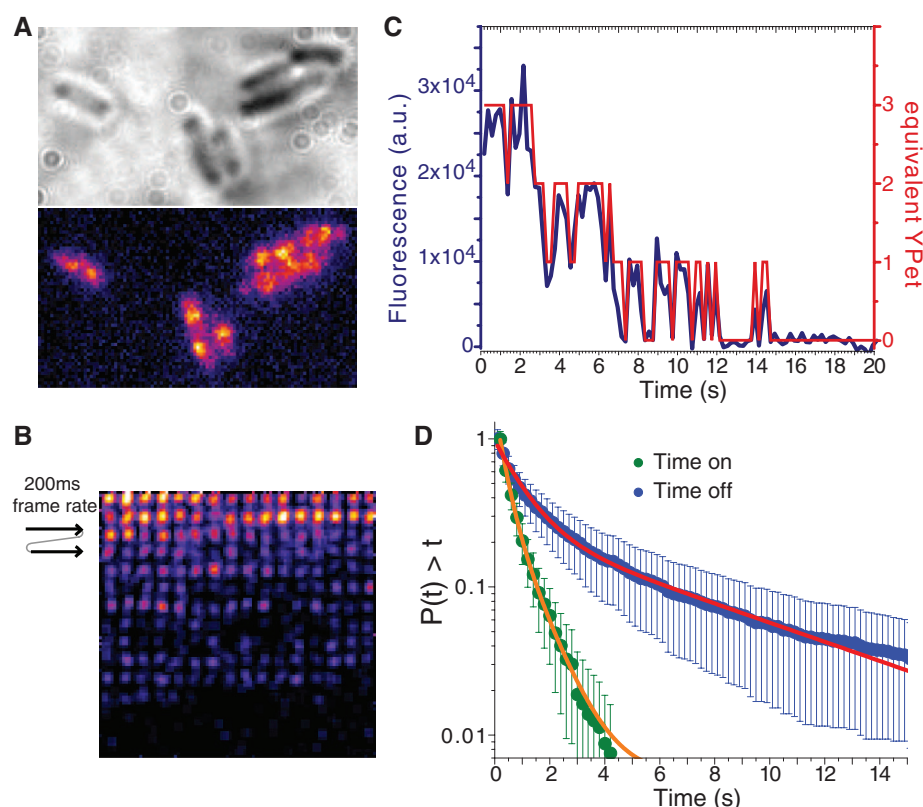
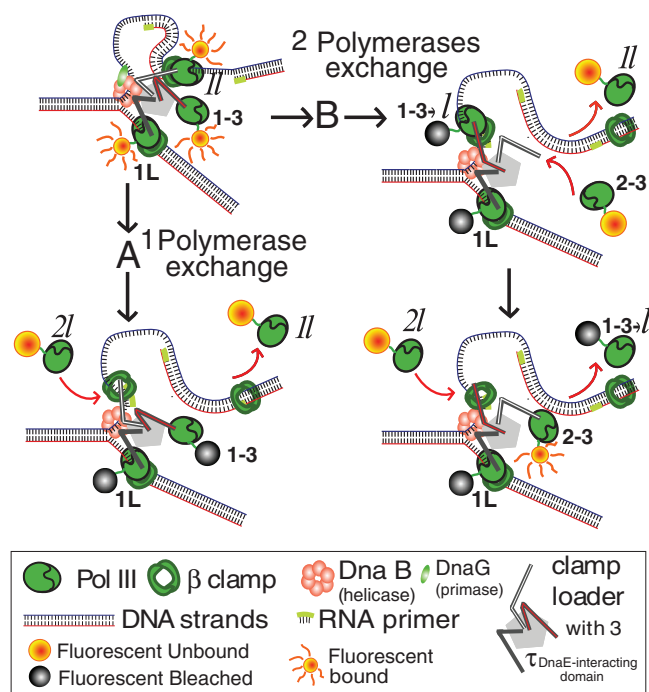


Fig. 2. Models of lagging strand synthesis. At the onset of the experiment, the three Pol III in the replisome can be detected: Pol_{lead} (1L), Pol_{lag} (1I), and the third Pol III (1-3). Each Pol III interacts with a τ (DnaX) subunit of the clamp loader complex through a domain represented here by a colored line: dark gray (τ -Pol_{lead}), white (τ -Pol_{lag}), or red (τ -third Pol). If no polymerase was exchanged, as previously accepted, after a photobleaching phase the replisome would not recover a fluorescent signal. This was not observed. (Pathway A) The one polymerase exchange model. Within about 3 to 6 s, Pol_{lead} (1L) and the third Pol III (1-3) are photobleached, but binding of new Pol_{lag} from the pool can be detected (2I), which replaces the previous Pol_{lag} in the replisome. (Pathway B) The two polymerases exchange model. If the third, photobleached, Pol III (labeled 1-3) is used as Pol_{lag} (B, first step), the 0→1 transition reflects the binding of a new fluorescent Pol III to the empty τ but not to DNA. This new fluorescent Pol III is denoted 2-3 on the figure, because it is a new “third” (not DNA-bound) Pol III; it binds to the available τ subunit, previously bound to Pol_{lag}. At the end of this OF synthesis (B, second step), the photobleached Pol_{lag} leaves DNA and is replaced by a fluorescent protein from the pool (2I), resulting in a 1→2 transition. The third Pol III (1-3) is shown here as binding to the lagging strand template at the OF primer (B, first step), but similar 0→1→2 transitions are expected after the replacement of Pol_{lag} (1I) by the third Pol in the course of an OF synthesis. Interruption of OF synthesis before the encounter with the previous primer is predicted by the signaling release model (7, 17, 21). Our results are also compatible with models in which 0→1→2 transitions would correspond to Pol_{lead} exchange with a Pol from the pool, as observed in phages (17, 18), but we do not favor this model.



starting at two but fluctuating up to three, followed by three steps of photobleaching (figs. S30 and S31).
As can be seen in Fig. 1C and figs. S11 and S12, for the two Pol III subunits none of the three steps displayed a stable plateau. In contrast, such fluctuations were not observed with the τ subunit,

encoded by the *dnaX* gene, to which Pol III is attached (figs. S18 and S19) or when replication was blocked by inactivating the replicative helicase DnaB (*dnaBts* mutant at 42°C, fig. S21). Although the transitions from 2→1 and 1→0 could be interpreted as unbinding or photobleaching, the transitions 0→1 or 1→2 can unambiguously

ly be interpreted as the binding of a new single fluorescent protein (SOM section V), rendered detectable by its interaction with the replisome. Therefore, replication models in which no polymerase is exchanged can be excluded. All the analyzed replisome traces displayed bursts indicating that replication involves one polymerase

Fig. 3. SSB fluorescence intensity fluctuations. **(A)** Representative images showing SSB-mCherry interacting with individual replisomes. **(B)** Representative montage showing the localization of SSB-mCherry in one individual replisome over time. Each localization spot is taken with a frame rate of 200 ms. **(C)** Representative integrated fluorescence level trace of SSB-mCherry showing fluorescence bursts. **(D)** Zoom of two fluorescence bursts. **(E)** SSB Max-to-Max and min-to-min time delay distributions (3102 bursts analyzed). **(F)** τ_{fall} and τ_{rise} tail distributions. The two distributions show a single exponential decay. Exponential fit [$A1 \cdot \exp(-x/\tau1)$, red and blue lines] gives as mean time 850 ± 10 ms for τ_{rise} ($A1 = 1.01 \pm 0.01$, $\chi^2/\text{df} = 0.92$) and 920 ± 40 ms for τ_{fall} ($A1 = 0.99 \pm 0.03$, $\chi^2/\text{df} = 1.07$). Error bars are statistical errors.

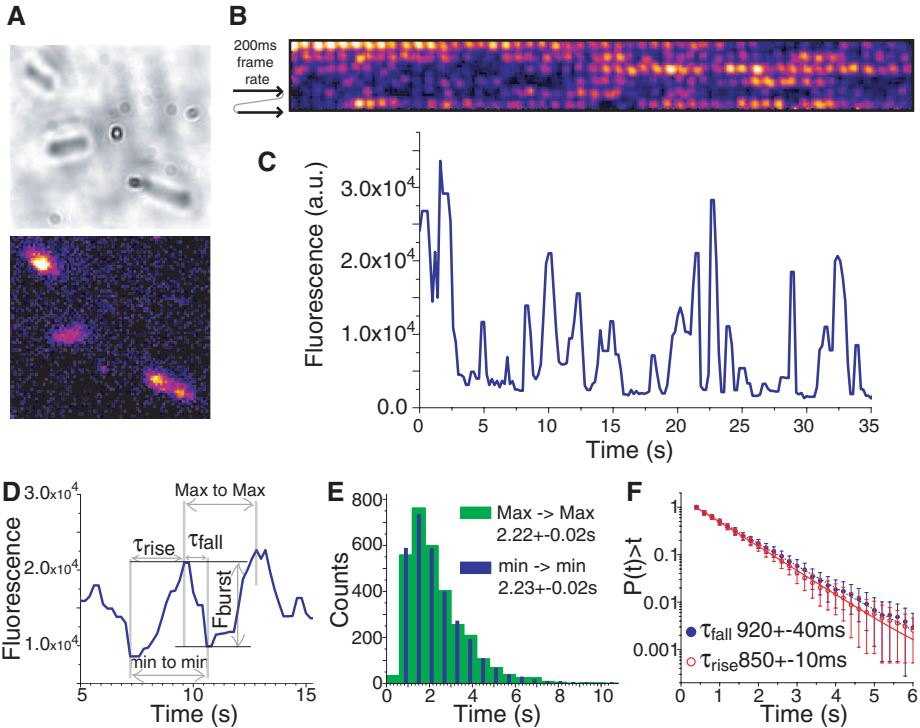
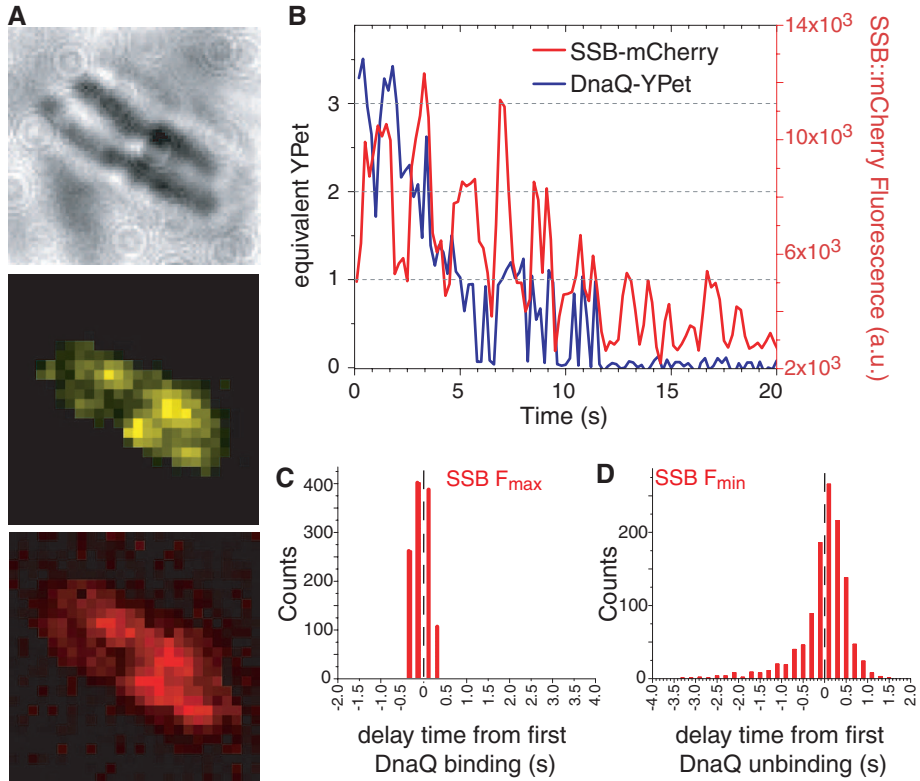


Fig. 4. Coincidence of DnaQ binding and fluctuation of SSB. **(A)** Representative images showing a picture of localization of DnaQ-YPet and SSB-mCherry in the same cells. **(B)** Representative integrated fluorescence trace in the same replisome of DnaQ, converted in equivalent YPet molecule, and SSB-mCherry. **(C)** Delay time distribution of SSB fluorescence maximum (F_{max}) in respect to the first localization frame for single DnaQ binding (1212 events). **(D)** Delay time distribution of SSB fluorescence minimum (F_{min}) in respect to the last localization frame for single DnaQ binding. The slightly variable delay can be attributed to stochasticity of the unbinding process or to the effects of photobleaching.



exchange (Fig. 2A); 0→1→2 transitions were observed in 20% of replisomes studied (fig. S13), suggesting that replication can also involve two polymerase exchanges (Fig. 2B).

To quantify exchange kinetics, we measured localization times of individual DnaQ-YPet (or DnaE-eYFP) proteins (on times) and times between individual localization events (off times) by using the 0→1 protein bursts. On- and off-time tail distributions for DnaQ-YPet and DnaE-eYFP showed exponential decays (Fig. 1D and fig. S22). Time constants obtained by fitting indicate an average Pol III localization time of ~1 s, with an average ~1-s pause before another binding event occurs. Other time constants could be attributed to photophysical effects (figs. S6, S7, S23, and S24 and tables S5 to S8).

Pol III exchange is potentially related to OF synthesis, and SSB is a marker of the single-stranded DNA template for OF synthesis. As expected, SSB was always localized either at mid-cell or at 1/4- and 3/4-cell lengths (Fig. 3 and fig. S14). If the same amounts of ssDNA are constantly formed by the helicase and copied by Pol_{lag}, then the amount of bound SSB should be constant. In contrast, variations in SSB content should be observed if phases where more ssDNA is formed by the DnaB helicase than copied by Pol_{III_{lag}} alternate with phases where OF synthesis is faster than helicase progression. The latter scenario is observed in individual replisomes: SSB integrated fluorescence showed the occurrence of fluorescence bursts over time (Fig. 3, B and C, and figs. S14, B and C, and S15), with an average period of ~2 s, an average time of fluorescence increase (τ_{rise}) of ~800 ms and an average time of fluorescence decrease (τ_{fall}) of ~900 ms (Fig. 3, D to F; fig. S25; and table S9). This result suggests that DnaB (coupled to Pol_{lead}) and Pol_{lag} do not progress at the same instantaneous speed. In our conditions (replication time about 50 min), each 2.2 s (duration of SSB bursts) about 1.5 kb of DNA are synthesized, in agreement with the size of OF in vivo (4).

To test whether Pol III and SSB oscillations (they are not pure oscillations because the period is exponentially distributed) are in phase, we monitored in the same cells the fluorescence localization of DnaQ-YPet and SSB-mCherry (Fig. 4, fig. S16, and table S10). For each DnaQ-YPet burst, we measured the delay between the first DnaQ localization image and the maximum of SSB intensity. In 72% of events localizing a single DnaQ, we observed an SSB fluorescence maximum in a window of ±300 ms flanking the DnaQ binding time (Fig. 4C and figs. S27 and S28) (an uncorrelated process would give 27% of coincidence). Therefore, most DnaQ binding events are followed by an immediate decrease in the amount of ssDNA-bound SSB, most often within the first 100 ms after Pol III binding (Fig. 4C). The majority of SSB fluorescence minimum positions were also temporally related to DnaQ unbinding positions (Fig. 4D). We pro-

pose that Pol_{lag} binding and unbinding events are directly responsible for SSB oscillations and that Pol_{lag} is renewed for each OF (Fig. 2A). The 28% oscillations that were not in phase can be attributed to exchanges involving two polymerases (fig. S13 and Fig. 2B). If the third Pol III is used as Pol_{lag}, then the newly captured Pol III remains in standby, and binding of the following Pol_{lag} to the free τ will amount to two fluorescent polymerases (Fig. 2B). The third Pol could be used either at the primer site—for example, when the capture of a new Pol_{lag} by the free τ subunit is delayed (Fig. 2B)—or in the course of an OF synthesis, when the initial Pol_{lag} is recycled before reaching the 5' end of the following OF according to the “signaling release model” (7, 17, 18). Two-polymerase exchanges might also reflect Pol_{lead} exchanges with a Pol from the pool, as reported in phages (17, 19). However, it would remain to be explained how Pol_{lead}, stabilized by its interactions with DNA, the β clamp, and τ , could be frequently released from the active holoenzyme during unimpeded DNA synthesis [T7 replisomes do not use sliding clamps or a clamp loader (6)]. Therefore, we favor a simpler model, which involves only Pol_{lag} exchanges.

The current view of *E. coli* replication is that the same Pol III is reused for the synthesis of successive OF (2), as observed in vitro when no free Pol III is available (9, 20, 21) and in agreement with the strong interaction between τ and Pol III (18). However, clamp loader and polymerase exchange has been observed in vitro for phage replisomes (22, 23), and conversely the normally exchanged β clamp could be reused when no free protein was available, suggesting flexibility of the replisome depending on the conditions (24). According to our model, (i) leaving the β clamp and DNA at the end of an OF might weaken interactions of Pol_{lag} with τ , (ii) the strength of the τ -Pol III interaction might favor the recapture of a new Pol_{lag}, and (iii) the concentration of free Pol III could be high enough for recapture in vivo in the vicinity of replication forks (15 Pol III in 0.6 μm^3 correspond to about 40 nM).

This work allows us to draw three conclusions on lagging strand synthesis in vivo. First, fluorescence localization of tagged core Pol III subunits reveals a highly regular exchange between one of the three Pol III bound to the replisome and the pool of Pol III. Second, 70% of the exchanges show a high coincidence with SSB fluctuations, supporting the idea that the exchanged Pol III is the one synthesizing the lagging strand and showing that OF synthesis starts immediately after Pol III binding. Third, the kinetics of SSB and Pol III fluctuations indicate that Pol_{lead} progresses with a speed different from Pol_{lag}. Our data suggest that the third Pol III in the holoenzyme may be used as Pol_{lag}, possibly when the synthesis of an OF is interrupted (signaling release) or when the capture of a new Pol_{lag} from the pool is delayed.

References and Notes

1. R. T. Pomerantz, M. O'Donnell, *Science* **327**, 590 (2010).
2. N. Y. Yao, M. O'Donnell, *Cell* **141**, 1088 (2010).
3. C. S. McHenry, *Annu. Rev. Biochem.* **80**, 403 (2011).
4. R. Okazaki, T. Okazaki, K. Sakabe, K. Sugimoto, A. Sugino, *Proc. Natl. Acad. Sci. U.S.A.* **59**, 598 (1968).
5. A. M. van Oijen, J. J. Loparo, *Annu. Rev. Biophys.* **39**, 429 (2010).
6. S. K. Perumal, H. Yue, Z. Hu, M. M. Spiering, S. J. Benkovic, *Biochim. Biophys. Acta* **1804**, 1094 (2010).
7. S. M. Hamdan, J. J. Loparo, M. Takahashi, C. C. Richardson, A. M. van Oijen, *Nature* **457**, 336 (2009).
8. S. M. Hamdan, C. C. Richardson, *Annu. Rev. Biochem.* **78**, 205 (2009).
9. N. Y. Yao, R. E. Georgescu, J. Finkelstein, M. E. O'Donnell, *Proc. Natl. Acad. Sci. U.S.A.* **106**, 13236 (2009).
10. S. J. Benkovic, A. M. Valentine, F. Salinas, *Annu. Rev. Biochem.* **70**, 181 (2001).
11. R. Reyes-Lamothe, D. J. Sherratt, M. C. Leake, *Science* **328**, 498 (2010).
12. P. McInerney, A. Johnson, F. Katz, M. O'Donnell, *Mol. Cell* **27**, 527 (2007).
13. X. S. Xie, P. J. Choi, G.-W. Li, N. K. Lee, G. Lia, *Annu. Rev. Biophys.* **37**, 417 (2008).
14. J. Yu, J. Xiao, X. Ren, K. Lao, X. S. Xie, *Science* **311**, 1600 (2006).
15. J. Elf, G.-W. Li, X. S. Xie, *Science* **316**, 1191 (2007).
16. R. Reyes-Lamothe, C. Possoz, O. Danilova, D. J. Sherratt, *Cell* **133**, 90 (2008).
17. J. J. Loparo, A. W. Kulczyk, C. C. Richardson, A. M. van Oijen, *Proc. Natl. Acad. Sci. U.S.A.* **108**, 3584 (2011).
18. C. D. Downey, C. S. McHenry, *Mol. Cell* **37**, 481 (2010).
19. J. Yang, Z. Zhuang, R. M. Roccasecca, M. A. Trakselis, S. J. Benkovic, *Proc. Natl. Acad. Sci. U.S.A.* **101**, 8289 (2004).
20. X. J. Li, K. J. Mariani, *J. Biol. Chem.* **275**, 34757 (2000).
21. F. P. Leu, R. Georgescu, M. O'Donnell, *Mol. Cell* **11**, 315 (2003).
22. D. E. Johnson, M. Takahashi, S. M. Hamdan, S. J. Lee, C. C. Richardson, *Proc. Natl. Acad. Sci. U.S.A.* **104**, 5312 (2007).
23. M. A. Trakselis, R. M. Roccasecca, J. Yang, A. M. Valentine, S. J. Benkovic, *J. Biol. Chem.* **278**, 49839 (2003).
24. N. A. Tanner *et al.*, *EMBO J.* **30**, 1830 (2011).

Acknowledgments: This work was initiated in S. X. Xie's laboratory with the help of G. W. Li. We thank V. Croquette and D. Bensimon (ENS Paris), N. Dixon (University of Wollongong, Australia), S. X. Xie (Harvard University), and T. R. Strick (Institut J. Monod, Paris) for very helpful readings of the manuscript; A. Langlois de Septenville and S. Duigou for support and discussions all along this work; M. LeMasson for excellent technical assistance; J. Quintas, C. Goncalves-Domingues, and E. Nicolau for their help in the microscope mechanical manufacturing; R. Reyes-Lamothe and D. Sherratt for providing strains and sharing results; M. Cox for providing SSB antibodies; and S. Duigou for performing the Western experiment. Work in B.M.'s laboratory was supported by ANR-BLAN08-3_309268 and by a “Prix coup d'élan” from the foundation Bettencourt-Schueller. G.L. was supported by an Association pour la Recherche sur le Cancer postdoctoral grant A2009. Work in J.-F.A. laboratory was supported by Agence Nationale de la Recherche and by IUF.

Supporting Online Material

www.sciencemag.org/cgi/content/full/science.1210400/DC1
Materials and Methods
Figs. S1 to S32
Tables S1 to S10
References (25–28)

27 June 2011; accepted 7 December 2011
Published online 22 December 2011;
10.1126/science.1210400

Manganese Blocks Intracellular Trafficking of Shiga Toxin and Protects Against Shiga Toxicosis

Somshuvra Mukhopadhyay and Adam D. Linstedt*

Infections with Shiga toxin (STx)—producing bacteria cause more than a million deaths each year and have no definitive treatment. To exert its cytotoxic effect, STx invades cells through retrograde membrane trafficking, escaping the lysosomal degradative pathway. We found that the widely available metal manganese (Mn^{2+}) blocked endosome-to-Golgi trafficking of STx and caused its degradation in lysosomes. Mn^{2+} targeted the cycling Golgi protein GPP130, which STx bound in control cells during sorting into Golgi-directed endosomal tubules that bypass lysosomes. In tissue culture cells, treatment with Mn^{2+} yielded a protection factor of 3800 against STx-induced cell death. Furthermore, mice injected with nontoxic doses of Mn^{2+} were completely resistant to a lethal STx challenge. Thus, Mn^{2+} may represent a low-cost therapeutic agent for the treatment of STx infections.

Shiga toxin (STx)—producing bacteria of the *Shigella* genus and enterohemorrhagic *Escherichia coli* (EHEC) species infect more than 150 million individuals each year and cause more than a million deaths (1). There is no definitive medical treatment. Indeed, treatment with antibiotics is contraindicated because it increases the risk of STx release and life-threatening disease (1–3). STx consists of a catalytically toxic A subunit bound to a B subunit

that mediates its membrane trafficking from the cell surface through endosomes, the Golgi apparatus, and the endoplasmic reticulum (ER), where the toxin translocates to the cytosol and inactivates ribosomes (4). Direct trafficking of STx from early endosomes to the Golgi, bypassing late endosomes and lysosomes, is a crucial step that allows STx to avoid degradation. Small-molecule inhibitors targeting this step hold therapeutic promise, but the STx interactions responsible for its endosomal sorting remain unclear.

Exposure of cells to 50 to 500 μM manganese (Mn^{2+}) induces degradation of GPP130 (5, 6), a membrane protein that cycles between the Golgi and endosomes (7, 8). Because GPP130 plays

a role, albeit undefined, in endosome-to-Golgi trafficking of STx (9), we asked whether Mn^{2+} acts as a small-molecule inhibitor of STx. To investigate the effect of Mn^{2+} on STx trafficking, we used a fluorescently tagged version of the B subunit of STx (STxB) that exhibits transport kinetics identical to the holotoxin (10, 11). Whereas STxB efficiently trafficked from the cell surface to the Golgi in control cells, cells exposed to 500 μM Mn^{2+} lacked GPP130, and STxB accumulated in peripheral punctate structures resembling endosomes (Fig. 1, A and B). We confirmed that STxB did not reach the ER (fig. S1) by using a STxB version with a KDEL tag, which increases its retention in the ER (12).

The Mn-induced block in STxB trafficking was specific. There was no difference between Mn^{2+} -treated and control cells in cholera toxin B subunit (CTxB) trafficking (Fig. 1C and fig. S2), which follows the same route as STx to the Golgi (13). Moreover, Mn^{2+} did not affect epidermal growth factor (EGF) internalization and degradation (fig. S3) or ER-to-cell-surface trafficking of vesicular stomatitis virus G protein (fig. S4). Further, Mn^{2+} did not alter the localization or trafficking of GP73 and TGN46, endogenous proteins that constitutively cycle between the Golgi and endosomes, or Lamp2, which traffics from the Golgi to lysosomes (fig. S5). Finally, 500 μM Mn^{2+} did not affect cell viability (Fig. 1D).

The accumulation of STxB in intracellular punctae implies that Mn^{2+} blocks STxB after internalization. Indeed, STxB moved to Rab5-positive early endosomes and, instead of exiting to the Golgi, trafficked to Rab7-positive

Department of Biological Sciences, Carnegie Mellon University, Pittsburgh, PA 15213, USA.

*To whom correspondence should be addressed. E-mail: linstedt@andrew.cmu.edu

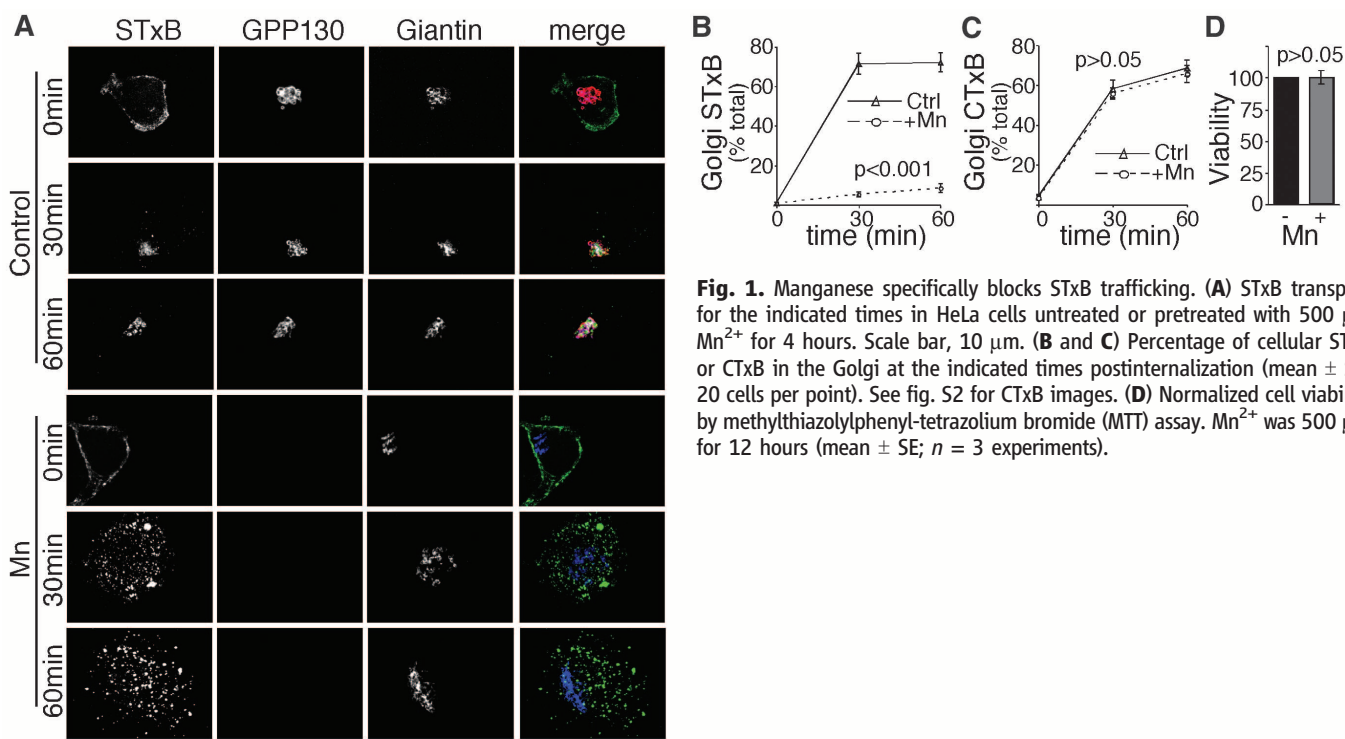


Fig. 1. Manganese specifically blocks STxB trafficking. **(A)** STxB transport for the indicated times in HeLa cells untreated or pretreated with 500 μM Mn^{2+} for 4 hours. Scale bar, 10 μm . **(B and C)** Percentage of cellular STxB or CTxB in the Golgi at the indicated times postinternalization (mean \pm SE; 20 cells per point). See fig. S2 for CTxB images. **(D)** Normalized cell viability by methylthiazolyl(phenyl)-tetrazolium bromide (MTT) assay. Mn^{2+} was 500 μM for 12 hours (mean \pm SE; $n = 3$ experiments).

late endosomes (Fig. 2A). Mn^{2+} did not alter Rab5 and Rab7 distribution (fig. S6). Exit to the Golgi involves tubules that extend from early endosomes (14). To determine whether Mn^{2+} blocks this step, we compared the early endosome localization of internalized STxB to EGF, which is excluded from tubular extensions and traffics to late endosomes. As expected, STxB was detected in endosomal tubules in control cells while EGF was excluded (Fig. 2, B and C, and fig. S7). STxB tubules contained the retromer component SNX-1 (fig. S8), confirming that they were bona fide Golgi-directed transport intermediates (14). GPP130 was also detected on STxB tubules and endosomes when trafficking of both proteins was synchronized (fig. S9). The sorting of STxB into endosomal tubules was abolished in Mn^{2+} -treated cells (Fig. 2, B and C). The block in tubulation appeared specific because the sorting of CTxB into endosomal tubules was not affected (fig. S10). Sorting of STxB into endosomal tubules was also blocked after small interfering RNA-induced depletion of GPP130 (fig. S11), suggesting that GPP130 is the target of Mn.

The presence of STxB in Rab7-positive endosomes suggests that Mn^{2+} may induce toxin degradation. Indeed, Mn^{2+} caused a dramatic loss of STxB (Fig. 2D and fig. S12). Degradation occurred after a lag and was blocked by dominant-negative Rab7 (Rab7-T22N), implying that STxB trafficked to, and was degraded in, lysosomes (Fig. 2D). Rab7-T22N did not affect STxB trafficking in control cells (fig. S13) because STxB normally bypasses late endosomes (15). Thus, Mn^{2+} diverts STxB to late endosomes

and lysosomes, where it is degraded. This is important from a therapeutic perspective because Mn-treated cells will not contain residual toxin that could escape to the cytosol over time.

To determine whether GPP130 is the Mn^{2+} target, we used a rescue approach with the goal of restoring endosome-to-Golgi trafficking of STxB by expression of an Mn^{2+} -insensitive GPP130 construct. GPP130 contains a short cytosolic domain, a single transmembrane domain, a coiled-coil luminal stem domain, and an acidic C terminus (fig. S14). The stem contains three targeting determinants: residues 36 to 87 and 176 to 245 confer Golgi localization, and residues 88 to 175 mediate endosome-to-Golgi cycling (16). Deletion of any of these makes GPP130 Mn^{2+} insensitive (5). Based on this, we generated GPP130₁₋₁₇₅-GFP (green fluorescent protein) and verified that it was Mn^{2+} insensitive but retained its ability to traffic between the Golgi and endosomes (fig. S15). Expression of this construct restored the ability of STxB to traffic to the Golgi after Mn^{2+} (Fig. 3, A and B), indicating that GPP130 was the target of Mn^{2+} . As a control, we generated GPP130_{Δ88-175}-GFP, an Mn^{2+} -insensitive construct that lacked residues 88 to 175 required for endosome-to-Golgi cycling. This construct failed to traffic out of the Golgi (fig. S15) and also failed to restore STxB trafficking (Fig. 3, A and B).

Of the known cellular factors involved in STxB trafficking, all but GPP130 are cytosolic, raising the possibility that STx evolved to avoid the degradative pathway by binding GPP130 in the lumen of early endosomes. Indeed, we observed

robust, direct, and specific binding of STxB to the GPP130 stem domain exhibiting a dissociation constant (K_d) of 150 nM (Fig. 3, C and D). Binding mapped to residues 36 to 87 (Fig. 3, E and F). Because deleting these residues yielded a construct, GPP130_{Δ36-87}-GFP, that cycled yet was Mn^{2+} insensitive (fig. S15), we could use the rescue assay to test the functional importance of STx binding to GPP130. GPP130_{Δ36-87}-GFP failed to rescue STxB trafficking to the Golgi (Fig. 3, A and B), indicating that the GPP130 luminal stem domain directly interacts with STxB to mediate STxB sorting into endosomal tubules (schematized in fig. S16). It is possible that other toxins similarly coopt proteins in the GPP130 pathway to escape degradation.

To determine whether Mn^{2+} protects cells against Shiga toxicity, we first performed a dose-response analysis in control cells using STx1. STx1, secreted by EHEC, has a B subunit identical to STx secreted by Shigella, and the A subunit differs in only one position (17). As expected (18), the lethal dose (LD_{50}) of STx1 was 0.05 ng/ml (Fig. 4A). Mn^{2+} protected STx1-treated HeLa cells (Fig. 4, A and B, and fig. S17A), and 50% cell death was not evident, even at a concentration 2000 times as high as the LD_{50} . The estimated protection factor was 3800 (Fig. 4B). Mn^{2+} by itself did not compromise viability (fig. S17).

Finally, we investigated whether Mn^{2+} protects mice during lethal Shiga toxicity. Intraperitoneal injection was used because this model has a definitive end point (death in 3 to 4 days) and recapitulates features of STx-induced renal

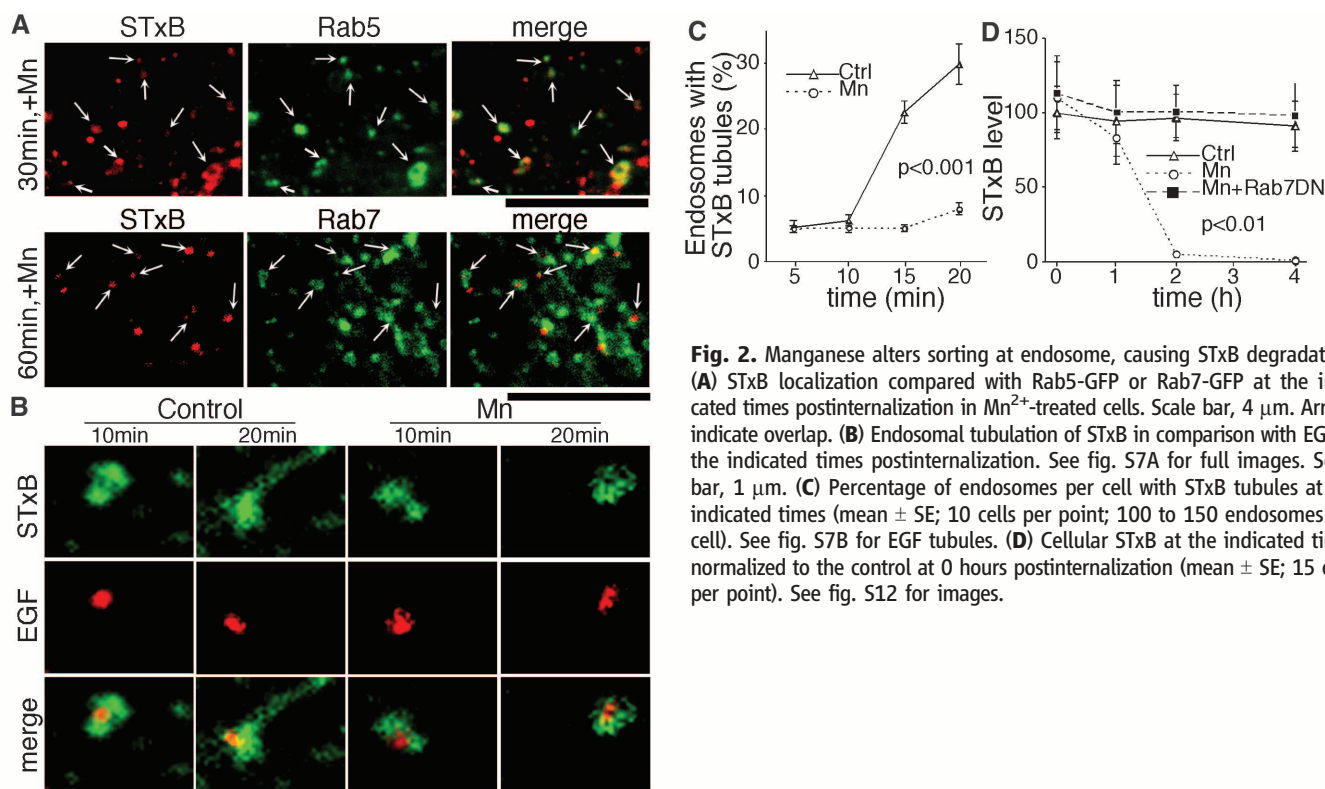


Fig. 2. Manganese alters sorting at endosome, causing STxB degradation. (A) STxB localization compared with Rab5-GFP or Rab7-GFP at the indicated times postinternalization in Mn^{2+} -treated cells. Scale bar, 4 μ m. Arrows indicate overlap. (B) Endosomal tubulation of STxB in comparison with EGF at the indicated times postinternalization. See fig. S7A for full images. Scale bar, 1 μ m. (C) Percentage of endosomes per cell with STxB tubules at the indicated times (mean \pm SE; 10 cells per point; 100 to 150 endosomes per cell). See fig. S7B for EGF tubules. (D) Cellular STxB at the indicated times normalized to the control at 0 hours postinternalization (mean \pm SE; 15 cells per point). See fig. S12 for images.

damage evident in humans (19–21). To identify a test dose for Mn²⁺, a concentration series was injected that yielded an apparent LD₅₀ of 125 mg per kg of weight (mg/kg) (Fig. 4C). Because Mn²⁺ is cleared from the system within hours (22), we also tested daily injections, and doses up to 50 mg/kg were not toxic and did not change body weight (Fig. 4D). Thus, as a proof of pro-

tection dose, we used 50 mg/kg Mn²⁺ once daily beginning 5 days before STx1 exposure, followed by 25 mg/kg Mn²⁺ once daily after toxin exposure. Life-threatening complications of STx infections in humans develop days after onset of enteric symptoms, providing an opportunity for treatment after diagnosis. Each mouse received a single injection of 25 μg/kg STx1.

Mice with no Mn²⁺ treatment became agitated and restless within 24 hours, lost 5 to 10% of body weight at 48 to 72 hours (Fig. 4E), and died at 72 to 96 hours (Fig. 4F). In contrast, all Mn-treated animals remained healthy and survived for the duration of the study (Fig. 4, E and F). Complete protection was also evident with daily Mn²⁺ injections of 25 mg/kg and 10 mg/kg,

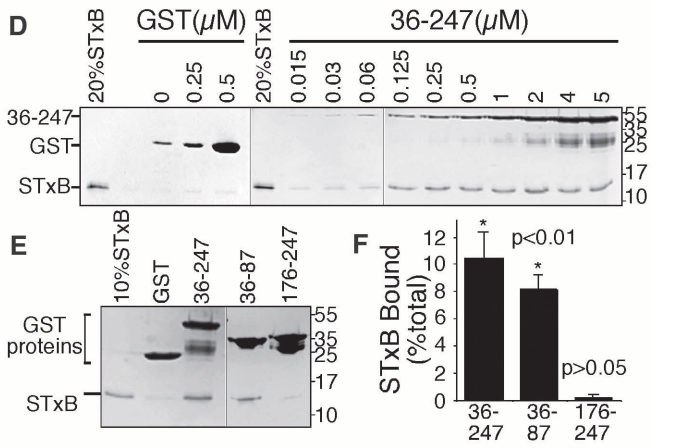
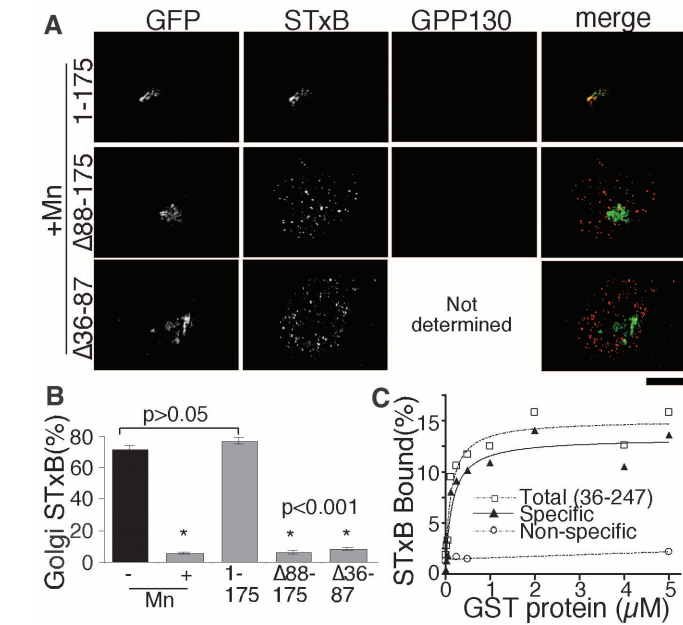


Fig. 3. GPP130 is the cellular Mn²⁺ target and directly binds STxB to mediate its endosome-to-Golgi trafficking. **(A)** STxB localization 30 min postinternalization in Mn-treated cells expressing the indicated constructs. Endogenous GPP130 was detected using an antibody to the acidic domain. Scale bar, 10 μm. **(B)** Percentage of cellular STxB in Golgi from **(A)**. Data for control and Mn²⁺ groups without GPP130 transfection are replotted from Fig. 1B (mean ± SE; 15 cells each). **(C and D)** Quantitation of His-STxB recovery after incubation with GST-GPP130₃₆₋₂₄₇ and the corresponding Coomassie-stained gels. **(E and F)** Coomassie-stained gels and quantitation of His-STxB recovery after incubation with 5 μM of the indicated GST constructs (mean ± SE; n = 3 experiments).

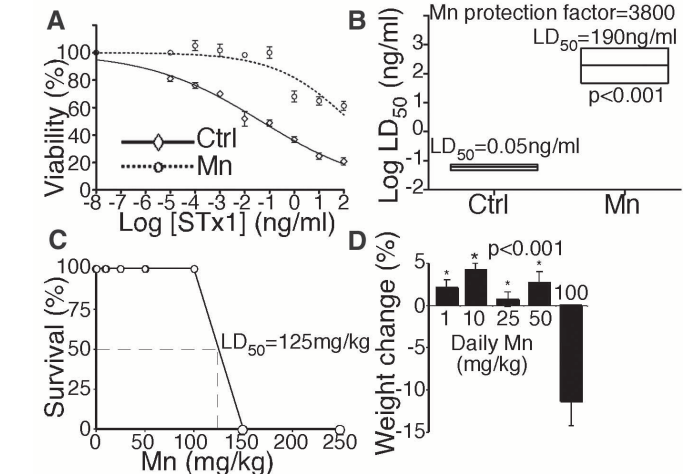
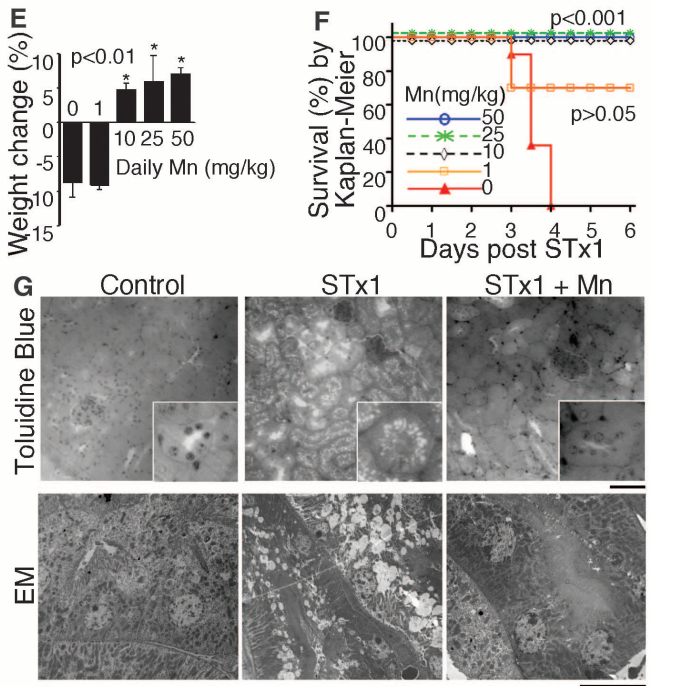


Fig. 4. Treatment with Mn²⁺ protects against STx1-induced death. **(A)** Cell viability by MTT assay after 24 hours exposure to STx1 at the indicated concentrations. Mn²⁺ sample was pretreated with 500 μM for 4 hours and then Mn²⁺ was reduced to 125 μM during STx1 exposure (mean ± SE; n = 3 experiments). **(B)** LD₅₀ with boxed 95% confidence interval from **(A)**. **(C)** Fraction of mice surviving injection of Mn²⁺ at the indicated concentration (n = 4 mice per dose). **(D)** Body weight change after 96 hours of daily Mn²⁺ injections at the indicated concentrations (n = 4 mice per dose, except n = 2 for 100 mg/kg). Only animals with depressed body weight exhibited locomotive or any other abnormalities. **(E)** Body weight change of mice injected with STx1 only (n = 6 mice) or STx1 and Mn²⁺ at the indicated concentration (n = 6 mice for 50 mg/kg Mn²⁺ and 4 for



other doses). Final weight recorded on day of death or on day 8 for survivors. **(F)** Survival curves from **(E)**. **(G)** Histology of kidneys by toluidine blue staining (scale bar, 100 μm; inset, 4X) and electron microscopy (scale bar, 10 μm).

but not 1 mg/kg (Fig. 4, E and F). As expected (21), histologic examination of the kidneys of STx1-treated mice revealed extensive damage in the cortical convoluted tubules, whereas animals protected by Mn^{2+} showed no STx1-induced renal damage (Fig. 4G). Thus, Mn^{2+} effectively protects against STx-induced toxicity and death in vivo even during fulminant systemic toxicosis.

In conclusion, Mn^{2+} may be effective in the management of STx infections. In contrast to other experimental strategies (20, 23–25), Mn^{2+} is an essential nutrient, its toxicology is well studied (26, 27), and it is already approved for oral and intravenous use. The low cost and wide availability of Mn^{2+} make it amenable for use in developing countries, where >95% of STx infections occur. Further, it may be possible to combine Mn^{2+} with antibiotic therapy because Mn^{2+} may block the toxic effects of STx released from dying bacteria.

References and Notes

1. T. Ochoa, T. G. Cleary, in *Oski's Pediatrics: Principles and Practice*, J. A. McMillan et al., Eds. (Lippincott Williams and Wilkins, Philadelphia, 2006), pp. 1116–1121.

2. K. L. Mohawk, A. R. Melton-Celsa, T. Zangari, E. E. Carroll, A. D. O'Brien, *Microb. Pathog.* **48**, 131 (2010).
3. C. S. Wong, S. Jelacic, R. L. Habeeb, S. L. Watkins, P. I. Tarr, *N. Engl. J. Med.* **342**, 1930 (2000).
4. M. E. Fraser, M. M. Chernaia, Y. V. Kozlov, M. N. James, *Nat. Struct. Biol.* **1**, 59 (1994).
5. S. Mukhopadhyay, C. Bachert, D. R. Smith, A. D. Linstedt, *Mol. Biol. Cell* **21**, 1282 (2010).
6. S. Mukhopadhyay, A. D. Linstedt, *Proc. Natl. Acad. Sci. U.S.A.* **108**, 858 (2011).
7. A. D. Linstedt, A. Mehta, J. Suhan, H. Reggio, H. P. Hauri, *Mol. Biol. Cell* **8**, 1073 (1997).
8. S. Puri, C. Bachert, C. J. Fimmel, A. D. Linstedt, *Traffic* **3**, 641 (2002).
9. R. Natarajan, A. D. Linstedt, *Mol. Biol. Cell* **15**, 4798 (2004).
10. F. Mallard, L. Johannes, *Methods Mol. Med.* **73**, 209 (2003).
11. Materials and methods are available as supporting material on Science Online.
12. L. Johannes, D. Tenza, C. Antony, B. Goud, *J. Biol. Chem.* **272**, 19554 (1997).
13. K. Sandvig, B. van Deurs, *Gene Ther.* **12**, 865 (2005).
14. V. Popoff et al., *J. Cell Sci.* **120**, 2022 (2007).
15. F. Mallard et al., *J. Cell Biol.* **143**, 973 (1998).
16. C. Bachert, T. H. Lee, A. D. Linstedt, *Mol. Biol. Cell* **12**, 3152 (2001).
17. M. E. Fraser et al., *J. Biol. Chem.* **279**, 27511 (2004).
18. I. S. Shin et al., *BMB Rep* **42**, 310 (2009).
19. S. Ishikawa et al., *Infect. Immun.* **71**, 3235 (2003).
20. K. L. Mohawk, A. D. O'Brien, *J. Biomed. Biotechnol.* **2011**, 258185 (2011).
21. V. L. Tesh et al., *Infect. Immun.* **61**, 3392 (1993).
22. H. Suzuki, O. Wada, *Environ. Res.* **26**, 521 (1981).
23. J. B. Saenz, T. A. Doggett, D. B. Haslam, *Infect. Immun.* **75**, 4552 (2007).
24. B. Stechmann et al., *Cell* **141**, 231 (2010).
25. S. Fukuda et al., *Nature* **469**, 543 (2011).
26. J. A. Moreno et al., *Toxicol. Sci.* **112**, 394 (2009).
27. M. Aschner, K. M. Erikson, E. Herrero Hernández, R. Tjalkens, *Neuromol. Med.* **11**, 252 (2009).

Acknowledgments: We thank D. R. Smith, T. H. Lee, J. S. Minden, J. L. Brodsky, and M. A. Puthenveedu for advice; N. N. Urban and J. Dry-Henich for help with animal work; Y. Creeger for fluorescence-activated cell sorting; S. Truschel and B. Ballou for protein preparation; and J. Suhan for electron microscopy. Supported by NIH grant R01GM084111 to A.D.L. and an American Heart Association fellowship to S.M. A patent on the use of Mn^{2+} to treat Shiga toxicosis is pending. The data reported in this paper are tabulated in the main text and in the supporting online material.

Supporting Online Material

www.sciencemag.org/cgi/content/full/335/6066/332/DC1
Materials and Methods
Figs. S1 to S17
References (28, 29)

28 October 2011; accepted 5 December 2011
10.1126/science.1215930

Illusions Promote Mating Success in Great Bowerbirds

Laura A. Kelley¹ and John A. Endler^{1,2*}

Sexual selection studies normally compare signal strengths, but signal components and sensory processing may interact to create misleading or attention-capturing illusions. Visual illusions can be produced by altering object and scene geometry in ways that trick the viewer when seen from a particular direction. Male great bowerbirds actively maintain size-distance gradients of objects on their bower courts that create forced-perspective illusions for females viewing their displays from within the bower avenue. We show a significant relationship between mating success and the female's view of the gradient; this view explains substantially more variance in mating success than the strength of the gradients. Illusions may be widespread in other animals because males of most species display to females with characteristic orientation and distance, providing excellent conditions for illusions.

Animals produce a vast array of sexual displays (1). Signal evolution can be driven by males exploiting sensory biases in females (2) but can be limited by psychophysics (3), cognitive mechanisms (4), and species recognition (5). Discussions of signal evolution normally consider only signal intensity (2–5), but signal components and receiver sensory processes may interact to create misleading or attention-capturing illusions (6–8) independently of signal strength.

Illusions can arise when the two-dimensional projection of a scene on the retina corresponds to

a three-dimensional scene that has geometry different from that of the real scene (6). An object viewed by an observer subtends an angle ϕ on the observer's eye, which is dependent on the object's size and distance (Fig. 1 and fig. S1). When objects of similar size increase in distance from an observer, their ϕ values decrease (Fig. 1A, Fig. 2B, and fig. S1A), and this information is unconsciously used to infer the size and distance of objects (6, 9). Forced-perspective illusions occur when the natural relationship between distance and ϕ is violated (6–9). A scene where objects decrease in size as distance increases (negative gradient) results in more rapidly decreasing ϕ than normal, making the scene appear larger than it is (Fig. 2C), a pattern often found in architecture [see references in (8)]. Conversely, a scene where objects increase in size with distance (positive gradient) results in ϕ remaining constant (Figs. 1B and 2A) or decreasing more slowly

ly than normal, and the scene appears smaller (Fig. 2A). Additional illusions may result from object arrangement (6) (fig. S2), from interactions between objects and perspective cues (6), and when the viewer's head is moved (7).

Male bowerbirds construct bowers that serve only to attract females for mating (10). Females assess potential mates via various traits, including the number and type of colored decorations (11–13), vocal mimicry (14), and male courtship display movements on the courts (15). Male great bowerbirds (*Ptilonorhynchus nuchalis*) construct bowers with an avenue 0.6 m in length, opening onto courts consisting of stones, shells, and bones, collectively called gesso (Fig. 1C), and the male presents colored objects over the gesso during display. Females view males displaying over the court from within the avenue and copulate within the avenue (10); this predetermined viewing geometry is an essential requirement for forced perspective (7–9). Males arrange gesso objects on their display courts so that they increase in size as distance from the bower increases (positive gradient; Fig. 1, B and C), creating forced perspective for the female within the avenue (8). Forced perspective could be an honest mate choice signal because males rapidly restore experimentally reversed gradients and vary in their gradient quality (8). To investigate whether this illusion influences mate choice, we tested for relationships between mating success and geometry. If the gradients or their generated perspective are important to females, then they should predict the degree of mating success.

We monitored the mating success and court gradients in the population in the eucalyptus woodland at Dregghorn cattle station (20.25°S, 147.73°E) (8). The strength of the gradient at each court is the slope (b) of the regression of

¹Centre for Integrative Ecology, School of Life & Environmental Sciences, Deakin University, Geelong, VIC 3216, Australia.

²School of Marine and Tropical Ecology, James Cook University, Townsville, QLD 4811, Australia.

*To whom correspondence should be addressed. E-mail: john.endler@deakin.edu.au

visual depth (d) or width (w) on distance (x) from the female's viewpoint within the bower avenue (Fig. 1 and fig. S1), and gradient strength is represented by b . All bowers had positive slopes on both courts. The gradient slopes successfully pre-

dicted the degree of mating success (Fig. 3A), with visible depth accounting for most of the variation (Table 1). We measured the perspective view quality according to the standard deviation of the visual

angles (s_ϕ) from the female viewpoint; a more regular (even) pattern or texture has a smaller s_ϕ . The regularity of the perspective pattern successfully predicted the degree of mating success (Fig. 3B), with both visible depth and width perspective effects significant (Table 1). The fit to the data is remarkably planar, with an adjusted r^2 of 0.96. This strong linear fit is not an artifact; there are no correlations between the ϕ means and variances (both $P > 0.52$). The most successful bowers have lower $s_{\phi d}$ and higher $s_{\phi w}$, which suggests that pattern regularity is more important in the vertical (depth) axis than in the horizontal (width) axis. Differential attention to vertical and horizontal axes is known in other animals, including humans (16). Bowerbirds may be subject to the horizontal-vertical illusion in which two objects of equal length perpendicular to each other result in the vertical object appearing longer (fig. S2A), as is known in chicks (6). The $s_{\phi d}$ and $s_{\phi w}$ coefficients have opposite signs (Table 1), making the prediction plane slant (Fig. 3). This arises because the mean object length/width ratio is 1.4; as the angle to the visual axis of oblong objects increases, ϕ_w increases and ϕ_d decreases. Rough-

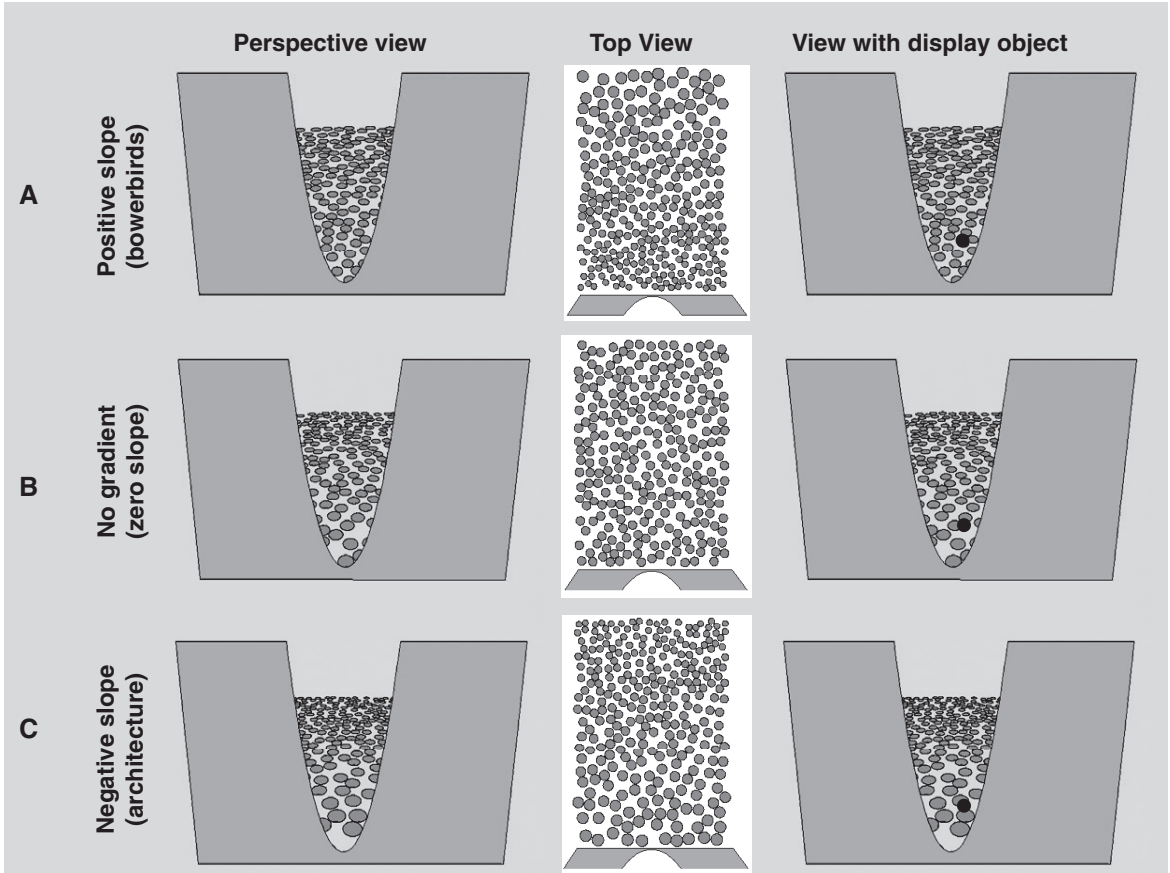
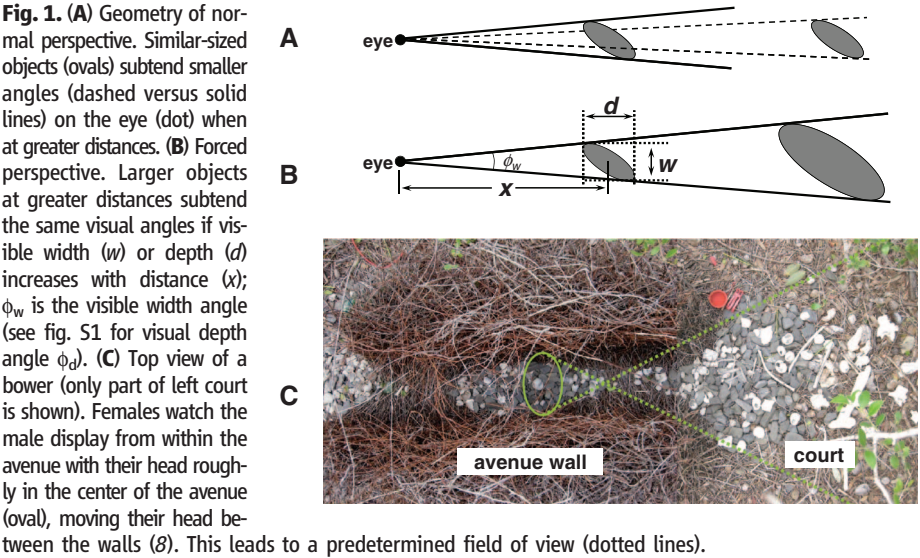


Fig. 2. Three-dimensional scale models of size-distance gradients on a bower court. Left column: Female view of the court from within the avenue (gray area); ovals are court gesso objects. Center column: Court and avenue entrance from above. Right column: Same as left column, with a display object (black) added. Males usually hold display objects at a low point close to the avenue entrance as shown. (A) Gesso with a positive size-distance gradient similar to that of a

typical great bowerbird court. (B) No gradient. (C) Negative gradient, as is often found in buildings designed to look large. The positive gradient produces the most regular pattern as seen from the avenue (smallest s_ϕ) and the smallest apparent court size. The Ebbinghaus illusion (fig. S2) makes the display object seem larger in the presence of the positive gradient than in the others, and the magnitude of the effect varies with different slopes (e.g., different males).

ly the same intermediate mating success was achieved with differing combinations of $s_{\phi w}$ and $s_{\phi d}$ (Fig. 3); there are many different ways of producing perspective that can favor the same degree of mating success.

The linear model Akaike information criterion (AIC) values and residuals are much smaller for the perspective view regularity s_{ϕ} than for the gradient slopes b (Table 1). This indicates that the degree of mating success is more strongly influenced by the perspective view of the court gradients from the female's position within the avenue (measured by s_{ϕ}) than by the strength of the gradients (b). Therefore, it is the visual effect (illusion) of forced perspective, rather than the gradient slopes, that significantly contributes to mating success.

There are seven possible consequences: (i) The degree of regularity in the perspective view varies among males and could be a mate choice criterion. (ii) The regular visual pattern may make the male's displayed objects more conspicuous; a regular background is less distracting than an irregular one. (iii) Forced perspective may make the court appear smaller than it is (Fig. 2C), possibly causing the display object to appear relatively larger. (iv) Display objects and gesso sizes are similar; 79% (ϕ_w) and 71% (ϕ_d) of the bowers

show no mean size difference (Kruskal-Wallis tests, all $P > 0.05$), and the display objects are slightly larger than the gesso in 57% (percentage with positive size difference in ϕ_w) and 79% (ϕ_d) of the bowers. This provides good conditions for the Ebbinghaus illusion (fig. S2B), where an object adjacent to smaller objects will appear larger than the same object next to larger objects (Fig. 2C). This illusion is known in chicks and mistle thrushes, with opposite effects on pigeons (6, 17). It will make display objects vary in apparent size, increasing their conspicuousness. (v) Because display objects are waved toward the female during display, their apparent size may change more rapidly during the display than if the court had normal perspective, and this will be further enhanced by the Ebbinghaus illusion. (vi) The female moves her head within the avenue walls during the male display, providing her with motion parallax depth cues (7) that will conflict with the false depth cues of forced perspective. (vii) Motion parallax gives females an estimate of the distance to display objects, yielding a size estimate that will conflict with illusory size estimates generated by forced-perspective and Ebbinghaus illusions.

Any of these seven effects might hold the female's attention longer than if absent, and still

longer if the illusions interact. For example, females will not mate unless they have spent more than about 55% of their total time in the avenue watching the male display (fig. S3), and the fraction of avenue time that a female watches a male display is higher for bowers with smaller differences between gesso and display object size ($t = 2.27$, $df = 14$, $P = 0.039$, $r^2 = 0.27$), as might be expected from the Ebbinghaus illusion. We have direct evidence only for the first effect, but one or more of the other six could also affect mating success. However, we have shown that illusions can affect mating success in ways unpredictable from signal intensity alone.

Our results raise the possibility that illusions may be used by other species during mate choice; sensitivity to visual illusions has been demonstrated in chicks, mistle thrushes, pigeons, and a gray parrot (6, 17–21). Mating illusions are a logical extension of the sensory exploitation part of sensory drive (2); here, males use sensory biases to mislead or hold attention rather than strongly stimulate. Moreover, the illusion magnitude (6) may be a direct-choice criterion. Illusions simply require predictable viewing geometry (8); for example, manakins and cock-of-the-rock clear the vicinity of their display courts with characteristic geometry, and in some species females view the male's display from a predictable location and direction (22). Even without environmental modification, males of most taxa usually present themselves to females in a particular orientation and move their patterns in particular directions relative to the female visual axis, making illusions possible. Furthermore, given that females in many species prefer males with larger color patches, illusions on the body such as the Ebbinghaus or Wundt-Jastrow (fig. S2) could also be used to alter the apparent size of such patches. This study indicates that illusions could have strong implications for the mode of evolution under sexual selection.

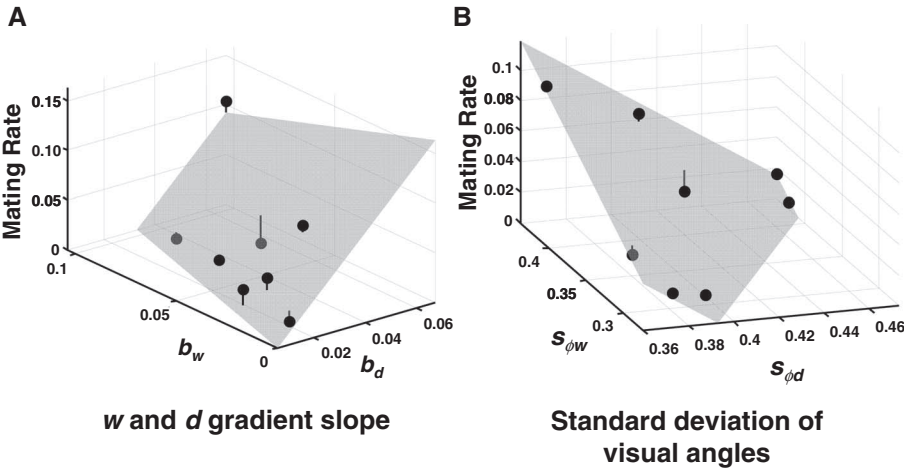


Fig. 3. Mating success predictors. The gray plane is the generalized linear model (23) of mating rate on the predictors. Dots are the observed values for each bower; vertical lines are the residuals (most are smaller than the dot size). (A) Mating success predicted from the slopes of visual depth and visible width on distance; adjusted $r^2 = 0.725$. (B) Mating success predicted by visual angle regularity; adjusted $r^2 = 0.945$.

Table 1. Generalized linear model (23) of mating rate (m) on gradient slopes (b_d , b_w) or visual angle standard deviation ($s_{\phi d}$, $s_{\phi w}$) resulting from variation in visible depth d and width w .

Gradient slopes (b) effects, full model $m = b_d + b_w$				Perspective view regularity (s_{ϕ}) effects, full model $m = s_{\phi d} + s_{\phi w}$			
	β	t (df = 5)	P		β	t (df = 5)	P
Intercept	-0.0162	-1.126	0.31	Intercept	0.210	7.66	0.00061
b_d	2.651	4.06	0.0097	$s_{\phi d}$	-0.912	-10.54	0.00013
b_w	-0.683	-2.031	0.098	$s_{\phi w}$	0.541	9.33	0.00024
Total adjusted $r^2 = 0.725$				Total adjusted $r^2 = 0.945$			
AIC = -37.69 (both b_d and b_w), -34.88 (without b_w), -28.02 (without b_d)				AIC = -50.584 (both $s_{\phi d}$ and $s_{\phi w}$), -29.28 (without $s_{\phi w}$), -27.43 (without $s_{\phi d}$)			

References and Notes

1. M. Andersson, *Sexual Selection* (Princeton Univ. Press, Princeton, NJ, 1994).
2. J. A. Endler, A. L. Basolo, *Trends Ecol. Evol.* **13**, 415 (1998).
3. K. L. Akre, H. E. Farris, A. M. Lea, R. A. Page, M. J. Ryan, *Science* **333**, 751 (2011).
4. M. Bateson, S. D. Healy, *Trends Ecol. Evol.* **20**, 659 (2005).
5. S. R. Pryke, M. Andersson, *Behav. Ecol.* **19**, 1116 (2008).
6. S. Coren, J. S. Girsig, *Seeing Is Deceiving: The Psychology of Visual Illusions* (Erlbaum, Hillsdale, NJ, 1978).
7. B. Rogers, A. Gyani, *Perception* **39**, 330 (2010).
8. J. A. Endler, L. C. Endler, N. R. Doerr, *Curr. Biol.* **20**, 1679 (2010).
9. H. E. Ross, C. Plug, in *Perceptual Constancy, Why Things Look as They Do*, V. Walsh, J. Kulikowski, Eds. (Cambridge Univ. Press, Cambridge, 1998), pp. 499–528.
10. C. B. Frith, D. W. Frith, *The Bowerbirds* (Oxford Univ. Press, Oxford, 2004).
11. J. R. Madden, *Behav. Ecol. Sociobiol.* **53**, 263 (2003).
12. G. Borgia, *Anim. Behav.* **33**, 266 (1985).
13. J. A. Endler, D. A. Westcott, J. R. Madden, T. Robson, *Evolution* **50**, 1795 (2005).
14. S. W. Coleman, G. L. Patricelli, B. Coyle, J. Siani, G. Borgia, *Biol. Lett.* **3**, 463 (2007).

15. G. L. Patricelli, J. A. C. Uy, G. Walsh, G. Borgia, *Nature* **415**, 279 (2002).
16. S. C. Dakin, R. J. Watt, *J. Vis.* **9**, 2.1 (2009).
17. N. Nakamura, S. Watanabe, K. Fujita, *J. Exp. Psychol.* **34**, 375 (2008).
18. N. Nakamura, K. Fujita, T. Ushitani, H. Miyata, *J. Comp. Psychol.* **120**, 252 (2006).
19. S. Watanabe, N. Nakamura, K. Fujita, *Cognition* **119**, 137 (2011).
20. K. Fujita, D. S. Blough, P. M. Blough, *Anim. Learn. Behav.* **19**, 283 (1991).
21. I. M. Pepperberg, J. Vicinay, P. Cavanagh, *Perception* **37**, 765 (2008).
22. J. A. Endler, M. Théry, *Am. Nat.* **148**, 421 (1996).
23. R. Development Core Team, *R: A Language and Environment for Statistical Computing* (R Foundation for Statistical Computing, Vienna, 2011; www.R-project.org).

Acknowledgments: We thank the Smith family for access and hospitality at Dregghorn Station; L. Endler for help in fieldwork and photograph analysis; Deakin University for financial support; and L. Barrett, B. Buttemer, J. Madden, S. Nakagawa, M. Richardson, J. Zeil, and two anonymous reviewers for excellent comments on the manuscript. The field research was done with an EPA-Queensland Parks and Wildlife Service permit (WISP01994004) and ethics approval

from Deakin University (A22-2010) and James Cook University (A1318). Data are in the supporting online material.

Supporting Online Material

www.sciencemag.org/cgi/content/full/335/6066/335/DC1
Materials and Methods
Figs. S1 to S3
Tables S1 to S4
Movies S1 and S2

9 August 2011; accepted 22 November 2011
10.1126/science.1212443

Activation-Induced B Cell Fates Are Selected by Intracellular Stochastic Competition

Ken R. Duffy,¹ Cameron J. Wellard,^{2,3} John F. Markham,⁴ Jie H. S. Zhou,^{2,3} Ross Holmberg,² Edwin D. Hawkins,⁵ Jhagvaral Hasbold,^{2,3} Mark R. Dowling,^{2,3*} Philip D. Hodgkin^{2,3,*†}

In response to stimulation, B lymphocytes pursue a large number of distinct fates important for immune regulation. Whether each cell's fate is determined by external direction, internal stochastic processes, or directed asymmetric division is unknown. Measurement of times to isotype switch, to develop into a plasmablast, and to divide or to die for thousands of cells indicated that each fate is pursued autonomously and stochastically. As a consequence of competition between these processes, censorship of alternative outcomes predicts intricate correlations that are observed in the data. Stochastic competition can explain how the allocation of a proportion of B cells to each cell fate is achieved. The B cell may exemplify how other complex cell differentiation systems are controlled.

Production of antibody by B cell-derived plasma cells is critical for an effective immune response (1), but B cell activation mechanisms leading to the formation of plasma cells are numerous and poorly understood. One known mechanism is for the B cell to use its surface receptor to capture and internalize antigen, which leads to presentation of T cell epitopes on its cell surface (2). Upon detection, a T cell delivers cell contact- and cytokine-mediated signals (3) that lead to B cell proliferation or changes in antibody type (isotype switching) (4), as well as differentiation into dividing plasmablasts (PBs) and sessile, long-lived plasma cells, both of which secrete antibody (5, 6). The heterogeneous B cell fates resulting from isotype switching and development into PBs can be replicated in vitro by stimulating naïve B cells through CD40 in addition to the cytokines interleukin 4

(IL-4) and IL-5 to simulate T cell interaction (7, 8), a method we used. As Blimp1 is a transcription factor that is selectively required for differentiation to PB, we used a Blimp1-GFP reporter mouse (9) to identify PBs by green fluorescent protein (GFP) expression and fluorescently labeled antibody against immunoglobulin G1 (IgG1) to identify cells switched to IgG1. After an initial 3-day culture, single-cell video microscopy was used to observe sorted cells from generations 1, 3, 5, and 7 that do not express Blimp1 or IgG1 and to optically track their times to isotype switch to IgG1, to differentiate to PBs, and ultimately to division or death (Fig. 1A and fig. S1) (10). Only one division round was followed because of the strong homotypic adhesion of B lymphoblasts, which leads to a loss of identity.

As found previously (11–15), division and death times were highly variable, and this was also true for times to isotype switching and commitment to become a PB (Fig. 1, B and C). Consistent with earlier population studies (11, 16), the dependence of frequency of isotype switching, as well as other parameters, on generation is apparent (Fig. 1, D and E). Despite the diverse range of experience of individual cells, the population-level response is insensitive to this variability (12, 13, 17–20), which presents the conundrum of how to reconcile the single-cell and population-level responses. Furthermore, these data have complex correlation structures, both

within single cells (intracellular) and between siblings (intercellular), which pose an additional challenge to any paradigm of understanding.

As a representative of intracellular correlation, for all cells that differentiate and go on to divide, Fig. 2A presents a scatter plot of times to these events, as well as estimates of Pearson's correlation coefficient (ρ). The latter reveals positive correlation coefficients for cells of each generation (ρ : 0.54, 0.59, 0.56, and 0.80). Analysis of other combinations shows that time to differentiate to PBs is positively correlated with time to death (fig. S2A) (ρ : 0.70, 0.54, 0.81, and 0.54), and with time to isotype switch (Fig. 2C) (ρ : –, 0.34, 0.29, and 0.51), where a dash indicates an insufficient number of observations to form an estimate. There is little evidence for correlation in time to isotype switch and time to division (Fig. 2B) (ρ : –, 0.17, –0.05, and –0.08) or death (fig. S2B) (ρ : –, 0.15, 0.08, and 0.11).

For intercellular dependencies, we can investigate the existence of concordance in sibling fates. Visual inspection of Fig. 1B suggests strong positive relatedness between siblings. To quantify the strength of concordance in opposing fates of siblings, we use Yule's Q (21). It takes a value in $[-1, 1]$, with 1 corresponding to perfect positive correlation, and 0 corresponding to no correlation in sibling fate (10). For our system, the opposing fates of siblings are death versus division, differentiation to PBs versus no differentiation to PBs, and isotype switching versus no isotype switching. Figure 2D plots Yule's Q for the division versus death outcome of siblings. It is high for all generations (Q : 0.97, 0.93, 0.90, and 0.96), which confirms strong sibling concordance in division or death fates: If a cell dies or divides, the likelihood that its sibling experiences the same fate is substantially higher than the likelihood of a cell chosen uniformly at random from the population at large has the same fate. All other fates display similar evidence of strong concordance: differentiate to PB versus not (Fig. 2E) (Q : 0.98, 0.98, 0.92, and 0.93) and isotype switch versus not (Fig. 2E) (Q : –, 0.98, 0.99, and 0.94).

This strong concordance justifies investigating correlations within the times to fates of siblings. We found strong correlation in time to fate between siblings (Fig. 2, F and G): ρ of 0.90, 0.93, 0.84, and 0.82 for division and ρ of 0.85, 0.79, 0.72, and 0.77 for death. For differentiation

¹Hamilton Institute, National University of Ireland, Maynooth, Ireland. ²Walter and Eliza Hall Institute of Medical Research, Parkville, Melbourne, Victoria 3052, Australia. ³Department of Medical Biology, University of Melbourne, Melbourne, Victoria 3052, Australia. ⁴Victoria Research Laboratory, National Information and Communications Technology (ICT) Australia, University of Melbourne, Melbourne, Victoria 3010, Australia. ⁵Immune Signalling Laboratory, Peter MacCallum Cancer Centre, Melbourne, Victoria 3002, Australia.

*These authors contributed equally to this work.

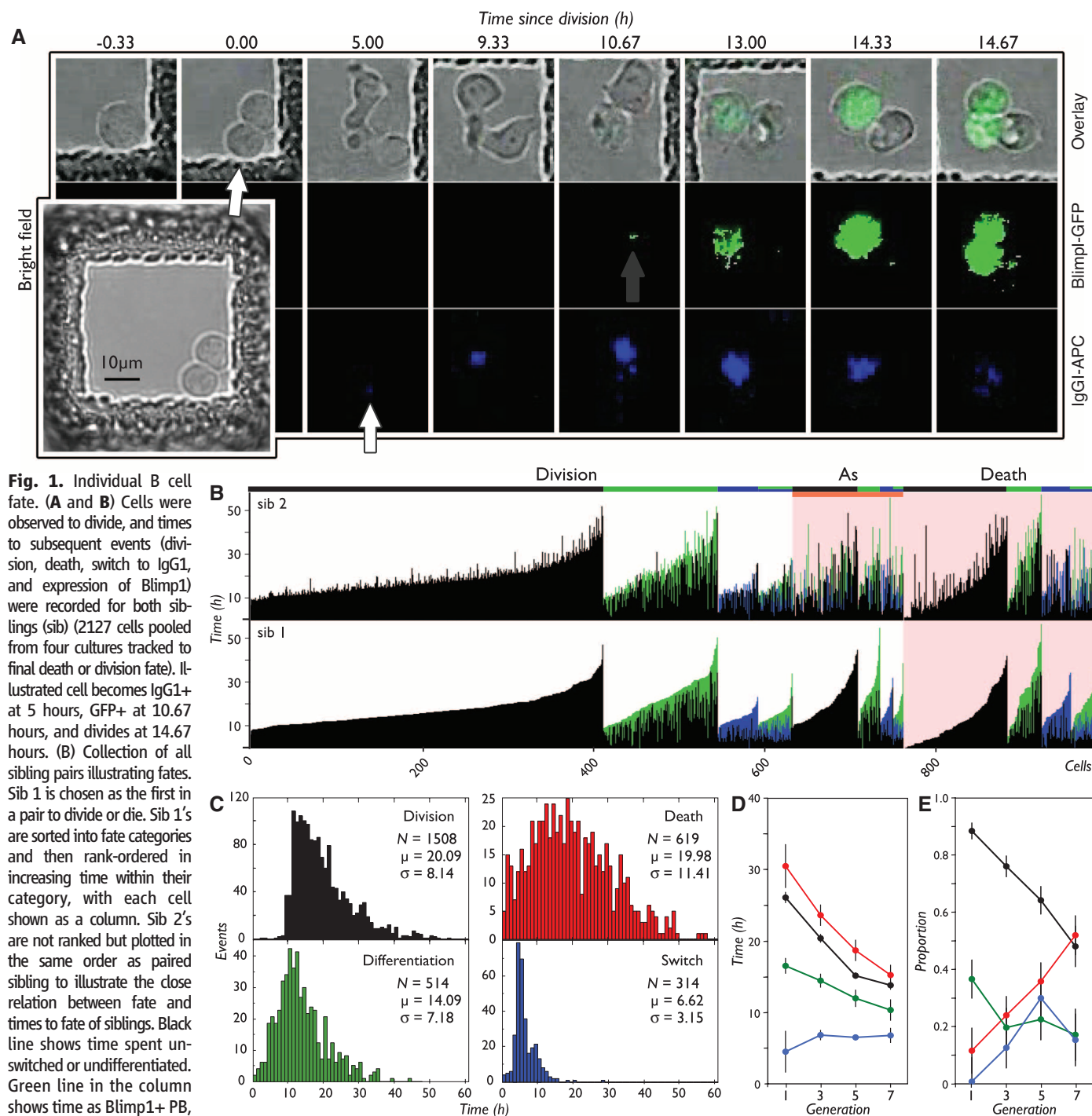
†To whom correspondence should be addressed. E-mail: hodgkin@wehi.edu.au

to PB and isotype switching, the former exhibits strong correlation (fig. S2C) (ρ : 0.75, 0.88, 0.92, and 0.94), whereas the latter is the exception and does not (fig. S2D) (ρ : $-$, 0.18, 0.29, and 0.28). Unexpectedly, correlation structure is also found in the nonconcordant fates of siblings (Fig. 2, H to J, and fig. S2, E to G).

These numerous sibling correlation structures would appear challenging for any simple mech-

anistic theory to explain them, as they suggest involved sharing of molecular machinery regulating features of isotype switching, development into a PB, division, and death. We challenged this deduction by questioning whether all of these features could be explained by a simple hypothesis of autonomous functional units in cells that are subject to competition. Such a hypothesis was proposed for division and death of lymphocytes

in the cyton model (11, 13, 22–25), whose fundamental tenet is that each cell's death or division fate is a consequence of competition between independent times for division and death. It posits the existence of two independent random variables in each cell determining times from division to fates: a time to division, T_{div} , and a time to death, T_{death} . We postulate the existence of two additional independent random variables



to fate. Number of cells (N), mean (μ), and standard deviation (σ) are shown. (D) Average time to divide (black), die (red), differentiate to PB (green), and switch (blue) per generation. (E) Proportion of cells undergoing each fate.

per cell. One, T_{diff} , determines a time to differentiate to PB, and the other, T_{switch} , determines time to isotype switching. Consistent with observations of T_{div} (13, 14, 20), with the exception of death, the corresponding process may not be in operation in every cell. This is encapsulated mathematically by assuming that the associated random variables can have a positive probability of being infinite.

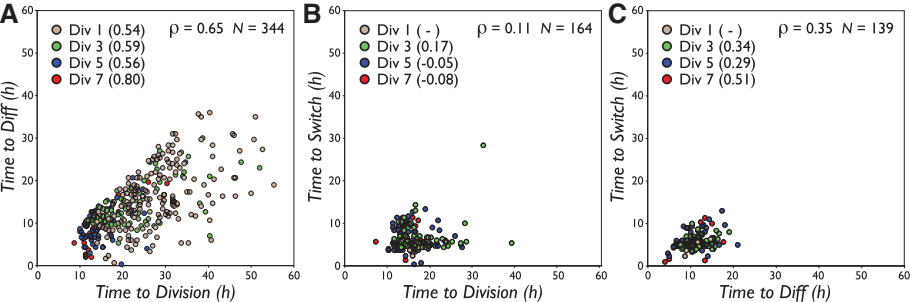
These times are subject to competition and censorship. If $T_{\text{death}} < T_{\text{div}}$, then the cell's fate is death at T_{death} , and the value T_{div} is not observed and vice versa. Thus, the larger value is censored. If $T_{\text{diff}} < \min(T_{\text{div}}, T_{\text{death}})$, then the cell is observed to differentiate to PB at time T_{diff} from birth, and otherwise the time is censored. If $T_{\text{switch}} < \min(T_{\text{diff}}, T_{\text{div}}, T_{\text{death}})$, then isotype switching is observed at T_{switch} , and otherwise its value is censored. Even though the random variables $\{T_{\text{switch}}, T_{\text{diff}}, T_{\text{div}}, T_{\text{death}}\}$ are independent, it is of fundamental importance that the distributions of the observed variables $\{T_{\text{switch}}^{\text{obs}}, T_{\text{diff}}^{\text{obs}}, T_{\text{div}}^{\text{obs}}, T_{\text{death}}^{\text{obs}}\}$ are distinct and correlated, as they have been altered by competition and censorship (10).

Because the times to concordant fate of siblings are related (Fig. 2, F and G, and fig. S2, C and D), although the model assumes that uncensored times within a cell are independent, we must allow for correlations between times to concordant fate in siblings. With a superscript 1 indicating times for one sibling and 2 for the other, we posit the existence of pairs $(T_{\text{switch}}^1, T_{\text{switch}}^2)$, $(T_{\text{diff}}^1, T_{\text{diff}}^2)$, $(T_{\text{div}}^1, T_{\text{div}}^2)$ and $(T_{\text{death}}^1, T_{\text{death}}^2)$, where the two random variables within each pair may be correlated, but they are independent across pairs. For each pair, we adopt the class of bivariate log-normal distributions with symmetric marginal distributions whose correlation structure is defined through a correlated Gaussian exponent (10). The model has 15 parameters, four means, four variances, four cross-correlations, and three probabilities of finiteness:

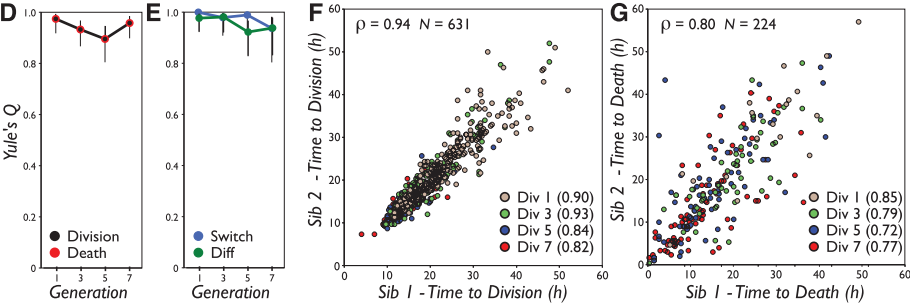
$$\theta = (\mu_{\text{switch}}, \mu_{\text{diff}}, \mu_{\text{div}}, \mu_{\text{death}}, \sigma_{\text{switch}}^2, \sigma_{\text{diff}}^2, \sigma_{\text{div}}^2, \sigma_{\text{death}}^2, \rho_{\text{switch}}, \rho_{\text{diff}}, \rho_{\text{div}}, \rho_{\text{death}}, \rho_{\text{switch}}, \rho_{\text{diff}}, \rho_{\text{div}})$$

Consider a parameterization, θ , defining the model. For a set of data, D , consisting of the times of fates of sibling cells, we calculate the likelihood that the model would generate the data $L(D|\theta)$ (10) and then determine $\theta_{\text{MAP}} = \arg \sup L(D|\theta)$, where “arg sup” reads “arguments of the supremum,” the maximum a posteriori parameterization defining our best-fit model. For each generation, we fit to a data set D , consisting of all siblings that share the same fate. This gives us sufficient data (382, 458, 330, and 254 observations in generations 1, 3, 5, and 7, respectively) to estimate all components of θ_{MAP} , but it means that the model's cross-fate predictions of the remaining data (145, 193, 234, and 131 cells, respectively) are extrapolations.

Intracellular fates



Intercellular concordant fates



Intercellular non-concordant fates

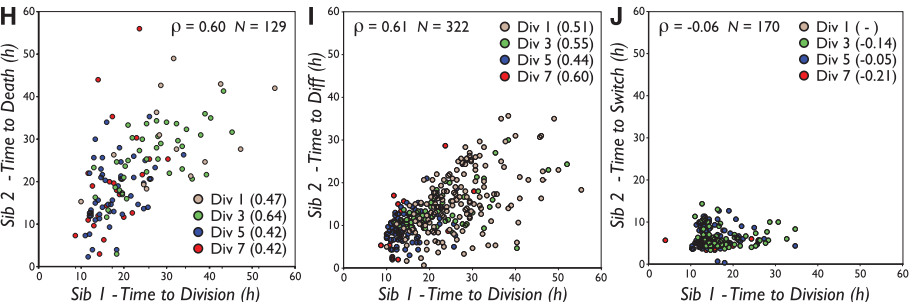


Fig. 2. Fate concordance and correlations. (A to C) Intracellular correlations (correlations in times to distinct fates within individuals) for each generation. Pearson's ρ is shown per generation and for cohort inclusive of all generations. (D) Measure of concordance of siblings in division versus death fate (red) shown as Yule's Q with 95% CIs. (E) Measure of concordance of siblings in isotype switch versus no isotype switch (blue) and development to PB versus no development to PB fate (green). (F and G) Times to intercellular concordant fates (siblings that share the same fate) and their correlation. (H to J) Times to intercellular nonconcordant fates and their correlation.

For generation 5, we plotted the uncensored marginal distributions for the independent random variables within a single sibling, as well as its censored match to observed data (Fig. 3A). The impact of competition is apparent in the substantially reduced mean and variance in the latter graphs and also in the reshaping of the distributions (see other generations in fig. S3). One indicator of whether the model's structure can capture key features of the data is comparison of average time to fate with the best-fit model. This is shown in Fig. 3, B to E, along with the measured and modeled proportion of cells that undergo division and isotype switching (death and differentiation to PBs) (fig. S4). A second indicator is its ability to capture the correlation observed in the times to concordant sibling fate (Fig. 3, H and I, and fig. S5). These good fits suggest that this simple model with four pairs of

independent random variables has sufficient flexibility to mimic the data.

Although intercellular concordant fate correlations are to be expected because of the cross-correlation parameters in our model, perhaps counterintuitively, it also predicts correlations within cells and between siblings. The uncensored variables are uncorrelated, so these correlations arise in the model exclusively as a consequence of its postulated competition and censorship (Fig. 3, F and G). With the exception of generation 7 (Fig. 3F), the predictions all lie within the 95% confidence intervals (CIs) of the measured values. Other fate combinations are shown in fig. S5, all of which also fall within 95% CIs of the measured values, with the exception of generation 5 death and differentiation to PB (10).

For asymmetric intercellular correlations where one sibling divides and the other dies,

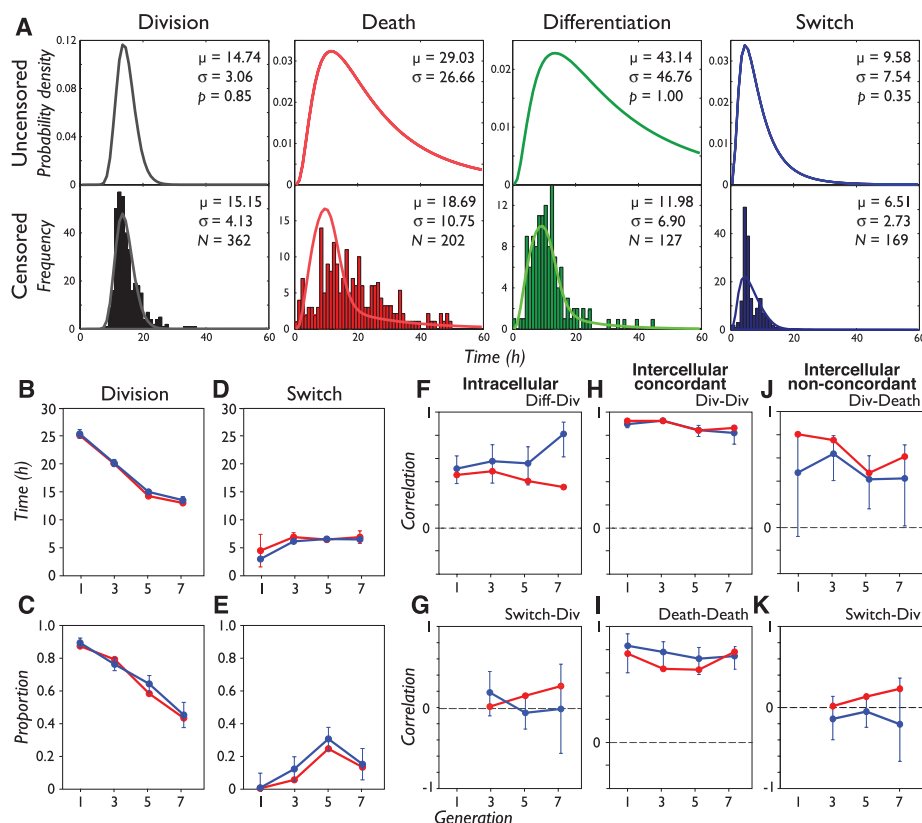


Fig. 3. Model of four independent fate times. (A) Fit of model to generation 5 data. (Top) Predicted uncensored distribution for each fate (lognormal mean, μ ; variance, σ ; likelihood of being finite, p). (Bottom) Predicted censored distribution overlaid on data. (B to K) Calculated model values (red) to data (blue). (B) Average time to divide. (C) Proportion of cells dividing per generation. (D) Time to switch. (E) Proportion switch per generation. (F and G) Intracellular fates. (H and I) Inter-cellular concordant correlations. (J and K) Inter-cellular nonconcordant fates.

division times across siblings are positively correlated, as are death times. Thus, the model predicts that one only observes asymmetric fates when time to division and time to death are close to each other, and hence, these are predicted to be positively correlated when observed (Fig. 3J). The model predicts that the correlations between time to division of one sibling and to isotype switch of the other are less correlated, as these two processes are typically separated in time and so do not strongly influence each other (Fig. 3K and fig. S5). Remarkably, with the exception of generation 5 death versus differentiation to PB, the model's predicted correlations lie within the 95% CIs for Pearson's ρ as measured in the data. Thus, not only is this simple mechanistic model of competing independent random variables capable of fitting the heterogeneous times, its predicted nontrivial cross-correlation structures that arise as a consequence of competition and censorship quantitatively match observed phenomena.

This analysis offers a mechanism to explain how lymphocytes reliably allocate a consistent proportion of cells to various populations even in the absence of specific signals, such as antigen, which may induce asymmetric cell division (26). This inherent randomness provides robustness to

loss of cells of a given class, which seems desirable in a system experiencing decentralized control. High-level order then appears not by explicit individual instructions to each cell, but by chemical signaling that shapes probability distributions and influences resultant laws of large numbers. As a consequence, this study draws attention to the stochastic epigenetic processes that influence the expression levels of the many molecular regulators of division, death, and differentiation within each cell (27–29), as it is likely that these quantitative differences will ultimately explain this shaping of distributions. Competing intracellular processes may also underlie the robust allocation of multiple fates during proliferation and differentiation in other cell systems from the embryonic to hematopoietic.

References and Notes

- M. K. Slifka, R. Ahmed, *Curr. Opin. Immunol.* **10**, 252 (1998).
- A. Lanzavecchia, *Nature* **314**, 537 (1985).
- D. C. Parker, *Annu. Rev. Immunol.* **11**, 331 (1993).
- R. L. Coffman, D. A. Leiman, P. Rothman, *Adv. Immunol.* **54**, 229 (1993).
- I. C. MacLennan *et al.*, *Immunol. Rev.* **194**, 8 (2003).
- D. Paus *et al.*, *J. Exp. Med.* **203**, 1081 (2006).

- S. L. Nutt, N. Taubenheim, J. Hasbold, L. M. Corcoran, P. D. Hodgkin, *Semin. Immunol.* **23**, 341 (2011).
- J. Hasbold, L. M. Corcoran, D. M. Tartinton, S. G. Tangye, P. D. Hodgkin, *Nat. Immunol.* **5**, 55 (2004).
- A. Kallies *et al.*, *J. Exp. Med.* **200**, 967 (2004).
- Materials and methods are available as supporting material on Science Online.
- A. V. Gett, P. D. Hodgkin, *Nat. Immunol.* **1**, 239 (2000).
- E. K. Deenick, A. V. Gett, P. D. Hodgkin, *J. Immunol.* **170**, 4963 (2003).
- E. D. Hawkins, M. L. Turner, M. R. Dowling, C. van Gend, P. D. Hodgkin, *Proc. Natl. Acad. Sci. U.S.A.* **104**, 5032 (2007).
- E. D. Hawkins, J. F. Markham, L. P. McGuinness, P. D. Hodgkin, *Proc. Natl. Acad. Sci. U.S.A.* **106**, 13457 (2009).
- S. L. Spencer, S. Gaudet, J. G. Albeck, J. M. Burke, P. K. Sorger, *Nature* **459**, 428 (2009).
- P. D. Hodgkin, J. H. Lee, A. B. Lyons, *J. Exp. Med.* **184**, 277 (1996).
- V. P. Badovinac, B. B. Porter, J. T. Harty, *Nat. Immunol.* **3**, 619 (2002).
- S. G. Tangye, D. T. Avery, E. K. Deenick, P. D. Hodgkin, *J. Immunol.* **170**, 686 (2003).
- R. J. De Boer, D. Homann, A. S. Perelson, *J. Immunol.* **171**, 3928 (2003).
- M. L. Turner, E. D. Hawkins, P. D. Hodgkin, *J. Immunol.* **181**, 374 (2008).
- G. U. Yule, *J. R. Stat. Soc.* **75**, 579 (1912).
- V. G. Subramanian, K. R. Duffy, M. L. Turner, P. D. Hodgkin, *J. Math. Biol.* **56**, 861 (2008).
- K. R. Duffy, V. G. Subramanian, *J. Math. Biol.* **59**, 255 (2009).
- C. Wellard, J. Markham, E. D. Hawkins, P. D. Hodgkin, *J. Theor. Biol.* **264**, 443 (2010).
- J. F. Markham, C. J. Wellard, E. D. Hawkins, K. R. Duffy, P. D. Hodgkin, *J. R. Soc. Interface* **7**, 1049 (2010).
- J. T. Chang *et al.*, *Science* **315**, 1687 (2007).
- R. N. Germain, *Science* **293**, 240 (2001).
- H. Cedar, Y. Bergman, *Nat. Rev. Immunol.* **11**, 478 (2011).
- D. A. Hume, *Blood* **96**, 2323 (2000).
- D. Day *et al.*, *Immunol. Cell Biol.* **87**, 154 (2009).

Acknowledgments: The data presented in this paper are tabulated in the main paper and in the Supporting Online Material. This work was supported by the Australian National Health and Medical Research Council (NHMRC) (program grant 575500; fellowships, E.D.H., M.R.D. and P.D.H.), Victorian State Government Operational Infrastructure support, Australian Government NHMRC Independent Research Institute Infrastructure Support Scheme (IRIS), and Science Foundation Ireland (grant RFP-ENE530, K.R.D.). J.F.M. was supported by National ICT Australia (NICTA), which is funded by the Australian government's Backing Australia's Ability initiative, in part through the Australian Research Council. The authors thank D. Day (Swinburne University of Technology) and Microsurfaces Pty. Ltd. for providing the microgrids (30), S. Nutt and A. Kallies for Blimp1 reporter mice, and R. DeBoer and D. Tartinton for helpful feedback on the manuscript. "A cell population system and process" (U.S. Patent Application 12/312,933) describes computational algorithms based on competing fates that can be used to calculate and predict immune outcomes. Authors who are listed inventors are P.D.H., M.R.D., C.J.W., J.F.M., and E.D.H.

Supporting Online Material

www.sciencemag.org/cgi/content/full/science.1213230/DC1
Materials and Methods
Figs. S1 to S5
References

26 August 2011; accepted 29 November 2011
Published online 5 January 2012;
10.1126/science.1213230

Asymmetric B Cell Division in the Germinal Center Reaction

Burton E. Barnett,^{1,3} Maria L. Ciocca,^{1,3} Radhika Goenka,² Lisa G. Barnett,³ Junmin Wu,^{1,3} Terri M. Laufer,^{3,4} Janis K. Burkhardt,^{2,5} Michael P. Cancro,² Steven L. Reiner^{1,3,*†}

Lifelong antibody responses to vaccination require reorganization of lymphoid tissue and dynamic intercellular communication called the germinal center reaction. B lymphocytes undergo cellular polarization during antigen stimulation, acquisition, and presentation, which are critical steps for initiating humoral immunity. Here, we show that germinal center B lymphocytes asymmetrically segregate the transcriptional regulator Bcl6, the receptor for interleukin-21, and the ancestral polarity protein atypical protein kinase C to one side of the plane of division, generating unequal inheritance of fate-altering molecules by daughter cells. Germinal center B lymphocytes from mice with a defect in leukocyte adhesion fail to divide asymmetrically. These results suggest that motile cells lacking constitutive attachment can receive provisional polarity cues from the microenvironment to generate daughter cell diversity and self-renewal.

Humoral immunity requires an antigen-specific B cell to proliferate, differentiate, and self-renew. Refinement of antibody responses occurs in the germinal center (GC), a dynamic lymphoid structure where B cells with high-affinity receptors are selected to proliferate and give rise to antibody-secreting plasma cells and memory B cells (1, 2). Intravital imaging has indicated that B cells engage in prolonged motile contacts with follicular helper T (T_{FH}) cells before dividing and entering the GC (3, 4). In the GC, B cells acquire antigen from synapsis with follicular dendritic cells (FDCs) (5, 6), and clones with higher-affinity receptors are thought to compete for subsequent contact with T_{FH} cells by presenting greater abundance of antigen (3, 7). However, the signals that promote disparate fate choices and regeneration of selected B cells are incompletely understood.

T lymphocytes engaged in immune responses appear to obtain polarity cues from antigen-presenting cells, yielding asymmetric division and diversification of daughter cell fates (8–10). Selection of B cells before and within the GC is linked to acquisition and presentation of antigen, processes characterized by provisional polarity of B cells (11). Therefore, we asked whether selected B cells might receive external polarity cues that could foster asymmetric division. To test this,

we examined the morphology of splenic GC B cells from immunized mice to ascertain localization of key proteins (12). We initially examined the receptor for interleukin-21 (IL-21R) and the transcriptional regulator Bcl6, which function to

initiate and maintain GC B cell identity, respectively (13–16).

In GC B cells undergoing mitosis 8 days after immunization, Bcl6 and IL-21R asymmetrically segregated to one side of the plane of division in 44 and 43% of cells, respectively (Fig. 1A). In contrast, the transcription factor interferon regulatory factor 4 (IRF4) (17) and the transmembrane receptor B220 were symmetrically distributed (11% asymmetric). Additionally, we observed asymmetry of Bcl6 in mitotic cells earlier (day 5) and later (day 15) after immunization (Fig. 1B). In premitotic GC B cells, Bcl6 was localized within the nucleus, whereas IL-21R and the cell-polarity regulator atypical protein kinase C ζ (PKC ζ) colocalized with the microtubule organizing center (MTOC) in a polarized manner (fig. S1). PKC ζ remained polarized in mitotic cells (Fig. 1C), suggesting that B cell asymmetric division has evolutionarily conserved features (8–11, 18).

GC B cell division is thought to occur in a zone relatively free of FDCs and T_{FH} cells (7). Thus, we tested whether B cells could break free of polarity cues and retain an imprint of asymmetry. We mechanically disrupted splenic

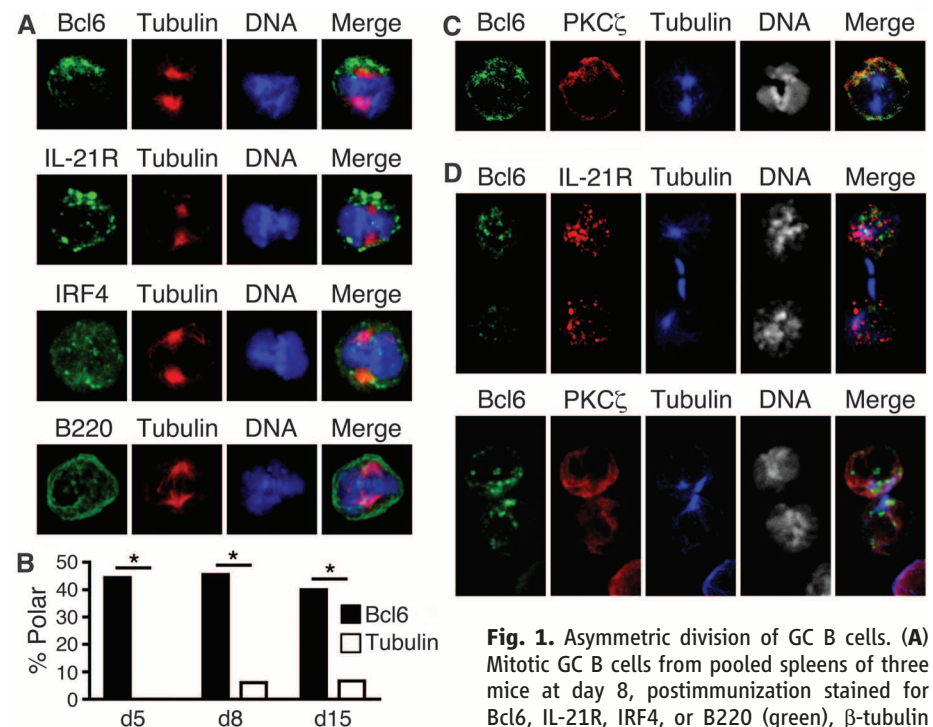


Fig. 1. Asymmetric division of GC B cells. (A) Mitotic GC B cells from pooled spleens of three mice at day 8, postimmunization stained for Bcl6, IL-21R, IRF4, or B220 (green), β -tubulin (red), and DNA (blue). Compared to tubulin: Bcl6 asymmetry 44%, $n = 16$ mitoses, $P < 0.05$; IL-21R asymmetry 43%, $n = 14$, $P < 0.05$; IRF4 asymmetry 11%, $n = 18$, $P > 0.05$; B220 asymmetry 11%, $n = 18$, $P > 0.05$. (B) Asymmetric mitoses of Bcl6 (black bars) and tubulin (white bars) at days 5, 8, and 15 postimmunization. $n = 9, 16, 15$, respectively; $*P < 0.05$. P values were calculated with χ^2 tests. (C) Bcl6 and PKC ζ cosegregate asymmetrically during mitosis at day 8 postimmunization. Bcl6 and PKC ζ were asymmetric in 44 and 38% of mitoses, respectively, and were 100% cosegregated when both were asymmetric. $n = 16$ mitoses. (D) Isolated GC B cells undergoing cytokinesis maintain asymmetry. Bcl6, IL-21R, and PKC ζ were asymmetric in 45, 53, and 61% of divisions, respectively, and had 100% cosegregation when both were asymmetric. Analysis of Bcl6 and IL-21R, $n = 13$ cytokinetic cells; analysis of Bcl6 and PKC ζ , $n = 13$. All data are representative of two or more experiments.

¹Abramson Family Cancer Research Institute, University of Pennsylvania, Philadelphia, PA 19104, USA. ²Department of Pathology and Laboratory Medicine, University of Pennsylvania Perelman School of Medicine, Philadelphia, PA 19104, USA. ³Department of Medicine, University of Pennsylvania Perelman School of Medicine, Philadelphia, PA 19104, USA. ⁴Philadelphia Veterans Affairs Medical Center, Philadelphia, PA 19104, USA. ⁵Children's Hospital of Philadelphia, Philadelphia, PA 19104, USA.

*To whom correspondence should be addressed. E-mail: sreiner@columbia.edu

†Present address: Department of Microbiology and Immunology and Department of Pediatrics, College of Physicians and Surgeons of Columbia University, New York, NY 10032, USA.

intercellular contacts into single-cell suspensions and cultured unattached GC B cells for 3 hours in the presence of cytochalasin B to arrest cells undergoing cytokinesis. Cells cleaving in isolation retained the property of asymmetric distribution of Bcl6, IL-21R, and PKC ζ (Fig. 1D). In mitotic and cytokinetic cells, PKC ζ cosegregated with Bcl6 and IL-21R in all instances where both were asymmetric (Fig. 1, C and D). PKC ζ also colocalized with IL-21R at the single MTOC of interphase blasts in vivo (fig. S1), as has been observed in vitro for PKC ζ and antigen-presenting components of the B cell synapse (11). Thus, the daughter cell with preferential inheritance of Bcl6, IL-21R, and PKC ζ may have arisen from the side of the B cell that was once proximal and presenting antigen to a T_{FH} cell.

To determine whether T_{FH} cell-associated signals promote mitotic B cell polarity, we stim-

ulated naïve, CD23⁺ B cells in vitro with or without addition of an antibody to CD40 (anti-CD40) to mimic a critical signal from T_{FH} cells. Anti-CD40 in the culture media increased mitotic PKC ζ polarity compared with baseline stimulation, whereas provision of anti-CD40 by adherence to the culture-dish bottom further increased the frequency of mitotic PKC ζ asymmetry (Fig. 2A). Thus, CD40 signaling, as occurs when B cells present antigen to and receive cognate help from T_{FH} cells, appears to facilitate asymmetry by providing and/or focusing a polarity cue to the B cell.

Further evidence that extrinsic contact may be critical for B cell asymmetric division was obtained from two separate in vivo approaches. First, we transferred naïve B cells into lymphocyte-deficient mice (*Rag1*^{-/-}) wherein excess growth factors support brisk lymphocyte division without the need for antigen stimulation or cell-cell contact. Unimmunized B cells undergoing ho-

meostatic division exhibited infrequent polarity of PKC ζ (11%) compared with B cells from immunized mice (38%) (Fig. 2B).

It has been suggested that optimal B cell–T cell adhesion requires LFA-1–intercellular adhesion molecule-1 (ICAM-1) interactions (19), and humans with leukocyte adhesion defects may exhibit impaired antibody production (20). Second, we tested whether ICAM-1 is required for B cells to divide asymmetrically after immunization. The frequencies of mitotic GC B cells that asymmetrically segregated Bcl6 and PKC ζ were substantially reduced in the absence of ICAM-1 (Fig. 2B), suggesting that cell-cell adhesion may be critical to the polarity cue received by asymmetrically dividing B cells. The absence of optimal cell adhesion had functional correlates beyond defective asymmetric B cell division insofar as immunized *Icam1*^{-/-} mice exhibited substantial defects in generating antibody-secreting cells (Fig. 2C), despite relative preservation of germinal-center composition (fig. S2).

GC selection appears to license a B cell with a high-affinity receptor to proliferate (7). The present findings suggest that coupling receptor affinity to proliferation may do more than amplify the fittest cells. Coupling affinity to proliferation and asymmetric division may also provide the fittest cell with a robust mechanism, like that of a stem cell, to ensure its life-long renewal (8, 18). Further investigation will be required to identify the fate of daughter B cells arising from asymmetric divisions before and during the GC reaction and the requirements for cell diversification and regeneration in the immune response to pathogens and vaccines. Finally, it will be important to determine whether asymmetric division following facultative polarity is a widely conserved feature of mammalian differentiation and regeneration in normal and neoplastic cells.

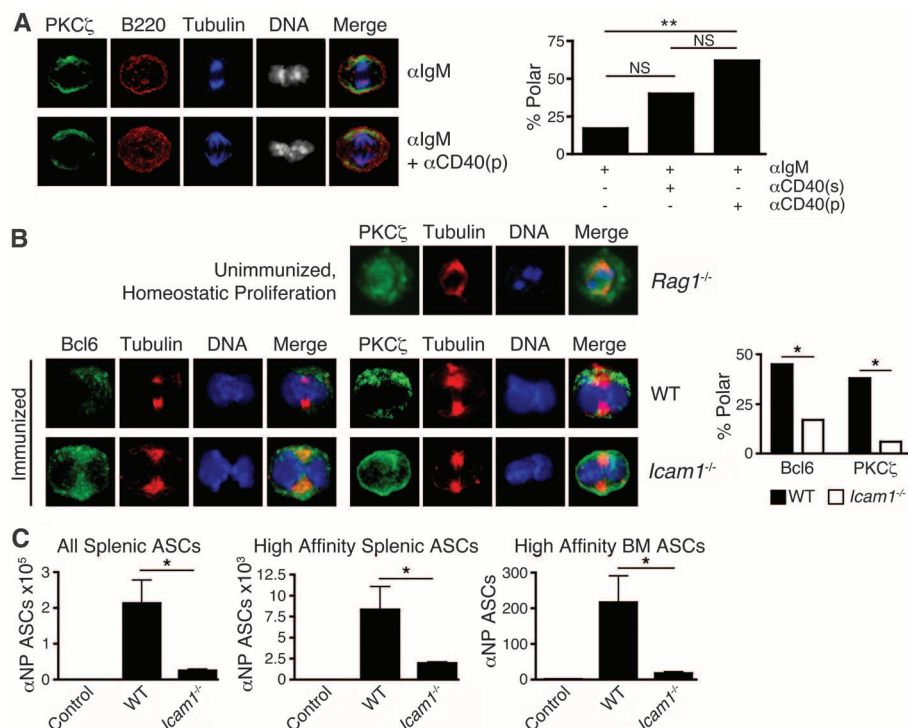


Fig. 2. Polarity cues are required for asymmetric division of B cells. **(A)** Naïve B cells simulated 36 hours with anti-immunoglobulin M, with or without anti-CD40 to mimic a key contact-mediated signal from T_{FH} cells. Anti-CD40 was withheld, added solubly to media (s), or coated on cell culture plates (p). (Left) Representative microscopy of no added anti-CD40 (upper row) and plate-bound anti-CD40 (lower row). (Right) Quantification of mitoses exhibiting asymmetry of PKC ζ in indicated conditions. Left to right: $n = 18, 20$, and 21 mitoses, respectively. NS: $P > 0.05$. ** $P < 0.01$ by χ^2 test. **(B)** (Upper row) B cells undergoing homeostatic proliferation in *Rag1*^{-/-} mice exhibit low incidence of asymmetric mitoses (11%, $n = 19$ mitoses from pooled spleens of three recipients) compared with GC B cells from immunized mice (38%, $n = 16$ mitoses); $P < 0.05$. (Lower rows) Defective asymmetric division in adhesion-deficient mice. (Left) GC B cells from three pooled spleens of day-8 immunized wild-type (WT) and *Icam1*^{-/-} mice stained for indicated components. (Right) quantification of GC B cell mitoses exhibiting asymmetry of Bcl6 and PKC ζ from indicated genotypes. Left to right: $n = 33, 18, 16$, and 18 mitoses, respectively. * $P < 0.05$ by χ^2 test. Similar results obtained at day 5. **(C)** *Icam1*^{-/-} mice have impaired antibody responses to immunization. Quantification of antibody-secreting cells (ASCs) from immunized WT and *Icam1*^{-/-} mice at day 14 postimmunization, compared with adjuvant-only injected WT mice (control). $n = 6$ mice per group, NS: $P > 0.05$. * $P < 0.05$ by unpaired student's t test. All data are representative of two or more experiments.

References and Notes

1. I. C. MacLennan, *Annu. Rev. Immunol.* **12**, 117 (1994).
2. S. L. Nutt, D. M. Tarlinton, *Nat. Immunol.* **12**, 472 (2011).
3. H. Qi, J. L. Cannons, F. Klauschen, P. L. Schwartzberg, R. N. Germain, *Nature* **455**, 764 (2008).
4. T. Okada et al., *PLoS Biol.* **3**, e150 (2005).
5. K. Suzuki, I. Grigorova, T. G. Phan, L. M. Kelly, J. G. Cyster, *J. Exp. Med.* **206**, 1485 (2009).
6. T. A. Schwickert et al., *Nature* **446**, 83 (2007).
7. G. D. Victora et al., *Cell* **143**, 592 (2010).
8. J. T. Chang et al., *Science* **315**, 1687 (2007).
9. J. T. Chang et al., *Immunity* **34**, 492 (2011).
10. J. Olliaro et al., *J. Immunol.* **185**, 367 (2010).
11. M. I. Yuseff et al., *Immunity* **35**, 361 (2011).
12. Materials and methods are available as supporting material on Science Online.
13. A. L. Dent, A. L. Shaffer, X. Yu, D. Allman, L. M. Staudt, *Science* **276**, 589 (1997).
14. B. H. Ye et al., *Nat. Genet.* **16**, 161 (1997).
15. M. A. Linterman et al., *J. Exp. Med.* **207**, 353 (2010).
16. C. Tunyaplin et al., *J. Immunol.* **173**, 1158 (2004).
17. U. Klein et al., *Nat. Immunol.* **7**, 773 (2006).

18. J. A. Knoblich, *Nat. Rev. Mol. Cell Biol.* **11**, 849 (2010).
 19. J. L. Cannons *et al.*, *Immunity* **32**, 253 (2010).
 20. A. Fischer, A. Durandy, G. Sterkers, C. Griscelli, J. Immunol. **136**, 3198 (1986).

Acknowledgments: We thank J. Chaix, S. Gordon, M. Paley, and L. Rupp for assistance. We are grateful for funding from the NIH (grants AI042370 and AI076458 to S.L.R.,

T32GM07229 to B.E.B., T32HD007516 and 3T32GM007170-3651 to M.L.C., T32AI055428 to R.G., and AI065644 to J.K.B.), the U.S. Department of Defense (grant W81WWXWH1010185 to M.P.C.), Veterans Administration (grant BX000435 to T.M.L.), and the Abramson family (to S.L.R.). The data reported in this paper are tabulated in the main paper and in the supporting online material. The authors declare no conflicts of interest.

Supporting Online Material

www.sciencemag.org/cgi/content/full/science.1213495/DC1
 Materials and Methods
 Figs. S1 and S2

2 September 2011; accepted 4 November 2011
 Published online 15 December 2011;
 10.1126/science.1213495

Tuning of Natural Killer Cell Reactivity by NKp46 and Helios Calibrates T Cell Responses

Emilie Narni-Mancinelli,^{1,2,3} Baptiste N. Jaeger,^{1,2,3} Claire Bernat,^{1,2,3} Aurore Fenis,^{1,2,3} Sam Kung,⁴ Aude De Gassart,^{1,2,3} Sajid Mahmood,⁴ Marta Gut,⁵ Simon C. Heath,⁵ Jordi Estellé,⁵ Elodie Bertoso,^{1,2,3} Frédéric Vely,^{1,2,3,8} Louis N. Gastinel,⁶ Bruce Beutler,⁷ Bernard Malissen,^{1,2,3} Marie Malissen,^{1,2,3} Ivo G. Gut,⁵ Eric Vivier,^{1,2,3,8*} Sophie Ugolini^{1,2,3,9*}

Natural killer (NK) cells are lymphocytes involved in antimicrobial and antitumoral immune responses. Using *N*-ethyl-*N*-nitrosourea mutagenesis in mice, we identified a mutant with increased resistance to viral infections because of the presence of hyperresponsive NK cells. Whole-genome sequencing and functional analysis revealed a loss-of-function mutation in the *Ncr1* gene encoding the activating receptor NKp46. The down-regulation of NK cell activity by NKp46 was associated with the silencing of the *Helios* transcription factor in NK cells. NKp46 was critical for the subsequent development of antiviral and antibacterial T cell responses, which suggests that the regulation of NK cell function by NKp46 allows for the optimal development of adaptive immune responses. NKp46 blockade enhanced NK cell reactivity in vivo, which could enable the design of immunostimulation strategies in humans.

Natural killer (NK) cells are cytolytic and cytokine-producing lymphocytes that can directly kill transformed and microbe-infected cells. They also participate in the shaping of adaptive immune responses (1–3). While screening for altered NK cell phenotypes in C57BL/6J mice carrying *N*-ethyl-*N*-nitrosourea (ENU)-induced mutations, we identified a mouse pedigree with NK cells that were hyperreactive in responses to the prototypic NK cell tumor target cell line, YAC-1, in vitro (Fig. 1A). These mice were bred for the establishment of a homozygous stock. The phenotype was named *Noé* and appeared to result from a single autosomal recessive mutation. Furthermore, resting *Noé* NK cells were more responsive when stimulated by monoclonal antibody (mAb) cross-linking of the NK1.1-activating receptor (fig. S1A). This higher reac-

tivity of *Noé* NK cells was not associated with an increase in NK1.1 cell surface expression (fig. S1B) and was also observed after stimulation with a combination of interleukin 12 (IL-12) and IL-18 cytokines (fig. S1C). In addition, NK1.1-stimulated *Noé* NK cells were less sensitive to the phosphatidylinositol 3-kinase inhibitor wortmannin, which prevents signal transduction (fig. S1D). Thus, *Noé* NK cells displayed a broad increase in reactivity to various stimuli in vitro, compatible with a profound change in the threshold of NK cell responses. Mixed-bone marrow chimera experiments revealed that the hyperresponsiveness of *Noé* NK cells resulted from an intrinsic cellular modification (fig. S2).

We then investigated whether the *Noé* NK cells were also hyperresponsive in vivo. In the C57BL/6J background, NK cells play a key role in the early control of mouse cytomegalovirus (MCMV) infection by recognizing the viral m157 protein via the activating receptor Ly49H (4, 5). Both *Noé* and wild-type (WT) animals survived infection with low doses of MCMV (fig. S3A), but only *Noé* mice survived infection with intermediate doses (Fig. 1B). High doses were lethal for both strains, but *Noé* mice survived significantly longer than WT animals (fig. S3B). This greater resistance of *Noé* mice was dependent on NK cells, as the injection of NK cell-depleting NK1.1 monoclonal antibody (mAb) resulted in the death of *Noé* mice after infection (Fig. 1C). Consistent with their resistance to MCMV infection, *Noé* mice had

MCMV loads in the spleen and liver that were four-fifths and five-sixths, respectively, of those in WT animals 4 days after infection (Fig. 1D). We detected no difference in the frequencies of Ly49H⁺ NK cell between *Noé* and WT mice (fig. S4), but the frequencies of interferon- γ (IFN- γ)-producing and degranulating CD107a⁺ NK cells ex vivo were $53 \pm 11\%$ and $33 \pm 8\%$ (means \pm SD) higher, respectively, in *Noé* mice than in WT mice 1.5 days after infection (Fig. 1E). These results suggested that *Noé* mice were more resistant to MCMV infection because of a greater responsiveness of NK cells in vivo.

We then sought to identify the recessive mutation responsible for the broad hyperresponsiveness of *Noé* NK cells by resequencing the whole genome of a *Noé* mouse and a control WT mouse (table S1). We focused on a mutation of the *Ncr1* gene that was present in all *Noé* mice. *Ncr1* encodes the NK cell-activating receptor NKp46, which is conserved in mammals and expressed by all mature NK cells (6). This mutation resulted in the replacement of the tryptophan 32 residue with an arginine residue (W32R) (fig. S5). *Ncr1* transcript levels were found to be similar in *Noé* and WT NK cells (fig. S6A), but we were unable to detect NKp46 at the surface of NK cells from *Noé* mice (Fig. 2A and fig. S6B). Flow cytometric analysis of human embryonic kidney (HEK) 293T cells transfected with the WT and *Noé* NKp46 sequences tagged at the N terminus (fig. S7A) revealed that, even though the NKp46 protein bearing the W32R substitution was detected intracellularly, it was not expressed at the cell surface (fig. S7B). The W32R mutation thus abolishes the cell surface expression of NKp46 on the NK cells of *Noé* mice.

We then used genetic complementation to formally assess the direct involvement of the NKp46^{W32R} mutation in the hyperresponsiveness of *Noé* NK cells. Mice homozygous for the W32R mutation, henceforth referred as to *Ncr1*^{Noé/Noé} mice, were crossed with transgenic mice in which the cell surface expression of human NKp46 protein is restricted on NK cells (huNKp46 Tg) (6). We analyzed F₂ animals lacking mouse NKp46 expression but expressing the human NKp46 protein (*Ncr1*^{Noé/Noé} huNKp46 Tg) and compared them with their nontransgenic *Ncr1*^{Noé/Noé} or WT littermates (fig. S8). After coculture with YAC-1 tumor targets, the reactivity of IL-2-activated *Ncr1*^{Noé/Noé} NK cells complemented with the human NKp46 protein was similar to that of WT NK cells (Fig. 2B). Human NKp46 also restored the sensitivity of *Ncr1*^{Noé/Noé} mice to MCMV infection (Fig. 2C). Thus, the

¹Centre d'Immunologie de Marseille-Luminy, Aix-Marseille University, Campus de Luminy case 906, 13288 Marseille, France.
²INSERM U1104, 13288 Marseille, France. ³CNRS, UMR7280, 13288 Marseille, France. ⁴Apotex Center, Department of Immunology, University of Manitoba, Winnipeg, Manitoba R3E 0T5, Canada. ⁵Centre Nacional d'Anàlisi Genòmica (CNAG), Parc Científic de Barcelona, 08028 Barcelona, Spain. ⁶INSERM U850, University of Limoges, University Hospital Limoges, 87060 Limoges, France. ⁷Center for Genetics of Host Defense, University of Texas Southwestern Medical Center, Dallas, TX 75390, USA. ⁸Assistance Publique—Hôpitaux de Marseille, Hôpital de la Conception, 13385 Marseille, France. ⁹Institut Paoli-Calmettes, Centre de Lutte Contre le Cancer, 13273 Marseille, France.

*To whom correspondence should be addressed. E-mail: vivier@ciml.univ-mrs.fr (E.V.); ugolini@ciml.univ-mrs.fr (S.U.)

NKp46^{W32R} mutation was responsible for the NK cell phenotype in *Noé* mice.

NKp46 is associated with immunoreceptor tyrosine-based activation motif (ITAM)-bearing polypeptides—such as CD3 ζ and FcR γ , which transduce potent activating signals when triggered (7)—and has been seen as a stimulatory receptor involved in effector functions (8–11). To confirm the role of NKp46 in the down-regulation of NK cell responsiveness, we studied *Ncr1*^{Cre/Cre} knock-in mice (12), in which the sequence of the NKp46 protein is WT but which also display a severe impairment of NKp46 expression on the plasma membrane of NK cells (fig. S9, A and B) because of a decrease in *Ncr1* transcript levels (fig. S9C). Like *Noé* NK cells, *Ncr1*^{Cre/Cre} NK cells were hyperresponsive to YAC-1 target cells and NK1.1 stimulation (fig. S9, D and E), and *Ncr1*^{Cre/Cre} mice were more resistant to MCMV infection than WT animals (fig. S9F). Thus, mutation of *Ncr1* resulted in enhanced NK cell reactivity and greater resistance to MCMV infection in two independent mouse genetic models.

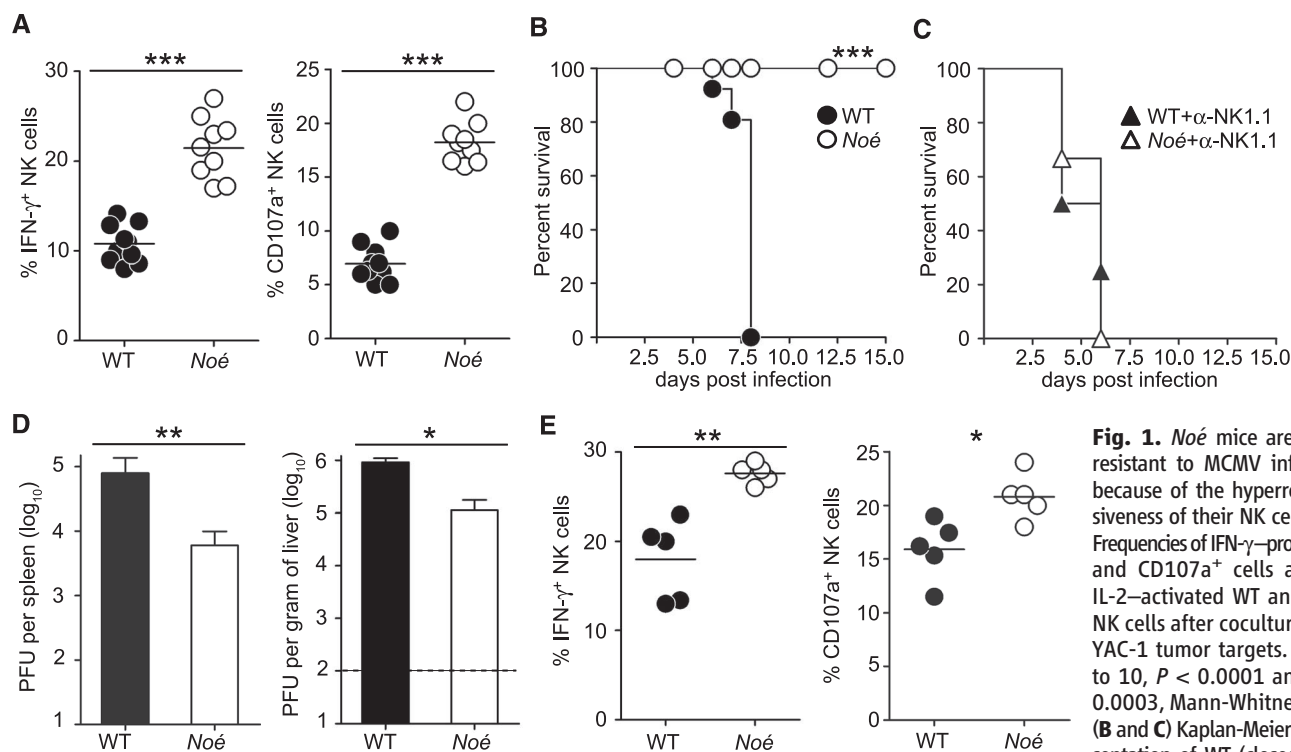
We investigated whether this phenotype was restricted to MCMV infection or could be generalized to other models of infection. We studied H1N1PR8 influenza, as *Ncr1* knockout mice have been reported to be highly susceptible to this infection (9). By contrast, *Ncr1*^{Noé/Noé} and *Ncr1*^{Cre/Cre} mice were more resistant to H1N1PR8 infection

than the WT (fig. S10, A and B). This greater resistance was associated with a higher frequency of IFN- γ -producing NK cells in the lungs of *Ncr1*^{Noé/Noé} mice 2 and 3 days after infection (fig. S10C). One possible explanation for this discrepancy is that the DNA deletions introduced in *Ncr1* knockout mice removed three potential intronic microRNAs (miRNAs) (miR-1195, miR-1935, and miR-3470a). It thus remains to be tested whether these deletions are responsible for the phenotypes described in this model, as described for the deletion of miR-211 in the intronic region of the *melastatin* gene, which is entirely responsible for the tumor phenotype of *melastatin* knockout mice (13).

NKp46 is expressed early in NK cell differentiation—after the induction of NK1.1 expression but before CD11b up-regulation—and is then uniformly expressed by all CD11b⁺ NK cells (6, 12). We dissected the mechanisms by which NKp46 affected NK cell development by identifying genes displaying differential expression between NK1.1⁺CD11b[−] and NK1.1⁺CD11b⁺ NK cells in WT mice, in a pan-genomic transcriptomic analysis (14). We identified the *Ilzf2* gene (also known as *Helios*), which encodes a member of the Ikaros transcription factor family, as being down-regulated in NK1.1⁺CD11b⁺ cells as compared with NK1.1⁺CD11b[−] NK cells (fig. S11, A and B). It is noteworthy that the ectopic expression of *Helios* in B cells modified their threshold of

reactivity, which led to hyperresponsiveness to antigen (15). *Helios* transcripts were twice as abundant in the NK1.1⁺CD11b⁺ NK cells of *Ncr1*^{Noé/Noé} mice as in those of WT mice (Fig. 2D). Genetic complementation of the *Ncr1*^{Noé} mutation in *Ncr1*^{Noé/Noé} huNKp46 Tg mice restored *Helios* transcript levels in NK1.1⁺CD11b⁺ NK cells to those in WT mice (Fig. 2D). Furthermore, *Helios* down-regulation was also impaired in NK1.1⁺CD11b⁺ NK cells from *Ncr1*^{Cre/Cre} mice (fig. S11C). Of note, the silencing of *Helios* in NK cells from *Ncr1*^{Noé/Noé} mice restored their reactivity to that of WT NK cells (Fig. 2E and fig. S12). These data are consistent with a model in which *Helios* down-regulation is involved in the regulation of NK cell reactivity via NKp46.

NK cell cytotoxicity and cytokine production help to shape adaptive T cell responses (2, 16, 17). During MCMV infection, NK cells can limit T cell responses by decreasing the amount of viral antigen available and by killing activated T cells (18, 19). We therefore investigated the effect of the hyperresponsiveness of the NK cells of *Ncr1*^{Noé/Noé} mice on T cell responses. In *Ncr1*^{Noé/Noé} mice, the frequency of splenic CD8⁺ T cells specific for the immunodominant MCMV peptide m45 presented by H-2D^b was lower than that in the WT, by a factor of two 7 days after infection and by a factor of three 10 days after infection (Fig. 3A). At the peak of the response, *Ncr1*^{Noé/Noé} mice had frequencies of IFN- γ -



and *Noé* mouse survival after infection with 5300 plaque-forming units (PFU) of MCMV per gram of body weight (gBW). *n* = 15 to 20, *P* < 0.0001, log-rank Mantel-Cox test. (C) NK cells from WT and *Noé* mice were depleted by treatment with NK1.1-specific mAb on the day before MCMV infection. (D) Viral loads (means \pm SD) in the spleen and liver of WT and *Noé* mice 4 days after MCMV infection. Dotted lines indicate the detection limit. *n* = 10, ***P* = 0.0079 and **P* = 0.0112, Mann-Whitney test. (E) Frequencies of IFN- γ -producing and CD107a⁺ NK cells in the spleen of WT or *Noé* mice 1.5 days after MCMV infection. *n* = 5, ***P* = 0.0079 and **P* = 0.0159, Mann-Whitney test. All data result from a pool of two to three independent experiments.

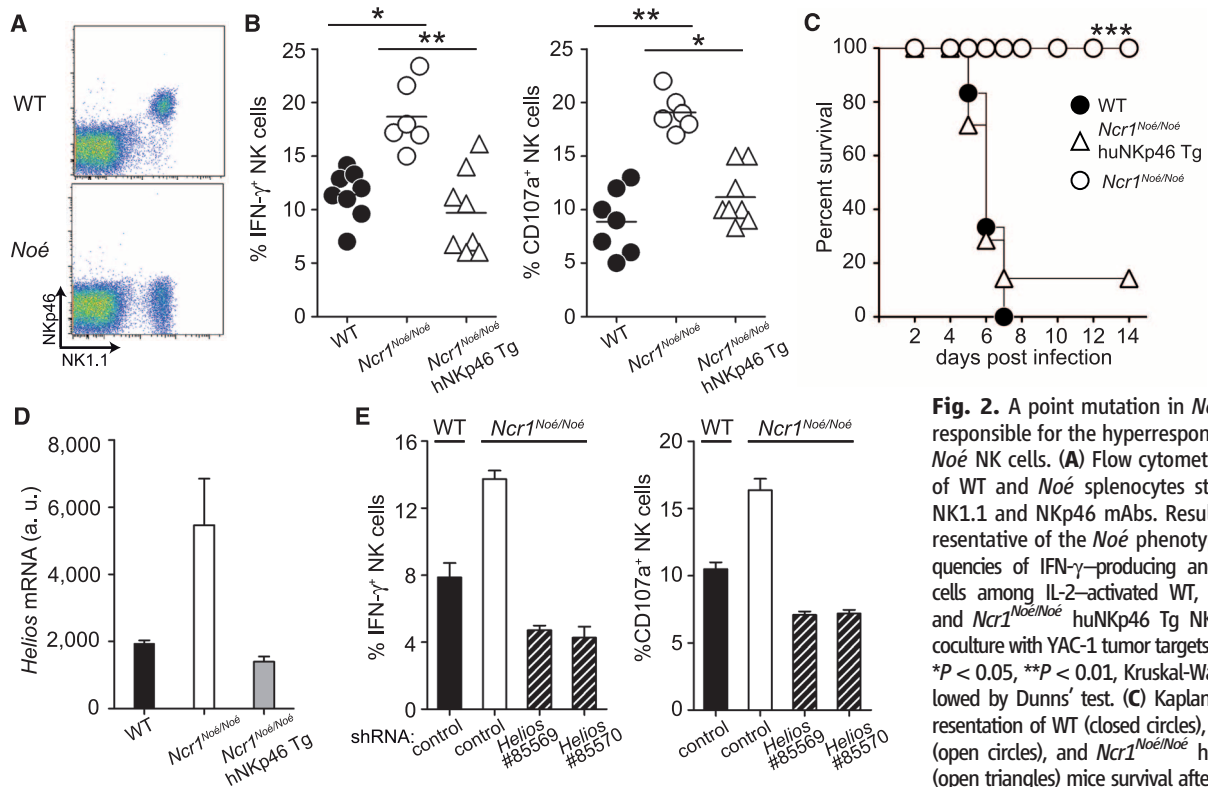


Fig. 2. A point mutation in *Ncr1* gene is responsible for the hyperresponsiveness of *Noé* NK cells. **(A)** Flow cytometric analysis of WT and *Noé* splenocytes stained with NK1.1 and NKp46 mAbs. Results are representative of the *Noé* phenotype. **(B)** Frequencies of IFN- γ -producing and CD107a⁺ cells among IL-2-activated WT, *Ncr1*^{Noé/Noé}, and *Ncr1*^{Noé/Noé} huNKp46 Tg NK cells after coculture with YAC-1 tumor targets. $n = 6$ to 8 , $*P < 0.05$, $**P < 0.01$, Kruskal-Wallis test followed by Dunn's test. **(C)** Kaplan-Meier representation of WT (closed circles), *Ncr1*^{Noé/Noé} (open circles), and *Ncr1*^{Noé/Noé} huNKp46 Tg (open triangles) mice survival after MCMV infection with 5300 PFU/gBW. $n = 8$ to 10 ,

$P < 0.0001$, log-rank Mantel-Cox test. In (A to C), data result from a pool of two to three independent experiments. **(D)** *Helios* transcripts were quantified by reverse transcription polymerase chain reaction in sorted CD11b⁺ bone marrow NK cells from WT, *Ncr1*^{Noé/Noé}, and *Ncr1*^{Noé/Noé} huNKp46 Tg mice. Results are normalized with respect to *Gapdh* (glyceraldehyde phosphate dehydrogenase) and expressed as means \pm SD in arbitrary units. The data correspond to two independent experiments with a total of six animals per group. **(E)** IL-2-activated WT and *Ncr1*^{Noé/Noé} NK cells were transduced with *Helios* or *EGFP* control short hairpin RNA. Data show frequencies of IFN- γ -producing and CD107a⁺ NK cells (means \pm SD) after coculture with YAC-1 tumor targets. The data correspond to two independent experiments with a total of six transductions per group.

producing CD8⁺ and CD4⁺ T cells lower than those of the WT by a factor of 2 to 3 (Fig. 3, B and C). In *Ncr1*^{Noé/Noé} huNKp46 Tg mice, the frequency of H-2D^b/m45⁺ CD8⁺ T cells (Fig. 3D) and of IFN- γ -producing cells among CD8⁺ (Fig. 3E) and CD4⁺ T cells (Fig. 3F) was restored to that in WT mice. Thus, the hyperresponsiveness of NK cells improved virus control but limited subsequent T cell responses.

Hyperresponsive NK cells might therefore be advantageous initially but become disadvantageous during a secondary challenge if the capacity to mount a memory immune response was impaired. We tested this hypothesis by analyzing the CD8⁺ T cell protective immunity generated in response to intracellular bacteria *Listeria monocytogenes* (*Lm*)-expressing ovalbumin (OVA), which is completely cleared after primary infection, unlike MCMV. During *Lm* infection, NK cells are activated by cytokines, such as IL-12 (20). Consistent with their broad hyperresponsiveness, the frequencies of IFN- γ -producing NK cells were $36\% \pm 3.2\%$ (mean \pm SD) higher in *Ncr1*^{Noé/Noé} mice than in the WT 24 hours after infection with *Lm*-OVA (Fig. 3G). After primary *Lm*-OVA infection and rechallenge 30 days later, the percentages of memory *Lm*-OVA-specific CD8⁺ T cells capable of producing IFN- γ were $35\% \pm 4.4\%$

and $36\% \pm 4\%$ (means \pm SD) lower in *Ncr1*^{Noé/Noé} mice than in WT mice and *Ncr1*^{Noé/Noé} huNKp46 Tg mice, respectively (Fig. 3H). This alteration in the quality of *Lm*-OVA-specific CD8⁺ memory T cells in *Ncr1*^{Noé/Noé} mice was associated with a bacterial load in the spleen 12 times that in WT mice and *Ncr1*^{Noé/Noé} huNKp46 Tg littermates (Fig. 3I). Thus, the hyperresponsiveness of NK cells during the T cell-priming phase affected the generation of fully protective memory T cells. Evolution in mammals may have resulted in the counterselection of hyperreactive innate immunity mechanisms despite their efficiency during the first encounter with a pathogen, to favor the emergence of adaptive immune responses, which efficiently control high doses of pathogens upon reexposure.

The dissection of NK cell education and tolerance has, to date, focused on the role of inhibitory receptors recognizing self-MHC (major histocompatibility complex) class I molecules. The engagement of these inhibitory receptors increases NK cell responsiveness (21–27). Our analysis of *Ncr1*^{Noé/Noé} mice implicated the activating receptor NKp46 as a checkpoint in NK cell tuning and revealed another aspect of NK cell education in which the engagement of NKp46 down-regulates NK cell responsiveness.

These results are consistent with observations made for other activating receptors (28–31).

Apart from the interaction between NKp46 and viral hemagglutinins reported in a previous study (32), no cellular ligand for NKp46 has yet been identified. We found that NKp46 mAbs blocked the activation of NK cells by autologous CD11c⁺-enriched spleen cells (fig. S13). In order to block NKp46 during NK cell development, we selectively depleted NK cells by injecting diphtheria toxin into NK-DTR/EGFP (NDE) transgenic mice, which express the diphtheria toxin receptor and enhanced green fluorescent protein (6), and then treated mice during NK cell repopulation with either a blocking NKp46 mAb or with an isotype control mAb for 13 days (Fig. 4A and fig. S14). After coculture with YAC-1 tumor targets, NK cells isolated from NKp46 mAb-treated animals had $60\% \pm 8\%$ and $38\% \pm 11\%$ (mean \pm SD) more IFN- γ -producing and CD107a⁺ NK cells, respectively, than NK cells from control mice (Fig. 4A). Thus, the treatment of NKp46-sufficient mice with blocking NKp46 mAbs mimicked the phenotype observed in *Ncr1*^{Noé/Noé} and *Ncr1*^{Cre/Cre} mice, which supports a model in which NK cell tuning via NKp46 occurs after interaction with endogenous ligands. The nature and regulation of the endogenous NKp46 ligands

Fig. 3. Hyperresponsive NK cells limit T cell immunity. (A to E) Mice were infected with a dose of 1600 PFU of MCMV/gBW. (A) Frequencies of MCMV-specific CD8⁺ T cells among total CD8⁺ T cells (means \pm SD) were measured by H-2D^b/m45 pentamer staining in spleens from WT (closed symbols) and *Ncr1^{Noe/Noe}* (open symbols) mice at the indicated time points after infection. $n = 5$ to 7, $*P < 0.05$ and $***P < 0.001$, two-way analysis of variance (ANOVA) with Bonferroni correction. (B and C) Ex vivo restimulation of (B) spleen H-2D^b/m45-specific CD8⁺ T cells or (C) liver CD4⁺ T cells. Frequencies of IFN- γ -producing cells among total CD8⁺ or CD4⁺ T cells are shown. $n = 5$ to 7, $**P < 0.01$ and $***P < 0.001$, Two-way ANOVA with Bonferroni correction. (D) Frequencies of H-2D^b/m45⁺CD8⁺ T cells among total CD8⁺ T cells in the spleen of WT, *Ncr1^{Noe/Noe}*, and *Ncr1^{Noe/Noe}* huNKP46 Tg littermates 7 days after infection. (E and F) Ex vivo restimulation of (E) spleen H-2D^b/m45-specific CD8⁺ T cells or (F) liver CD4⁺ T cells. The frequencies of IFN- γ -producing cells are shown for WT, *Ncr1^{Noe/Noe}*, and *Ncr1^{Noe/Noe}* huNKP46 Tg mice 7 days after infection. $n = 5$, $**P < 0.01$ and $***P < 0.001$, Kruskal-Wallis test followed by Dunn's test. (G) Mice were injected with 10^4 *Lm*-OVA bacteria, and the frequencies of IFN- γ -producing cells were determined in the spleen after 24 hours. $n = 5$, $*P = 0.0119$, Mann-Whitney test. (H and I) Mice were injected with 10^4 *Lm*-OVA bacteria and challenged 1 month later with 5×10^5 bacteria. (H) Five days after secondary challenge, the frequencies of H-2K^b/OVA⁺CD8⁺ T cells and IFN- γ -producing CD8⁺ T cells were determined in the spleen of WT, *Ncr1^{Noe/Noe}* and *Ncr1^{Noe/Noe}* huNKP46 Tg littermates. Data show the frequencies of IFN- γ -producing cells among H-2K^b/OVA⁺ CD8⁺ T cells. $n = 4$ to 10, $*P < 0.05$ and $**P < 0.01$, Kruskal-Wallis test followed by Dunn's test. (I) Bacterial loads (means \pm SD) in the spleen of WT, *Ncr1^{Noe/Noe}*, and *Ncr1^{Noe/Noe}* huNKP46 Tg littermates 2 days after secondary challenge. $n = 5$ to 10, $**P < 0.01$ and $***P < 0.001$, Kruskal-Wallis test followed by Dunn's test. All data result from a pool of two to four independent experiments.

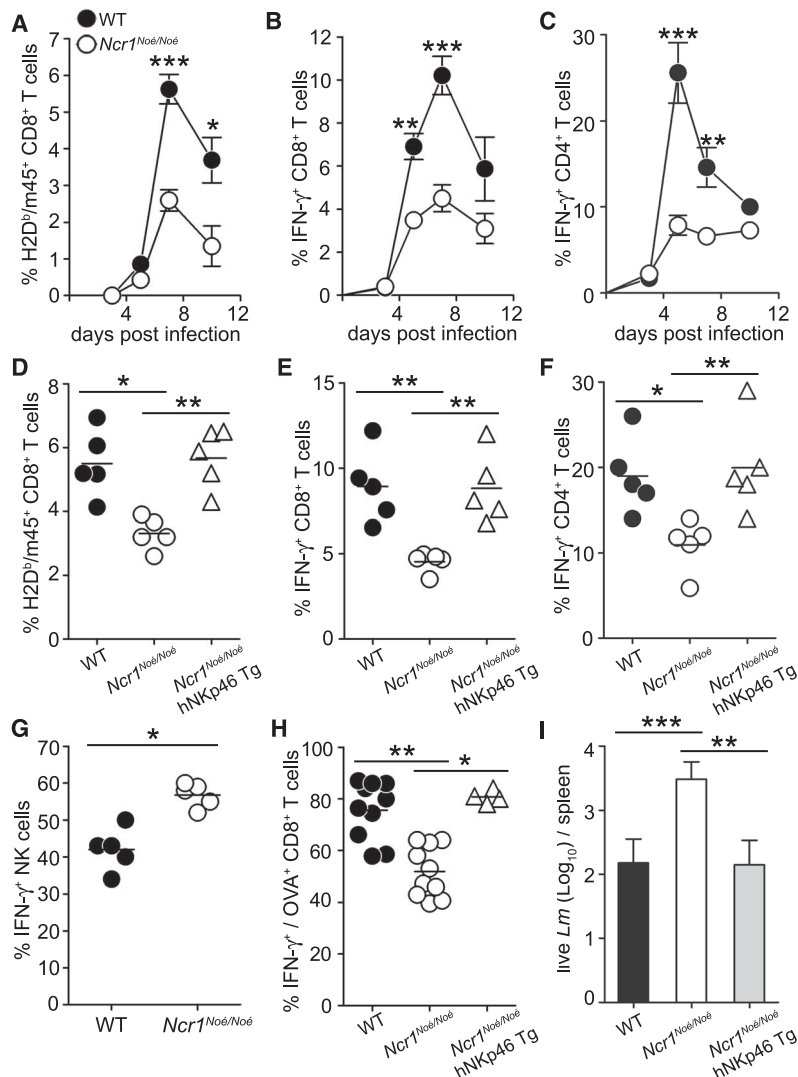
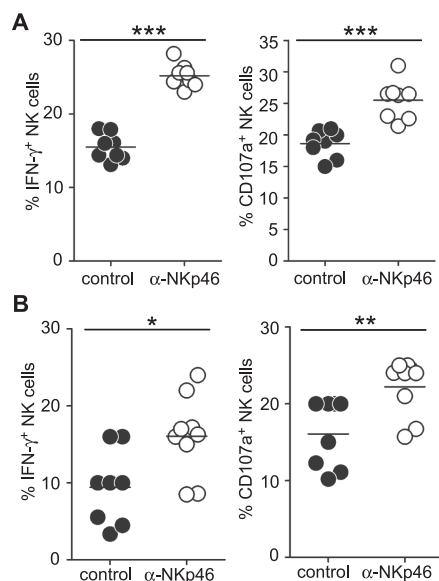


Fig. 4. NKp46 mAbs boost NK cell responsiveness. (A) NDE mice were treated with diphtheria toxin to deplete NK cells. Upon reconstitution of the NK cell compartment, mice were treated with NKp46 or control mAbs every 2 to 3 days for 9 days. Spleen cells from NKp46-treated and control antibody-treated mice were analyzed on day 13 (see fig. S13). Data show frequencies of IFN- γ -producing and CD107a⁺ cells among IL-2-activated NK cells from NDE mice after a coculture with YAC-1 tumor targets. $n = 8$, $***P = 0.0009$, Mann-Whitney test. (B) The same experiments were carried out in WT mice. $n = 8$ to 9, $*P = 0.03$ and $**P = 0.0081$, Mann-Whitney test. All data result from a pool of two independent experiments.



remain to be determined. Our findings suggested that NKp46 blockade could be used as an immunotherapeutic strategy to enhance NK cell ef-

fector functions. We thus evaluated whether we could modify the responsiveness of NK cells by injecting the NKp46 mAb, at steady state, in WT

mice. Short treatments lasting 24 to 72 hours were sufficient to saturate NKp46 receptors (fig. S15, A to D), but did not increase the reactivity of NK cells (fig. S15, E and F). By contrast, in vivo blockade of NKp46 by the mAb for 13 days was sufficient to enhance NK cell responsiveness to YAC-1 tumors (Fig. 4B). Altogether, our results reveal the role of the conserved activating NK cell receptor NKp46 in NK cell function. They also pave the way for the counterintuitive use of blocking NKp46 mAbs to boost NK cell activity, as an immunostimulation strategy of particular relevance for patients with T cell deficiencies, such as those occurring after hematopoietic stem cell transplantation.

References and Notes

1. S. H. Lee, T. Miyagi, C. A. Biron, *Trends Immunol.* **28**, 252 (2007).
2. D. H. Raulet, *Nat. Immunol.* **5**, 996 (2004).
3. E. Vivier et al., *Science* **331**, 44 (2011).
4. M. G. Brown et al., *Science* **292**, 934 (2001).
5. H. Arase, E. S. Mocarski, A. E. Campbell, A. B. Hill, L. L. Lanier, *Science* **296**, 1323 (2002).
6. T. Walzer et al., *Proc. Natl. Acad. Sci. U.S.A.* **104**, 3384 (2007).

7. A. Pessino *et al.*, *J. Exp. Med.* **188**, 953 (1998).
8. E. Cagnano *et al.*, *J. Invest. Dermatol.* **128**, 972 (2008).
9. R. Gazit *et al.*, *Nat. Immunol.* **7**, 517 (2006).
10. C. Gur *et al.*, *Nat. Immunol.* **11**, 121 (2010).
11. G. G. Halftick *et al.*, *J. Immunol.* **182**, 2221 (2009).
12. E. Narni-Mancinelli *et al.*, *Proc. Natl. Acad. Sci. U.S.A.* **108**, 18324 (2011).
13. C. Levy *et al.*, *Mol. Cell* **40**, 841 (2010).
14. L. Chiossone *et al.*, *Blood* **113**, 5488 (2009).
15. S. Dovati *et al.*, *J. Immunol.* **175**, 3508 (2005).
16. S. H. Lee, K. S. Kim, N. Fodil-Cornu, S. M. Vidal, C. A. Biron, *J. Exp. Med.* **206**, 2235 (2009).
17. S. N. Waggoner, M. Cornberg, L. K. Selin, R. M. Welsh, *Nature* **10.1038/nature10624** (2011).
18. D. M. Andrews *et al.*, *J. Exp. Med.* **207**, 1333 (2010).
19. K. Soderquest *et al.*, *J. Immunol.* **186**, 3304 (2011).
20. C. S. Tripp, S. F. Wolf, E. R. Unanue, *Proc. Natl. Acad. Sci. U.S.A.* **90**, 3725 (1993).
21. S. Kim *et al.*, *Nature* **436**, 709 (2005).
22. N. C. Fernandez *et al.*, *Blood* **105**, 4416 (2005).
23. N. Anfossi *et al.*, *Immunology* **25**, 331 (2006).
24. P. Brodin, T. Lakshminathan, S. Johansson, K. Kärre, P. Höglund, *Blood* **113**, 2434 (2009).
25. D. H. Raulet, R. E. Vance, *Nat. Rev. Immunol.* **6**, 520 (2006).
26. W. M. Yokoyama, S. Kim, *Immunity* **24**, 249 (2006).
27. M. T. Orr, L. L. Lanier, *Cell* **142**, 847 (2010).
28. D. E. Oppenheim *et al.*, *Nat. Immunol.* **6**, 928 (2005).
29. J. C. Sun, L. L. Lanier, *J. Exp. Med.* **205**, 1819 (2008).
30. S. K. Tripathy *et al.*, *J. Exp. Med.* **205**, 1829 (2008).
31. B. Zafirova *et al.*, *Immunity* **31**, 270 (2009).
32. O. Mandelboim *et al.*, *Nature* **409**, 1055 (2001).

Acknowledgments: We thank J. Ewbank, M. Bléry, J.-C. Andrau and P. Kruse for advice; D. Dilg for bioinformatics analysis; M. Dalod for MCMV reagents; M. C. Carroll for H1N1; G. Lauvau for *Lm*-OVA; M. Roger for mice handling; and the Centre d'Immunologie de Marseille-Luminy (CIML) mouse house and cytometry core facilities. This work was supported by an European Research Council advanced grant (E.V. and S.U.); Functional Genomics in Mutant Mouse Models as Tools to Investigate the Complexity of Human Immunological Disease (MUGEN), Network of Excellence and Mechanisms to Attack Steering Effectors of Rheumatoid Syndromes with Innovated Therapy Choices (MASTERSWITCH), Integrating Project from European Union (B.M. and M.M.); University of Manitoba Dean of Medicine Strategic Fund and Natural Sciences and Engineering Research Council (S.K.); Agence Nationale de la Recherche (E.V. and S.U.); Equipe labellisée "La Ligue," Ligue Nationale contre le Cancer (E.V. and S.U.); Agence pour la Recherche sur le Cancer (E.M.N.); Axa research fund (B.N.J.); and institutional grants from INSERM, CNRS, and Aix-Marseille University to the CIML. E.V. is a cofounder of and shareholder in Innate-Pharma. E.N.M., E.V., and S.U. designed, analyzed the experiments, and wrote the paper; C.B. identified *Noe* mouse during ENU screen; E.N.M. and A.F. performed and analyzed the experiments;

S.K. and S.M. provided lentiviral vectors and protocols to transduce NK cells; A.D.G. generated Helios-expressing vectors; B.N.J., F.V., M.G., I.G.G., J.E., and S.C.H. performed the sequencing and the bioinformatics analysis; L.N.G. generated the model for NKp46^{W32R}; M.M. and B.M. initiated and conducted the early phases of the ENU screen; and B.B. and E.B. helped in the ENU screen. The data reported in this paper are tabulated in the main paper and in the Supporting Online Material. Microarray data have been deposited at the National Center for Biotechnology Information GEO repository under accession no. GSE13229 and have been reported elsewhere (13). Ensembl accession number for *Ikzf2* is ENSMUST00000027146. Material Transfer Agreements are required for use of the following reagents: *Noe* mice, NKp46-specific mAb, NKp46^{Cre/Cre} mice, *Helios* short hairpin RNA, and control lentiviral vectors. The invention (U.S. Patent Application 61/499,485; NKp46-mediated NK cell tuning; E.N.M., S.U., and E.V.) relates to compounds that inhibit NKp46.

Supporting Online Material

www.sciencemag.org/cgi/content/full/335/6066/344/DC1
Materials and Methods
Figs. S1 to S15
Table S1
References (33–38)

21 October 2011; accepted 12 December 2011
10.1126/science.1215621

A SUMOylation-Dependent Transcriptional Subprogram Is Required for Myc-Driven Tumorigenesis

Jessica D. Kessler,^{1,2} Kristopher T. Kahle,^{3,4} Tingting Sun,¹ Kristen L. Meerbrey,^{1,2} Michael R. Schlabach,³ Earlene M. Schmitt,^{1,2} Samuel O. Skinner,^{1,5} Qikai Xu,³ Mamie Z. Li,³ Zachary C. Hartman,⁶ Mitchell Rao,² Peng Yu,² Rocio Dominguez-Vidana,^{1,2} Anthony C. Liang,³ Nicole L. Solimini,³ Ronald J. Bernardi,⁷ Bing Yu,⁸ Tiffany Hsu,^{1,2} Ido Golding,^{1,5} Ji Luo,⁸ C. Kent Osborne,^{9,10,11,12} Chad J. Creighton,^{9,13} Susan G. Hilsenbeck,^{9,10,13} Rachel Schiff,^{9,10,11,12} Chad A. Shaw,² Stephen J. Elledge,^{3*} Thomas F. Westbrook^{1,2,7,9*}

Myc is an oncogenic transcription factor frequently dysregulated in human cancer. To identify pathways supporting the Myc oncogenic program, we used a genome-wide RNA interference screen to search for Myc-synthetic lethal genes and uncovered a role for the SUMO-activating enzyme (SAE1/2). Loss of SAE1/2 enzymatic activity drives synthetic lethality with Myc. Inactivation of SAE2 leads to mitotic catastrophe and cell death upon Myc hyperactivation. Mechanistically, SAE2 inhibition switches a transcriptional subprogram of Myc from activated to repressed. A subset of these SUMOylation-dependent Myc switchers (SMS genes) is required for mitotic spindle function and to support the Myc oncogenic program. SAE2 is required for growth of Myc-dependent tumors in mice, and gene expression analyses of Myc-high human breast cancers suggest that low SAE1 and SAE2 abundance in the tumors correlates with longer metastasis-free survival of the patients. Thus, inhibition of SUMOylation may merit investigation as a possible therapy for Myc-driven human cancers.

Cancers are driven by genomic alterations that result in the activation of proto-oncogenes and the inactivation of tumor suppressor genes. Removing oncogene function can often reverse the tumorigenic phenotype, a phenomenon referred to as “oncogene addiction” (1, 2), and cancer researchers have focused on exploiting oncogene addiction by discovering and targeting cancer-causing oncogenes (3). However, many oncogenes such as *Ras* and *Myc* have proven difficult to inhibit pharmacologically, highlighting the need for complementary approaches. One such

approach is based on the concept of non-oncogene addiction (NOA), which postulates that oncogenic mutations confer dependencies on cellular processes that can be exploited therapeutically (4–6). The genes and signaling pathways underlying such oncogenic support processes are largely unexplored, and because these genes are not themselves oncogenes or otherwise mutated in cancer, they cannot be identified through direct analyses of cancer genomes and epigenomes.

The NOA pathways supporting the classical c-Myc oncogene (referred to herein as *Myc*) are

poorly understood. The *Myc* gene, which codes for a basic helix-loop-helix zipper transcription factor, is frequently dysregulated in cancer cells by amplification, mutation, overexpression, or protein stabilization (7). Amplification or overexpression of Myc occurs in ~25% of breast cancers (8–11) and are associated with poor prognosis (12). Genetic experiments have shown that Myc is required for tumor maintenance and progression in several types of malignancy (13, 14). However, despite three decades of research, there is no effective method to inhibit Myc in human cancer.

Oncogenic activation of Myc promotes a delicate balance in cells, conferring both pro- and anti-tumorigenic properties (2, 15, 16). This raises the interesting possibility that the balance between these opposing properties could be influenced by inhibiting *Myc* oncogenic support pathways. To

¹Verna and Marrs McLean Department of Biochemistry and Molecular Biology, Baylor College of Medicine, Houston, TX 77030, USA. ²Department of Molecular and Human Genetics, Baylor College of Medicine, Houston, TX 77030, USA. ³Howard Hughes Medical Institute, Department of Genetics, Harvard Medical School, Division of Genetics, Brigham and Women's Hospital, Boston, MA 02115, USA. ⁴Department of Neurosurgery, Massachusetts General Hospital, Boston, MA 02115, USA. ⁵Department of Physics, University of Illinois, Urbana, IL 61801, USA. ⁶Department of Clinical Cancer Prevention, M.D. Anderson Cancer Center, Houston, TX 77030, USA. ⁷Department of Pediatrics, Baylor College of Medicine, Houston, TX 77030, USA. ⁸Medical Oncology Branch, National Cancer Institute, Center Drive, Bethesda, MD 20892, USA. ⁹Dan L. Duncan Cancer Center, Baylor College of Medicine, Houston, TX 77030, USA. ¹⁰The Lester and Sue Smith Breast Center, Baylor College of Medicine, Houston, TX 77030, USA. ¹¹Department of Medicine, Baylor College of Medicine, Houston, TX 77030, USA. ¹²Department of Molecular and Cellular Biology, Baylor College of Medicine, One Baylor Plaza, Houston, TX 77030, USA. ¹³Division of Biostatistics, Baylor College of Medicine, Houston, TX 77030, USA.

*To whom correspondence should be addressed. E-mail: thomasw@bcm.edu (T.F.W.); selledge@genetics.med.harvard.edu (S.J.E.)

search for pathways required for cells to tolerate the *Myc* oncogene, we performed a genome-wide genetic screen for Myc–synthetic lethal (MySL) short hairpin RNAs (shRNAs) in human mammary epithelial cells (HMECs) engineered with an inducible *c-Myc*–estrogen receptor fusion transgene (Myc-ER HMECs) (fig. S1A). Induction resulted in increased expression of known Myc targets (fig. S1B) and a modest decrease in HMEC proliferation rate (fig. S1C). HMECs are ER-negative, and in the absence of Myc-ER, do not respond to tamoxifen (fig. S2). Using this system, we screened for shRNAs that alter cell fitness only in the presence of aberrant Myc signaling (screen design in Fig. 1A).

To identify MySL shRNAs, we transduced Myc-ER HMECs with a retroviral library of 74,905 shRNAs targeting 32,293 unique transcripts in three independent replicates. Transduced Myc-ER HMECs were propagated in the absence or presence of Myc-ER induction, and the relative change in shRNA-barcode abundance was measured in both cell states (Myc-off and Myc-on). We identified 403 MySL shRNAs exhibiting more than a twofold decrease in abundance in the Myc-on state (relative to the Myc-off state) ($P < 0.02$; Fig.

1B, fig. S3, and table S1). Content analysis [Gene Ontology (GO)] indicated that these candidates were highly enriched for ion channels and enzymes functioning in ubiquitin-like protein conjugation (including SUMOylation) ($P = 0.002$). Components of the mitotic spindle were also highly enriched among MySL candidates (Fig. 1C). Analysis of the MySL candidates using Human Protein Reference Database (HPRD) revealed a highly connected protein-protein interaction network, with many components of this network playing a role in the mitotic spindle (Fig. 1D; protein labels shown in fig. S4), suggesting that Myc hyperactivation may impose a stress on proper mitotic progression (17).

Among MySL candidates were several genes previously implicated in the survival of Myc hyperactivated cells (*GSK3 β* , *FBXW7*, and *PTK2*; fig. S5A) (18–20). In addition, shRNAs targeting MDM2 exhibited Myc synthetic lethality, whereas p53-targeting shRNAs enhanced proliferation in a Myc-selective manner (Fig. 1B and fig. S5B). Myc promotes p53 activation (2, 21–23), and these dependencies are consistent with the role of p53 defects in promoting Myc-induced tumorigenesis (2, 21, 22).

We also identified many candidates with previously unknown roles in Myc biology. To prioritize these, we rank ordered MySL genes using a modified two-way analysis of variance that we developed to summarize the effects of all shRNAs for a given gene. Using this method, we identified eight genes exhibiting Myc synthetic lethality with a $P \leq 0.001$ (table S2). The most significant candidate from both of these analyses was the SUMO-activating enzyme (SAE) subunit 2 (SAE2/UBA2) ($P < 0.00001$), a critical component of the sole SUMO-activating enzyme necessary for SUMO conjugation to proteins (24). Multiple SAE2-shRNAs exhibited Myc synthetic lethality in the primary screen (fig. S5C). The primary screen also identified SAE1, the heterodimeric partner of SAE2 (table S2). Thus, we focused on SAE and the potential synthetic lethal interaction between SUMOylation and Myc.

To explore the physiological importance of the Myc–SAE2 synthetic lethal interaction, we transduced Myc-ER HMECs with two independent shRNAs targeting SAE2 or a control shRNA and measured the effect of Myc activation on HMEC proliferation. SAE2-targeting shRNAs depleted SAE2 protein (fig. S6A) and profoundly

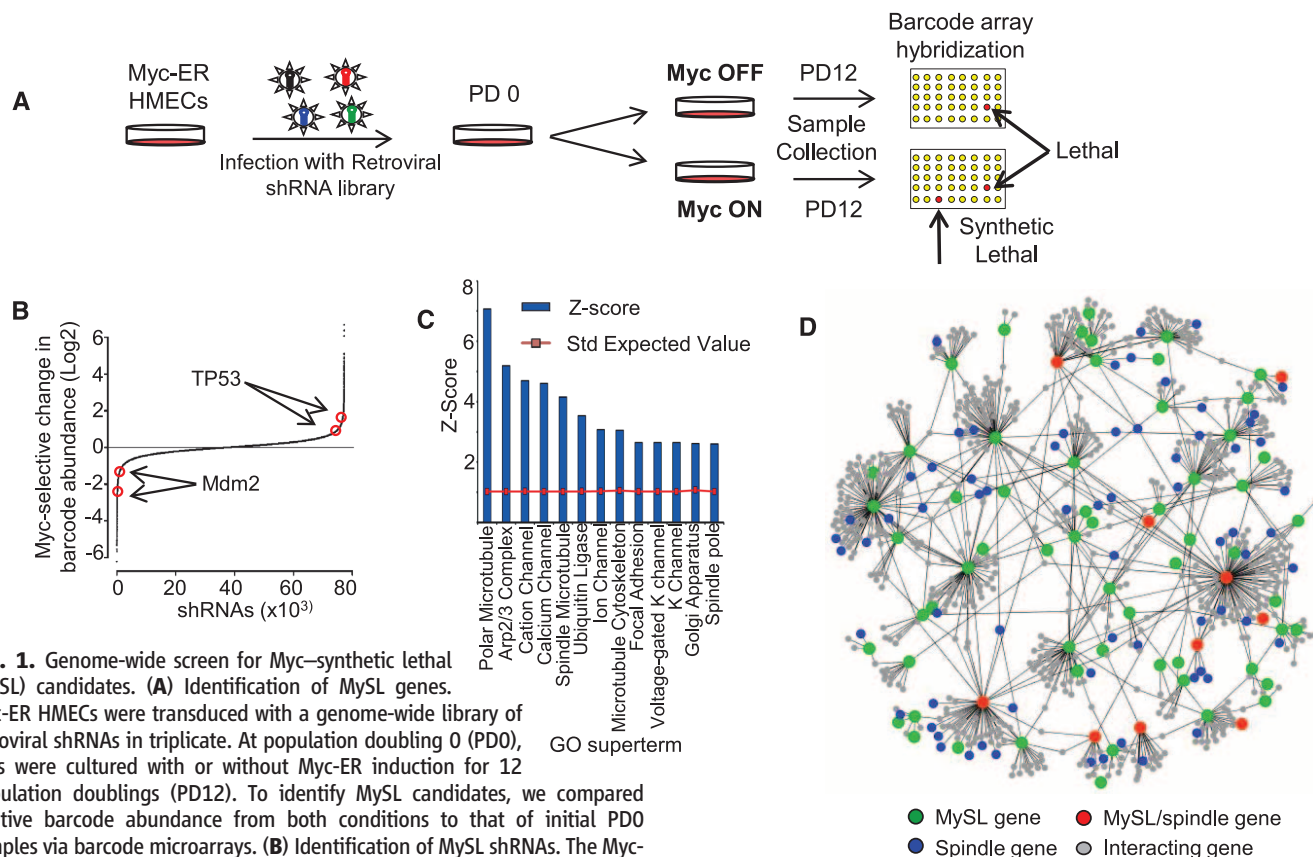


Fig. 1. Genome-wide screen for Myc–synthetic lethal (MySL) candidates. **(A)** Identification of MySL genes. Myc-ER HMECs were transduced with a genome-wide library of retroviral shRNAs in triplicate. At population doubling 0 (PD0), cells were cultured with or without Myc-ER induction for 12 population doublings (PD12). To identify MySL candidates, we compared relative barcode abundance from both conditions to that of initial PD0 samples via barcode microarrays. **(B)** Identification of MySL shRNAs. The Myc-selective effect of all shRNAs from the genome-wide library are graphed [y axis represents median difference between Myc-ER-on and Myc-ER-off groups (log 2)], with a ratio < -1.0 indicating a decrease of at least twofold. shRNAs are shown on the x axis (rank ordered by MySL effect). **(C)** Multiple cellular processes are required to tolerate the Myc oncogenic state. MySL candidates were analyzed for gene ontology (GO; Z scores for enriched cellular components and processes). **(D)** MySL proteins engage in a highly connected

interaction network that regulates the mitotic spindle. Protein-protein interactions between the top 100 MySL proteins were analyzed via HPRD. Green indicates a MySL protein, blue indicates a protein with a known role in mitotic spindle function, red indicates a MySL protein with a known role in spindle function, and gray indicates a protein that interacts with a MySL protein.

increased doubling time upon Myc induction (Fig. 2A, left graph; representative images in right panels). Similar results were observed when a constitutive Myc transgene was expressed together with shSAE2, indicating that these observations are not an artifact of the Myc-ER fusion system (fig. S7). Notably, two independent SAE2 shRNAs elicited a Myc-synthetic lethal phenotype (Fig. 2A), and restoration of SAE2 protein abundance with a SAE2 wild-type cDNA suppressed the MySL phenotype of SAE2 shRNA (Fig. 2, C and D; described below), indicating that the Myc-SAE2 synthetic phenotype is not due to an RNA interference (RNAi) off-target effect. Furthermore, multiple shRNAs targeting SAE1 and the downstream SUMO E2-conjugating enzyme UBE2I (UBC9) (fig. S6, B and C) were also synthetically lethal with Myc hyperactivation (Fig. 2A, middle and right graphs), demonstrating that SUMOylation interference is synthetically lethal with hyperactivated Myc.

We next investigated whether SUMOylation is required for cells to tolerate aberrant Myc activation. Depletion of SAE2 decreased abundance of SUMO1- or SUMO2/3-modified proteins (Fig. 2B), indicating global impairment of SUMOylation in these cells. To determine whether SAE2 enzymatic activity is required to support Myc, we engineered Myc-ER HMECs with an inducible SAE2-shRNA (pINDUCER11-shSAE2) (25) to-

gether with constitutive shRNA-resistant cDNAs encoding wild-type (WT) SAE2, catalytically inactive SAE2-C173S, or control enhanced green fluorescent protein (eGFP). SAE2 WT and mutant cDNAs restored SAE2 to endogenous SAE2 levels (Fig. 2C). Restoration of WT SAE2 suppressed the MySL phenotype of SAE2 shRNA (Fig. 2D). However, SAE2-C173S failed to suppress the synthetic lethality of SAE2-shRNA (Fig. 2D), indicating that SAE2 enzymatic activity is required to prevent the Myc-SAE2 synthetic lethal interaction. Together, these data suggest that SUMOylation is required for HMECs to tolerate aberrant Myc signaling.

A key question is how SAE2 depletion in the presence of Myc hyperactivation impairs proliferation. This could be due to changes in the cell cycle and/or cell death, so we examined the effects of Myc hyperactivation and SAE2 depletion on these processes. In SAE2-depleted cells, Myc induction increased the number of cells with a G₂/M DNA content (fig. S8A) accompanied by a concomitant accumulation of aberrant (>2N) DNA content (Fig. 3A and fig. S8A). These cell cycle defects were followed by a significant apoptotic response (Fig. 3B and fig. S8, B and C). The increase in G₂/M and >2N DNA content is characteristic of mitotic defects known to cause mitotic catastrophe and apoptosis. A potential mitotic defect is supported by our observation that MySL

genes are enriched for genes involved in the mitotic spindle (Fig. 1D), suggesting that Myc hyperactive cells might experience mitotic stress. To explore this possibility, we examined mitotic spindles in Myc hyperactive cells in the presence or absence of SAE2 depletion. As hypothesized, Myc-active, SAE2-inactive HMECs exhibited significantly more spindle defects (defects in >25% of all mitoses) than cells expressing Myc or shSAE2 alone (Fig. 3, C and D; $P = 7 \times 10^{-7}$). These defects, which included abnormal spindle number and lagging chromosomes, might explain the extensive aneuploidy and apoptosis observed. Collectively, these data suggest that the Myc-SAE2 genetic interaction results in dysregulation of the mitotic spindle, which may in turn contribute to synthetic lethality.

We next investigated how Myc hyperactivation and SAE2 depletion result in the mitotic aberrations. Myc hyperactivation induces different cellular consequences (e.g., proliferation, apoptosis, senescence) depending on the genetic and epigenetic context. If this is due to the ability of Myc to regulate distinct transcriptional programs, loss of SAE2 may lead to mitotic dysfunction by altering Myc's transcriptional program. Therefore, we used gene expression profiling to define the transcriptional effects of Myc with or without SAE2 inactivation. Myc activation alone in HMECs led to significant changes in the level

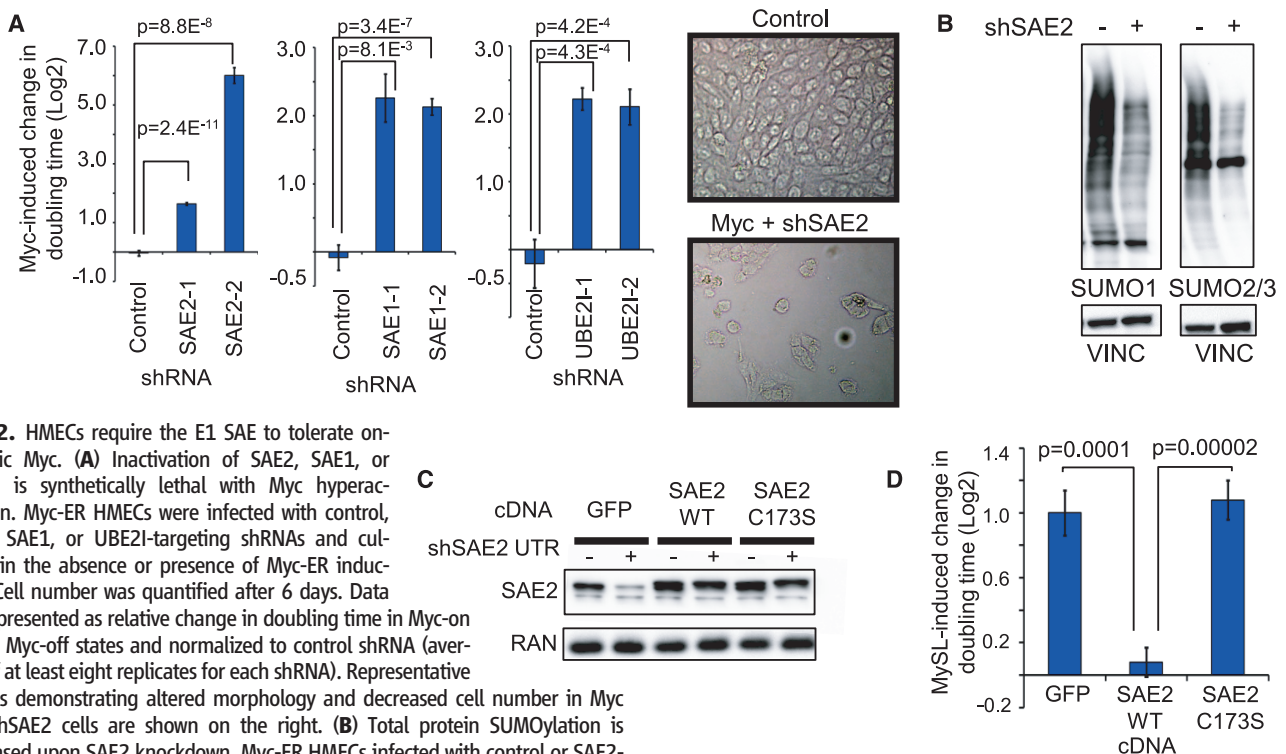


Fig. 2. HMECs require the E1 SAE to tolerate oncogenic Myc. (A) Inactivation of SAE2, SAE1, or UBE2I is synthetically lethal with Myc hyperactivation. Myc-ER HMECs were infected with control, SAE2, SAE1, or UBE2I-targeting shRNAs and cultured in the absence or presence of Myc-ER induction. Cell number was quantified after 6 days. Data are represented as relative change in doubling time in Myc-on versus Myc-off states and normalized to control shRNA (average of at least eight replicates for each shRNA). Representative images demonstrating altered morphology and decreased cell number in Myc and shSAE2 cells are shown on the right. (B) Total protein SUMOylation is decreased upon SAE2 knockdown. Myc-ER HMECs infected with control or SAE2-shRNA-encoding virus were analyzed for SUMO1, SUMO2/3, and vinculin (loading control) protein abundance. (C and D) SAE2 catalytic activity is required to tolerate Myc hyperactivation. Myc-ER HMECs transduced with a doxycycline (dox)-inducible shRNA targeting the SAE2 untranslated region (plnducer11-mir-SAE2 UTR-eGFP) were subsequently infected with a virus expressing GFP, SAE2 WT, or SAE2 C173S cDNAs. Western blots were performed to confirm depletion

of SAE2 (C). Cells were cultured with or without Dox and in the absence or presence of Myc-ER induction, and cell number was quantified after 8 days. The y axis indicates the relative change in growth of shSAE2-expressing cells due to Myc induction in the presence of the indicated transgenes (average of eight replicates) (D). Error bars in (A) and (D) represent the SEM.

of 605 mRNAs ($P < 0.05$; Fig. 3E, left panel). Surprisingly, 22.5% (86/383) of Myc-induced transcripts are not induced or become repressed in response to Myc when SAE2 is depleted (Fig. 3E, right panel), suggesting that a portion of the Myc transcriptional response is “switched” depending on the status of SAE2 function. Because the expression of these genes switches from Myc-induced to Myc-repressed in a SAE2-dependent manner, we termed these genes SUMOylation-dependent Myc switchers (or SMS genes).

MESH analysis revealed that SMS genes were significantly enriched for regulators of the mitotic spindle ($P < 4.9 \times 10^{-12}$) (fig. S9A), and mining of published literature revealed that 17 of 86 SMS genes have been shown genetically to participate in the assembly or integrity of mitotic spindles (26–31). Each of these spindle-related genes is induced by Myc hyperactivation (Fig. 3F and fig. S9B, blue bars) but exhibits a strong SAE2-dependent switch in their Myc response (Fig. 3F and fig. S9B, red bars). These observa-

tions highlight regulation of spindle assembly as a key vulnerability in cells harboring the Myc-active, SAE2-inactive state, and suggest that SMS genes may be linchpins in the Myc-SAE2 synthetic lethal relationship. To test this hypothesis, we examined whether SMS genes known to play a role in the mitotic spindle are synthetically lethal with Myc. We found that three of the top four SMS genes (*CASC5*, *BARD1*, *CDC20*) were synthetically lethal with Myc hyperactivation, with depletion of SMS candidates leading to up to

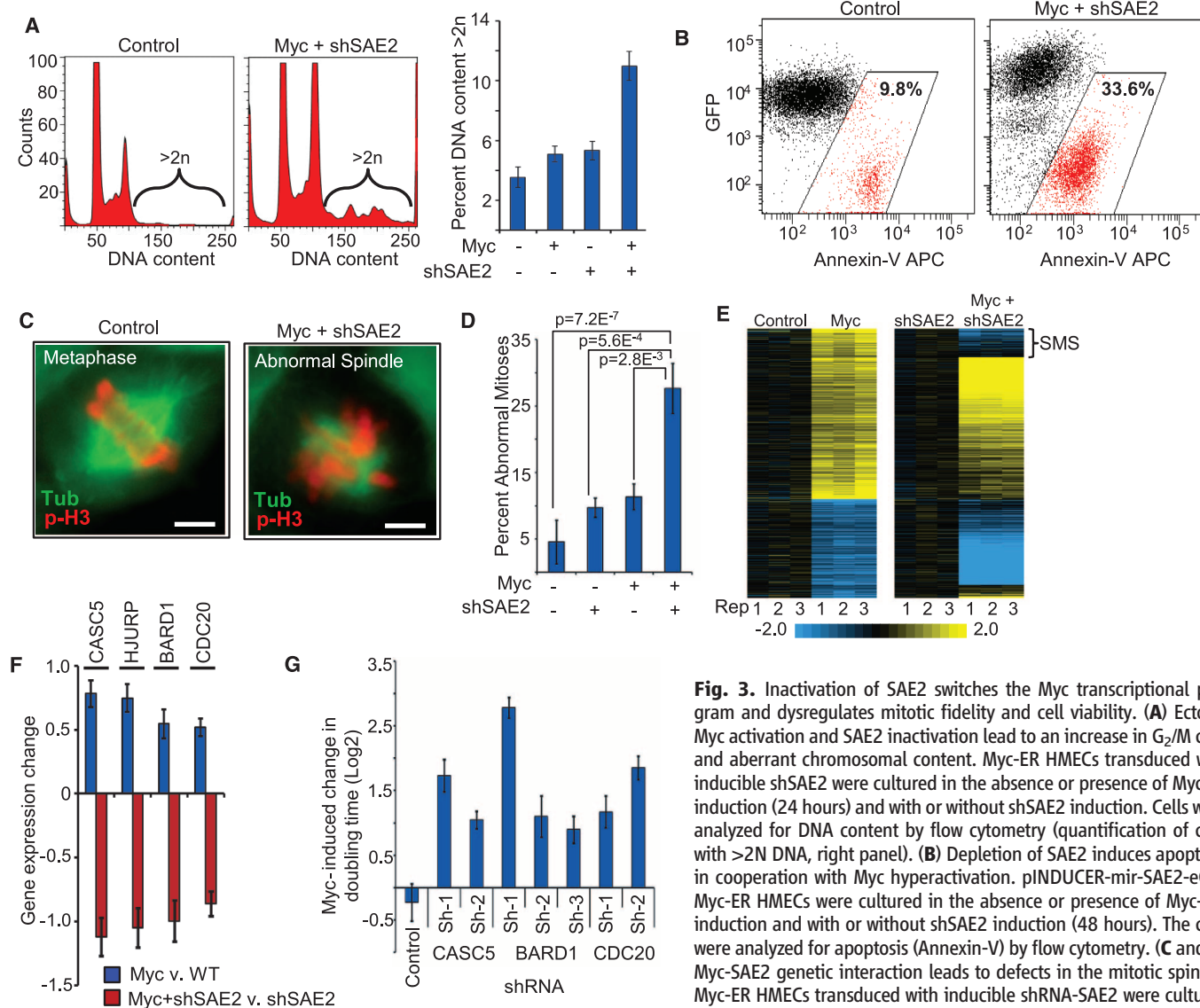


Fig. 3. Inactivation of SAE2 switches the Myc transcriptional program and dysregulates mitotic fidelity and cell viability. **(A)** Ectopic Myc activation and SAE2 inactivation lead to an increase in G₂/M cells and aberrant chromosomal content. Myc-ER HMECs transduced with inducible shSAE2 were cultured in the absence or presence of Myc-ER induction (24 hours) and with or without shSAE2 induction. Cells were analyzed for DNA content by flow cytometry (quantification of cells with >2N DNA, right panel). **(B)** Depletion of SAE2 induces apoptosis in cooperation with Myc hyperactivation. pINDUCER-mir-SAE2-eGFP Myc-ER HMECs were cultured in the absence or presence of Myc-ER induction and with or without shSAE2 induction (48 hours). The cells were analyzed for apoptosis (Annexin-V) by flow cytometry. **(C and D)** Myc-SAE2 genetic interaction leads to defects in the mitotic spindle. Myc-ER HMECs transduced with inducible shRNA-SAE2 were cultured in the absence or presence of Myc-ER induction (16 hours) and with or

without shSAE2 induction. Cells were stained for Tubulin (green) and phospho-H3 (red) to visualize mitotic defects. Images from (C) were quantified for both total and abnormal mitotic events (D). Data are represented as the percentage of abnormal mitoses (at least 100 mitotic events were counted per condition; P values are from Fisher's exact test). Scale bar, 5 μ M. **(E)** Loss of SAE2 alters the transcriptional response to Myc. HMECs expressing Myc-ER and dox-inducible SAE2-shRNA were analyzed by gene expression profiling in the absence or presence of Myc-ER induction and with or without SAE2-shRNA induction. All mRNAs altered by Myc-ER induction ($P < 0.05$, twofold) are shown. The effect of Myc-ER induction on mRNA levels in the absence or presence of shRNA-SAE2 induction are shown (left and right panels, respectively). mRNAs that change their response to Myc in the presence or absence of shSAE2 are termed “sumoylation-dependent Myc switchers,” or SMS genes. **(F)** Loss of SAE2 alters Myc control of spindle-regulatory genes. The effect of Myc in the absence or presence of shSAE2 (blue and red bars, respectively) is shown for the top 4 of 17 SMS genes with known roles in spindle integrity and function (see fig. S9B for the list of 17 SMS genes). **(G)** SMS genes are required to tolerate Myc hyperactivation. Myc-ER HMECs transduced with shRNAs targeting the indicated SMS genes were cultured in the absence or presence of Myc-ER induction for 6 days. Cell numbers were counted and analyzed as in Fig. 2A. Error bars in (A), (D), and (G) represent the SEM; error bars in (F) are the SE.

an eightfold Myc-selective increase in cell doubling time (Fig. 3G and fig. S10, A to C). These results suggest the SMS transcriptional subprogram may be required to tolerate the Myc oncogenic state.

The Myc-SAE2 synthetic lethal interaction suggests that Myc-driven cancers may be dependent on SAE2 and SUMOylation to support their tumorigenic phenotypes. To test this hypothesis, we first assessed the dependency of human breast cancer–derived cell lines on Myc function. The cells were transduced with control or Myc-targeting shRNA viruses and tested for clonogenicity. The clonogenicity of SUM159 and MDA-MB-231 breast cancer cells was significantly impaired by Myc depletion, whereas MCF7 and SKBR3 breast cancer cells were unaffected (Fig. 4A). We therefore classified the SUM159 and MDA-MB-231 cells as Myc-dependent and the MCF7 and SKBR3 cells as Myc-independent.

To determine whether Myc-dependent breast cancer cells are similarly dependent on SAE2 function, we transduced each breast cancer cell line with an inducible SAE2-shRNA lentivirus. SAE2 protein was significantly depleted in a doxycycline (dox)–dependent manner in each cell line (fig. S11A). SAE2 depletion decreased clono-

genic of the Myc-dependent breast cancer cells but had no effect on Myc-independent cells (Fig. 4B). Similarly, depletion of SAE2 also reduced the growth rate of Myc-dependent breast cancer cells, as determined by a multicolor competition assay (fig. S11B). By contrast, SAE2-shRNA had no effect or only modest effects on the proliferation of several normal cell types (fig. S12). Collectively, these results suggest that SAE2 is required for the growth and fitness of Myc-dependent breast cancer cells.

To determine if SAE2 is essential for the tumorigenicity of Myc-dependent cancer cells in vivo, we engineered Myc-dependent (SUM159 and MDA-MB-231) and Myc-independent (MCF7) breast cancer cells with a dox-inducible SAE2-shRNA, transplanted the cells into immunocompromised mice, and measured tumor volume over time. To circumvent the effects of SAE2 depletion on in vitro proliferation from confounding the tumorigenicity analyses, we treated the mice with or without dox only after tumor transplantation. SAE2 depletion inhibited tumor growth of Myc-dependent SUM159 and MDA-MB-231 tumors in vivo (Fig. 4C, left and middle panels), but had no significant effect on Myc-independent

MCF7 tumors (right panel). SAE2 depletion also increased survival time as compared to the animals that were not treated with dox (fig. S13). Furthermore, the tumors emerging in dox-treated mice contained fewer GFP/shSAE2-expressing cells, consistent with a selection against tumor cells depleted of SAE2 during tumor growth (fig. S14). Together, these data suggest that SAE2 function is required for tumorigenicity of Myc-dependent breast cancers.

The data derived from the above model systems would predict that Myc-high human breast cancers with low expression of the SUMO-activating enzyme may exhibit a less aggressive clinical behavior. To test this hypothesis, we compiled breast cancer data sets ($n = 1297$ patients) for which there was gene expression data (Affymetrix U133 platform only) and a common endpoint criterion (metastatic recurrence) (32–39). Tumors were stratified on the basis of Myc expression levels, with 432 and 429 tumors defined as Myc-high and Myc-low, respectively. We then determined if levels of SAE1 and SAE2 were associated with patient outcome (metastasis-free survival) in the Myc-high or Myc-low groups. In patients with Myc-high tumors, those with

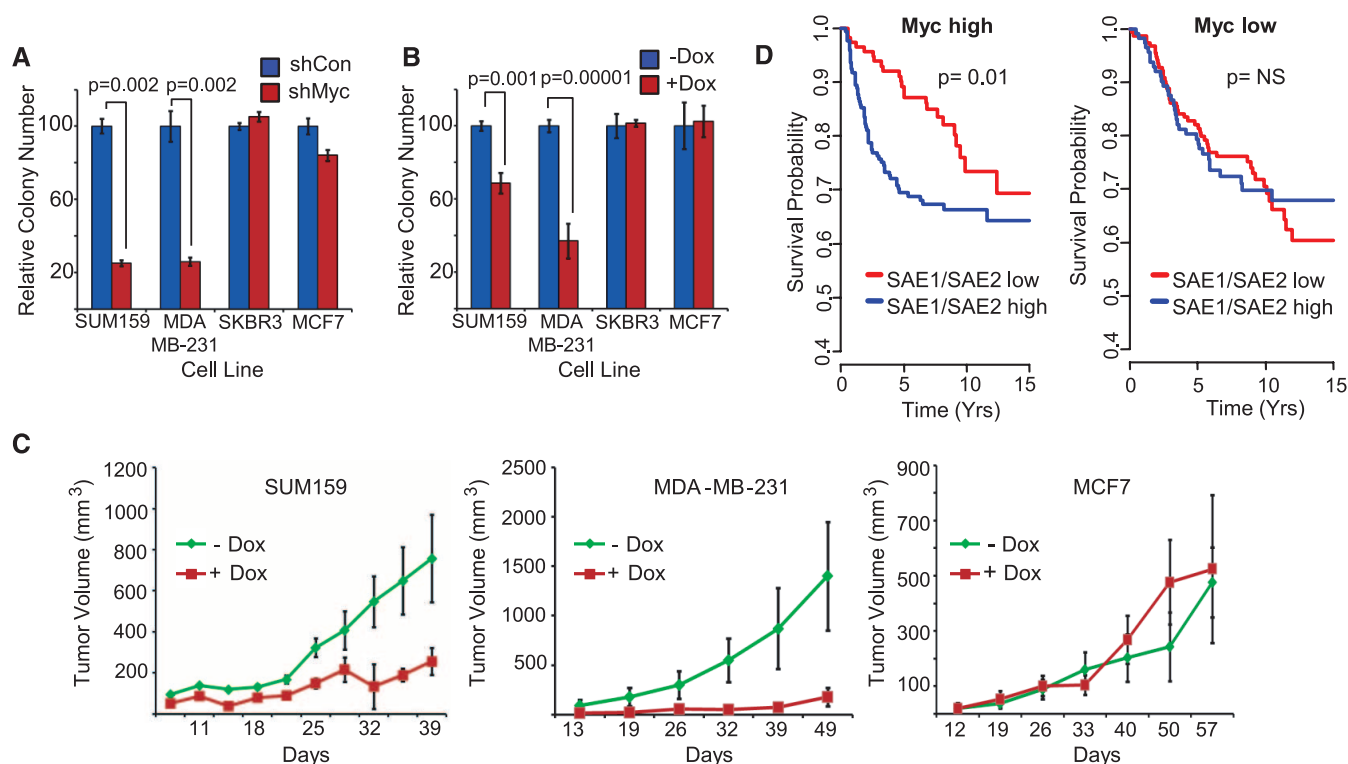


Fig. 4. The E1 SAE enzyme is required to support Myc-dependent human breast cancer cells in vitro and in mice. **(A)** Myc dependency in human breast cancer cells. Breast cancer–derived cell lines infected with control- or Myc-shRNA lentivirus were analyzed for clonogenic growth. Macroscopic colonies were quantified and normalized to control-shRNA-infected cells for each cell line. **(B)** Inactivation of SAE2 inhibits clonogenicity in Myc-dependent breast cancer cells. Breast cancer–derived cell lines infected with dox-inducible control- or SAE2-shRNA lentivirus were analyzed for clonogenic growth in the absence or presence of dox. **(C)** Inactivation of SAE2 inhibits tumorigenicity of Myc-dependent tumors. Myc-dependent (SUM159 and MDA-MB-231; left and middle panels, respectively) or Myc-

independent (MCF7, right panel) breast cancer cells infected with dox-inducible SAE2-targeting shRNA lentivirus were transplanted into nude mice. Recipient animals were treated with or without dox, and xenograft volume was measured over time. **(D)** Low SAE gene expression correlates with patient metastasis-free survival selectively in Myc-high breast cancers. The expression of SAE1 and SAE2 is inversely correlated with increased metastasis-free survival in patients with Myc-high tumors ($P = 0.01$, log-rank test). Tumors with the highest and lowest tertile of Myc mRNA expression were considered “Myc-high” and “Myc-low,” respectively. Patients with the highest and lowest tertile of SAE1 and SAE2 mRNA expression are shown as blue and red lines, respectively. Error bars in (A) to (C) represent the SEM.

lower-level expression of SAE1 and SAE2 had significantly better metastasis-free survival than those with higher SAE1 and SAE2 (Fig. 4D, left panel, $P = 0.01$ log-rank test). By contrast, lower-level expression of SAE1 and SAE2 did not correlate with outcome in patients with Myc-low tumors (Fig. 4D, right panel). This suggests that Myc hyperactivation leads to an increased dependency on SAE1 and SAE2 in human breast cancers.

We have shown here that the E1 SAE 1 and 2 enable cells to tolerate Myc hyperactivation. SAE1 and SAE2 represent enzymatic examples of the “non-oncogene addiction” concept, and their discovery illustrates the power of unbiased genetic screens for identifying potential new leads for cancer therapeutics. Loss of SUMOylation leads to substantial mitotic catastrophe and cell death by switching a subprogram of Myc transcriptional targets that support mitotic spindle function. Thus, inactivation of SAE2 mimics the mitotic disruption caused by spindle poisons, but in a genotype-specific way (i.e., selectively in cells that harbor oncogenic Myc activation). Notably, mitotic interference is a mainstay of cancer therapeutics, and agents such as taxanes that disrupt proper spindle function are used to treat a wide variety of cancers. However, a major limitation of this class of therapeutics is their toxicity to nontumor organ systems, thus limiting their therapeutic window. Our observation that inhibition of SUMOylation can mimic spindle poisons selectively in cells expressing hyperactivated Myc raises the possibility that drugs targeting the SUMO pathway may have the antitumor effects of spindle poisons with fewer side effects.

Myc promotes a balance of pro- and anti-tumorigenic properties, and mutations in Myc can shift this balance in pro- and anti-oncogenic Myc functions, demonstrating that distinct transcriptional (or other biochemical) functions of Myc may be segregated (15, 16). We propose that the Myc transcriptional program can be shifted to favor the anti-oncogenic state. Specifically, our data suggest that the inactivation of SAE2 drives synthetic lethality with the Myc oncogene by altering a subprogram of Myc transcriptional targets that supports proper mitosis and thus cell viability, a subprogram we term SUMOylation-dependent Myc switchers, or SMS genes. This SMS program is highly enriched in proteins that control spindle integrity, and the Myc-SAE2 synthetic lethal interaction elicits frequent aberrations in the mitotic spindle and eventual cell death. SUMOylation may thus contribute to Myc-induced oncogenesis at least in part by cooperating with Myc to maintain expression of Myc target genes involved in mitotic fidelity. These observations highlight the idea that altering distinct subprograms of Myc transcription (by SAE2 inactivation or other mechanisms) may be exploited as a therapeutic strategy in Myc-driven cancers, and more broadly, suggest that subverting transcriptional programs may be a general strategy in treating cancers driven by oncogenic transcrip-

tion factors that are notoriously difficult to target therapeutically.

References and Notes

1. I. B. Weinstein, *Science* **297**, 63 (2002).
2. S. W. Lowe, E. Cepero, G. Evan, *Nature* **432**, 307 (2004).
3. S. Jones et al., *Science* **321**, 1801 (2008).
4. J. Luo, N. L. Solimini, S. J. Elledge, *Cell* **136**, 823 (2009).
5. P. G. Richardson, C. Mitsiades, T. Hideshima, K. C. Anderson, *Annu. Rev. Med.* **57**, 33 (2006).
6. H. Farmer et al., *Nature* **434**, 917 (2005).
7. L. Soucek, G. I. Evan, *Curr. Opin. Genet. Dev.* **20**, 91 (2010) (Feb).
8. S. L. Deming, S. J. Nass, R. B. Dickson, B. J. Trock, *Br. J. Cancer* **83**, 1688 (2000).
9. M. J. van de Vijver et al., *N. Engl. J. Med.* **347**, 1999 (2002).
10. K. Chin et al., *Cancer Cell* **10**, 529 (2006).
11. A. S. Adler et al., *Nat. Genet.* **38**, 421 (2006).
12. Y. Chen, O. I. Olopade, *Expert Rev. Anticancer Ther.* **8**, 1689 (2008).
13. L. Soucek et al., *Nature* **455**, 679 (2008).
14. R. B. Boxer, J. W. Jang, L. Sintasath, L. A. Chodosh, *Cancer Cell* **6**, 577 (2004).
15. M. T. Hemann et al., *Nature* **436**, 807 (2005).
16. D. W. Chang, G. F. Claassen, S. R. Hann, M. D. Cole, *Mol. Cell. Biol.* **20**, 4309 (2000).
17. A. Menssen et al., *Cell Cycle* **6**, 339 (2007).
18. S. Rottmann, Y. Wang, M. Nasoff, Q. L. Deveraux, K. C. Quon, *Proc. Natl. Acad. Sci. U.S.A.* **102**, 15195 (2005).
19. Y. Wang et al., *Cancer Cell* **5**, 501 (2004).
20. E. A. Beierle et al., *J. Biol. Chem.* **282**, 12503 (2007).
21. F. Zindy et al., *Genes Dev.* **12**, 2424 (1998).
22. O. Vafa et al., *Mol. Cell* **9**, 1031 (2002).
23. H. Hermeking, D. Eick, *Science* **265**, 2091 (1994).
24. R. T. Hay, *Mol. Cell* **18**, 1 (2005).
25. K. L. Meerbrey et al., *Proc. Natl. Acad. Sci. U.S.A.* **108**, 3665 (2011).
26. V. Joukov et al., *Cell* **127**, 539 (2006).
27. L. Song, M. Rape, *Mol. Cell* **38**, 369 (2010).
28. T. Kiyomitsu, C. Obuse, M. Yanagida, *Dev. Cell* **13**, 663 (2007).
29. M. Shuaib, K. Ouararhni, S. Dimitrov, A. Hamiche, *Proc. Natl. Acad. Sci. U.S.A.* **107**, 1349 (2010).
30. J. Higgins et al., *BMC Cell Biol.* **11**, 85 (2010).
31. H. H. Silljé, S. Nagel, R. Körner, E. A. Nigg, *Curr. Biol.* **16**, 731 (2006).
32. S. Loi et al., *Proc. Natl. Acad. Sci. U.S.A.* **107**, 10208 (2010).
33. Y. Wang et al., *Lancet* **365**, 671 (2005).
34. C. Desmedt et al., TRANSBIG Consortium, *Clin. Cancer Res.* **13**, 3207 (2007).
35. L. D. Miller et al., *Proc. Natl. Acad. Sci. U.S.A.* **102**, 13550 (2005).
36. M. Schmidt et al., *Cancer Res.* **68**, 5405 (2008).
37. Y. Zhang et al., *Breast Cancer Res. Treat.* **116**, 303 (2009).
38. A. J. Minn et al., *Proc. Natl. Acad. Sci. U.S.A.* **104**, 6740 (2007).
39. A. J. Minn et al., *Nature* **436**, 518 (2005).

Acknowledgments: We thank C. Bland for critical comments on the manuscript and T. Mitchell, W. Choi, S. Songyang, and the BCM C-BASS and CCSC Cores for reagents and technical assistance. J.D.K. and K.L.M. are supported by NIH training grants T32HD05520/T32CA090221-09 and U.S. Department of Defense predoctoral fellowship W81XWH-10-1-0354, respectively. The Golding lab is supported by NIH grant R01GM082837, Human Frontier Science Program grant RGY70/2008, Welch Foundation grant Q-1759, and NSF grant 082265 (PFC: Center for the Physics of Living Cells). This work was supported by a Susan G. Komen for the Cure grant (KG090355), CPRIT grant (RP120583), and NIH grant (CA149196) to T.F.W., Specialized Program of Research Excellence developmental grant (P50 CA058183) to T.F.W., SU2C—American Association for Cancer Research Breast Cancer program grant to R.S. and C.K.O., and U.S. Army Innovator Award (W81XWH0410197) to S.J.E. S.J.E. is an Investigator with the Howard Hughes Medical Institute. T.F.W. is a scholar of The V Foundation and The Mary Kay Ash Foundation for Cancer Research. Gene Expression data are deposited in GEO (accession no. GSE34055).

Supporting Online Material

www.sciencemag.org/cgi/content/full/science.1212728/DC1
Materials and Methods
Figs. S1 to S14
Tables S1 and S2
References

16 August 2011; accepted 22 November 2011
Published online 8 December 2011;
10.1126/science.1212728

Locally Synchronized Synaptic Inputs

Naoya Takahashi,¹ Kazuo Kitamura,^{2,3} Naoki Matsuo,^{3,4} Mark Mayford,⁵ Masanobu Kano,² Norio Matsuki,¹ Yuji Ikegaya^{1,3*}

Synaptic inputs on dendrites are nonlinearly converted to action potential outputs, yet the spatiotemporal patterns of dendritic activation remain to be elucidated at single-synapse resolution. In rodents, we optically imaged synaptic activities from hundreds of dendritic spines in hippocampal and neocortical pyramidal neurons *ex vivo* and *in vivo*. Adjacent spines were frequently synchronized in spontaneously active networks, thereby forming dendritic foci that received locally convergent inputs from presynaptic cell assemblies. This precise subcellular geometry manifested itself during *N*-methyl-D-aspartate receptor-dependent circuit remodeling. Thus, clustered synaptic plasticity is innately programmed to compartmentalize correlated inputs along dendrites and may reify nonlinear synaptic integration.

Cortical microcircuits are nonrandomly intertwined and form cell assemblies that fire in a spatiotemporally orchestrated manner. This patterned activity is decoded by the dendrites of downstream neurons. Dendrites are arborized and electrically active (1), which allows them to exhibit local nonlinear membrane potential dynamics

(2–4) and to transform different spatiotemporal sequences of incoming inputs into different output patterns (5, 6). Therefore, knowing whether synaptic inputs are clustered or dispersed over dendrites at a given time (fig. S1) is critical for determining the dendritic computational power (7, 8); however, these dynamics are still poorly understood.

We monitored spontaneous synaptic inputs using dual patch-clamp recordings under confocal visualization from different apical dendritic

branches of individual CA3 pyramidal cells in rat hippocampal slices that were cultured for 12 to 19 days (fig. S2A) (9). Large postsynaptic potentials (that is, putative synchronized inputs) often occurred in only one branch (fig. S2B). The Euclidean distance in membrane potentials between two branches was distributed with a long tail (fig. S2C), suggesting that dendrites received spatially biased synchronous inputs.

Next, we intracellularly injected CA3 pyramidal cells with Fluo-5F through somatic patch-clamp pipettes (Fig. 1A) (10). We voltage-clamped a neuron at -30 mV and imaged the dendrites in an area of approximately $100 \times 100 \mu\text{m}^2$ that con-

tained an average of 98.5 ± 16.7 spines (mean \pm SD, ranging from 52 to 235 spines) (Fig. 1B). Transient calcium elevations occurred spontaneously in the spines (Fig. 1, C and D, and movie S1). These activities were spatially restricted within the spines (Fig. 1C) and were time-locked to the occurrence of spontaneous excitatory postsynaptic currents (EPSCs) in the patched neurons (fig. S3A). The local application of 1 mM L,D-2-amino-5-phosphonopentanoic acid (AP5), an *N*-methyl-D-aspartate (NMDA) receptor antagonist, abolished spine calcium events without affecting the overall frequency of the spontaneous EPSCs (fig. S3, B to G). The mean frequency

Fig. 1. Imaging of spontaneous synaptic inputs. (A) A stack image of a CA3 pyramidal cell filled with Fluo-5F. (B) The locations of 137 spines (red) monitored from the boxed region shown in (A). (C) Spontaneous calcium events of spines in the region boxed in (B). $\Delta F/F$, percent increase in fluorescence intensity. (D) The spatiotemporal pattern of the calcium events of the 137 spines. Each dot indicates a single event of a single spine. (E) The event frequencies are plotted versus the path distance from the soma. Each black dot represents a single spine ($n = 1084$ spines in 11 videos from 11 slices). Red dots and bars indicate the means \pm SDs. (F) A Lorenz curve representing the proportion of the total inputs that is assumed by the proportion of spines with the lowest input frequencies. (G) Distributions of the input frequencies and the head sizes of the spines.

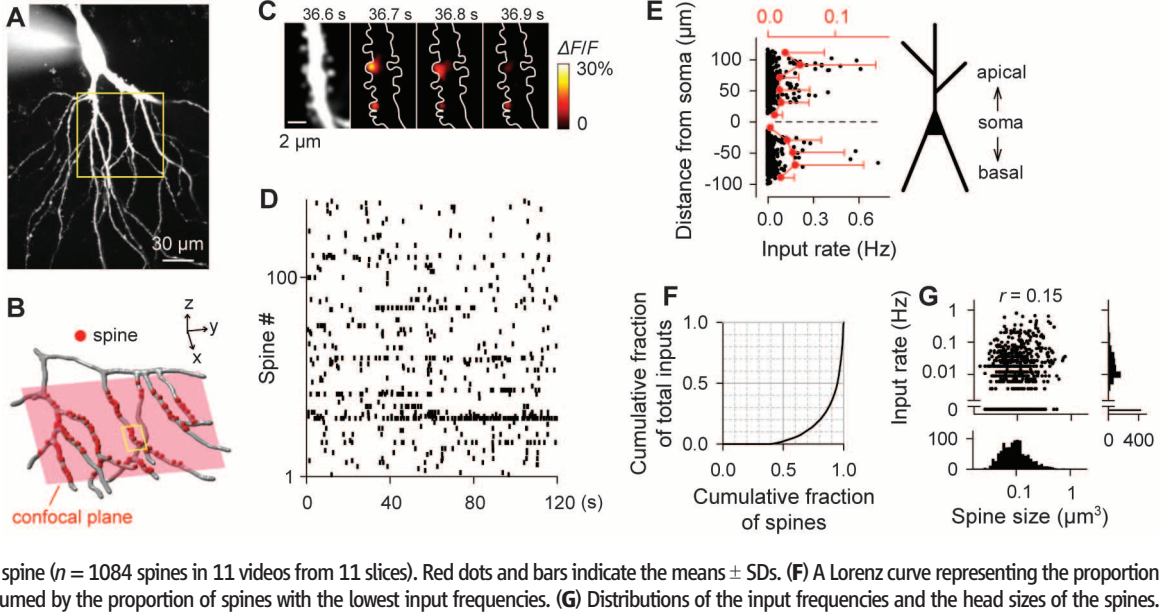
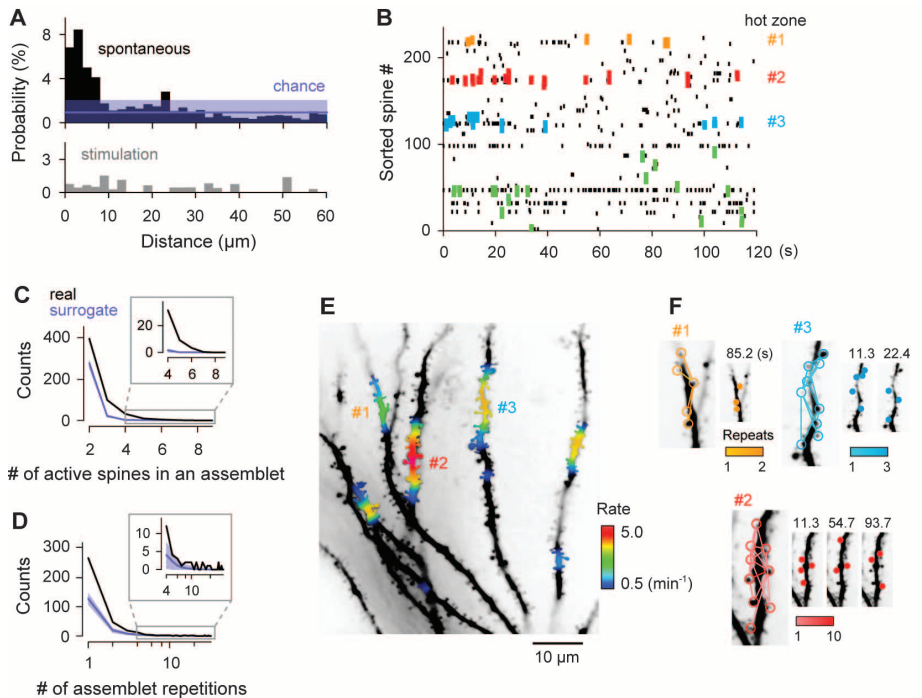


Fig. 2. Functionally clustered spine activity ex vivo. (A) (Top) The probability of observing spines coactivated within 100 ms as a function of the distance from a given spine ($n = 11$ videos from 11 neurons). The chance level and its 95% confidence intervals (purple) were estimated from the distribution of distances of more than $10 \mu\text{m}$. (Bottom) Spine coactivation in response to electrical stimulation of the CA3 stratum radiatum ($n = 16$ videos from 10 neurons). (B) Assemblies (thick dots) in a raster plot of 235 spines. Assemblies that appear in hot zones 1, 2, and 3 in (E) are colored in yellow, red, and blue; otherwise, they are colored in green. (C and D) Distribution of the number of spines participating in single assemblies (C) and the repetition numbers of each assembly (D). Chance (purple) was estimated by the random shuffling of inter-event intervals and is represented by the mean value of 1000 surrogates and their 95% confidence intervals. The data from 11 neurons are pooled. (E) A heat map of the frequency of assemblies in dendrites. (F) Representative assembly dynamics in hot zones 1, 2, and 3.



of spine activities was 1.5 events/min, which was approximately half the mean firing rate of the presynaptic neuron population (fig. S4). This difference may result from stochastic synaptic transmission, with a probability of about 50% between CA3 pyramidal cells *ex vivo* (11), as well as from false-negative detection of a fraction of spine calcium events.

The locations of spines were three-dimensionally determined post hoc to measure the path length from the soma along the dendrites. The spines did not differ with respect to activity levels between the basal and radial oblique dendrites or between the proximal and distal dendrites (Fig. 1E). Therefore, all data were pooled in the following analyses. The Gini coefficient of the spine activity was 0.78; approximately 20% of the spines exhibited 80% of the calcium activity (Fig. 1F). The activity frequency and the spine head size, each of which approximated a log-normal distribution, correlated only weakly with each other (Fig. 1G, Spearman's rank $r = 0.15$, $P = 5.9 \times 10^{-7}$).

We calculated the spatial correlations of spontaneous spine activities; for a given activity in a "focused" spine, the probability of observing activity in other spines in a time window of 100 ms was plotted as a function of the path length from the focused spine (Fig. 2A, top; $n =$

11 videos from 11 neurons in 11 slices). The probability was compensated with the spine density observed at a given distance to avoid sampling bias caused by the limited lengths of monitored dendritic segments. Spine coactivation was significantly more frequent within interspine intervals of 8 μm as compared to the chance level, which is defined here as the mean probability of observing spine activity at distances greater than 10 μm ($|Z| \geq 5.77$, $P \leq 8.0 \times 10^{-9}$, Z-test for a population mean). The spatially clustered spine activation was also significant as compared to randomized surrogates (fig. S5A, $P < 0.01$). We did not observe clustered synaptic inputs in fast-spiking parvalbumin-positive interneurons in the CA3 stratum pyramidale (fig. S6, $|Z| \geq 0.63$, $P \leq 0.53$; fig. S5B; $n = 11$ videos from eight neurons).

To examine the synaptic activation patterns *in vivo*, we conducted somatic whole-cell patch-clamp recordings (12) and two-photon calcium imaging from spines of layer 2/3 pyramidal cells in the barrel cortex of anesthetized young adult mice. Calcium activities were simultaneously monitored from 31.6 ± 13.7 spines (ranging from 16 to 48 spines) from 10 apical or basal dendrites of four cells (Fig. 3, A and B). Spontaneous activities frequently occurred in neighboring spines; the probability of observing the coactive spines significantly increased within 6 μm along the dendrites (Fig. 3C, $|Z| \geq 5.61$, $P \leq 2.1 \times 10^{-8}$; fig. S5C).

The synchronization of adjacent spines can be explained by five possible mechanisms: (i) convergent afferents from a population of spontaneously synchronized presynaptic neurons (cell assembly) (fig. S7A); (ii) multiple innervations of a single presynaptic axon (fig. S7B); (iii) spill-

over of diffusible molecules (such as glutamate) to neighboring synapses (fig. S7C); (iv) spatial segregation of spine excitation by local dendritic inhibition (fig. S7D); or (v) local depolarization-induced increase in a chance of calcium influx in neighboring spines. We can rule out mechanisms ii to v on the basis of the results of the three following experiments *ex vivo*. First, we applied electrical field stimulation to the CA3 stratum radiatum and produced synchronized network activity. The stimulation intensity was set to evoke a compound EPSC with an amplitude greater than 400 pA in the patched neurons. This cell assembly-irrelevant artificial synchronization did not generate spatially clustered spine activation (Fig. 2A, bottom, $|Z| \geq 0.45$, $P \leq 0.65$; fig. S5D; $n = 16$ videos from 10 neurons). This result is inconsistent with ii, iii, and v. Second, we can also rule out mechanism ii because biocytin reconstructions of synaptically connected neurons revealed that 51 of 55 (92.7%) putative synapses arising from 12 presynaptic neurons contacted single spines (fig. S8). Finally, we can exclude mechanism iv because spine activation remained clustered in dendrites that were disinhibited by the local application of 1 mM picrotoxin (fig. S9, $|Z| \geq 3.97$, $P \leq 7.2 \times 10^{-5}$; fig. S5E; $n = 8$ videos from eight neurons). Therefore, mechanism i appeared to be the most plausible mechanism (fig. S1A).

To intuitively depict the observed spine coactivation, we defined an "assemblat" as a cluster of synchronized spine activities in which the distance from any spine in the cluster to the next nearest spine in the cluster was less than 10 μm (Fig. 2B). In the entire sample of 11 videos *ex vivo*, 31.5% of the spines participated in at least one assemblat, and assemblat activity accounted for 29.5% of the total spine activity. In single assemblat events, an average of 3.6 ± 0.7 spines, ranging from 2 to 12 spines, were activated during a period of 59 ± 33 ms and within an area of 4.7 ± 3.3 μm^2 (Fig. 2C). Twenty-eight percent of the assemblats appeared more than once, and a portion of them repeated up to 30 times (Fig. 2D), whereas 58.9% of the spines that participated in one assemblat participated in other assemblats. The assemblat sizes and the numbers of repetitions were greater than the chance values expected by event-interval shuffling (Fig. 2, C and D, purple; $P < 0.001$), in which the time intervals between successive calcium events were randomly exchanged within each spine to collapse the time correlations between spines (13).

In regard to the population dynamics, 85.0% of the assemblats occurred sporadically, whereas the remaining 15.0% occurred in synchrony with other assemblats (fig. S10A). When synchronized, the assemblats tended to appear more than 80 μm apart from one other (fig. S10B).

Dendrites were spatially heterogeneous in emitting assemblats (Fig. 2, E and F). Therefore, we defined a hot zone as a continuous dendritic segment where a single assemblat or multiple assemblats that shared at least one spine occurred. The hot zones had an average area of 7.7 ± 6.7 μm^2 ,

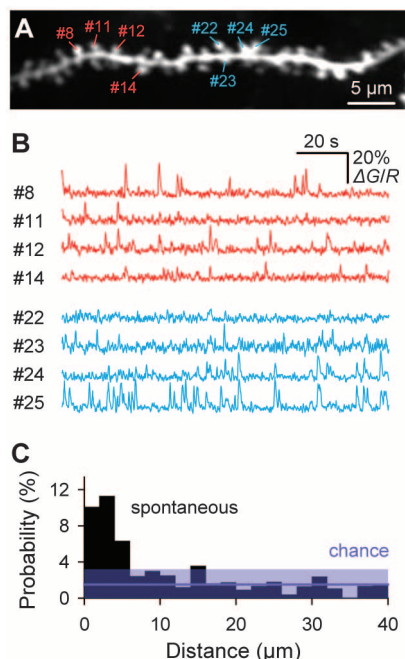


Fig. 3. Functionally clustered spine activity *in vivo*. (A) A stack image of dendrites of an Alexa 594-loaded layer 2/3 pyramidal cell in the mouse somatosensory cortex *in vivo*. (B) Typical traces of spontaneous calcium activity from eight spines shown in (A). (C) The probability of observing coactivated spines as a function of the inter-spine path distance ($n = 10$ dendritic segments in four cells). The chance level and its 95% confidence intervals (purple) were estimated from the distribution of distances of more than 10 μm .

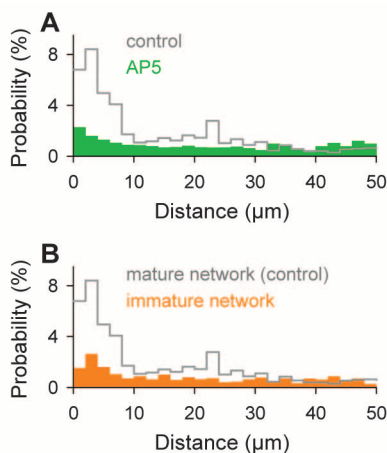


Fig. 4. NMDA receptor-dependent emergence of clustered synaptic inputs. (A) The probability of observing coactivated spines as a function of the path distance in slices cultivated in the chronic presence of 100 μM AP5 ($n = 8$ videos from eight neurons). (B) The probability of observing coactivated spines in immature networks of slices for 3 to 4 days *in vitro* ($n = 14$ videos from 14 neurons). Early calcium sparks in immature dendritic shafts were excluded from data analysis. The control is the same as in Fig. 2A.

ranging from 0.4 to 28.2 μm (fig. S11A), and exhibited an average of 2.7 ± 4.8 assemblets/min, ranging from 0.04 to 25.0 assemblets/min (fig. S11B). Hot zones were dispersed at a density of 1.8 ± 1.2 , ranging from 0 to 6, per 50 μm of dendritic length (fig. S11C). They are candidate sites for the initiation of dendritic spikes (14), but we rarely observed calcium sparks in the dendritic shafts, which may possibly be due to a lowered spine density in slice cultures (fig. S13B) as compared to cortical neurons in vivo.

Spines that participated in assemblets were larger in head size than nonparticipants (fig. S12), which suggests that assemblets are shaped by long-term synaptic plasticity (15). Indeed, adjacent spines were less synchronized in slices cultivated in the presence of 100 μM AP5 for 12 to 19 days (Fig. 4A, $|Z| \geq 1.05$, $P \leq 0.30$; fig. S5F; $n = 8$ videos from 8 neurons) and in immature slices cultivated for 3 to 4 days (Fig. 4B, $|Z| \geq 1.51$, $P \leq 0.13$; fig. S5G; $n = 14$ videos from 14 neurons) as compared to control mature slices ($P < 0.01$ each; Kolmogorov-Smirnov test). Neither the spine density nor the spontaneous or miniature EPSC levels differed between control and AP5-treated cultures (fig. S13). Thus, functional synaptic clustering is likely to develop through NMDA receptor-dependent circuit remodeling.

Consistent with this idea, we found that glutamate receptors were preferentially inserted into neighboring spines after behavioral exploration in vivo, using adult transgenic mice in which GFP-GluR1 is expressed under control of the *c-fos* promoter (figs. S5H and S14) (16). Thus, the loci of synaptic plasticity are spatially clustered over dendrites. The clustered plasticity may result from interspine interactions that heterosynaptically modulate the threshold for long-term potentiation, such as local depolarization-induced Mg^{2+} unblock of nearby NMDA receptors or intracellular diffusion of plasticity-associated molecules (17–20).

We found that synaptic inputs were frequently synchronized within a group of spines in the im-

mediate vicinity of one another. Given that ex vivo networks are subject to massive axon reorganization during cultivation without external inputs, our data indicate that the locally convergent connectivity that generates assemblets emerges through self-organization (fig. S15). Thus, the default principle for designing circuit topology is biased to facilitate dendritic compartmentalization (21). The resultant clustered synchrony may offer opportunities for associative learning, because vicinal spines encode different information (22, 23).

Because the video frame rate of our spine imaging was limited to a maximum of 20 Hz to maintain the signal-to-noise ratio, we could not determine the internal structure of assemblets; however, given that the ex vivo hippocampal network synchrony accompanies sharp waves and ripples (24), assemblets are expected to coordinate temporal activity sequences (25). Such sequential activation would facilitate nonlinear synaptic integration and enhance the computational power of a single neuron (5).

Note added in proof: Two recent studies have reported phenomena partly related to those described here, demonstrating activity-dependent clustering of synaptic inputs to developing dendrites of hippocampal slice cultures (26) and clustered synaptic plasticity in the developing somatosensory cortex (27).

References and Notes

1. M. London, M. Häusser, *Annu. Rev. Neurosci.* **28**, 503 (2005).
2. J. Schiller, Y. Schiller, G. Stuart, B. Sakmann, *J. Physiol.* **505**, 605 (1997).
3. N. L. Golding, N. Spruston, *Neuron* **21**, 1189 (1998).
4. J. Schiller, G. Major, H. J. Koester, Y. Schiller, *Nature* **404**, 285 (2000).
5. T. Branco, B. A. Clark, M. Häusser, *Science* **329**, 1671 (2010).
6. M. E. Larkum, J. J. Zhu, B. Sakmann, *Nature* **398**, 338 (1999).
7. M. Häusser, B. Mel, *Curr. Opin. Neurobiol.* **13**, 372 (2003).
8. A. Losonczy, J. C. Magee, *Neuron* **50**, 291 (2006).

9. T. Sasaki, N. Matsuki, Y. Ikegaya, *Science* **331**, 599 (2011).
10. Materials and methods are available as supporting material on Science Online.
11. J. M. Montgomery, P. Pavlidis, D. V. Madison, *Neuron* **29**, 691 (2001).
12. K. Kitamura, B. Judkewitz, M. Kano, W. Denk, M. Häusser, *Nat. Methods* **5**, 61 (2008).
13. Y. Ikegaya et al., *Science* **304**, 559 (2004).
14. S. Gasparini, M. Migliore, J. C. Magee, *J. Neurosci.* **24**, 11046 (2004).
15. M. Matsuzaki, N. Honkura, G. C. Ellis-Davies, H. Kasai, *Nature* **429**, 761 (2004).
16. N. Matsuo, L. Reijmers, M. Mayford, *Science* **319**, 1104 (2008).
17. C. D. Harvey, K. Svoboda, *Nature* **450**, 1195 (2007).
18. C. D. Harvey, R. Yasuda, H. Zhong, K. Svoboda, *Science* **321**, 136 (2008).
19. A. Losonczy, J. K. Makara, J. C. Magee, *Nature* **452**, 436 (2008).
20. A. Govindarajan, I. Israely, S. Y. Huang, S. Tonegawa, *Neuron* **69**, 132 (2011).
21. W. M. DeBello, *Trends Neurosci.* **31**, 577 (2008).
22. X. Chen, U. Leischner, N. L. Rochefort, I. Nelken, A. Konnerth, *Nature* **475**, 501 (2011).
23. Z. Varga, H. Jia, B. Sakmann, A. Konnerth, *Proc. Natl. Acad. Sci. U.S.A.* **108**, 15420 (2011).
24. N. Takahashi, T. Sasaki, W. Matsumoto, N. Matsuki, Y. Ikegaya, *Proc. Natl. Acad. Sci. U.S.A.* **107**, 10244 (2010).
25. A. K. Lee, M. A. Wilson, *Neuron* **36**, 1183 (2002).
26. T. Kleindienst, J. Winnubst, C. Roth-Alpermann, T. Bonhoeffer, C. Lohmann, *Neuron* **72**, 1012 (2011).
27. H. Makino, R. Malinow, *Neuron* **72**, 1001 (2011).

Acknowledgments: The authors are grateful to K. Morita (University of Tokyo) for his comments on the manuscript. This work was partly supported by Grants-in-Aid for Science Research from the Ministry of Education, Culture, Sports, Science and Technology of Japan (nos. 21220006, 22115003, 23115504, and 23800019); the Strategic Research Program for Brain Sciences (development of biomarker candidates for social behavior); and by the Funding Program for Next Generation World-Leading Researchers (grant LS023).

Supporting Online Material

www.sciencemag.org/cgi/content/full/335/6066/353/DC1
Materials and Methods
Figs. S1 to S15
References
Movie S1

27 June 2011; accepted 2 December 2011
10.1126/science.1210362

μDROP PLATE

The μDrop Plate is for the quick and easy measurement of samples down to 2 μL. The μDrop Plate provides a straightforward way of analyzing up to 16 microliter-scale samples simultaneously. The fixed-light path of the plate allows direct calculation of nucleic acid concentrations of the samples. Furthermore, users can detect dsDNA from a few micrograms to a few milligrams per milliliter, without needing to perform any dilutions. These characteristics make the μDrop Plate an ideal tool for photometric DNA or RNA quantitation and purity analysis. Samples are easily pipetted onto the μDrop Plate using a single- or eight-channel pipette. The plate is easily wiped clean, making it convenient for serial measurements. Additionally, the μDrop Plate is equipped with a cuvette slot, enabling endpoint, spectral, and kinetic measurements in a standard rectangular cuvette. The μDrop Plate has been designed for use with the Thermo Scientific Multiskan GO UV/Vis microplate and cuvette spectrophotometer, as well as the Thermo Scientific Varioskan Flash spectral scanning multimode reader.

Thermo Fisher Scientific

For info: 800-345-0206 | www.thermoscientific.com



BIOMOLECULAR IMAGING

Two new biomolecular imaging systems are available: the Typhoon FLA 9500 for imaging of multifuorescent, chemifluorescent, radioisotope-labeled, and colorimetric samples, and the Typhoon FLA 7000 IP for the dedicated study of radioisotope labeled samples. The Typhoon FLA 9500 is a versatile, high throughput laser scanner ideally suited to a multiuser environment. With a pixel resolution of up to 10 μm and a linear signal response over five orders of magnitude, the system provides precise quantitation in gels, blots, tissue sections, and arrays. A scanning area of 40 × 46 cm enables simultaneous imaging of 20 samples. The Typhoon 7000 IP is an entry-level scanner that enables high-speed, sensitive detection and quantitation of radioisotope-labeled samples. The model can scan over 10 image plates per hour, generating 16-bit images at up to 25 μm pixel resolution using storage phosphor screen technology.

GE Healthcare

For info: 800-526-3593 | www.gelifesciences.com

ISOELECTRIC FOCUSING SYSTEM

The PROTEAN i12 IEF system is the industry's only isoelectric focusing (IEF) system that is designed to simultaneously run up to 12 immobilized pH gradient (IPG) strips in 12 independently programmed lanes. For the best 2-D gel electrophoresis results, researchers optimize their sample preparation and first-dimension isoelectric focusing conditions to ensure adequate separation of complex samples. Because the optimal IEF conditions for different protein samples can vary significantly, each set of conditions must be tested separately. The PROTEAN i12 IEF system controls lanes separately, allowing researchers to set precise current limits for each lane. This enables the system to run different samples and pH ranges simultaneously while preventing differing samples from affecting each other, resulting in more reliable and reproducible focusing. The system also lets researchers test several optimization conditions simultaneously and run samples from different experiments together, both of which will speed their time to results.

Bio-Rad

For info: 800-424-6723 | www.bio-rad.com

LENTIVIRAL BIOSENSORS

A suite of LentiBrite lentiviral biosensors, prepackaged lentiviral particles encoding proteins fluorescently tagged with green or red fluorescent protein (GFP or RFP) are now available. The initial group of biosensors encode proteins responsible for cell structure such as actin and tubulin, a central marker of autophagy-LC3, and proteins that mark the onset of apoptosis. The biosensors enable detection of the presence or absence of a particular protein as well as the subcellular location of the protein in live cells under various states either by fluorescent microscopy or time-lapse video capture. Use of lentivirus to deliver fluorescently-tagged proteins into cells offers higher-efficiency transfection as compared with traditional chemical-based and other nonviral-based methods. In addition, the virus particles can be used to transfect dividing, nondividing, and difficult-to-transfect cells, such as primary and stem cells, leading to long-term, stable expression of the transgene with low immunogenicity.

EMD Millipore

For info: 800-645-5476 | www.millipore.com

PCR MASTER MIX

The GoTaq Long PCR Master Mix is an optimized enzyme mixture for improved long-range polymerase chain reaction (PCR). The new kit enhances PCR yield, sensitivity, and specificity and enables efficient amplification of up to 40 kb from lambda DNA or 30 kb from human genomic DNA. The new master mix is ideal for cloning genes, mutational analysis, and DNA sequencing. The GoTaq Long PCR Master Mix contains the high-performance GoTaq Hot Start Polymerase in a specially formulated mixture with a second proprietary thermal stable proofreading polymerase. The presence of a proofreading enzyme to repair DNA mismatches in the presence of a highly processive polymerase allows increased DNA elongation, resulting in longer DNA amplification. GoTaq Long PCR Master Mix consists of a master mix containing the polymerase and proofreading enzyme mixture, dNTPs, and MgCl₂. Also provided are control primers, human genomic control DNA, and nuclease-free water.

Promega

For info: 800-356-9526 | www.promega.com

Electronically submit your new product description or product literature information! Go to www.sciencemag.org/products/newproducts.dtl for more information.

Newly offered instrumentation, apparatus, and laboratory materials of interest to researchers in all disciplines in academic, industrial, and governmental organizations are featured in this space. Emphasis is given to purpose, chief characteristics, and availability of products and materials. Endorsement by *Science* or AAAS of any products or materials mentioned is not implied. Additional information may be obtained from the manufacturer or supplier.

There's only one
Science

Science Careers Advertising

For full advertising details, go to ScienceCareers.org and click **For Employers**, or call one of our representatives.

Tracy Holmes
Worldwide Associate Director
Science Careers
Phone: +44 (0) 1223 336525

UNITED STATES & CANADA
E-mail: advertise@sciencecareers.org
Fax: 303-289-5742

Tina Burks
Midwest/West Coast/
South Central/Canada
Phone: 202-326-6577

Elizabeth Early
East Coast & Corporate
Phone: 707-376-6578

Mardi Gallun
Sales Administrator
Phone: 202-326-6582

Online Job Posting Questions
Phone: 202-312-6375

EUROPE & REST OF WORLD
E-mail: ads@science-int.co.uk
Fax: +44 (0) 1223 326532

Simona Jax
Phone: +44 (0)1223 326529

Lucy Nelson
Phone: +44 (0)1223 326527

Kelly Grace
Phone: +44 (0) 1223 326528

JAPAN
Makiko Hara
Phone: +81 (0) 90-9833-9982
E-mail: mhara@aaas.org
Fax: +81 (0) 3-6569-4491

CHINA & TAIWAN
Ruofei Wu
Phone: +86-1367-1015-294
E-mail: rwu@aaas.org

All ads submitted for publication must comply with applicable U.S. and non-U.S. laws. Science reserves the right to refuse any advertisement at its sole discretion for any reason, including without limitation for offensive language or inappropriate content, and all advertising is subject to publisher approval. Science encourages our readers to alert us to any ads that they feel may be discriminatory or offensive.

Science Careers
from the journal *Science* AAAS

POSITIONS OPEN



A full-time **POSTDOCTORAL RESEARCH FELLOW** position is anticipated in the laboratory of **Dr. YiPing Chen** in the Department of Cell and Molecular Biology, Tulane University. The laboratory conducts research in the roles of signaling pathways and transcription of factors in craniofacial development and pathogenesis. Experiences in mouse genetics, craniofacial development, embryonic manipulation, and molecular biology are required. Good oral and writing skills are necessary, and dental background highly preferred. Salary commensurate with experience. Applicants should send curriculum vitae and the names of three references to **e-mail: ychen@tulane.edu**.

Tulane University is an Equal Opportunity /ADA/Affirmative Action Employer and encourages minority and female applicants to apply.

ASSISTANT PROFESSOR, TENURE-TRACK Animal Integrative Biology

The Department of Biology at the University of Florida (UF) is seeking applications for a tenure-track faculty position beginning August 2012 at the Assistant Professor level whose work is at the interface of animal physiology and either behavior or development. We are seeking candidates who will develop an internationally recognized, externally funded research program that builds on the strengths and interconnects the department's expertise in the fields of behavior, development, evolution, ecology, genetics, systematics, morphology, and physiology.

The successful candidate will be expected to contribute to the teaching of undergraduates in the areas of animal physiology and either animal behavior or developmental biology and to offer graduate seminars/courses in these or more specialized areas. A Ph.D. is required.

The Department of Biology has a strongly collegial environment that fosters collaborative interdisciplinary research and teaching that emphasizes integration of the above research areas within the framework of evolutionary principles. It enjoys strong ties with the Florida Museum of Natural History, UF Genetics Institute, UF Emerging Pathogens Institute and multiple University centers in biomedical, veterinary, environmental, and agricultural sciences. For more information on the department, go to **website: <http://www.biology.ufl.edu>**.

Interested applicants must apply online at **website: <http://jobs.ufl.edu>** (requestion #0810207). For full consideration, the application should include curriculum vitae, statements of research interests and teaching philosophy (of no more than three pages each), a maximum of three reprints in PDF format and names of three references. For more information, please go to our **website: <http://www.biology.ufl.edu/jobs/aib.aspx>**. Review of applications will begin on January 31, 2012. Our department is committed to diversity as a component of excellence. Women, minorities and members of other underserved groups are encouraged to apply. The University of Florida is an Equal Opportunity Institution.

POSTDOCTORAL POSITION available to work on (1) relations between protein editing and glycemic index, (2) roles of ubiquitin pathway in regulation of cell cycle, or differentiation or (3) changes in ubiquitin conjugate pool dynamics in response to stress. Tufts University Medical School is a highly collaborative and productive environment, located in downtown Boston. We are about 20 minutes from Harvard, MIT, and Boston University. Candidates should have at least two English language first-authored papers. Send curriculum vitae, a list of grades received in graduate science courses and a two-page research proposal of how your research would further the objectives of our group, as indicated above, to: **Allen Taylor, Laboratory for Nutrition and Vision Research, HNRCA, Tufts University, 711 Washington Street, Boston, MA 02111, telephone: 617-556-3156, fax: 617-556-3132, E-mail: allen.taylor@tufts.edu**.

POSITIONS OPEN



TENURE-TRACK FACULTY POSITION Center for Cardiovascular Research University of Illinois at Chicago College of Medicine

The University of Illinois at Chicago (UIC) Center for Cardiovascular Research (CCVR) in the College of Medicine seeks outstanding faculty candidates with expertise in cardiac mitochondrial biology, metabolism, non-coding RNA, or epigenetics. Consideration will be given to applicants at all ranks (**ASSISTANT, ASSOCIATE, FULL PROFESSORS**).

Successful candidates will demonstrate the ability to garner extramural grant support and are expected to lead comprehensive and innovative research programs that focus on heart failure, diabetes, obesity, metabolic syndrome, and hypertension. A commitment to excellence in teaching is also required. Minimum degree requirements are a Ph.D. or M.D. degree with three or more years of postdoctoral training. Attractive startup packages are available, commensurate with experience.

Applicants will submit a letter of interest, stating a research plan, a curriculum vitae, and names of at least three references. For more information on the CCVR, visit **website: <http://www.ccvr.uic.edu>**.

Apply online only at **website: <https://jobs.uic.edu/default.cfm?page=job&jobID=13483>**.

UIC is an Affirmative Action/Equal Opportunity Employer.

TENURE-TRACK FACULTY POSITIONS in Immunology/Inflammation

The Department of Pathology, Microbiology, and Immunology, School of Medicine, University of South Carolina (USC) invites applications for two tenure-track **ASSISTANT PROFESSOR** positions in Immunology/Inflammation. Outstanding applicants working in an area complementing our existing faculty research interests (**website: <http://pmi.med.sc.edu/>**) will be considered. The candidates must have a Ph.D. or equivalent, and at least three years of postdoctoral research experience. Preference will be given to candidates who have shown evidence of independence and currently active grant funding. Successful candidates are expected to develop a strong extramurally funded research program. They must participate in the teaching mission of the department. Competitive salary and startup funds are available. Please submit curriculum vitae and statement of research plans to: **Dr. Mitzi Nagarkatti, Chair, Department of Pathology, Microbiology, and Immunology, University of South Carolina School of Medicine, Columbia, SC 29208 or e-mail: immunology@uscmcd.sc.edu**. Kindly arrange to submit three letters of recommendation. The search will start immediately and continue until the positions are filled. *USC Columbia is an Equal Opportunity/Affirmative Action Employer, and encourages applications from women and minorities and is responsive to the needs of dual career couples.*

DIRECTOR

U.S. Geological Survey Western Fisheries Research Center, Seattle. Molecular to ecosystem scale fisheries research throughout the Western U.S.; six laboratory locations support genetic, conservation, habitat, climate change, and other investigations. Competitive salary and federal benefits. Apply at **website: <http://www.usajobs.gov>**. Title: Western Fisheries Research Center Director, GS-0401/0482-15. *The federal government is an Equal Opportunity Employer.*

POSTDOCTORAL POSITION Germline Stem Cells

Studies include culture, differentiation and gene activity of male germline stem cells. See *Science* 316, 404 (2007) & *PNAS* 106, 21672 (2009). Send curriculum vitae, names of three references, and a letter describing research experience to: **R. L. Brinster, School of Veterinary Medicine, University of Pennsylvania. Email: cpope@vet.upenn.edu**.

Director, Office for Policy in Clinical Research Operations, Division of AIDS

The National Institute of Allergy and Infectious Diseases (NIAID) is seeking an exceptional and visionary leader to take on the role of the director, Office for Policy in Clinical Research Operations (OPCRO) in the Division of AIDS (DAIDS). The OPCRO director is responsible for oversight of a number of critical functions to ensure 1) the sound conduct of clinical trials; 2) compliance with applicable regulations, standards, and good practice guidelines; 3) study participant safety and welfare; and 4) study quality and integrity. The OPCRO director oversees four branches composed of 20 federal employees as well as a number of on-site contractors. The OPCRO director also serves as a key advisor to the DAIDS director and to scientific programs on all clinical research oversight issues; provides objective, experience-based guidance and oversight; and is responsible for identifying and resolving a variety of complex clinical trials management, policy, and administrative issues. These issues require close coordination and interfacing with other programs within NIAID, NIH, other federal agencies, pharmaceutical companies, and patient advocacy and community groups.

Qualifications: Applicants must possess an M.D. or equivalent degree with specialization in internal medicine, infectious diseases, or any other medical specialty that will lead to expertise in infectious diseases research with a focus on HIV/AIDS. In addition, the candidate must have demonstrated skills in 1) working both independently and collaboratively in planning, organizing, and conducting/overseeing clinical trials; 2) serving effectively in clinical research program administration; and 3) effective communications and collaborations.

Application Process: Provide curriculum vitae, bibliography, and a three-page summary explaining 1) your vision for HIV/AIDS clinical research; 2) your reasons for being interested in the position; and 3) the specific leadership skills and experience you would bring to the HIV/AIDS clinical research programs at NIAID. Submit application package to Mr. Robert Gulakowski, Office of the Director, DAIDS, NIAID, 6700-B Rockledge Drive, Room 4140, Bethesda, MD 20892-7620, and reference announcement number DAIDS-11-03.

The deadline for receipt of applications is January 31, 2012. Direct any inquiries to Mr. Gulakowski at rgulakow@niaid.nih.gov or 301-496-0545. All information provided by applicants will remain confidential and will be reviewed only by authorized NIAID officials.



NIAID

National Institute of Allergy and Infectious Diseases

The successful candidate will be appointed under the Title 42(f) authority at a salary commensurate with experience. The maximum annual base salary is \$230,000, with a maximum total annual compensation limit of \$240,000. A full package of benefits is also available, including retirement; health, life, and long-term care insurance; annual and sick leave; and a thrift savings plan (401K equivalent). This position is subject to financial disclosure requirements.

To learn more about NIAID and how you can play a role in this exciting and dynamic research organization, visit us on the Web at www.niaid.nih.gov/careers/dtcl.



U.S. DEPARTMENT OF HEALTH AND HUMAN SERVICES
National Institutes of Health



National Institute of Allergy and Infectious Diseases
Proud to be Equal Opportunity Employer

The Faculty of Medicine of the University of Basel, Switzerland, invites applications for the position of a Research Professorship in

Translational Oncology

The successful candidate will be appointed as research group leader in the Department of Biomedicine and also act as vice head of the Division of Medical Oncology at the University Hospital Basel. The appointment for this position will be at the level of an Assistant or Associate Professorship, depending on the qualification of the candidate.

The position is open to candidates with the following qualifications:

- Medical diploma and Board Certificate in Medical Oncology
- Experience and broad knowledge in translational oncology
- Excellent publication record and innovative research in translational/experimental oncology
- Habilitation or equivalent academic qualification (e.g. PhD degree)
- Experience in management, social competence and strong integrative capabilities
- Experience in translating basic research oncology into clinical practice

In addition, the following profile is desirable:

- Initiative and willingness for interdisciplinary cooperation with the Basel Network of Excellence in Life Sciences
- Visionary qualities and enthusiasm
- Competence and initiative in teaching students of the medical school and residents in Translational Oncology

Teaching at the University of Basel is in German. Successful non-German speaking candidates will be expected to learn German within 2–3 years.

Application deadline is 10.3.2012

For additional information please contact:

Prof. Primo Schär, Head of the Search Committee, Basel, primo.schaer@unibas.ch, phone: +41 61 267 07 67.

Information about how to submit your application is available at:

<http://medizin.unibas.ch/dekanat/bewerbungen.html>.

Please send your application as 5 pdf-files to bewerbungen-medizin@unibas.ch



MEDICAL UNIVERSITY OF SOUTH CAROLINA

PROFESSOR AND CHAIR

DEPARTMENT OF BIOCHEMISTRY AND MOLECULAR BIOLOGY

The Medical University of South Carolina College of Medicine invites applications and nominations for the position of PROFESSOR AND CHAIR of its Department of Biochemistry and Molecular Biology. Applicants must possess a PhD and/or MD, a distinguished record of scientific research and extramural funding, administrative and leadership skills, and a commitment to education and academic excellence. The selected individual will report directly to the Dean of the College of Medicine and will be expected to foster new areas of research within the department while supporting and enhancing current research strengths.

The Medical University of South Carolina is in the midst of an exciting period of growth with recent NCI designation for the Hollings Cancer Center, a CTSA award, two new research buildings, and new clinical outreach facilities under construction. This is an outstanding opportunity for the right candidate in a city known for its enviable quality of life. Nominations and inquiries may be directed to **Peter Kalivas, PhD, Chair, Biochemistry Chair Search Committee, in care of Jennifer Nail** at nallj@musc.edu.

Interested individuals should submit a letter of interest, curriculum vitae, and the names and contact information of three references via the MUSC employment website at <https://www.jobs.musc.edu>, requisition ID#047955.

*MUSC is an Equal Opportunity Employer,
promoting workplace diversity.*

Faculty and Core Facilities Manager Positions: A New Institution for Plant Science and Biotechnology Chinese Academy of Sciences

The Chinese Academy of Sciences (CAS) is launching a new research institution with an initial emphasis on plant stress biology and expected expansion to other important areas of plant science and biotechnology. With joint funding from the Chinese central government, CAS, and the Shanghai municipality and in affiliation with the Shanghai Institutes for Biological Sciences, the new institution aims to become a world's leading center for plant-related research. It will curate innovative, vibrant, and interactive research groups synergized by a battery of state-of-the-art core facilities.

Highly motivated and talented candidates are sought for faculty positions at various levels, including well-established, mid-level and junior principal investigators (PI) and supporting PIs/core facility managers. Candidates of all nationalities who conduct cutting-edge research on any important areas of plant biology and/or have experience in managing genomics, proteomics, bioinformatics/computational biology, or cell imaging core facilities are encouraged to apply.

The supporting PIs will manage relevant core facilities (50%) and conduct collaborative and independent research (50%). All PIs will be provided with competitive packages including set-up and annual operating funds, and research staff members at various levels as well as with attractive salaries and benefits.

All candidates must have postdoctoral experiences and significant research accomplishments in relevant research fields. For the supporting PI positions, preferences will be given to candidates with extensive experiences in managing relevant core facilities. Qualified candidates should send a cover letter, CV, statement of experiences and future research interests, and arrange to have at least three references sent to:

Mr. Weijun Wang

Address: 320 Yue-yang Road, Shanghai, 200031, China

E-Mail: wjwang@sibs.ac.cn

Tel: 0086-21-54920027

Fax: 0086-21-54920078

FACULTY POSITIONS: Open Rank

King Abdullah University of Science and Technology (KAUST) is an international graduate-level, merit-based research university dedicated to advancing science and technology through innovative and collaborative research and to address challenges of regional and global significance.

Located on the Red Sea coast of Saudi Arabia, KAUST offers superb research facilities, generous assured research funding, and internationally competitive salaries. Further information can be found at: <http://www.kaust.edu.sa>.



As part of the expansion of the Bioscience Program we invite applications from exceptional candidates in the areas of:

- Plant biology with an emphasis on abiotic stress responses
- Cell and molecular biology
- Biophysics with an emphasis on structure determination by NMR and EM
- Systems biology
- Pathogen biology
- Genomics and functional genomics
- High resolution imaging applied to biological processes

Applicants should have a proven track record, as well as the ability to establish a high impact research program and a commitment to teaching and research training at the graduate level. Applications must include a complete curriculum vitae with publication list, a research plan, a statement of teaching interests, and the names and contact information of at least three references. Please submit your application electronically as a single PDF file addressed to the Bioscience Search Committee at BioS_Search@kaust.edu.sa. Priority will be given to applications received before 29 February 2012 and positions will remain open until filled. **Please identify the position in which you are applying to in the subject heading of the email.**

ANNOUNCEMENTS



2012 Distinguished Innovator Awards

The Lupus Research Institute invites applications for Distinguished Innovator Awards, a new global funding program that will run in parallel with our established Novel Research Grant program. Distinguished Innovator Awards will provide outstanding scientists with up to US \$1 million to conduct novel research into the fundamental causes of lupus and lay the groundwork for a cure.

Scientists who have not previously worked in lupus are encouraged to apply, as are researchers working outside of the US.

Now offering two unique grant programs, the LRI is the world's leading private supporter of novel research in lupus.

Deadline for Letter of Intent: February 29, 2012

Deadline for Applications: April 2, 2012

For full guidelines visit our website

www.lupusresearchinstitute.org



Vienna International Post-Doctoral Training in Molecular Life Sciences

The Max F. Perutz Laboratories offer a unique post-doctoral training program, 'Vienna International Post-Doctoral Training in Molecular Life Sciences' (VIPS), with support from the Austrian Ministry of Science and Research and the City of Vienna.

Join us in reinventing the postdoc career!

We take the traditional **postdoctoral fellowship** and add **extra independence, funding and support**. We place it in our thriving research environment to foster scientific excellence.

What we offer:

- A fast-track to the next step in your career
- Support in research design
- Independence: your own research budget and travel funds
- Grant application support
- Mentoring and coaching
- A small, friendly, but nonetheless stimulating scientific environment
- Career guidance and training
- Competitive salary and full health coverage
- A welcome package including assistance with visas
- On-site childcare

Our profile:

MFPL is part of the Vienna Biocenter Campus, a center for world class research. We offer a wide range of research areas, from Biochemistry, Cellular Biology, Immunobiology to Organismal Biology, Bioinformatics, Structural Biology and Neurosciences.

Apply to spend your post-doctoral training in a thriving scientific environment in the world's most liveable capital city!

Application Deadline 29 February 2012
www.mfpl.ac.at/vips

Contact: Gabriele Permoser, e-mail: vips@mfpl.ac.at

The Max F. Perutz Laboratories are a joint-venture of the University of Vienna and the Medical University of Vienna.





**Faculty Position in
Host-Pathogen Interactions**
**DEPARTMENT OF MICROBIOLOGY AND
IMMUNOLOGY**
**LSU HEALTH SCIENCES CENTER,
SHREVEPORT, LA**

Applications are invited for a tenure-track faculty position at the rank of Assistant or Associate Professor for a scientist working in an area of host-pathogen interactions including, but not limited to, molecular aspects of infection, interaction of the bacterial, parasitic, or viral pathogen with the immune system, or mechanisms of immune evasion. Applicants should have a Ph.D. or M.D. degree, several years of postdoctoral experience, and a history of high quality publications. Responsibilities include teaching graduate and medical students and directing a nationally competitive research program. The Department faculty of 18 members directs 40 doctoral and postdoctoral trainees and an interdepartmental NIH-funded Center for Molecular and Tumor Virology. The Department is well equipped for molecular research and is augmented by the LSUHSC Core Facility which offers BSL-3PLUS laboratories and 'state-of-the-art' biotechnologies such as flow cytometry, confocal microscopy, laser capture microdissection, DNA array analyses, proteomics, small animal imaging, etc. A Research Incentive Plan allows nationally funded investigators to receive unrestricted funds for research as well as salary augmentation.

Applicants should send a *curriculum vitae* and statement of research goals and funding and arrange for three letters of reference to:

Dr. Dennis J. O'Callaghan, Boyd Professor and Head
Department of Microbiology and Immunology
LSU Health Sciences Center
1501 Kings Highway
Shreveport, LA 71130

AA/EEO



The Hollings Cancer Center and the Medical University of South Carolina (MUSC) announce exciting recruitment opportunities for faculty at the Assistant Professor, Associate Professor and Professor level. Successful candidates will carry out independent research in areas related to cancer biology and drug development. Such areas may include cancer stem cells, tumor microenvironment, gene transcription, cell cycle control, signal transduction, DNA damage response mechanisms but with an emphasis on potential drug targets and therapeutic development. Faculty will be located in state-of-the-art laboratories in a new building developed to focus on cancer therapeutics. Outstanding resources and research support is available.

The Hollings Cancer Center is a National Cancer Institute designated cancer center; MUSC holds an NIH-funded Clinical and Translational Science Award. There are multiple complementary shared resources in place, including a Drug Discovery Screening Core, a Drug Metabolism and Clinical Pharmacology Core, Translational Research Laboratory, and a Proteomics facility. Located on the Atlantic coast of South Carolina, Charleston boasts one of the nation's most historic and picturesque downtown areas, beautiful beaches, and international cultural events such as the Spoleto Festival USA.

Interested candidates should send their CV, a summary of future research plans, and three references to:

Philip H. Howe, Ph.D.
Associate Director for Basic Sciences
Hollings Cancer Center
Medical University of South Carolina
Charleston, SC 29425
campbth@musc.edu

*MUSC is an Equal Opportunity Employer,
promoting workplace diversity.*



Basic Biomedical Sciences
The University of New Mexico
Department of Biology

The Department of Biology at the University of New Mexico invites applications for a full-time, tenure-track probationary appointment at the Assistant Professor level, beginning Fall 2012.

Preferred Qualifications: The successful candidate will demonstrate excellence in research as evidenced by pre and post-doctoral work; have a demonstrated publication record in peer-reviewed journals; be committed to establishing an internationally recognized and externally funded research program in any area of **basic biomedical science**; preference is given to areas that complement existing strengths in the Department of Biology; have promise of a commitment to excellence in teaching at the undergraduate through graduate level; and enthusiasm for working in a broad biology department with diverse research strengths is a must. This position is associated with The University of New Mexico's combined BA/MD program - a partnership between the College of Arts and Sciences and the School of Medicine (<http://hsc.unm.edu/som/combinedbamd/index.shtml>). Teaching responsibilities will include participation in one of the core biology courses that are required for the BA/MD students; either Biology 201 Molecular Cell Biology or Biology 202 Genetics. The successful candidate will be expected to develop upper level undergraduate and graduate courses in his or her area of expertise, and to mentor graduate students. For information on the Biology Department see <http://biology.unm.edu>.

Minimum Qualifications include a Ph.D. and post-doctoral experience by the start of the position. For complete details or to apply, please visit: <https://unmjobs.unm.edu/> and reference the posting number **0814073**. Review of applications will commence on **February 29, 2012**. The position will remain open until filled. To apply applicants must submit a letter of interest, curriculum vitae, three (3) recent publications, statements of research and teaching interests, a list of three (3) references, and must arrange submission of at least three (3) letters of recommendation. The letters of recommendation should be emailed as PDF attachments to BAMDFAC@unm.edu before the best consideration deadline. Questions can be directed to **Prof. Rob Miller, rdmiller@unm.edu**.

The University of New Mexico is an Equal Opportunity/Affirmative Action Employer and Educator. Women and underrepresented minorities are encouraged to apply.

WOMEN IN SCIENCE

forging new pathways in green science

Read inspiring stories of women working in "Green Science" who are blending a unique combination of enthusiasm for science and concern for others to make the world a better place.



Download this free booklet
ScienceCareers.org/LorealWiS



This booklet is brought to you by the AAAS/Science Business Office in partnership with the L'Oréal Foundation



Faculty Positions in Cancer Biology

The Solid Tumor Program at the Ohio State University Comprehensive Cancer Center and the College of Medicine invites applications for tenure-track faculty positions at the levels of Associate and Full Professor. Outstanding individuals using and/or developing mouse models of cancer are encouraged to apply. Preference will be given to funded individuals with research programs that span a wide range of topics in cancer biology including genetics, signaling, cell cycle, cell differentiation, DNA repair, transcription, DNA replication and repair, checkpoint control, cachexia, metabolism, aging, tumor microenvironment. Additional information about the OSUCCC is available at <http://cancer.osu.edu>. Applicants should submit via email a single PDF containing a letter of interest, *curriculum vitae*, description of future research plans, and the names of at least three potential referees to: **Barbara Nesbitt, ATTN: Search Committee Chair, Solid Tumor Program, The Ohio State University, Columbus OH 43210, (barbara.nesbitt@osumc.edu).**

The Ohio State University is an Equal Opportunity Employer committed to the recruitment of candidates traditionally underrepresented on university faculties and encourages applications from women, minorities, veterans, and individuals with disabilities. Flexible work options are available. EEO/AA Employer. Ohio State is an NSF Advance Institution.



TEMPLE UNIVERSITY SCHOOL OF MEDICINE DEPARTMENT OF PATHOLOGY AND LABORATORY MEDICINE NEUROSCIENTIST

The Department of Pathology and Laboratory Medicine at the Temple University School of Medicine seeks outstanding basic and translational neuroscientists for tenure leading faculty positions. The appointment may be made at any rank dependent on qualifications. Applicants should have an MD and/or PhD degree and are expected to have, or establish creative independent research programs and participate in teaching graduate and medical students. Areas of special interest are in neurovascular biology, stroke, glial biology, neurotoxic effects of drug and alcohol abuse in the central nervous system (CNS), and drug delivery into CNS. The research environment is interdisciplinary and highly collaborative. Attractive laboratory space, including a new BSL-3 facility, is available for the appointed investigators. Applicant should electronically submit a *curriculum vitae*, brief statement of research accomplishments, and future research plans to Patricia.Harper@tuhs.temple.edu. Four letters of recommendation should be sent to **Dr. Yuri Persidsky, Professor and Chair, Department of Pathology and Laboratory Medicine, Temple University School of Medicine, 3401 North Broad Street, Philadelphia, PA 19140**. Review of applications will begin **February 2012**, and will continue until all positions are filled.

Temple University is committed to enhancing the diversity of its faculty and encourages applications from women and minorities.



Laboratory Director of the SLAC National Accelerator Laboratory

Operated by Stanford University for the United States Department of Energy

Stanford University invites nominations and applications for the position of Director of SLAC National Accelerator Laboratory. SLAC, one of the world's leading research laboratories, is a U.S. Department of Energy Office of Science multi-program national laboratory. Established in 1962 at Stanford University in Menlo Park, California, 34 miles south of San Francisco, the laboratory's mission is to explore the ultimate structure of matter and the properties of energy, space and time – at the smallest and largest scales, in the fastest processes and at the highest energies – through robust scientific programs, excellent accelerator-based user facilities and valuable partnerships. The Director of the Laboratory reports to the President and Provost of Stanford University. The Director is responsible to the President of the University for the effective, responsible and safe operation of the laboratory in support of the mission of the Department of Energy. The Director reports to the Provost for all academic matters involving SLAC and its faculty.

The Director leads the development and implementation of the Laboratory's scientific vision, goals and objectives. The position serves as the lab's highest-level liaison with the DOE and other government, public and private organizations. The Director exercises overall leadership and administration of the Laboratory's programs and operations. The Laboratory maintains an outstanding and growing workforce of approximately 1,600 highly trained and award-winning faculty, scientists, engineers, computer scientists and other professionals, with an annual operating budget of approximately \$400 million. Six scientists have been awarded the Nobel Prize for work carried out at SLAC and the future of the laboratory promises to be just as extraordinary. The scientific environment is enriched by over 3,000 visiting scientists annually from universities, laboratories and industrial concerns from the U.S. and foreign countries.

Major existing facilities include the Linac Coherent Light Source (LCLS), the world's most powerful X-ray free electron laser. LCLS creates unique light that can see details to the size of atoms and processes that occur on the femtosecond time scale. Initial LCLS results have met with such success that expansion plans for LCLS-II are already underway. Other facilities include the Stanford Synchrotron Radiation Lightsource based on the 3 GeV SPEAR3 ring; the Instrument Science Operations Center for the Fermi Gamma-ray Space Telescope; the Photon Ultrafast Laser Science and Engineering laboratory (PULSE); FACET, a high-energy beam test facility for accelerator, radiation and material science; and the Kavli Institute for Particle Astrophysics and Cosmology (KIPAC). SLAC will lead the development of the camera for the Large Synoptic Survey Telescope and is an important component of the EXO program to develop increasingly sensitive double-beta decay experiments to elucidate the nature of neutrinos. The Stanford Institute for Materials and Energy Research (SIMES) is a multi-disciplinary joint institute of SLAC Photon Science and Stanford University. The SUNCAT (Sustainable eNergy through CATalysis) Center for Interface Science and Catalysis is a partnership between SLAC and the Department of Chemical Engineering at Stanford University. SLAC maintains a world-leading accelerator research program to ensure that the accelerator-based scientific programs remain at the forefront of the field. The laboratory also has the staff and facilities to advance the state of the art in particle theory, particle detector electronics, microwave power generation and control and scientific computation. In addition, SLAC is in the midst of infrastructure renewal, including major building projects that will transform SLAC into an even more robust laboratory.

Candidates should be recognized scientific leaders with vision, commitment to excellence in research, proven management skills and the interpersonal skills to work effectively with all SLAC constituencies. In addition, candidates should demonstrate the following:

- Strong credentials in scientific research and research management
- Direct experience in developing, constructing and operating major research facilities
- Political acumen and competency in organizational dynamics
- A record of obtaining funding as well as knowledge of how funding decisions are made on the agency – particularly DOE – and Congressional level
- Strategic thinking and execution skills
- Excellent communications skills
- Proficiency in lab operations and community relations

Stanford University is an Affirmative Action Equal Opportunity Employer.

Please note: This position is subject to U.S. Department of Energy approval.

Please submit applications by **February 29, 2012** to Director_search@slac.stanford.edu in PDF format OR hardcopy to US Postal address:

**SLAC Director Search
c/o Angel M. Smith
SLAC National Accelerator Laboratory
2575 Sand Hill Road, MS75
Menlo Park, CA 94025**

Get a Career Plan that Works.

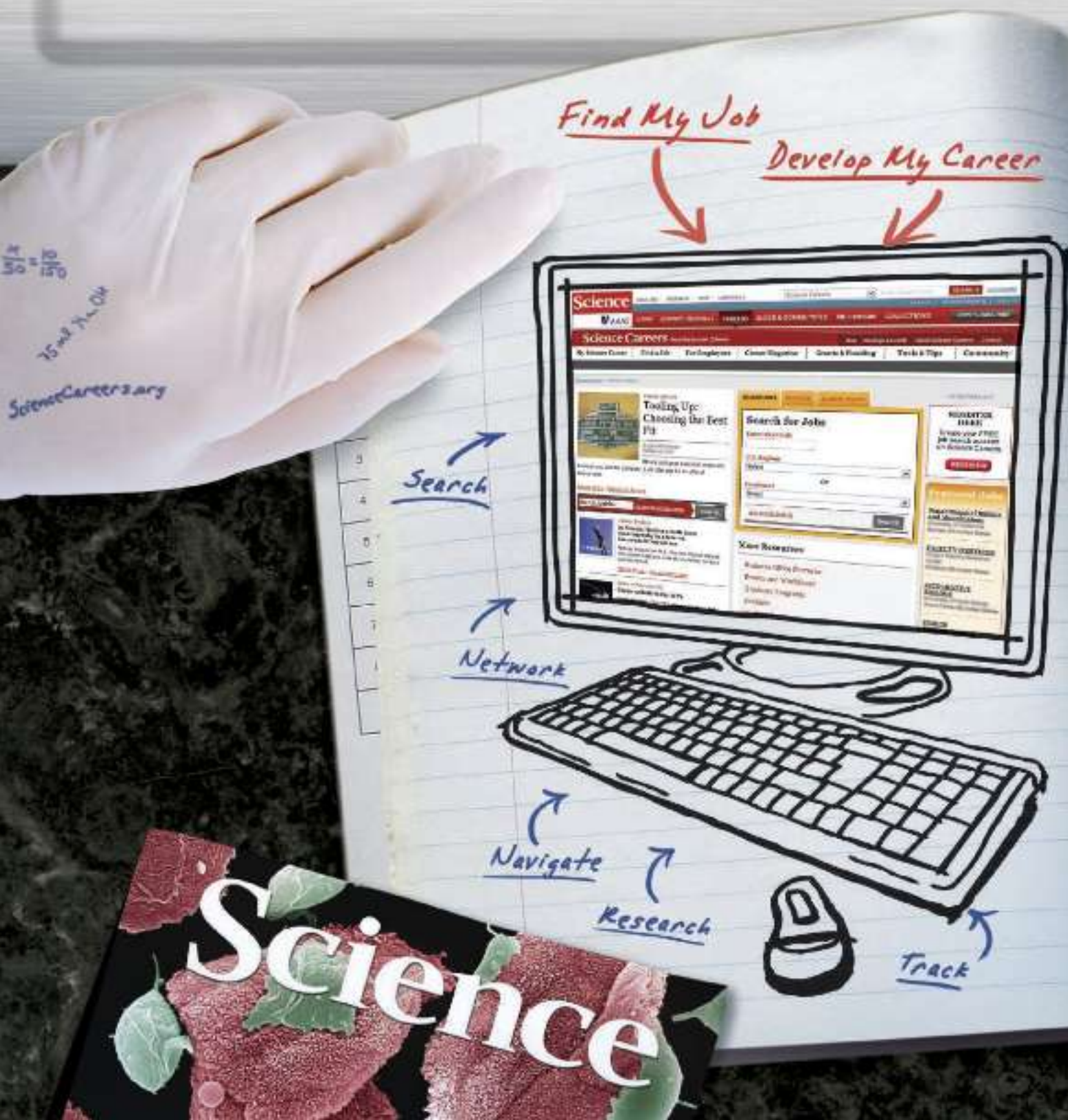
An exceptional career requires insightful planning and management. That's where *Science Careers* comes in. From job search to career enhancement, *Science Careers* has the tools and resources to help you achieve your goals. Get yourself on the right track today and get a real career plan that works. Visit ScienceCareers.org.

Science Careers

From the journal *Science*



ScienceCareers.org





Neuroscience Positions

The California Institute of Technology invites applications for tenure-track professorial positions in the Division of Biology. Positions in **Systems Neuroscience** are open to investigators studying the neural mechanisms and circuit properties that underlie behavior. Positions in **Cellular and Molecular Neuroscience** are aimed at applicants whose research programs concern molecular and/or cellular aspects of physiology, behavior, or neural development. Successful applicants are expected to develop innovative research programs and should also have a commitment to undergraduate teaching. Preference will be given to candidates at the Assistant Professor level; however, consideration will also be given to more senior applicants. Appointment is contingent upon completion of Ph.D.

Please submit online application at <http://biology.caltech.edu/Positions> and include a brief cover letter, curriculum vitae, relevant publications, and a description of proposed research. Instructions will be given for submission of letters of reference when you apply on-line. Applications will be accepted until the positions are filled.

The California Institute of Technology is an Equal Opportunity/Affirmative Action Employer. Women, minorities, veterans, and disabled persons are encouraged to apply.

MEETINGS



**Quest for Research
Excellence Conference
on
Research Integrity**

*Education, Research,
and Regulation*

**MARCH 15-16, 2012
Georgetown University
Washington, D.C.**

www.regonline.com/QUESTCONFERENCE



Science Careers

is the forum that
answers questions.

Visit our
**ENHANCED
WEBSITE!**



Science Careers is dedicated to opening new doors and answering questions on career topics that matter to you. We're the go-to career site for connecting with top employers, industry experts, and your peers. We're the source for the latest and most relevant career information across the globe.

With community feedback and a professional atmosphere, our careers forum allows you to connect with colleagues and associates to get the advice and guidance you seek.

Science Careers Forum:

- » Relevant Career Topics
- » Advice and Answers
- » Community, Connections, and More!

Visit the forum and get your questions answered today!



**Your Future
Awaits.**

Science Careers

From the journal *Science*



ScienceCareers.org



AAAS is here – helping scientists achieve career success.

Every month, over 400,000 students and scientists visit ScienceCareers.org in search of the information, advice, and opportunities they need to take the next step in their careers.

A complete career resource, free to the public, *Science* Careers offers a suite of tools and services developed specifically for scientists. With hundreds of career development articles, a grants and scholarships database, webinars and downloadable booklets filled with practical advice, a community forum providing real-time answers to career questions, and thousands of job listings in academia, government, and industry, *Science* Careers has helped countless individuals prepare themselves for successful careers.

As a AAAS member, your dues help AAAS make this service freely available to the scientific community. If you're not a member, join us. Together we can make a difference.

To learn more, visit aaas.org/plusyou/sciencecareers



The future of qPCR is here, and it's digital.



That's **ddPCR**evolutionary.

Bio-Rad's QX100™ Droplet Digital™ PCR system provides a measure of target DNA molecules with unrivaled precision and accuracy. The QX100 system partitions each sample into 20,000 individual nanoliter-sized droplets. PCR-positive and PCR-negative droplets from every sample are then counted to provide absolute target quantification in digital form. The QX100 system provides a revolutionary approach to target DNA quantification.

- Detect rare target sequences with unmatched sensitivity for cancer and viral research
- Measure small differences in target copy number variations (down to 1.2x differences)
- Determine gene expression levels without a standard curve or $\Delta\Delta C_q$

Visit www.bio-rad.com/ad/DropletPCR or contact your Bio-Rad Sales Representative to learn more.

Research. Together.

Nobel Laureates

Published in

Science

Science has published
articles by Nobel Laureates
since the award's inception!

2010 Recipients

Chemistry

Akira Suzuki
Ei-ichi Negishi

Medicine

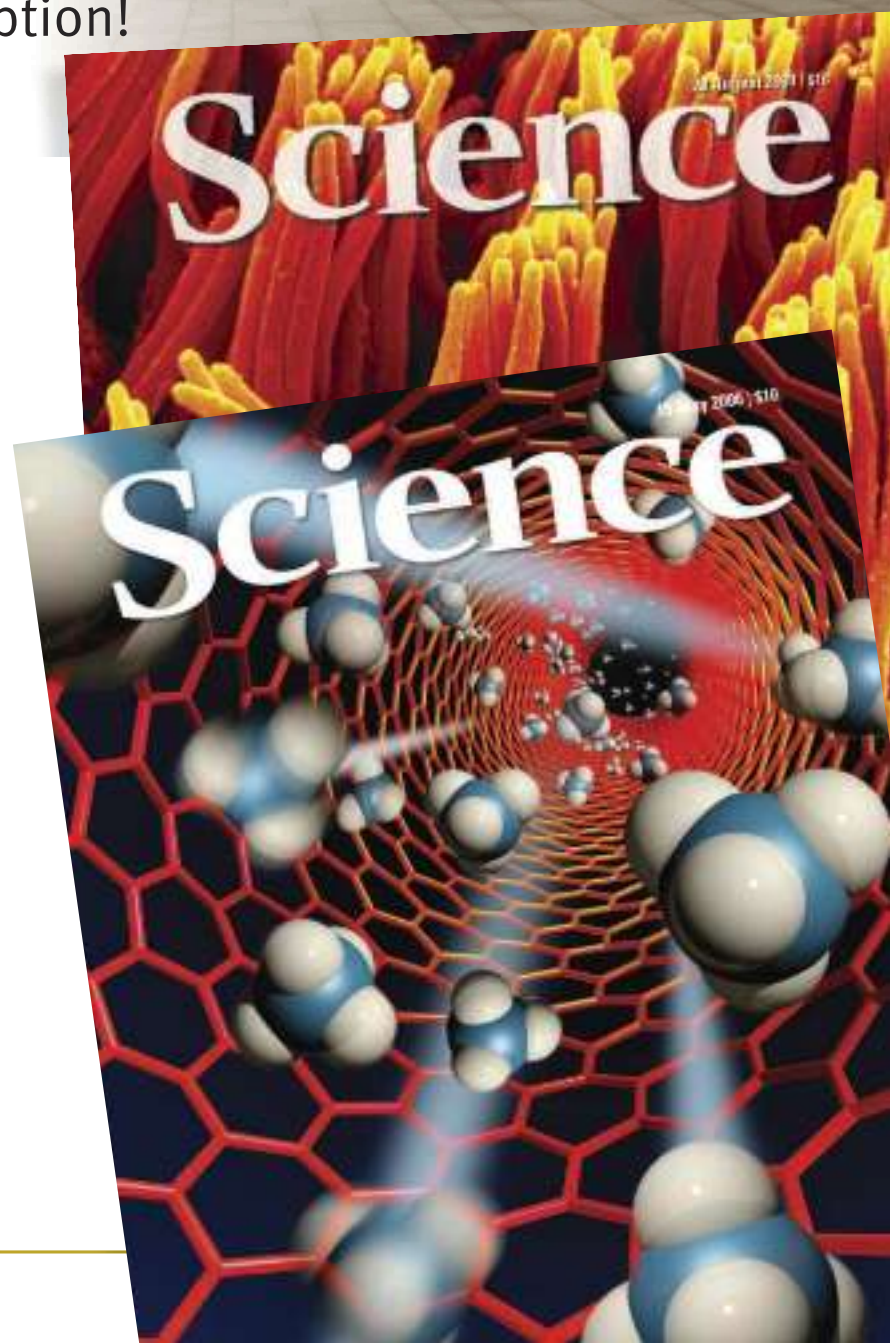
Robert G. Edwards

Physics

Andre Geim
Konstantin Novoselov

**Visit our
database!**

ScienceOnline.org/nobelprize



NEW

Women in Science Booklet

Science and the L'Oréal Foundation present



Read inspiring profiles of women
making a difference in biology.

Free download at
ScienceCareers.org/LOrealWIS

Now available:
Reagent sets for
Ion Torrent™



Take the next step.

Library Prep Reagents for Next Gen Sequencing

Isn't it time to break away from the constraints of standard workflows for NGS sample prep? With NEBNext® reagents for DNA and RNA, take advantage of multiple product formats and custom options to tailor solutions for your specific needs.

Available for the leading sequencing platforms, NEBNext reagents allow you to take the next step in designing the workflow that works for you.

www.NEBNext.com

Scan this code to learn more
about how NEBNext reagents
deliver flexibility to your
sample prep workflow



Need a code reader? Go to 2dscan.com from your mobile browser,
search for 'ScanLife' in your app store or text SCAN to 43588

Ion Torrent™ is a trademark of Life Technologies, Inc.

Science Mobile App Now Available for Android Phones



They say you never know when inspiration will strike. Download the *Science* mobile app for Android devices and be ready the next time you're inspired to read the latest news, research, and career advice from *Science* on your mobile phone.

To download the *Science* mobile app for Android visit content.aaas.org/mobile, visit the Android Market on your phone, or just scan this barcode.



Features include:

- Summaries and abstracts from *Science*, *Science Translational Medicine*, and *Science Signaling*.
- Ability to e-mail full-text links.
- The latest news from *ScienceNOW*.
- Career advice articles from *Science Careers*.
- Access to the *Science* weekly podcast and other multimedia.
- Content caching for reading without wi-fi access.





Learn how current events are impacting your work.

ScienceInsider, the new policy blog from the journal ***Science***, is your source for breaking news and instant analysis from the nexus of politics and science.

Produced by an international team of science journalists, *ScienceInsider* offers hard-hitting coverage on a range of issues including climate change, bioterrorism, research funding, and more.

Before research happens at the bench, science policy is formulated in the halls of government. Make sure you understand how current events are impacting your work. Read *ScienceInsider* today.

www.ScienceInsider.org

*Science***Insider**

Breaking news and analysis from the world of science policy



μDROP PLATE

The μDrop Plate is for the quick and easy measurement of samples down to 2 μL. The μDrop Plate provides a straightforward way of analyzing up to 16 microliter-scale samples simultaneously. The fixed-light path of the plate allows direct calculation of nucleic acid concentrations of the samples. Furthermore, users can detect dsDNA from a few micrograms to a few milligrams per milliliter, without needing to perform any dilutions. These characteristics make the μDrop Plate an ideal tool for photometric DNA or RNA quantitation and purity analysis. Samples are easily pipetted onto the μDrop Plate using a single- or eight-channel pipette. The plate is easily wiped clean, making it convenient for serial measurements. Additionally, the μDrop Plate is equipped with a cuvette slot, enabling endpoint, spectral, and kinetic measurements in a standard rectangular cuvette. The μDrop Plate has been designed for use with the Thermo Scientific Multiskan GO UV/Vis microplate and cuvette spectrophotometer, as well as the Thermo Scientific Varioskan Flash spectral scanning multimode reader.

Thermo Fisher Scientific

For info: 800-345-0206 | www.thermoscientific.com



BIOMOLECULAR IMAGING

Two new biomolecular imaging systems are available: the Typhoon FLA 9500 for imaging of multifuorescent, chemifluorescent, radioisotope-labeled, and colorimetric samples, and the Typhoon FLA 7000 IP for the dedicated study of radioisotope labeled samples. The Typhoon FLA 9500 is a versatile, high throughput laser scanner ideally suited to a multiuser environment. With a pixel resolution of up to 10 μm and a linear signal response over five orders of magnitude, the system provides precise quantitation in gels, blots, tissue sections, and arrays. A scanning area of 40 × 46 cm enables simultaneous imaging of 20 samples. The Typhoon 7000 IP is an entry-level scanner that enables high-speed, sensitive detection and quantitation of radioisotope-labeled samples. The model can scan over 10 image plates per hour, generating 16-bit images at up to 25 μm pixel resolution using storage phosphor screen technology.

GE Healthcare

For info: 800-526-3593 | www.gelifesciences.com

ISOELECTRIC FOCUSING SYSTEM

The PROTEAN i12 IEF system is the industry's only isoelectric focusing (IEF) system that is designed to simultaneously run up to 12 immobilized pH gradient (IPG) strips in 12 independently programmed lanes. For the best 2-D gel electrophoresis results, researchers optimize their sample preparation and first-dimension isoelectric focusing conditions to ensure adequate separation of complex samples. Because the optimal IEF conditions for different protein samples can vary significantly, each set of conditions must be tested separately. The PROTEAN i12 IEF system controls lanes separately, allowing researchers to set precise current limits for each lane. This enables the system to run different samples and pH ranges simultaneously while preventing differing samples from affecting each other, resulting in more reliable and reproducible focusing. The system also lets researchers test several optimization conditions simultaneously and run samples from different experiments together, both of which will speed their time to results.

Bio-Rad

For info: 800-424-6723 | www.bio-rad.com

LENTIVIRAL BIOSENSORS

A suite of LentiBrite lentiviral biosensors, prepackaged lentiviral particles encoding proteins fluorescently tagged with green or red fluorescent protein (GFP or RFP) are now available. The initial group of biosensors encode proteins responsible for cell structure such as actin and tubulin, a central marker of autophagy-LC3, and proteins that mark the onset of apoptosis. The biosensors enable detection of the presence or absence of a particular protein as well as the subcellular location of the protein in live cells under various states either by fluorescent microscopy or time-lapse video capture. Use of lentivirus to deliver fluorescently-tagged proteins into cells offers higher-efficiency transfection as compared with traditional chemical-based and other nonviral-based methods. In addition, the virus particles can be used to transfect dividing, nondividing, and difficult-to-transfect cells, such as primary and stem cells, leading to long-term, stable expression of the transgene with low immunogenicity.

EMD Millipore

For info: 800-645-5476 | www.millipore.com

PCR MASTER MIX

The GoTaq Long PCR Master Mix is an optimized enzyme mixture for improved long-range polymerase chain reaction (PCR). The new kit enhances PCR yield, sensitivity, and specificity and enables efficient amplification of up to 40 kb from lambda DNA or 30 kb from human genomic DNA. The new master mix is ideal for cloning genes, mutational analysis, and DNA sequencing. The GoTaq Long PCR Master Mix contains the high-performance GoTaq Hot Start Polymerase in a specially formulated mixture with a second proprietary thermal stable proofreading polymerase. The presence of a proofreading enzyme to repair DNA mismatches in the presence of a highly processive polymerase allows increased DNA elongation, resulting in longer DNA amplification. GoTaq Long PCR Master Mix consists of a master mix containing the polymerase and proofreading enzyme mixture, dNTPs, and MgCl₂. Also provided are control primers, human genomic control DNA, and nuclease-free water.

Promega

For info: 800-356-9526 | www.promega.com

Electronically submit your new product description or product literature information! Go to www.sciencemag.org/products/newproducts.dtl for more information.

Newly offered instrumentation, apparatus, and laboratory materials of interest to researchers in all disciplines in academic, industrial, and governmental organizations are featured in this space. Emphasis is given to purpose, chief characteristics, and availability of products and materials. Endorsement by *Science* or AAAS of any products or materials mentioned is not implied. Additional information may be obtained from the manufacturer or supplier.

AAAS ANNUAL MEETING

Be Part of a Winning Team



Vancouver is a dynamic, multicultural city set in a spectacular natural environment. It was the proud host of the 2010 Olympic and Paralympic Winter Games. In 2012 it hosts the world's annual Olympiad of Science, 16-20 February.

AAAS organizes an international conference annually—4 days of symposia, lectures, seminars, workshops, and poster sessions that cover every area of science, technology, and education. We also organize a unique community science showcase that offers an array of hands-on demonstrations and other family friendly activities.

Attendees constitute a highly educated, global market that promotes the effective use of research and practice.

They represent nearly all U.S. states and territories as well as up to 55 countries. Technologically savvy, our attendees are always looking for new and improved tools and resources.

Take this opportunity to select or design your sponsorship and secure your exhibit space.

For more information about sponsorship opportunities and the exhibition, contact Isabel Patterson, AIM Meetings, (703) 549-9500; ipatterson@aimmeetings.com. For the program, go to www.aaas.org/meetings.



Presenting sponsor

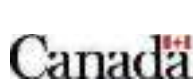


Gold



a place of mind
THE UNIVERSITY OF BRITISH COLUMBIA

Silver




Bronze



Council of Canadian Academies
Conseil des académies canadiennes

AAAS thanks

THE  KAVLI FOUNDATION for its generous support of the Science Journalism Awards.

Bioidentify.

Pinpoint the functional gene targets for your miRNA with the MISSION® Target ID Library.

The MISSION Target ID Library enables transcriptome-wide identification of gene targets regulated by microRNA and other non-coding RNA. Simplify target identification with these easy steps: transfect library, select, transfect miRNA and select target clones.

sigma.com/targetid

biosilencing